UNIVERSITY OF SOUTHAMPTON

Experimental studies on a liquid ultrasonic cylindrical waveguide

by

Maruthi Nikhil Banda

Thesis for the degree of Doctor of Philosophy

in the

Faculty of Engineering and Environment
Institute of Sound and Vibration Research

July, 2017

UNIVERSITY OF SOUTHAMPTON
Faculty of Engineering and Environment

Doctor of Philosophy

ABSTRACT

Experimental studies on a liquid ultrasonic cylindrical waveguide.

by Maruthi Nikhil Banda

This thesis presents research work on an ultrasound assisted stream (UAS) device, commercially known as the "Starstream device". The UAS device combines ultrasonic energy with a stream of flowing liquid, which could be directed onto target surfaces for contaminant removal. At the start of this project, the focus was towards understanding the response of the device and to improve its performance. Research work thus included studies into acoustic cavitation, capillary instability, electrochemistry & microbubble generation, and transducer design. The required control over flow rate, liquid temperature, and speed of sound was achieved by modifying and upgrading the existing experimental setup.

During the experiments, the adverse influence of unwanted microbubbles was successfully reduced by employing an ultrasonic standing wave cylindrical column (called the outgasser). The performance of the outgasser was quantified using acoustic and photographic observations, and its use demonstrated an increase in the pressure output of the device. The non-linear response of the device was quantified and was correlated to the non-linear response of the piezoelectric transducer. The non-linear response was classified into linear, transition, and non-linear regimes.

The linear regime of the UAS device was investigated experimentally at resonance at off-resonance frequencies of the transducer, under different loading conditions (air, water, bubble-free liquid, bubbly-liquid). Bubbly-liquid was electrolysed in the liquid stream and the microbubbles generated were optically measured. Discussions of the experimental results were supported by the investigations on the electrical impedance of the transducer by employing lumped-parameter modelling (under different loading conditions).

The operation of the device in its non-linear regime was found to be characterized by a novel capillary instability formation of the cylindrical stream. The capillary instabilities were simultaneously investigated using high-speed optical and acoustical techniques at different liquid flow rates, surface tension values, and viscosity conditions. An external technique to control them was successfully implemented. Finally, a combination of experimental kits and techniques reported in the thesis was shown to improve the performance of the existing UAS device.

Declaration of Authorship

I, Maruthi Nikhil Banda , declare that the thesis entitled *Experimental studies on a liquid ultrasonic cylindrical waveguide* and the work presented in the thesis are both my own, and have been generated by me as the result of my own original research. I confirm that:

- this work was done wholly or mainly while in candidature for a research degree at this University;
- where any part of this thesis has previously been submitted for a degree or any other qualification at this University or any other institution, this has been clearly stated;
- where I have consulted the published work of others, this is always clearly attributed;
- where I have quoted from the work of others, the source is always given. With the exception of such quotations, this thesis is entirely my own work;
- I have acknowledged all main sources of help;
- where the thesis is based on work done by myself jointly with others, I have made clear exactly what was done by others and what I have contributed myself;

Signed:.....

Date:.....

Acknowledgements

This thesis is commercial in confidence. It is my pleasure acknowledge several individuals who were instrumental in the completion of my Ph.D. research.

This work would not be possible without the help and guidance of Professor Tim Leighton and Dr. Peter Birkin.

Thanks to:

Professors Phil Joseph and Victor Humphrey for very many useful discussions. Dr. Doug Offin for his help in the chemistry lab and Dr. Jian Jiang for his help at the start of this project. Maureen Mew for proofreading. Dr. Andrew Hurrell for constructive criticism. The ISVR Rayleigh Scholarship which made my Ph.D. a reality. The Royal Society Brian Mercer Award for funding.

Dr. Philippe Blondel, whose unwavering support through the toughest of time was unmatched. Roy Wyatt for his continued confidence in me and for his kindness.

ISVR which was my home for 4 years, all the friends with whom I shared countless lunch hours, coffee breaks, sci-fi discussions, movie ratings, debates, and of-course acoustics.

Laurence, Fabio, Mengyang, Guido, Alicia.

Dipo, Prasad, Murali, Ashish, and Mithilesh.

My parents for all the support they have given me over the years. Pinky, Vikram, and little Sivansh for their kind hearts. Attaygaru, Mavayyagaru, Pratyu, and Lohith for their genuine interest.

Pravallika and Aarav, I may have started this without you, but never would have been able to get here without.

Above all, Balaamba & Hanuman for everything.

Contents

List of Figures

List of Tables

Symbols

a	Mean radius of a cylindrical stream	mm
a_1	Mean radius of stream at specific distance from the tip	mm
a_t	Radius of transducer face in contact with the liquid	mm
A	Cross sectional area of a piezo element	mm^2
A_a	Area of the transducer face in contact with the liquid	mm^2
A_m	Pressure amplitude of mode m	Pa
b	Overall damping for a free bubble	s^{-1}
b_f	Overall damping for a forced bubble	s^{-1}
b_v	Viscous damping for a bubble	s^{-1}
b_{th}	Thermal damping for a bubble	s^{-1}
b_{rad}	Radiative damping for a bubble	s^{-1}
B	Susceptance	mS
B_l	Bulk modulus of bubble-free liquid	Pa
c	Speed of sound in bubble-free water	$m.s^{-1}$
c_m	Speed of sound of bubbly mixture	$m.s^{-1}$
C	Constant	NAe
C_1	Clamped capacitance	pF
C_e	Motional capacitance (mechanical compliance)	pF
C_{LF}	Low frequency capacitance	pF
d_{33}	Short-circuit compliance coefficient	pm/V
dp/dt	Slope of the pressure-time plot	Pa/s
d_b	Distance between two bubbles	μm
$\boldsymbol{e}_r$	Radial unit vector	NA
f_0	Natural frequency of a bubble	Hz
f	Excitation frequency	Hz
f_c	Cut-off frequency	Hz
f_{cap}	Excitation frequency for capillary waves	Hz
f_{ins}	Measured capillary instability frequency	Hz
f_s	Sampling frequency	Hz
F	Faraday's Constant	$C.mol^{-1}$
F_1	Primary Bjerknes forces	N
F_2	Secondary Bjerknes forces	N
$F_{R_1R_2}$	Force between two bubbles	N
F_b	Average force on transducer face	N
G	Conductance	mS
i_t	Current flowing into the ultrasonic transducer	mA
I	Current passing through electrolyte	mA
I_0	Modified Bessel function I kind, first order	NA
I_1	Modified Bessel function I kind, second order	NA

j	Complex number ($\sqrt{-1}$)	NA
J_m	Bessel function of first kind of order m	NA
k_{cap}	Capillary wavenumber in axial direction	mm^{-1}
k_r	Wavenumber in radial direction	mm^{-1}
k_t	Wavenumber in the medium	mm^{-1}
k_z	Wavenumber in axial direction	mm^{-1}
K	Compressibility of bubble-free liquid	Pa^{-1}
K_1	Constant	NA
K_a	Compressibility of air	Pa^{-1}
K_m	Compressibility of bubbly liquid	Pa^{-1}
l	Natural number	NA
L	Breakup length of stream	mm
L_e	Motional inductance	mH
L_s	Length of a piezo stack	mm
L_x	Room length in X-direction	m
L_y	Room length in Y-direction	m
L_z	Room length in Z-direction	m
m	Modal number	NA
m_1	Number of acoustic cycles	NA
M	Number of Moles	NA
M_r	Radiation mass	$\mathrm{kg.rad}^{-1}$
M_{er}	Equivalent variable for radiation mass	$\mathrm{kg.V}^2\mathrm{.N}^{-2}\mathrm{.rad}^{-1}$
n	Number of electrons required for electrolysis	NA
n_1	Number of bubble radial oscillations	NA
nb	Number of eigen frequencies of a rectangular block	NA
n_p	Number of piezo elements in a stack	NA
n_x	Number for nodal plane in X-direction	NA
n_y	Number for nodal plane in Y-direction	NA
n_z	Number for nodal plane in Z-direction	NA
N	Number of bubbles	NA
NV	Product of N and V	$\mu\mathrm{m}^3$
N_1	Number of bubble per unit volume	$\mu\mathrm{m}^{-3}$
N_{em}	Transformer ratio	$\mathrm{N.V}^{-1}$
p	Pressure parameter	Pa
p_s	Mean pressure inside a cylindrical liquid stream	Pa
P_0	Hydrostatic pressure in liquid	Pa
P_{bl}	Blake threshold pressure	Pa
P_g	Gas pressure inside the bubble	Pa
P_{ge}	Equilibrium gas pressure inside the bubble	Pa
P_i	Pressure inside the bubble	Pa
P_{ie}	Equilibrium pressure inside the bubble	Pa
P_L	Pressure in the liquid	Pa
$P_n(r_0)$	Pressure at measurement location	Pa
$P_n(r_1)$	Incident pressure at source location	Pa
P_t	Average pressure on transducer face	Pa
P_v	Vapour pressure inside the bubble	Pa
P_σ	Laplace pressure due to surface tension	Pa
P_ω	Transfer function for pressure within a rectangular block	Pa
q	Growth rate of capillary disturbance	s^{-1}
Q	Charge passing through electrolyte	C

Q_e	Electrical quality factor	C
Q_m	Mechanical quality factor	C
r	Radial parameter in a cylindrical waveguide	mm
$\boldsymbol{r}_0$	3D location of source	NA
$\boldsymbol{r}_1$	3D location of receiver	NA
r_a	Principal radius of curvature cylindrical waveguide	mm
r_w	Principal radius of curvature in a cylindrical waveguide	mm
R	Instantaneous bubble radius	μm
$\ddot{R}$	Acceleration of bubble wall	μm.s^{-2}
R_0	Mean bubble radius	μm
R_1	Electrical dissipation resistance	Ω
R_a	Lower limit for bubble radius	μm
R_b	Upper limit for bubble radius	μm
R_e	Motional resistance	Ω
R_r	Radiation resistance	N.s.m^{-1}
R_{er}	Equivalent radiation resistance	V^2.s.N^{-1}.m^{-1}
R_{crt}	Critical radius	μm
R_{max}	Maximum radius achieved by a bubble	μm
Re	Reynold's Number	–
SD	Standard deviation of a bubble size distribution	μm
S_{33}^E	Piezoelectric strain coefficient	pm/V
t	Time parameter	s
t_0	Time for an acoustic cycle	s
t_1	Pulse repetition period (PRP)	s
t_2	Pulse length	s
T_{max}	Maximum temperature observed at a bubble interior	K
u_0	Stream flow velocity	m.s^{-1}
u_t	Vibrational velocity of transducer face	m.s^{-1}
V	Volume of a spherical bubble	μm^3
V_1	Volume of a spherical bubble of radius R_1	μm^3
V_2	Volume of a spherical bubble of radius R_2	μm^3
V_c	Volume of a liquid	μm^3
V_g	Volume of a gas in cloud	μm^3
V_{pa}	Voltage input to power amplifier	V
V_t	Voltage across ultrasonic transducer terminals	V
V_w	Volume of pure water in bubble cloud	m^3
We	Weber Number	–
W_a	Acoustic power	W
W_d	Di-electric power	W
W_e	Electrical power	W
x_0	Absolute value of dimensional vector in X-direction	m
X_{ml}	l^{th} zero of J_m	NA
X_r	Radiation reactance	N.s.m^{-1}
y_0	Absolute value of dimensional vector in Y-direction	m
Y	Electrical admittance	mS
z_0	Absolute value of dimensional vector in Z-direction	m
Z	Axial parameter in cylindrical waveguide	mm
Z_e	Electrical impedance	Ω
Z_r	Radiation impedance	N.s.m^{-1}

α_{cap}	Temporal growth rate of capillary waves	NA
β	Void Fraction (Gas Volume fraction)	NA
γ	Polytropic exponent	NA
δ_n	Damping constants of modes in rectangular block	s^{-1}
η	Instantaneous radial displacement of stream	mm
η_1	Radial displacement of stream from mean position	mm
θ	Azimuthal parameter in cylindrical waveguide	rad
κ	heat conduction factor	NA
λ	Capillary Wavelength	mm
μ	Dynamic liquid viscosity	$mm^2.s^{-1}$ (cSt)
τ	Surface tension	$mN.m^{-1}$
ρ	Density of bubble-free liquid	$kg.m^3$
ρ_1	Density of Rho-c material	$kg.m^3$
ρ_a	Density of air	$kg.m^3$
ρ_m	Density of bubbly liquid	$kg.m^3$
Ψ	Mode shape in cylindrical co-ordinates	Pa
ω	Radial excitation frequency	$rad.s^{-1}$
ω_a	Anti-resonance frequency of a transducer	$rad.s^{-1}$
ω_n	Eigen frequency of rectangular block	$rad.s^{-1}$
ω_r	Resonance frequency of a transducer	$rad.s^{-1}$
ω_{tr}	Resonance frequency of a piezo transducer	$rad.s^{-1}$
ω_{cap}	Circular capillary excitation frequency	$rad.s^{-1}$
ω_0	Radial natural frequency of a bubble	$rad.s^{-1}$
∇^2	Laplacian operator	NA
∇P	Variational in pressure	Pa

यस्य त्वेतानि चत्वारि वानरेन्द्र यथा तव ।

धृतिर्दृष्टिर्मतिर्दाक्ष्यं सः कर्मसु न सीदति ॥

- आकाशाचारीणि

इति महाकवि वाल्मीकि विरचितम्
श्रीमद् रामायण महाकाव्य मध्ये
सुन्दराकान्ड अन्तर्गतम्
(१५. १. १९८)

Chapter 1

Introduction

1.1 The ultrasound activated stream device

The study pertaining to the use of ultrasonic energy either in diagnostic medicine or in ultrasonic cleaning baths or for heavy-duty industrial cleaners covers many research disciplines [1] and has strong commercial applications [2] attached to it. The safe application of ultrasonic energy in diagnostic medicine [3] is strictly controlled by published guidelines [4]. With the safety of the users in mind, they are generally advised against inserting hands into ultrasonic baths while they are turned on. Cleaning baths are advertised as quick and easy devices to remove contaminants from machine tools, jewellery, dental/surgical instruments, watches etc. Ultrasonic cleaning baths employ large amplitude ultrasonic pressure waves to agitate the liquid inside their reservoirs (or tanks). Therefore, the size of the tank restricts the maximum dimension of objects that can be cleaned within them. It was shown that the acoustic pressure field inside an ultrasonic cleaning bath can easily be altered by placing a small object (for example, a coin) in its tank [5]. Consequently, the presence of an object in the tank has an impact on the cleaning efficiency [5].

An alternative suggestion to cleaning using ultrasonic energy is by employing a stream of liquid [5, 6]. An ultrasound activated liquid stream (henceforth shortened to UAS) device offers advantages in portability, no limit on target size, and possible multiplicity on the number of UAS units that could be deployed as an array. An existing benchtop UAS device - commercially named “Starstream” - was studied and reported in this thesis. The broad aim of this thesis is to improve the performance of the existing UAS device by employing new experimental equipment and by studying its pressure output. A schematic of the construction and the working procedure of the UAS device in a laboratory arrangement are presented below.

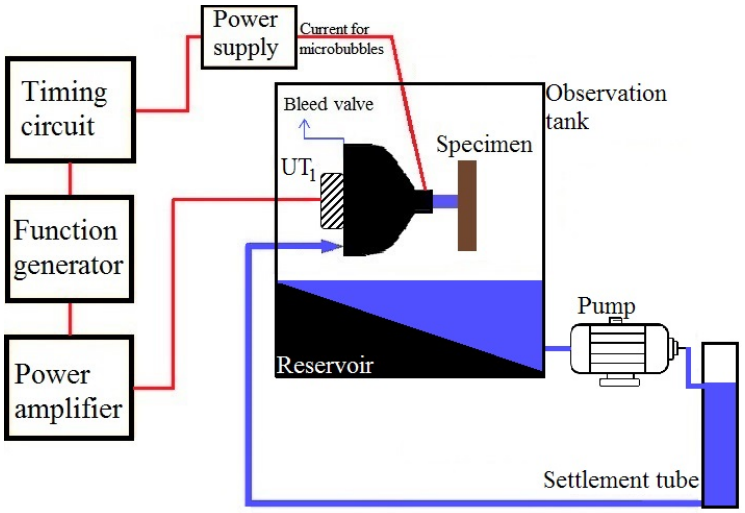

Figure 1.1: A schematic for the ultrasound activated stream device (UAS or "Starstream" device) in a liquid recycling arrangement. The blue line represents the liquid path and the red line represents the electrical path. Specimens to be cleaned are rigidly held in the stream at a distance of 20 mm from the nozzle tip.

The UAS device (or "the device") consists of a conical shaped nozzle made from a two-part polymer procured from Acoustic Polymers Ltd. The polymer was advertised as having characteristic acoustic impedance properties similar to that of water [7]. The cone was manufactured by pouring the mixture (of the two parts polymer) into a polytetrafluoroethylene (PTFE) mould and allowing the mixture to cure for 48 hours. The broad side of the cone was then attached to a polycarbonate sheet with holes provided for water inlet and a bleed valve. A commercial ultrasonic transducer (UT_1) with its resonance frequency at 135 kHz was glued to the centre of the polycarbonate sheet. Deionized (DI) water with (some) additives was generally used as the working liquid[1] and was circulated in a closed loop using a pump. Figure 1.1 shows the UAS device operating in a closed loop liquid recycling arrangement.

The liquid path also consists of a settlement tube, which was used for removing the unwanted microbubble population in the liquid (by the buoyancy principle). The unwanted microbubbles in the liquid could either be generated at the pump blades or could be entrained by the liquid stream leaving the nozzle when it plunges into the reservoir. The settlement tube was a glass tube of 70 mm internal diameter (ID) and 73 mm outer diameter (OD). The water inlet and outlet for the settlement tube were provided via holes made into large bung plugs at both its ends. The liquid in circulation generally fills half the volume of the settlement tube (when laid down along its length).

The liquid flow rate was generally maintained between 1.8 to 2.2 litre.min^{-1}. The conical chamber at its narrow end had provision for generating microbubbles in the

[1]In this thesis, "water" refers to DI water (generally) taken from a PUR1TE device. The word "liquid" is reserved for DI water with additives such as salt, different types of surfactants, or glycerol.

liquid by electrolysis. For this purpose, two 100 μm diameter platinum (Pt) wires (their location is marked in Figure 1.1) were used as electrodes. In order to aid electrolysis additives added to the DI water were 0.1 M Sodium Sulphate (salt at 14.2 g per litre), and 2 mM Do-Decyl Sodium Sulphate (SDS, surfactant at 0.576 g per litre). The narrow outlet of the cone is termed "the nozzle" and has an opening diameter of 10 mm. The liquid flows out of the nozzle along with the microbubbles (generated by electrolysis at the edge of the nozzle) and impinges onto the target surface of the specimen held rigidly. Specimen were cleaned by the ultrasonic energy in the liquid and were assisted by the motion of microscopic bubbles in the ultrasonic field (refer to Figure 1.2). The liquid then collects in the observation tank, which could either be recycled or drained.

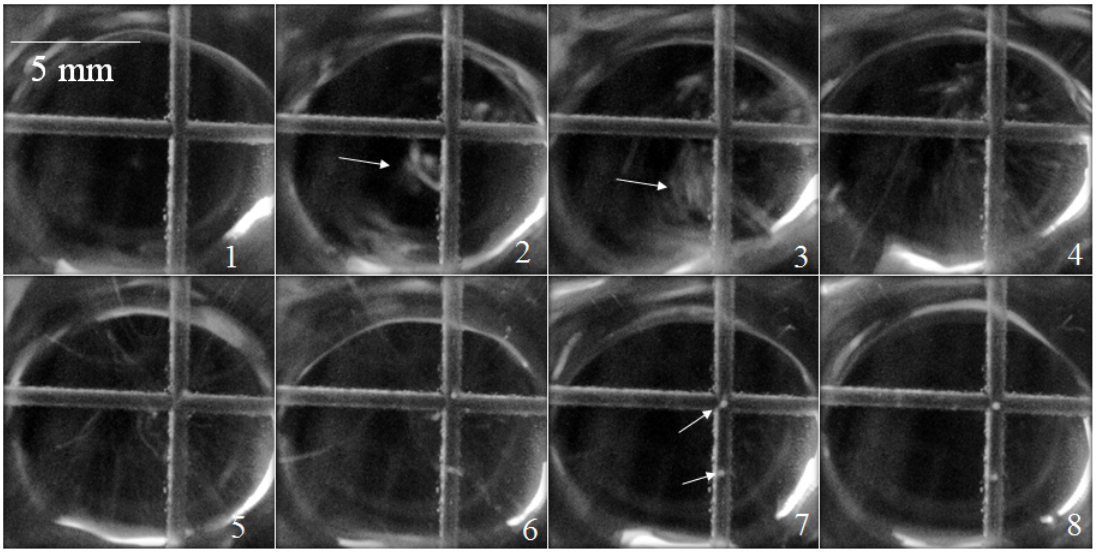

Figure 1.2: A series of images extracted from a high-speed video recording, when the camera is directed onto the stream of liquid emerging from the nozzle and hitting a transparent sheet of glass. Each image is 8 ms apart.

The red path in Figure 1.1 represents the electrical circuit used for pulsing the transducer (UT_1) and for generating electrolytic microbubbles. The transducer UT_1 generates pulses of ultrasound and the resultant pressure waves travel down the conical chamber, out of the nozzle, and into the stream [6]. The timing pattern for pulsing both the transducer and the bubble current were maintained by a home built timing circuit box. The signals for the microbubble generation and the ultrasonic signal were triggered alternatively with a short delay (generally around 40 ms), as demonstrated in Figure 2 of reference [6] and Figure 3a of reference [8]. This small delay allowed the bubbles to travel from the electrodes to target surface along with liquid (at a velocity of 0.42 m.s^{-1} for flow rate of 2.0 litre.min^{-1}). The ultrasonic signal was then triggered and the shear forces generated at the bubble walls assisted in dislodging and removing the contaminants.

For observing and recording the motion of microbubbles in the stream of liquid exiting the UAS device, a Phantom V5.1C high-speed camera was used. The stream was directed onto a transparent glass sheet (placed in-between the nozzle and camera), with cross-wire shaped grooves cut into it. Figure 1.2 shows a series of snapshots spaced 8 ms apart recorded at 1000 frames per second (fps) with 500 μs exposure time per frame. The circular feature visible in each frame is the outer edge of the stream. Bubble clouds generated at the electrodes (as highlighted by the white arrow) can be seen in frames 2 and 3, which then travel downstream with the liquid (as seen in frames 3 and 4). When the ultrasonic transducer was activated (here, between frames 4 and 5) the bubbles clump together influenced by the acoustic radiation forces [9] and are directed towards the cross shaped crevice (frames 6 and 7). In frame 8 bubbles can be seen to stay in the crevice, powered by the ultrasonic energy. Once the transducer was turned off, the microbubbles dislodged from the crevice and were observed to wash away (not shown in the figure). This process repeats itself, as fresh liquid carrying microbubbles arrives at the target surface. Similar observations were reported [10] during experiments conducted on cleaning of silicon wafers immersed in water baths activated by ultrasound in the MHz regime.

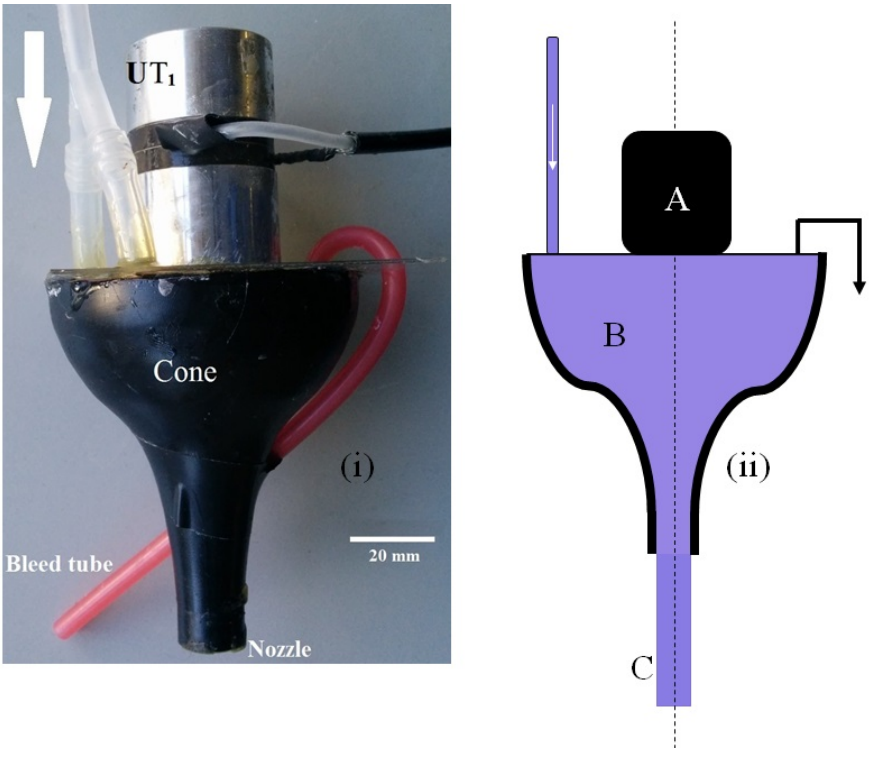

Figure 1.3: Part (i) is a snapshot of the UAS device, with transducer UT_1 and the conical chamber attached onto a polycarbonate sheet. The white scale bar is 20 mm long. Part (ii) is a line sketch of the device. The working parameters in regions marked as "A", "B" and "C" influence the performance of the device. These regions were studied extensively.

In the UAS device, the conical chamber plays an important role in containing the liquid, directing it into a stream, and acting as a waveguide for the ultrasonic energy. A snapshot of the conical chamber is shown in part (i) of Figure 1.3 along with the transducer (UT_1), the liquid inlet and bleed tubes. Water inflow direction is marked by a white arrow and the inlet tube is connected to a Y-junction connector. The red coloured tube is the bleed pipe for taking the excess air out of the conical chamber. Part (ii) of Figure 1.3 shows a line sketch representation of the device with liquid in blue. Regions "A", "B" and "C" in part (ii) of Figure 1.3 mark the different regions of the device that influence its performance. These are region "A" - the power input to the ultrasonic transducer UT_1, region "B" - the acoustic properties of the liquid inside the conical chamber, and region "C" - the stability of the cylindrical stream that exits the nozzle. Changes to system properties such as the variation in power input to the transducer, the increase in or decrease of the void fraction of liquid in operation, and the capillary instabilities on stream surface, can either improve or degrade the cleaning efficiency of the device. To improve the performance of the UAS device a detailed knowledge of the interdependence between the regions "A", "B" and "C" is needed.

The next section presents the motivation for this thesis and the aims that were derived from them. Then, a brief introduction to each chapter in this thesis is provided.

1.2 Motivation and thesis structure

The motivation for this thesis was driven by the research necessitated to understand and improve the performance of the UAS device. For the device to perform better, research should be directed towards understanding the relationship between the input power, the acoustic properties of the liquid inside the conical chamber, and the stability of the stream. Although the device operating in a laboratory benchtop arrangement, as shown in Figure 1.1, successfully demonstrated cleaning [11, 12], it had scope for improvement. For example:

- it was observed that the settlement tube required up to 30 minutes to remove the unwanted microbubbles from the working liquid,
- it was presented in technical reports [13, 14] that the acoustic pressure output from the device increases non-linearly with linear increase in voltage input to the power amplifier, and
- the cylindrical stream exiting the nozzle was observed to be unstable under some operating conditions.

In this thesis, the acoustic pressure output (as measured outside the nozzle and in the stream) was used to assess the performance of the device. Hence it is important to design experimental techniques that control the influence of system variables affecting the pressure output. These system variables are liquid flow rate, viscosity, surface tension, liquid temperature, and void fraction. Subsequently, the following points were identified as the aims of this thesis:

1. redesigning the experimental setup (shown in Figure 1.1) to aid effective control of system parameters,
2. quick and effective restraint over unwanted microbubble population present in the liquid,
3. study of the response of the transducer in relation to input,
4. response of the device to bubble-free liquid,
5. response of the device to bubbly liquid at known void fractions and,
6. study of the capillary stability of the cylindrical stream.

The next section provides a brief overview of the contents of each individual chapter in this thesis.

1.2.1 Thesis Structure

The ultrasonic pressure oscillations set-up in a liquid are the source for many physical phenomena that aid in cleaning. These include acoustic cavitation [15], hot spot formation [16], viscous microstreaming patterns [17, 18], the sudden collapse of bubbles [19], surface waves on the microbubbles [20, 21] etc. These physical phenomena will be introduced and discussed in Chapter 2. A brief discussion on acoustic propagation in waveguides and capillary instabilities will also be presented.

Chapter 3 presents the modified experimental kit that aids in the control of liquid temperature and it features a new design for liquid inlet to the conical chamber, an active technology to remove unwanted microbubble population from the liquid (called the outgasser), and an electrolysis chamber that can generate microbubbles of known void fraction and size. Extensive acoustic and photographic studies investigating the effectiveness and the response time of the outgasser will be presented. The aim of these observations is to demonstrate that the outgasser is effective and quicker in restraining unwanted bubble population of the liquid in its cylindrical column when compared with

the settlement tube. This chapter ends with a suggestion to replace the settlement tube with the outgasser.

Chapter 4 focuses on the electrolysis of microbubbles in a custom-made generation chamber and presents the optical observations of the bubble size distribution (BSD) generated. This bubble generation chamber was designed to take bubble-free liquid from the outlet of the outgasser and to feed bubbly liquid into the conical chamber. To estimate the BSD generated under different flow rates, electrode currents, and surfactant concentrations the liquid leaving the generation chamber was imaged using high-speed videography. The images from the videography were then used to estimate the BSD, and the influence of various working parameters on BSDs generated will be discussed in detail. These microbubbles were used to investigate the response of the UAS device to bubbly liquid.

Chapter 5 presents the response of the UAS device to bubble-free liquid at the resonance frequency of UT_1 (135 kHz). This includes experimental studies into the response of the ultrasonic transducer at different operating conditions and identification of its linear and non-linear regimes. These results will be combined with the measurements of acoustic pressure in the stream under similar operating conditions. The non-linear pressure output of the device will be discussed in detail and its relationship to the power dissipated in the transducer will be presented. The influence of the outgasser on the performance of the device will also be presented and discussed.

Chapter 6 presents the response of the device to bubbly liquid at resonance (135 kHz) and off-resonance (120 kHz - 145 kHz) frequencies. Observations on the pressure output when using bubbly liquid are aided by the discussions of power dissipated in the transducer. The off-resonance performance of the device will be discussed by considering the changes to the input electrical impedance of UT_1, measured using an impedance analyzer. The measured electrical admittance values were compared with the results from lumped parameter modelling of the transducer. The conclusions of this chapter discuss the advantages and limitations of the modelling technique and compares them with the experimental results on the UAS device when using bubbly liquid.

Chapter 7 moves onto the investigation of the non-linear regime based capillary instability phenomenon observed on the stream exiting the nozzle. The influence of system parameters (flow rate, liquid temperature, surface tension, and viscosity) on the stability of the stream will be presented. The radial capillary instabilities formed on the stream reduce its intact length and restricts the propagation of ultrasonic energy beyond its breakup length. The temporal evolution of the instability process was studied using acoustic and photographic observations and will be presented. A practical solution that improves the intact length of the stream will be presented.

Chapter 8 presents the conclusions of this thesis based on the research work presented in Chapters 3 to 7. This chapter also provides suggestions for further research and development on the UAS device.

The next section presents the summary of this chapter.

1.3 Summary

An introduction to the UAS device is presented in this chapter. The working principle and the basic laboratory based experimental setup are detailed. The aims of this thesis, derived from the requirement to improve the performance of the device are presented and the thesis structure, divided into individual chapters, was detailed.

To understand the dynamics of the fluid and the dynamics of the microbubbles during operation of the UAS device, a detailed knowledge of their physical principles is required. Hence, a review of previous works reported on bubble acoustics, acoustic cavitation, and sonochemistry was conducted. The next chapter presents a brief summary of research works in these fields and serves as an introduction to various terminology that is employed in this thesis.

Chapter 2

Literature review

The UAS device (or the Starstream device), which combines the liquid flow in a waveguide with ultrasonic energy and directs them through a nozzle was, introduced in Chapter 1. The primary aim of this device is to remove contaminants from the surface of a specimen placed in the liquid stream that exits the nozzle. Chapter 1 detailed the research focus and the aims of this thesis. The motivation of this thesis follows the requirement to understand the operation of the device and to find solutions that improve its performance. The performance establishing parameters include improvement in the repeatability of the pressure output, control over the microbubble population in the liquid, and improved cleaning distance (where distance is measured from the nozzle tip to the surface of a specimen).

To understand the various physical phenomena that are encountered while employing ultrasonic energy in liquids, a review of the literature in the associated fields is important. For the UAS device, this implies research directed towards understanding the interaction between regions "A" (power dissipated in the transducer) and "B" (the acoustical properties of the liquid), as represented in Figure 1.3. This chapter is designed to serve as an introduction to various allied research fields such as acoustic propagation in liquids, the influence of ultrasound on microbubbles, acoustic propagation through waveguides, and to interpret various physical phenomena that could be observed whilst the device is in operation.

A compilation of the discussions and the relevant work carried out in these research fields is presented in this chapter as follows:

- an introduction to bubble dynamics, acoustic cavitation, and related phenomena such as radiation forces, cavitation harmonics, sonoluminescence etc., is presented in Section 2.1,

- the principles of sonochemistry are discussed in Section 2.2, and
- acoustic propagation in waveguides is reviewed in Section 2.3.

In addition, it is well known that a stream of liquid emitted into another fluid (in this case, the liquid stream is ejected into air) is inherently unstable and breaks up into droplets due to restoring surface tension forces [22]. The formation of capillary instabilities on a liquid stream and its subsequent breakup implies that the propagation distance for the ultrasonic energy from the UAS device could be limited. Subsequently, the length up to which the stream is unbroken (called the intact length) becomes important. The basic principles of capillary instability phenomenon are introduced in Section 2.3.1. This chapter concludes with a summary of the literature presented in these individual sections and its applicability to this thesis.

2.1 Bubble acoustics

The study of acoustics concerns the propagation of energy in a medium in the form of a disturbance. Periodic or sudden variations in local density (or particle velocity) of a fluid medium (triggered by any means) could initiate longitudinally propagating waves at the speed of sound c. The speed of sound c is related to the density (ρ) and the fluid compressibility (K) of the medium. For a propagating acoustic wave in a medium, the local compression and rarefaction regions subject it to local compressive and tensile forces respectively.

In such scenarios, it was observed that very pure and degassed water can withstand large values of static tension (or negative pressures) up to 27 MPa (or 270 bar) at 20^{o}C before the liquid "ruptures" (see Briggs (1950) [23]). However, in practical situations, a fluid may not be able to withstand such large negative pressure amplitude. This is because the working liquid - for example, present either near a propeller or in vivo - may not be pure, may contain dissolved gases or additives, and may have pre-existing voids/nuclei [15, 24]. These pre-existing nuclei (or bubbles) in a liquid will alter their size and shape in response to external pressure fields (either static or varying) [15, 25]. Due to the differences in the compressibility (and density) of the surrounding liquid and the gassy interior of the pre-existing nuclei, the ability of the liquid to withstand tension (or negative pressure) is greatly reduced.

The study of bubble acoustics focuses on the dynamics of gas bubbles influenced by external pressure fields, the physical effects and phenomena that are observed in the working liquid under acoustic insonation [26], and the respective fluid dynamic forces involved. As the timescales involved with the rate of change of microbubble size are very

short, different mathematical and specialized experimental techniques are used to analyse, observe and record their evolution, growth, and collapse phases. The wide variety of applications of these studies include the investigations of liquids flowing over fixed surfaces [27] and the studies in acoustic/ultrasonic cavitation fields [20]. Subsequently, in bubble dynamics studies, understanding the nucleation (and or extinction) of a void could be considered as the first step.

Reynolds in 1897 reported nucleation of bubbles in a pipe filled with liquid, which was exposed to static negative pressures [28]. However, the mathematical modelling of the sudden extinction of a spherical cavity in a large expanse of liquid by Rayleigh in 1917 [29] is generally considered as the first major development towards understanding bubble dynamics or cavitation phenomenon [30]. Rayleigh's analysis evaluates the pressure generated in the liquid as a result of the void annihilation, whilst neglecting the influence of liquid surface tension. With advances in high-speed imaging and numerical methods aided with faster computing power, it is now well understood that the collapse of a microbubble in a liquid follows a complex series of events that result in an almost adiabatic growth and sudden disintegration. These series of events are known to trigger shock waves in liquids [31]. Studies such as investigations of harmonic oscillations of bubbles about their mean position in acoustic fields [32], surface wave formation on the bubble walls [21, 33], and non-linear dynamics of the fluid at the bubble-liquid interface [34] were undertaken to investigate the influence of acoustic forces on bubbles.

Acoustic cavitation is a non-linear phenomenon with well-defined pressure thresholds for initiating its various stages [35]. When a single bubble or a cloud of bubbles present in an expanse of liquid undergo cavitation, many interesting phenomena were observed to occur in conjunction including recorded local high temperatures [16], sonoluminescence [36], and the creation of free radicals [37]. Related events such as the collapse of a cluster of bubbles [34] and radiation forces acting between two microbubbles in an acoustic field [38, 39] also form part of the dynamics of bubbles in liquids. Light emission [40] and audible acoustics [41, 42] are known to occur from strongly cavitating acoustic fields. These phenomena are further discussed in Section 2.1.2.2.

For linearly oscillating bubbles in liquids, the balance of fluid dynamic forces creates microstreaming patterns [17, 18] at the liquid-bubble interface, which is known to assist ultrasonic cleaning. On the other hand, non-linear phenomena such as collapse of bubbles near a boundary [19, 43] under strong ultrasonic fields and resulting high speed jetting [44] were carefully investigated to understand the damage caused by cavitating bubbles on impellers, their positive influence on ultrasonic cleaning, and to evaluate safety considerations during shock wave lithotripsy. Target surfaces that were in contact

with collapsing bubble clouds were found to be eroded [31], and this effect is attributed to the jetting action of collapsing microbubbles.

Research works on these phenomena generally have their foundation in the mathematical model of a single bubble undergoing linear oscillations in an external pressure field. When a single bubble of mean radius R_0 is formed (or nucleated) in a liquid (either by natural means such as under a breaking wave or by artificial means, for example, in an intense ultrasonic field), the pressure inside the bubble (P_i) is slightly higher than the pressure in the liquid outside the bubble wall (P_L), by [20]

$$P_i = P_L + P_\sigma, \tag{2.1}$$

where P_σ is the added pressure inside the bubble due to surface tension (τ) at the bubble-liquid interface (Laplace pressure). This added pressure is defined as

$$P_\sigma = \frac{2\tau}{R_0}. \tag{2.2}$$

The pressures that counteract these compressive forces created by P_L and P_σ are the gas pressure (P_g) and the vapour pressure (P_v) inside the bubble. Under equilibrium conditions (denoted by suffix "e"), P_{ie} can be used for total internal pressure, P_{ge} for gas pressure inside the bubble, and the equality $P_L = P_0$ applies i.e., the pressure in liquid immediately outside the bubble P_L can be taken as equivalent to hydrostatic pressure amplitude P_0 at a far distance from the bubble. Under this equilibrium, the surface tension force P_σ attempts to (slowly) dissolve the contents of the bubble into the surrounding liquid. Since P_σ is inversely proportional to the mean bubble radius (equation 2.2), smaller bubbles (here meant in the order of few micrometres) have comparatively larger surface tension compared with bubbles with a millimetre diameter. The smaller bubbles are generally prevented from dissolving into the liquid either by the presence of surface active molecules (surfactant), or by a mechanism defined as the ionic skin model [20], or even by the presence of another bubble at the nucleation sites such as a crevice [45]. In the static equilibrium condition, the gas pressure inside the bubble (P_{ge}) is given by

$$P_{ge} = P_0 + \frac{2\tau}{R_0} - P_v. \tag{2.3}$$

On the other hand, when a bubble is not in its equilibrium, (for example, when an external pressure of amplitude P_L is applied to the liquid), the bubble changes its size. The gas inside a bubble generally undergoes polytropic expansion or compression (with polytropic exponent γ based on the gassy interior) during a change in its shape

[46]. Then, the instantaneous pressure of gas inside the bubble (P_g) is related to the equilibrium pressure (P_{ge}) by

$$P_g = P_{ge}\left(\frac{R_0}{R}\right)^{3\gamma}, \tag{2.4}$$

where parameter R refers to the instantaneous radius of the bubble. Using equations 2.1 to 2.4 we get

$$P_L = \left(P_0 + \frac{2\tau}{R_0} - P_v\right)\left(\frac{R_0}{R}\right)^{3\gamma} + P_v - \frac{2\tau}{R}. \tag{2.5}$$

In quasi-static equilibrium conditions, if an external static acoustic pressure of amplitude P_L is reduced isothermally (i.e. γ =1), the bubble radius would slowly increase but will stay in equilibrium with the surrounding liquid. A critical radius could then be defined (for bubbles of very small radius) for a surface tension force which cannot hold the bubble in its spherical shape. This happens when the static negative pressure applied to the fluid P_L exceeds a critical limit. In this scenario, any further reduction in the pressure amplitude would cause the bubble to undergo sudden growth. This threshold is called the Blake threshold pressure for a bubble of specified radius [35]. It should be noted that the Blake threshold only estimates the negative pressure required for sudden explosive growth, but does not deal with the eventual (and more practical) collapse of the bubble caused by the inertial forces in the liquid.

In the quasi-static case, the critical radius R_{crt} for the onset of explosive expansion can be evaluated by differentiating equation 2.5 with respect to R and equating the result to zero. In such a case (and under isothermal conditions),

$$R_{crt} = \sqrt{\frac{3R_0^3}{2\tau}\left(P_0 + \frac{2\tau}{R_0} - P_v\right)}. \tag{2.6}$$

Equation 2.6 can be used to calculate the Blake threshold pressure (P_{bl}) for a bubble of mean radius R_0. This is given by [20]

$$P_{bl} = P_v - \frac{4\tau}{3R_{crt}}. \tag{2.7}$$

Equation 2.7 can be used to infer the lower limit of the pressure threshold amplitude for initiating cavitation.

2.1.1 Free and forced bubble oscillations

In free field conditions (for example, either under a breaking wave or upon removal of the acoustic field in a liquid), the balance of forces makes the bubbles present in the liquid undergo linear oscillation about their mean position. These bubble oscillations can be mathematically approximated using the model of a lightly damped harmonic linear oscillator [30, 47], where the gas inside the bubble provides the stiffness force and the liquid surrounding the bubble provides the inertia force.

When a bubble is oscillating, the temporal derivative of R (or the temporal derivative of instantaneous volume of the bubble V [20]) is generally employed to evaluate the change in the shape of the bubble with time. In such situations, the term b is generally used to denote the overall damping contribution. The damping of a bubble in motion could be attributed to three different mechanisms: the viscous damping (b_v) at the liquid-bubble interface, thermal damping (b_{th}) - as a result of energy exchange between gas inside the bubble and the liquid (can be quantified using κ, if the processes are reversible), and the acoustic radiation damping (b_{rad}) - the scattering and radiation of acoustic energy due to the compressibility of gas and the acoustic interactions. The combination of the three damping factors contributes to the total damping of the bubble ($b = b_v + b_{th} + b_{rad}$) [30, 32].

For a freely oscillating bubble, the natural frequency of its oscillation and its damping can be estimated from the near exponential decay of its radial breathing mode oscillations [48]. The natural frequency of oscillation f_0 (or $\omega_0/2\pi$) in Hz of a single bubble (neglecting the surface tension and heat conduction into the liquid) is generally given by [49]

$$f_0 = \frac{\omega_0}{2\pi} = \frac{1}{2\pi R_0}\sqrt{\frac{3\gamma P_0}{\rho}}, \tag{2.8}$$

where ρ is the density of the liquid. The value of γ for a single bubble (with a diatomic gas as its interior) varies from 1.0 for isothermal oscillations to approximately 1.40 for adiabatic growth and collapse phases [46]. Under ambient pressure conditions, with an air bubble undergoing isothermal oscillations ($\gamma = 1$), equation 2.8 is reduced to its well-known form, called the Minnaert's equation [30]

$$f_0 R_0 \approx 3\ m.s^{-1}, \tag{2.9}$$

and accordingly, the resonant frequency for an air bubble of 30 μm mean radius is approximately 100 kHz.

If the liquid is under the influence of an external acoustical field, applied at frequency f (or $\omega/2\pi$), any bubble present in the liquid would undergo forced oscillations

and the phase of these oscillation depends on their initial mean radius R_0. In forced dynamics, the bubble will oscillate at frequency f and will lose energy from the incident acoustic wave via different damping mechanisms. The damping coefficients of a forced bubble (b_f) are dependent on insonation frequency. For a bubble of initial radius R_0, as the frequency of excitation f increases, the viscous damping remains constant, thermal damping decreases with frequency, and the acoustic radiative damping increases with frequency [32]. The Rayleigh-Plesset equation (RP or Rayleigh Plesset Noltingk Neppiras Portitsky equation)[1] is generally used to predict the non-linear motion of bubbles by relating the instantaneous bubble radius (R) to the system properties such as: surface tension (τ), viscosity (μ), and applied pressure (P_L) [9, 49]. This equation was often employed to study the dynamics of bubbles undergoing acoustic cavitation [9, 20, 50].

When a bubble is exposed to an external forcing, its response can be strongly influenced by having the imposed frequency f either close, or equal to the natural frequency of the bubble f_0. It can also be influenced by the presence of other bubbles in its vicinity [47, 51], its distance from a rigid boundary (if it exists) [19], or even by the boundary conditions imposed on the liquid container in which the bubble is held. Research encompassing all these studies and associated phenomena is termed as the study of acoustic cavitation. Acoustic cavitation was briefly introduced in the previous section and will be discussed in detail in Section 2.1.2.

2.1.2 Acoustic cavitation

Acoustic cavitation has been an active research area for over 60 years. The definition of the word "cavitation" varies with context and generally applies to the dynamics of cavities in liquids [15] either under the influence of external pressure oscillations [32] or influenced by natural causes [1]. In this regard, Apfel in his 1981 paper stated: "The words 'acoustic cavitation' mean different things to different people depending on their experiences and the particular circumstance" [35]. The study of acoustic cavitation is broad in its focus and was mostly driven by the practical applications such as: evaluating the oceanic bubble population, power ultrasonics, sonochemistry, medical ultrasound, ultrasonic cleaning etc. The studies in cavitation could prioritise different regimes such as the non-linear and sudden collapse of a microbubble (or a population thereof) under strong external ultrasonic fields [52], stable oscillations of bubbles, and associated phenomena thereof [49]. Studies were also directed towards quantifying cavitation using various techniques [53, 54]. Broadly (at the present time) acoustic cavitation is classified into noninertial and inertial regimes, although the words "stable" and "transient" cavitation were earlier used in their place [1, 20].

[1] The RP equation is derived from the incompressible Navier-Stokes equations [20].

Inertial cavitation of bubbles is characterized by explosive growth and violent collapse phases, with the inertia of the liquid playing a dominant role during the collapse phase. It is also known that the collapse of microbubbles (driven by pressure fields) generally occurs at a timescale very much smaller than the time period of the driving acoustic cycle [36, 40]. During the final stages of inertial collapse, the temperature of the gas inside the bubble increases rapidly. The maximum value of bubble interior temperature (T_{max}) was estimated to be as high as 5000 K [55, 56]. These large temperatures inside the bubble are thought to be a source for the formation of free radicals (such as $\dot{H}$, $\dot{OH}$) in water [37, 57], and is responsible for light emission [40]. The sudden collapse of a bubble wall, its subsequent rebound, and associated high-energy events of noninertial cavitation are either unwanted (for example, in medical ultrasound) or essential (in ultrasonic cleaning) depending on the application.

Noninertial cavitation refers to a regime where, under the influence of an external sound field, the bubble undergoes oscillations (either linearly or non-linearly) around an equilibrium size without undergoing violent collapse. This regime is sometimes also termed as the "cushioned collapse" [20]. Noninertial cavitation is characterised by the absence of high energy phenomena (related to violent collapse) such as hot spots formation, jetting, erosion of target surfaces, free radical formation etc. The noninertial cavitation in acoustic fields can occur repeatedly over many cycles and may be in phase or out of phase with the driving pressure field [49]. The bubble wall motion in this cavitation regime was also observed to be responsible for microstreaming patterns detected around an active bubble [58].

The differentiation between inertial and noninertial regimes for a bubble can be broadly understood by observing equation 2.10. This equation relates the acceleration of bubble wall motion ($\ddot{R}$) to the inertial force in liquid (IF) and applied external pressure force (PF) [1] as,

$$\ddot{R} = IF + PF. \tag{2.10}$$

If the term PF dominates the series of events, then the mechanism could be termed as noninertial cavitation and if the IF term is dominant then the mechanism could be termed as inertial cavitation. To understand the differences between inertial and noninertial cavitation and their relationship to system variables, various mathematical and experimental research techniques are generally employed. The importance of these two strands of research can be demonstrated using Figures 2.1 and 2.2.

Figure 2.1a shows the results of a numerical simulation tracking the changes on a normalized bubble radius (ratio of R/R_0) with respect to normalized time (t/t_0, where a value of 1 represents one acoustic cycle) taken from reference [59]. A single bubble under the influence of 0.5 MPa acoustic pressure excited at frequency 3 MHz (f) was

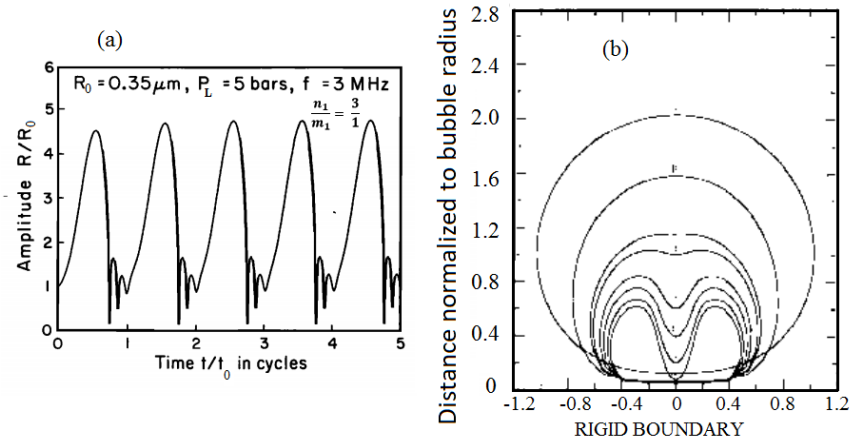

Figure 2.1: Examples of numerical simulations of inertial cavitation on bubbles, taken from the literature. Part (a) is the variation in normalized bubble radius with normalized time [59], and part (b) is the mathematical simulation of involute formation and hourglass shape of a vapour bubble collapsing near a rigid boundary [44]. The symbols in this figure are modified to match the nomenclature in this thesis.

evaluated to oscillate 3 times for every one acoustic cycle (as represented by ratio n_1 to m_1). Figure 2.1b taken from reference [44] shows the involution and jetting formation of a vapour bubble near a rigid boundary, when the distance between the boundary and the centre of the bubble, at the start of the simulation, is equal to the bubble radius. The final shape of the bubble observed in Figure 2.1b is called the hourglass and is considered to be the shape bubbles take prior to their characteristic involute jetting. These two simulations provide insights into the complex nature and shapes that bubbles take under different operating conditions.

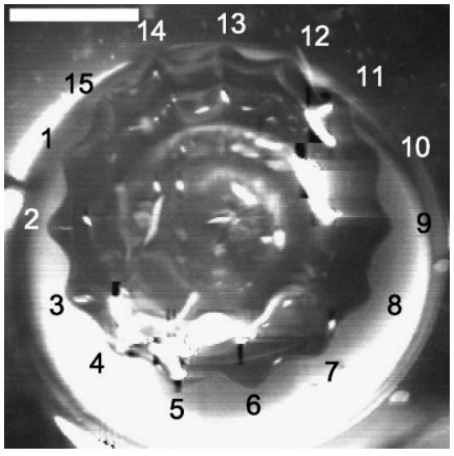

Figure 2.2: A snapshot of Faraday wave formation on a bubble wall held under a glass rod (in the background), taken from reference [60]. The white scale bar is 2 mm.

On the other hand, Figure 2.2 shows a snapshot taken using a high-speed camera, recording the formation of Faraday waves [60] on a bubble held under a glass rod

(restricting the rise of the bubble against buoyancy). The bubble is under the influence of a 1.297 kHz ultrasonic signal and demonstrates a special form of noninertial cavitation, called Faraday waves, with surface mode number 15 excited on the bubble wall. Figures 2.1 and 2.2 demonstrate the importance of using both the theoretical and experimental studies in bubble dynamics.

As can be observed from Figure 2.1b, the presence of an external rigid boundary influences the dynamics of a bubble in the liquid. Plesset and Chapman in 1971 considered the inertial collapse of a spherical bubble next to a rigid boundary [19] and found that the involute shaped jet forms to balance the fluid dynamic forces between its top and bottom surfaces [19]. This involute jet formation was investigated (both mathematically [44] and experimentally [43, 61]) and the velocity of jetting was confirmed to be between 130 $m.s^{-1}$ and 180 $m.s^{-1}$. The collapse of bubbles and involute jetting was presented as the primary reason for erosion and pitting observed on high-speed impellers [44, 61].

For bubbles located far from a boundary and those that exist in a large expanse of liquid, the dynamics and collapse of bubbles were quantified by Noltingk and Neppiras in 1950 (based on Rayleigh's studies). Noltingk and Neppiras evaluated the response of gas filled bubbles (and voids) to applied pressure waves and demonstrated that individual bubbles grew up to 2.3 times their initial radii during expansion [52]. This ratio of ($R_{max}/R_0 = 2.3$) is generally considered as the radial limit for inertial cavitation to occur in a bubble [35], where R_{max} is the maximum radius attained by a bubble.

Since the occurrence of acoustic cavitation is dependent on many working parameters such as the frequency of operation, pressure field, and acoustical properties of the liquid, studies in acoustic cavitation require an evaluation of precise threshold pressure amplitudes to initiate these events. These thresholds are similar to the occurrence of a static threshold (Blake threshold, equation 2.7), but for the dynamic case. The thresholds were generally investigated in an attempt to classify the different cavitation events, to understand the transition between noninertial to inertial cavitation, and to record several related phenomena. The cavitation pressure thresholds are discussed in the next section.

2.1.2.1 Cavitation pressure thresholds

Consider a bubble undergoing noninertial cavitation under the influence of an external acoustic field. This bubble could alter its dynamic motion from the noninertial regime to the inertial regime by changing some or all of the following factors [15, 62]: insonation frequency, driving pressure amplitude, the amount of dissolved gas in the liquid, or time.

Hence a clear definition of the thresholds including the influence of working parameters is important. At constant excitation frequency (below the resonance frequency of the bubble), a bubble of equilibrium radius R_0 under low acoustic pressure amplitude is known to undergo linear (breathing mode) oscillations around its centre [63]. However, as the incident pressure increases, non-linear phenomena such as generation of non-spherical surface wave formation on the bubble wall (Faraday waves [21]), and sonoluminescence [64] were observed. As the pressure amplitude increases further and when the frequency of excitation is kept constant, the bubble oscillations become highly non-linear [26, 32] to the point of explosive growth and subsequent sudden collapse [15]. This series of events implies that different pressure thresholds exist for these different transition events.

For inertial cavitation to take place, the pressure in the liquid must at least exceed the Blake threshold [34, 35, 65], in which case any pre-existing nuclei will grow rapidly even under quasi-static tension. Since the Blake threshold only predicts the onset of sudden expansion and does not deal with the subsequent collapse phase of bubbles, it provides one of the thresholds for inertial cavitation to occur. A second threshold is used to determine the applied pressure at which an acoustically excited bubble will rapidly expand and then suddenly collapse (with bubble wall velocities reaching the local speed of sound [35]) and is defined as the inertial cavitation threshold [66].

A different (and third) threshold exists for a process called the rectified diffusion. The threshold for rectified diffusion determines if a linearly oscillating bubble of mean size R_0 increases its size gradually over many acoustic cycles [67]. Thus, acoustic cavitation also features rectified diffusion of bubbles [67, 68] where a slow growth in the gas content occurs as a result of applying the sound field over many acoustic cycles. The growth rate of rectified diffusion depends on factors such as surface tension, dissolved concentration of the gas in the liquid [68], the initial size of microbubbles, and their exposure to the sound field [69]. Once the rectified diffusion threshold pressure is exceeded, the bubble radius grows gradually over a few acoustics cycles, probably reaches the equivalent radius for its resonance in the applied sound field, undergoes violent collapse, and fragments into smaller bubbles (or microcavities). The process might repeat itself. Apfel, in 1981, used these three threshold regimes to provide an overall plot demonstrating the transition between the three regimes for a wide range of bubble radii [35].

Holland and Apfel in 1989 reported studies on the threshold pressure for initiating the inertial cavitation regime in a single bubble, with a focus on the safe use of ultrasound for diagnostic medicine [66]. An equation, based on the maximum bubble interior temperature at 5000 K [70] as the criterion for inertial cavitation, was used to determine critical negative pressure (in MPa) for individual bubble radii ranging from

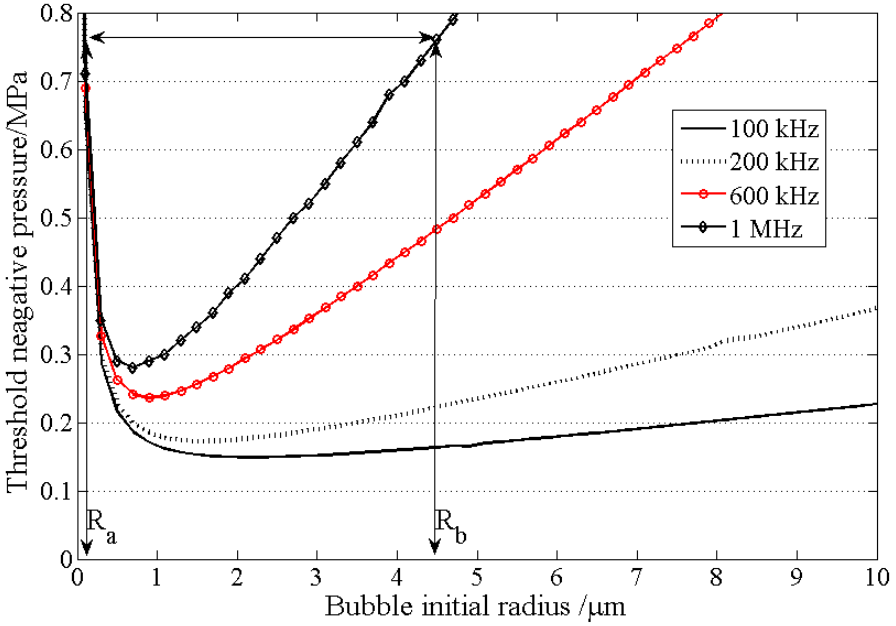

Figure 2.3: An evaluation of inertial cavitation pressure threshold for initial bubble radii varying from 0 to 10 μm, using equation (11) from Holland and Apfel (1989).

0 to 20 μm [66]. The famous U-shaped curves (see Figure 2.3) demarcate, for a given pressure, the regions where inertial cavitation is likely to happen and those where inertial cavitation is unlikely to happen. This study by Holland and Apfel is extended here by evaluating equation 11 from reference [66] for frequencies as small as 100 kHz and for bubble radii between 0 and 10 μm. For example, at 1 MHz insonation frequency (as shown in Figure 2.3), bubbles between radii R_a and R_b require approximately 0.75 MPa of negative acoustic pressure amplitude to undergo energetic expansion and subsequent sudden collapse. Bubbles of radii above R_b do not inertially cavitate at 0.75 MPa at 1 MHz or to put in other words, all the bubbles in radius range from 0 to 10 μm can inertially cavitate at an applied pressure of 0.25 MPa at 100 kHz. Similar analysis and observations were also reported by Ahmadi et al. [71] in 2012.

It should also be noted that studies on estimation of threshold pressure amplitudes to initiate inertial cavitation regime sometimes feature bubble interior temperatures as low as 1500 K [72]. It is interesting to note that results similar to that shown in Figure 2.3 and reported in reference [73] formed the basis for the term Mechanical Index (MI), a safety index used in diagnostic ultrasound [3, 74]. With different authors using different inertial cavitation thresholds such as R_{max}/R_0 >2, or T_{max} >5000 K, or bubble wall velocity greater than the local speed of sound of the liquid, it is important to keep in mind the target application before deciding upon a particular threshold value.

It should be understood that the intense physical phenomena that can be initiated in liquids are dependent on the amplitude of pressure applied. The dynamics of microbubbles in response to these applied acoustic fields triggers these phenomena. Some of these phenomena were mentioned in previous sections and will be further discussed in Section 2.1.2.2.

2.1.2.2 Phenomena associated with acoustic cavitation

Acoustic cavitation in ultrasonic fields is the source for many intense physical phenomena. For example, high energy inertial cavitation is characterised by tonal and broadband acoustic emissions from the liquid [41, 75]. In such cases, the frequency content of the audible emission was generally found to be dependent on the incident pressure amplitude [42] and is regarded as characteristic noise associated with cavitation events [76]. For example, at low insonation pressure amplitudes, only the fundamental (f) of the driven signal was detected [42] in the frequency content of the signal recorded by a hydrophone placed in the insonated liquid. At higher incident acoustic pressures, but below the threshold for inertial cavitation, pressure amplitudes at f and particularly *2f* were detected, with pressure values recorded at *2f* proportional to the square of pressure value at insonation frequency (f) [77]. The appearance of subharmonic terms (i.e., *f/2*) in the recorded data was also observed [77, 78]. Above the inertial cavitation pressure threshold, there is a definite increase in broadband acoustic emission from the liquid along with the presence of sub and ultraharmonic terms [41, 76]. It was also suggested and shown [76] that, by gradually increasing the driving voltage to the ultrasonic transducer (at a fixed frequency) and by tracking the acoustic emission from the liquid, the threshold value for inertial cavitation could be easily observed [76].

In addition to harmonic acoustic emission, at some working conditions energy is also emitted from collapsing bubbles in the form of light during acoustic cavitation. The phenomenon of light emission from either a single microbubble or a cloud of microbubbles held under strong acoustic fields [16, 40] is termed as sonoluminescence. Sonoluminescence studies were used to investigate both the presence of cavitation in a liquid and to understand the process of light generation. Gaitan et al. in 1992 experimentally demonstrated the sonoluminescence from a single bubble in a stable (noninertial) cavitation field [64], which paved the way for reclassification of cavitation regimes from stable/unstable to being based on the inertia of the liquid (noninertial/inertial cavitation). Studies were also conducted to observed sonoluminescence emission from a cloud of bubbles collapsing near the antinodes of a standing wave [79], in sonochemical reactors activated at a few randomly spaced ultrasonic frequencies [80], and at 1 kHz frequency resolution [81]. Determination of the pressure thresholds to identify the onset

of sonoluminescence [72] in liquids, the mechanism thought to be the reason for light emission [36], and evaluation of the speed of sound in bubbly liquids [82] by measuring sonoluminescence from bubble clouds are some of the well-known studies in this area. Sonoluminescence studies also helped in determining the peak temperature reached in the bubble interior, by observing the emission spectra in different liquids [55].

Sonoluminescence is strongly influenced by the inertial and dynamical force balance of the liquid in the experimental container.The balance of forces around a microbubble under acoustic insonation is known to cause the liquid in its immediate vicinity to flow around its outer surface [18]. The different patterns formed by the viscous motion of liquid around cavitating microbubbles, known as microstreaming, was known to assist ultrasonic cleaning by inducing large shear forces in the liquid [18]. Experimental investigation of cavitation microstreaming was presented in the figures reported by Elder in 1958 [18] and is beautifully photographed using particle image velocimetry (PIV) by Tho et al. in 2007 [58]. The bubble wall motion in liquid (such as those observed in Figure 1.2) demonstrate the influence of fluid microstreaming and influence of radiation forces in acoustic fields.

Radiation forces acting on either a single or multiple bubbles in an acoustic field requires special attention and will be discussed in Section 2.1.3.

2.1.3 Radiation forces

A bubble present in an acoustic field experiences a force caused by a change in momentum between its extremities. This force is governed by Newton's second law and is generally termed the radiation force. The forces experienced by bubbles in acoustic fields were first observed by Bjerknes (father, son duo) and were classified into primary and secondary Bjerknes forces. Primary Bjerknes force (F_1) is caused by the "Primary" acoustic field and the subsequent motion of individual bubbles influenced by the gradient in acoustic pressure [9]. Secondary Bjerknes force (F_2) is defined as the force of attraction or repulsion between two bubbles influenced by the primary acoustic field. For example, in the UAS device, the microbubbles electrolysed at the end of the nozzle (when insonated by pressure pulses) are under the influence of both primary and secondary Bjerknes forces. So, in the UAS device depending on the size distribution of the microbubbles generated by electrolysis, the primary and secondary Bjerknes forces in travelling acoustic fields [10] play an important role in the cleaning operation. To understand these processes, a brief introduction to the acoustic radiation forces is necessary.

For a spherical bubble of volume V influenced by a time-averaged ("$\langle\rangle$") acoustic pressure gradient ∇P, the force acting on it by the acoustic field is given by [83]

$$F_1 = -\langle V.\nabla P\rangle. \tag{2.11}$$

This force can cause the population of bubbles to move towards either acoustic nodes or antinodes (in a standing wave field) depending on the respective bubble sizes and insonation frequency. In a standing acoustic wave field, bubbles smaller than resonance travel to the pressure antinode and bubbles larger than resonance travel to the pressure nodes [9], but the radiation force on resonant bubbles should vanish [84].

On the other hand, when two or more bubbles are present in an acoustic field, the re-radiated acoustical energy between two bubbles (or even a population of bubbles) generates either attractive or repulsive forces between them, depending on their individual phase of oscillation [85]. This force depends upon the strength of acoustic fields applied [86], radial distance between individual bubbles (d_b), and is given by [83, 86]

$$F_2 = \langle F_{R_1 R_2}\rangle = \frac{\rho}{4\pi d_b^2}\langle\frac{\partial V_1}{\partial t}.\frac{\partial V_2}{\partial t}\rangle\mathbf{e}_r. \tag{2.12}$$

The sign of the terms in the brackets $\langle\rangle$ determines if the force acting between two bubbles is either attractive or repulsive and $\mathbf{e}_r$ is the radial unit vector. Attractive secondary Bjerknes forces in strong cavitation fields cause coalescence of smaller bubbles. The larger coalesced bubbles then move in the field and settle in a location where ∇P is the smallest for them. Due to the radiation forces (in strong cavitation fields) acting on the microbubble population, filamentary structure formation and liquid streamers are frequently reported [20, 87].

It is obvious from the studies reported till here that, a single bubble rarely occurs in the acoustic field. Bubbles are generally created as a cloud (for example, beneath breaking waves) [88], externally introduced as a population by various means [47, 89, 90], and are sometimes present in the form of a cluster at the face of the transducer [65]. The size and distribution of these individual bubbles in a cloud depends on their process of creation and strongly influences the acoustic propagation in the liquid. The influence of bubble cloud dynamics on acoustic propagation is discussed in Section 2.1.4 and relates to the influence of region "B" (of Figure 1.3) on the performance of the UAS device.

2.1.4 Multi-bubble dynamics and bubble clouds

The dynamics of a cloud of bubbles in response to an incident acoustic field is generally very different when compared to the dynamics of a single bubble to the same field.

In general, the presence of a bubble cloud (either beneath a breaking wave or in an ultrasonic field) is known to influence acoustical properties of the medium it is in. For example, in oceans, the collective oscillation of a cloud of bubbles as a single entity was identified as a dominant source of noise at low frequencies (at 100's of Hz) [50, 88, 91]. The low frequency acoustic emission from a cloud of bubbles is generally modelled using a spherical cloud as the model [92, 93], along with the influence of shell effect on the scattering of the acoustic signal from a cloud [91]. In presence of such bubbly clouds, an acoustical wave propagating through it can be strongly attenuated. This attenuation is caused both by the scattering of incident waves and by the absorption of acoustic energy [94].

Scattering predominantly occurs due to acoustic impedance mismatch between the medium in which the bubbles are present and the bubbles themselves. For example, an insonated bubble cloud present within a tissue could trigger unwanted reflections and unwanted increase in local acoustic intensity, which is predominantly driven by the scattering events at the interfacial boundary. This mechanism gains more importance if the acoustic source employed is focused in nature. It is known that in tissues insonated by high-intensity focused ultrasound (HIFU) transducers, therapeutic microbubbles were known to migrate towards the transducer face and alter the focal point of the transducer, in turn causing tissue damage [95].

On the other hand, the absorption of acoustic energy passing through a cloud of bubbles is influenced by the resonant frequency of individual bubbles in the cloud [93], the number of bubbles present in it, and by the characteristics of the surrounding media. The number of bubbles in a given volume of liquid can be quantified using the void fraction β (also termed as the gas volume fraction). The influence of void fraction on the speed of sound is studied both in a laboratory setting [96] and in the ocean coastline [97]. The speed of sound in bubbly liquid (c_m) is different (and generally smaller) to that of the phase speed of sound c in bubble-free liquid.

The value of c_m could be mathematically estimated using some simplifying assumptions. If a monodisperse microbubble population with a mean radius R_0 is present in an expanse of liquid, then the void fraction β can be defined as

$$\beta = \frac{4}{3}\pi R_0^3 N_1, \tag{2.13}$$

where N_1 is the number of bubbles present in a unit volume of a liquid. On the other hand, for a liquid of known total volume V_c, if the gas bubbles of different radii occupy a volume V_g (the volume of pure water being V_w), then

$$V_c = V_w + V_g, \tag{2.14}$$

and the void fraction β can be written as

$$\beta = \frac{V_g}{V_c}. \tag{2.15}$$

The influence of a population of microbubbles at different void fraction (β) values on the speed of sound c_m is presented in Section 2.1.5.

2.1.5 Speed of sound in bubbly liquids

An acoustic disturbance in a fluid medium propagates at the wave speed (also called the phase speed) c, which (within the linear limits) is related to the bulk modulus of the liquid B_l (inverse of compressibility K) and the density of the medium ρ. This is given by

$$c = \sqrt{\frac{B_l}{\rho}} = \sqrt{\frac{1}{K\rho}}. \tag{2.16}$$

In bubble-free water, the speed of sound is generally quoted to be between 1460 and 1500 m.s^{-1}. The presence of microbubbles in the liquid affects both its overall compressibility and mean density [49], subsequently changing its speed of sound. The speed of sound in bubbly liquid (i.e., in bubble water mixture) c_m can be written as

$$c_m = \frac{1}{\sqrt{K_m \rho_m}}, \tag{2.17}$$

where,

$$\rho_m = \beta\rho_a + (1-\beta)\rho, \tag{2.18}$$

and

$$K_m = \beta K_a + (1-\beta)K. \tag{2.19}$$

The suffixes a and m refers to material properties of air and bubbly liquid respectively. Using equations 2.18 and 2.19 in 2.17, we get the speed of sound in bubbly liquid as

$$c_m = \frac{1}{\sqrt{[\beta\rho_a + (1-\beta)\rho][\beta K_a + (1-\beta)K]}}. \tag{2.20}$$

The density of gas inside the bubbles is generally small (almost 1000 times) compared to that of the density of water surrounding it and can generally be neglected [94].

For void fractions between 10^{-4} to 10^{-1}, the equation 2.20 can be simplified to [98]

$$c_m \approx \frac{1}{\sqrt{\beta\rho K_a}} = \sqrt{\frac{\gamma P_0}{\beta\rho}}, \tag{2.21}$$

and in isothermal operating conditions

$$c_m = \sqrt{\frac{P_0}{\beta\rho}}. \tag{2.22}$$

Equation 2.20 is generally called the Wood's equation or Mallock-Wood's equation to give credit to its other contributor [99]. It should be noted that the Wood's equation is valid for a homogeneous mixture of bubbly liquid incident at low frequencies [100], or to put it in other words, equation 2.20 could be approximately applied when the operating frequency of the incident acoustic signal is far away from the resonance frequency of the individual bubbles in the cloud. Equation 2.20 is generally used to estimate c_m at different void fraction values (β) and a plot drawn using equation 2.20 is presented in Figure 4.1. The influence of speed of sound in bubbly liquids at different operating frequencies is nicely demonstrated using figure 2 of reference [101], which shows that the value of c_m may sometimes exceed c, depending on the size of individual bubbles in the cloud and when the incident acoustic frequency is above the frequency of individual bubble resonances.

Assuming that the bubble size distribution in an expanse of liquid is homogeneous and the gas inside the bubble is compressed isothermally in an acoustic field, a plane wave free field assumption can be valid for studying acoustic propagation at low void fractions. This assumption is valid in practical situations such as in the ocean top layer or for some pipe flows. The study of plane wave free field acoustic propagation in bubbly liquids by Commander and Prosperetti in 1989 received widespread attention for its modelling of acoustic attenuation [94] and for evaluating the related phase speed of sound. However, it was argued by some authors [102] that the use of plane wave free field approximation might disregard the acoustic propagation in the pipe material itself when the pipe material has acoustic impedance similar to that of (or stronger than that of) the liquid it carries inside it. Studies considering the influence of acoustic propagation in the liquids stored in strongly resonant containers demonstrated that the reverberation of sound in the container will influence both the damping factor [103] and resonance frequency [104] of the bubbles.

Clusters of bubbles were also observed to be present in the liquid beneath ultrasonic transducers during cavitation induced by large acoustic amplitudes. To investigate the cluster dynamics, sonochemical cells were successfully employed [105] whilst

employing multiple sensors [106] including high-speed cameras, hydrophones, and electrochemical sensors [34, 105]. Sonochemistry involves studying the influence of liquid chemistry on acoustic propagation. The next section presents a brief review of research studies carried out in sonochemistry.

2.2 Sonochemistry

Electrochemistry studies the use of electrical potential across electrodes immersed in an electrolyte and its associated effects. The passage of electrons or electrical charge aids chemical reactions at these electrodes and in the liquid. Prominent applications of electrochemistry include metal deposition at the electrode surfaces, gas evolution from electrolytic liquids, and film formation. On the other hand, sonochemistry deals with the study of chemical processes under the influence of acoustic fields. The intense effects of acoustic energy focused at the centre of microbubbles during their collapse phase work as a strong catalyst for chemical reactions [55]. These chemical reactions are influenced by associated hot spot formation observed during bubble collapse [16, 70], and the jetting action of microbubbles close to an external boundary. The use of ultrasonic energy reportedly provided an increased reactivity in metal powders by over 100,000 times [107, 108], when compared with the reactivity rates achieved without the presence of cavitation. The practical applications of sonochemistry include accelerated reaction rates, particle size reduction on target substrates, ultrasonic cleaning, and even altered end products in some reactions [109].

The containers used for these experiments are generally called sonochemical cells (experimental vessels fitted with ultrasonic transducers). These sonochemical cells can be used to study different cavitation events such as single or multi-bubble sonoluminescence [81], chemical reactions rates [109], observing the collapse of a cluster of bubbles near a transducer [34], and for recording erosion or mass transfer during cavitation [105]. Because cavitation could be influenced by many factors such as the material of the container, volume of the liquid used in the experiments, and additives to liquids etc., a very careful control on the system parameters is required to achieve repeatability, failure of which led some authors to term this research field as a black art [110].

Experimental results in sonochemistry have shown that collapsing bubbles can attain high pressure of up to 100 MPa and local heating and cooling rates of up to 10^{10} $K.s^{-1}$ [16]. These high pressures and temperatures concentrated into a small region are thought to cause chemical reactions to accelerate in generally cold liquids. These high temperatures generated during intense cavitation were also known to create free radicals

$\dot{H}, \dot{OH}$ in water [37, 57]. The presence of free radicals in liquids during cavitation was primarily investigated for safe use of ultrasonic energy in diagnostic medicine [111].

Research investigating sonochemiluminescence, a phenomenon similar to sonoluminescence [112], which studies light emission from insonated liquids in the presence of luminol or other chemicals was involved in the developmental phases of the UAS device. Sonochemistry was also used to investigate the inertial and noninertial cavitation near the ultrasonic transducers [65, 82]. Sonochemical observations were employed in addition to the acoustical or photographic observations of different cavitation processes [53], thus creating a series of multiple scientific observations of cavitation and bubble dynamics in sonochemical reactors.

The review of research studies presented until here envelops the works associated with regions "A"' and "B" of Figure 1.3. A knowledge of acoustic propagation in waveguides will extend the review of background literature to cover the influence of region "C" of Figure 1.3.

2.3 Acoustical waveguides

Acoustic waveguides could either be rectangular in shape (rooms, thin layers [113]), or be cylindrical in shape (streams), or may have a variable cross section (musical instruments, engine intakes), or could be exponential/hyperbolic shaped (horns). A knowledge of the source location and the boundary conditions imposed on the waveguide will generally help in evaluating the distribution of acoustic energy within it. A stream of liquid issuing from a nozzle, with the objective of transmitting acoustic pressure pulses through it, could be considered as a cylindrical waveguide. The acoustic field parameter inside the cylindrical waveguide is governed by the homogeneous acoustical wave equation. This wave equation is derived from the conservation of mass and momentum principles considered along with the equation of state. The homogeneous linearised wave equation is given as [114]

$$\frac{1}{c^2}\frac{d^2p}{dt^2} - \nabla^2 p = 0. \tag{2.23}$$

where $p(r,\theta,Z)$ is the pressure field in cylindrical coordinates inside the waveguide, t is the time parameter, and ∇^2 represents the cylindrical Laplacian operator. Different types of boundary conditions could be enforced upon this equation namely: hard walled, impedance matched, and pressure release [115] boundary conditions. In this thesis, the conical chamber was manufactured from impedance matching polymer, which has advertised acoustic impedance similar to that of water. Hence the outer boundary of the

conical chamber acts similar to a pressure release boundary. Subsequently, the conical chamber acts as a conical water waveguide for ultrasonic energy propagation.

It must be noted that the closed form solution of acoustical propagation for converging shaped nozzles are only valid for cylindrical, parabolic, and hyperbolic profiles [116]. Although studies directed towards acoustical propagation in ducts (or pipes) with slowly varying cross sectional areas [117] and propagation in curved liquid streams [118] were reported earlier, it was found that these studies could not be extended to the present shape of the conical chamber. Of more relevance are the studies related to acoustic horns [119, 120], where the focus is on the evaluation of real and imaginary parts of acoustic radiation impedance Z_r at the inlet port of different shaped horns.

Nevertheless, a review of acoustic propagation in straight cylindrical waveguides will provide insights into the response of the UAS device, the results of which can then be compared with discussions present in references such as [119].

The sound field or the pressure amplitude in a straight cylindrical waveguide (of mean radius a) could be evaluated by solving the wave equation 2.23 with a pressure release boundary condition enforced upon it. For time harmonic solutions, (imposed by a time harmonic source of the form $e^{j\omega t}$, where j is a complex parameter), the solutions for the wave equation are given by

$$p(r, \theta, Z) = \Psi(r, \theta) e^{\pm j k_z Z}, \tag{2.24}$$

where $\Psi(r, \theta)$ represents the pressure field distribution across the cross section of the stream, at a location Z with axial wavenumber as k_z. For a stream that stays cylindrical in shape in the region of study, the variables of the solution in the pressure field are separable. Hence, the solution can be written as

$$p(r, \theta, Z) = A_m J_m(k_r r) e^{(jm\theta \pm j k_z Z)}. \tag{2.25}$$

Here the parameter A_m is the pressure amplitude of the azimuthal mode m, k_r is the radial wavenumber, J_m is the Bessel function of first kind of order m. The dispersion relation relating the input disturbance at frequency ω, phase sound speed c, and the radial wavenumber k_r to the axial wavenumber k_z is given by

$$k_z = \pm \sqrt{\left(\frac{\omega}{c}\right)^2 - k_r^2}. \tag{2.26}$$

Thus, the value of axial wavenumber (k_z) could be either real or complex, depending on the value inside the square root of equation 2.26. Real values of k_z imply a propagating

wave along Z and the imaginary value for k_z imply the presence of an evanescent wave (the amplitude of which decays exponentially along Z from the source location). The radial part of the propagating wave, with wavenumber k_r is influenced by the boundary condition applied to the waveguide. For a pressure release boundary condition applicable at $r = a$, the value of $J_m(k_r.a)= 0$, a being the mean radius of the stream. The solutions of the Bessel function are given by X_{ml}/a, where X_{ml} is the l^{th} zero value for J_m. So we get,

$$k_z = \pm\sqrt{\left(\frac{\omega}{c}\right)^2 - \left(\frac{X_{ml}}{a}\right)^2}. \tag{2.27}$$

Therefore, at a given excitation frequency ω, for a fixed sized waveguide and a known speed of sound c the solutions of Bessel function X_{ml} decides whether a disturbance is either a propagating wave or an evanescent wave[2]. A cutoff frequency can thus be defined for a waveguide, as the frequency of disturbance above which the energy can propagate along Z (without exponential decay). The cutoff frequency can be evaluated from equation 2.27 by equating k_z to zero. This is given by

$$f_c = \frac{cX_{ml}}{2\pi a}. \tag{2.28}$$

For a straight cylindrical water stream of 10 mm mean diameter, the values of modal frequencies (based on the solutions of Bessel function, i.e., values of X_{ml}) were evaluated using equation 2.28, by assuming the speed of sound c in bubble-free liquid at 1480 m.s^{-1}. The first modal frequency at m, l values of (0,1), where X_{ml} is 2.4048 units, gives the cutoff frequency at approximately 113 kHz. Cutoff frequencies can also be evaluated for exponential and conical shaped horns [119] based on their flare rate. For example, under the assumption that linearised plane wave is in propagation through the waveguide, a hyperbolic shaped horn and an exponential shaped horn of the same length, throat (or neck) area, and mouth area have the same value for the cutoff frequency [121]. However, the performance of acoustical horns is strongly dependent on the radiation impedance encountered by the source at the neck (or inlet) of the horn [119, 121]. The radiation impedance would change with frequency and defines the characteristics of the horn and its efficiency.

In the case of the UAS device, the radiation impedance faced by the UT_1 transducer must take into account the mounting conditions and the dimensions of the transducer. The acoustic radiation impedance faced by the UT_1 transducer under different

[2]Note that there is no plane wave propagation in a cylindrical stream with a pressure release boundary condition because $p_{(r=a)}$=0).

loading conditions (such as placing the UT_1 either in air, or water, or UAS device filled with water) was investigated at different operating frequencies and the results will be discussed in Chapter 6.

It is important to take into account practical considerations while employing the solutions of the wave equation for acoustic propagation in liquid streams (such as the applicability of equation 2.28 to the UAS device). For example, a stream whose diameter narrows significantly, along its length will have a direct influence on the acoustic propagation and cutoff frequency along its length [122, 123]. Similarly, sudden changes to the geometrical cross sectional area of the stream or breaking up of the stream into individual droplets (due to the formation of capillary instabilities) will also affect the acoustic propagation inside it.

The important observation from these considerations and the first obstacle to long distance acoustic propagation in the UAS device is the formation of capillary instabilities on the stream. It is well known that the interface of a stream of liquid discharged into another fluid is innately unstable and its stability is influenced by the inertial and interfacial force balance [124–126]. The next section serves as a preliminary introduction to the formation of capillary instability on liquid streams.

2.3.1 Instabilities of cylindrical streams in air

Study of instability formation and breakup of liquid streams is a research field with many practical applications attached to it. Pioneering work by Lord Rayleigh laid the mathematical foundation by investigating the exponential growth of instabilities on liquid streams[3] and their free surface [124]. It is known that the breakup process of a stream of liquid can either be activated by internal disturbances in the flow [127] (such as pump fluctuations or flow noise of the system) or can be controlled by employing external disturbances [128] (such as using energy from a transducer/speaker). The capillary breakup process of a liquid stream generally follows the sequence:

- surface waves start to form on the stream, influenced by a disturbance,
- the local increase in the stream diameter due to the surface waves causes necking of the stream on either side of the swelling and,
- the instability grows in amplitude (either temporally or spatially), the neck becomes smaller and subsequently pinches off the stream into droplets,

[3]The terminology "liquid jet" is very commonly used in literature when referring to capillary instability formation or Rayleigh-Plateau instability formation. To avoid confusion with another phenomenon that is encountered later, the word "stream" in the present thesis associates to the word "jet" from the literature. The term microjetting is used and defined in Chapter 7.

The droplets formed are classified into major (large) and satellite (small) droplets. The formation of these major and satellite droplets are either important or undesirable depending on the application. A very comprehensive mathematical analysis of stream breakup with associated fluid parameters was published by Lin in 2002 [22]. The study of capillary instabilities on a stream of liquid is important to estimate its intact length (the length for which the stream of liquid stays "intact" and is not broken down), to evaluate the diameter of droplets generated, and their dependency on external forcing functions. The restoring force for capillary instabilities is the surface tension of the liquid [127], while the surrounding fluid (here air) and liquid viscosity provide damping for the growth of instabilities [127].

Spatial growth of instabilities [129] which applies to the experimental studies that use external excitation (for example, using ultrasonic transducers on micrometer diameter streams), experimental investigations on the temporal evolution of stream into droplets [128, 130, 131], and linear/non-linear mathematical analysis of the breakup process [132, 133] are popular directions in which research has developed. The commercial applications of liquid breakup such as triggering breakup using external means (via acoustic energy) [127, 134] and atomization of fuel in injection ports of internal combustion engines [125] are also prevalent. Practical applications of stream breakup generally aim at formation of uniform droplet diameter. Ultrasonic energy generated using piezo crystals [134], in the MHz frequency regime, is generally used to tune and aid the breakup process. Consequently, the diameter of the streams for ink-jet or fuel atomization applications is limited to a few hundreds of micrometres [125]. In research relevant to the UAS device, response of liquid streams to internal modulated ultrasonic radiation pressure [122, 134] and investigation into controlling the breakup length by using electrically charged liquid streams [125] were rigorously investigated on micrometer sized streams. Atomization of micron sized liquid streams to a form fine mist or a fine spray using ultrasonic energy [135], or with the help of high velocity airflow over the nozzle (termed as Kelvin-Helmholtz instability) are also quite popular.

It is important to note that, whilst the studies on capillary stream breakup focus either on attaining an effective control of the disintegration process to form droplets of known diameter or to control breakup length of stream, in the UAS device it is vital to have longer intact lengths of the stream. This ensures propagation of ultrasonic energy to longer distances from the nozzle tip.

According to Rayleigh's temporal linearised theory for capillary disturbances generated on a stream [124], if a stream of equilibrium radius a, is perturbed by a small

quantity η, then the time dependent stream radius $r(t)$ is given by

$$r(t) = a + \eta(t)cos(k_{cap}Z), \tag{2.29}$$

where the parameter k_{cap} (or $2\pi/\lambda$) is the wavenumber of the capillary disturbance along the axis of symmetry Z of the stream, λ is the capillary wavelength of the disturbance generated on the stream and t represents time. The time dependent parameter $\eta(t)$ is the radial surface displacement of the stream from its mean position. Figure 2.4 shows an example snapshot of capillary waves forming on a stable microstream of 6.35 mm mean diameter and its eventual breakup into major and satellite droplets. The breakup process was triggered by an acoustic disturbance at frequency (f_{cap}) 600 Hz [127] applied using a speaker. It can be observed from the figure that the capillary disturbance grows exponentially along the length of the stream (spatial parameter). The capillary frequency f_{cap} is related to the capillary wavelength λ by

$$f_{cap} = \frac{u_0}{\lambda}, \tag{2.30}$$

where u_0 is the flow velocity of the liquid stream.

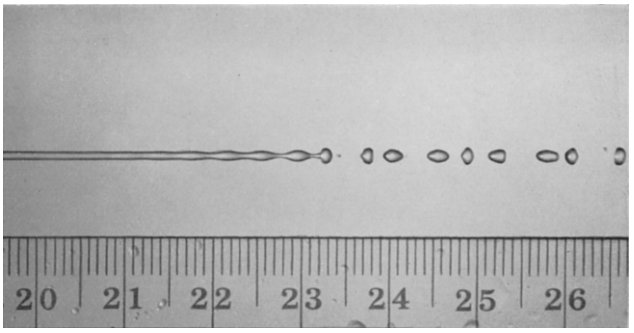

Figure 2.4: A photograph showing droplet formation and breakup of a capillary water stream subject to an acoustic disturbance, taken from [127].

It is important to note that Rayleigh's theory of temporal growth rate of capillary disturbances is valid for applications corresponding to infinite Weber number (We) [129]. The temporal growth rate also means that the instability on the stream grows exponentially at every point (which is not practically possible during experiments) and not just along the axial direction (which is more practical [122, 129]).

Using linearised theory, the temporal growth rate (α_{cap}) for an instability wave on the stream is equal to

$$\alpha_{cap} = e^{qt}, \tag{2.31}$$

where q is a complex number providing the growth parameter of the surface wave relating to the wavenumber k_{cap}. The growth parameter q of an exponentially growing surface wave can be related as [136]

$$q^2 = \frac{\tau}{\rho a^3} \frac{(1 - k_{cap}^2 a^2) k_{cap} a I_1(k_{cap} a)}{I_0(k_{cap} a)}, \tag{2.32}$$

Here I_0 and I_1 are the modified Bessel functions of the first kind, in first and second order respectively. Equation 2.32 gives the growth rate of a surface wave on a stream, when the influence of the liquid viscosity could be neglected. The influence of introducing the viscosity of liquid into the governing equations as derived by Rayleigh [137] was observed to be only applicable to highly viscous liquids streams [125]. Mathematical and experimental studies on the influence of additives such as glycerol (to increase liquid viscosity) were reviewed and discussed by authors in references [125] and [127].

From equation 2.32 it could be observed that, for a liquid stream of radius a (if ρ, τ are known), there are a specific set of capillary wavenumbers that destabilize the equilibrium of the stream. The values of these unstable wavenumbers are restricted by (1-$k_{cap}^2 a^2$). For a liquid stream in dynamic equilibrium with its surroundings, the Laplace pressure provides the difference between the pressure inside and outside of the stream. Under the action of surface tension restoring force, this is governed by the well-known equation

$$\Delta P = \tau \left(\frac{1}{r_a} + \frac{1}{r_w} \right), \tag{2.33}$$

where r_a and r_w are principal radii of curvature of a deformed stream and ΔP is the fluctuation in pressure above the mean pressure inside the liquid stream (which in equilibrium is equal to P_0). The suffixes a and w represent the two fluids (air and water respectively). Equation 2.33 demonstrates that any change in the equilibrium pressure might displace the stream surface. Once disturbances of sufficient amplitude are set-up on the system, they build up due to the energy minimisation principle of the surface tension. This eventually leads to the breakup.

To evaluate the influence of changes in liquid surface tension on the unstable capillary frequencies and growth rates, equation 2.32 was used with a 10 mm diameter water stream as a model. Three different liquid flow rates were employed for the simulation, starting from 2 litre.min^{-1}, 3 litre.min^{-1} and 4 litre.min^{-1}. Two different surface tension values were considered at 72 mN.m^{-1}, and at 35 mN.m^{-1}. It can be observed from Figure 2.5 that, as the surface tension of the liquid decreases (for example, by addition of surfactant to the working liquid), the growth parameter (q) was found to reduce, but the unstable frequencies were not altered. However, with a 33% increase in flow rate (from 3 to 4 litre.min^{-1}), the range of unstable frequencies increases by a factor of 25%. So, if an input disturbance is strong enough to cause capillary disturbances on a liquid surface, the presence of surface active elements will not predominantly change formation and growth of surface waves.

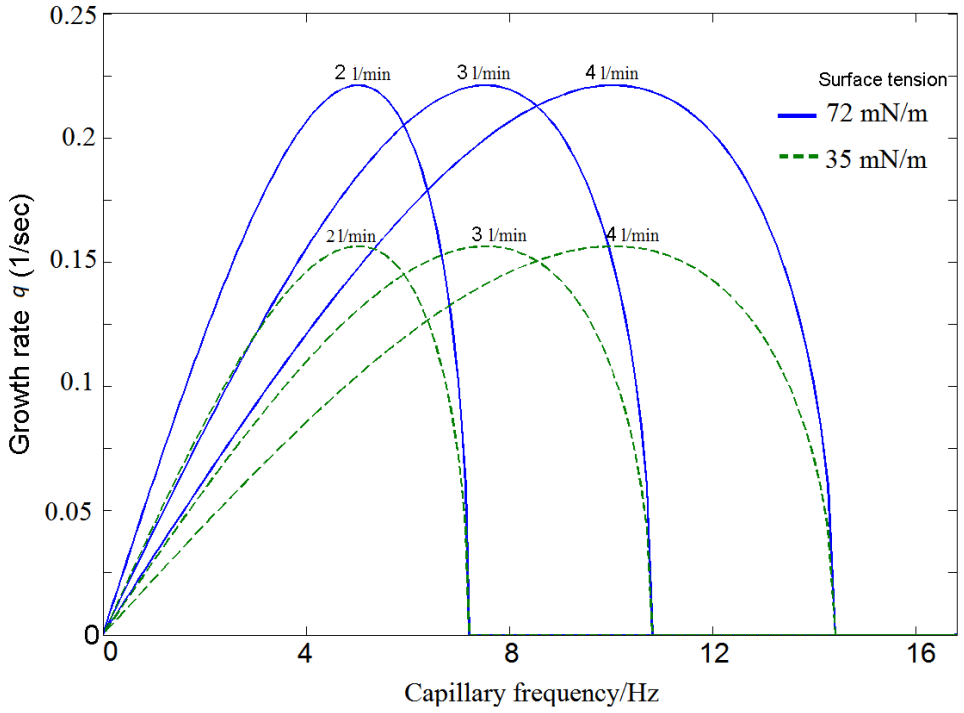

Figure 2.5: Theoretical capillary breakup frequencies and their growth rates for a 10 mm mean diameter cylindrical water stream, evaluated at two different flow rates and two different surface tension values, using equations 2.30 and 2.32.

For a free cylindrical liquid stream with mean diameter (a) of 10 mm and flowing at 2.0 litre.min^{-1}, the breakup length (or the intact length) could be calculated using equations given in references [125, 126]. This mathematical breakup length was found to be 55.9 cm and the maximum unstable capillary frequency was found to be 5 Hz, using very low Weber number (We) approximation.

The presence of cavitation in the liquid is also known to create capillary waves on the free surfaces of a liquid. In work done by Mir [138], the cavitation action caused by the ultrasound was mathematically modelled as a sequence of impulses and this model was incorporated into the investigation of capillary oscillations. Works published were also directed towards the capillary stationary waves in rectangular tanks, to study the acoustic streaming effects generated at the flat air-water interfaces [139]. Standing capillary waves formed in rectangular tanks were reported to be affected by the changes in both the viscosity and surface tension of the working liquid [139]. The presence of a target in the path of the liquid stream was shown to create stationary capillary waves (i.e., non-travelling) on the stream [140].

On the other hand, cavitating liquid streams, where cavitation was achieved by high velocity liquid flow in narrow pipes, were found to have smaller intact lengths when compared with the non-cavitating liquid streams [126]. Formation of quickly collapsing

voids in liquid streams [141], triggered by an ND-Yag laser, were also reported in relation to the studies of capillary stream stability. These studies demonstrate the different techniques by which the stability of a liquid stream could be disturbed externally. The importance of stream stability on the performance of the UAS device will be reported in Chapter 7.

This concludes the review of relevant literature associated with the physical principles of acoustical propagation in liquids. The next section presents the conclusions of this chapter.

2.4 Conclusions

The working principles of the UAS device (or the Starstream device) encompass the research fields of bubble acoustics, acoustic cavitation, sonochemistry, and acoustic propagation in cylindrical ducts. During the operation of the device, ultrasonic energy travels down the conical waveguide and the liquid is known to undergo intense cavitation, providing energy for the cleaning process. The ultrasonic energy present in the liquid (or the influence of region "A" as shown in Figure 1.3) influences the performance of the UAS device. In commercial ultrasonic cleaning, different phenomena generated during acoustic cavitation by frequent agitation of microbubbles present in the liquid are exploited. The high energy inertial cavitation events that occur at the collapse phase of a microbubble aid in the removal of contaminant particles from the exposed substrates (in ultrasonic cleaning baths).

As an introduction to different terminology and the phenomena that occur in the liquid when acoustic energy propagates through the UAS device, this chapter presented a brief introduction and review of studies on acoustic cavitation in liquids, which has been an active research field for over 60 years. Relevant research studies such as: improved chemical reaction rates in liquids [56], determination of oceanic bubble population in the surf zone [97], acoustic propagation in pipe flows in presence of bubbles [142], sonochemistry and allied studies [109], safety considerations in diagnostic medicine [37], and drug delivery using ultrasonic contrast agents [143] were discussed. The inertial or non-inertial cavitation regimes in a liquid under acoustic insonation are known to trigger different physical phenomena. These regimes were investigated (earlier) in conjunction with the development of the UAS device. In this regard, work done on simultaneous scientific observations of physical events using acoustic and electrochemical sensors [106, 112, 144], and high-speed photography [145] were summarized. Investigations into cavitation harmonics, broadband noise emission, and sonoluminescence of the liquid

stream were detailed. The use of such multiple simultaneous scientific observations to study acoustic cavitation is termed a study in acoustoelectrochemistry [106].

Research areas related to propagation of acoustical energy in waveguides [122, 146], the capillary stability of liquid stream in air [130], and influence of void fraction in acoustic propagation in liquids [94] were introduced. Reviews on different microbubble generation processes and different sizing techniques were summarized in references [89, 147] and will be discussed in detail in Chapter 4.

The next chapter deals with the development of individual components of the experimental setup that will assist in attaining effective control of working parameters in the benchtop version of the UAS device.

Chapter 3

Experimental setup and studies on an ultrasonic outgasser

3.1 Introduction

The working principle of the UAS device was presented in Chapter 1. The key components of the UAS device and the system parameters that influence its pressure output (as measured and quantified outside the nozzle) were marked in Figure 1.3. The key components of the UAS device are region "A" or the power input into the transducer, region "B" or the acoustic properties of the liquid, and region "C" or the ability of the cylindrical stream to act as a waveguide for the ultrasonic signal (i.e., its boundary conditions, and the stability of the stream surface).

The UAS device works by exploiting the non-linear acoustical phenomena generated in the liquid within its conical chamber. These phenomena are initiated by the large amplitude pressure waves generated by ultrasonic transducer UT_1 (under certain input conditions). The study of linear and non-linear propagation of acoustic energy in liquids and its relationship with the power dissipated in the acoustic transducer are the focus of research in acoustic cavitation. Chapter 2 provided a brief literature review and summary of research works in acoustic cavitation. Discussions were focused towards introducing the related physical phenomena that are observed in liquids under acoustic insonation. The simultaneous acoustic and photographic observation of various cavitation-related physical phenomena reported in conjunction with acoustoelectrochemical studies [144] were also summarized, keeping in mind the importance of those studies to this thesis. A brief introduction was also provided on acoustic propagation in waveguides and capillary stability of liquid streams issued into air.

This chapter is dedicated to the development and testing of an upgraded experimental setup (detailed in Section 3.2). This setup was designed to improve the reliability of acoustic pressure measurements recorded from the UAS device. Individual Sections in this chapter will detail the modifications made to the original experimental setup (shown in Figure 1.1). These modifications include a new inlet system to reduce the turbulence of the liquid flowing into the conical chamber, a technique for recording acoustic pressure in the stream, and an active technology (called the outgasser) for removing the unwanted microbubble population. In this chapter, investigates the effectiveness of the outgasser (presented in Section 3.3). It will be shown that the performance of the outgasser is superior to that of the settlement tube shown in Figure 1.1. The conclusions of this chapter will be discussed in Section 3.4.

3.2 Modified experimental setup

A schematic of the modified experimental setup i.e., an upgrade over the kit shown in Figure 1.1, is presented in Figure 3.1. In the new kit, the liquid was circulated using a Hailea fountain pump HX 8860. The outlet of the pump was connected to a GEMS FT 110 turbine type flow meter (S.No: 173937-C) and flow valve combination to control the flow rate. The liquid leaving the flow valve enters the settlement tube and then moves into the ultrasonic outgasser. The acoustic properties of the liquid inside the conical chamber are influenced by the effectiveness of the settlement tube (or the ultrasonic outgasser) in removing the unwanted microbubble population.

To make the liquid free of unwanted microbubbles either the settlement tube or the outgasser were employed. The bubble-free liquid exiting either the settlement tube or the outgasser can be directly fed into the conical chamber. On the other, hand the bubble-free liquid could be fed into a bubble generation chamber G which adds microbubbles to it by electrolysis. This generation chamber, G, contains two 100 μm diameter wires made of 99.9 % pure Platinum (Pt) (procured from Advent Research Materials) and were used as electrodes. Results of the optical investigation of bubble size distribution generated by electrolysis in chamber G will be presented in Chapter 4. Therefore, the two Pt electrodes that were located at the end of the conical chamber that are generally employed during cleaning operations were removed.

To investigate the response of the UAS device to different input conditions, an experimental procedure was designed which tracks the electrical input power dissipated in the transducer along with a record of the acoustic pressure in the stream. Knowledge of acoustic properties of the liquid inside the conical chamber, which could either be bubble-free or bubbly, is very important. Investigations on the response of the UAS

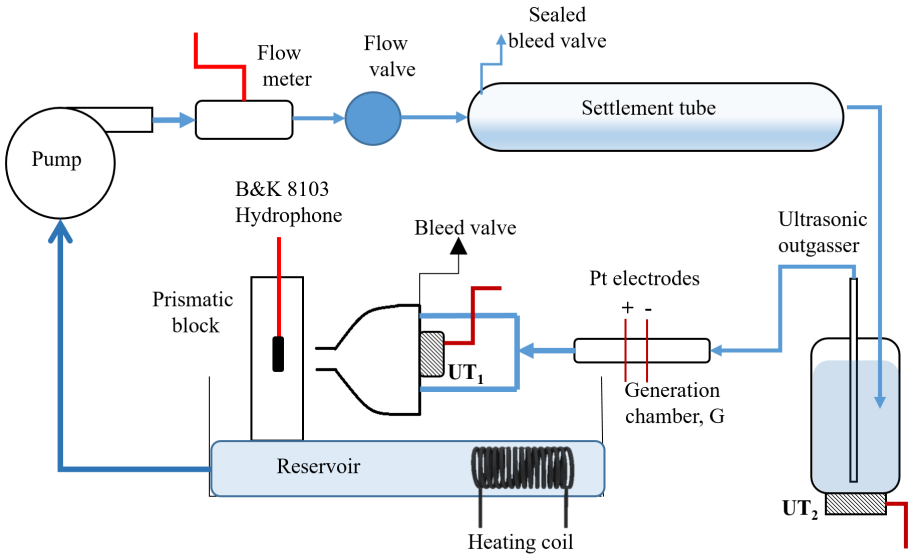

Figure 3.1: A schematic of the modified experimental setup (earlier version in Figure 1.1) used in this thesis. Featuring the ultrasonic outgasser, bubble generation chamber, and four-port inlet into the conical chamber. The sketch is not to scale and shows the liquid circulation path (electrical circuit not shown).

device carried out using the kit in Figure 3.1 will be presented in Chapter 5 (when using bubble-free liquid) and Chapter 6 (when using bubbly liquid).

The liquid leaving either the outgasser (bubble-free liquid) or the bubble generation chamber G (bubbly liquid) travels into the broad side of the conical chamber employing a four-port inlet. Liquid flows through the conical chamber and leaves via the nozzle. The liquid stream exiting the nozzle was directed onto a hydrophone placed within a prismatic block made from the acoustic matching material. The liquid then falls into the reservoir, where its temperature was maintained with the help of a hollow copper heating coil (shown in black). The liquid temperature needs to be maintained constant during experiments to minimize variations in the dissolved gas content [148]. It was found that in closed loop operation (as demonstrated in Figure 3.1) the pump adds energy to the liquid and raises its temperature with time[1]. The heating coil was used to maintain the liquid temperature at approximately 28^{o}C and the hollow copper tubes of the heating coil were filled with hot water circulated from a thermostatic bath (Camlab Limited). A Digitron Instrumentation digital thermometer was used for measuring the temperature of the liquid in the reservoir.

The working liquid contains salt and surfactant as additives, whose concentrations were detailed in Chapter 1. Table 3.1 presents the measured values of surface tension and viscosity of the working liquid at different concentrations of SDS per one litre of DI

[1]When transducer UT$_1$ was turned off and when the pump worked continuously for 1 hour, the liquid temperature increased from room temperature of 21^{o}C to 29^{o}C

water. The surface tension was measured using a CSC DuNoy Tensiometer no: 70535 and viscosity was measured using SI Analytics Ubbelohed Viscometer type 532-00/0, apparatus no: 1056456. The error values in parenthesis refer to standard error for the measurements.

Table 3.1: Measured values of surface tension and viscosity of the working liquid used in experiments.

Liquid used	Temperature ^{o}C	Surface tension mN/m	Viscosity mm^2/s
DI Water	18	77.2 (±0.1)	1.05 (±0.03)
	22	76.7 (±0.1)	0.98 (±0.05)
	37.5	70.9 (±0.1)	0.69 (±0.08)
	52	71.4 (±0.2)	0.52 (±0.18)
	62	65.2 (±0.2)	0.44 (extrapolated)
DI water with 1 mM SDS	26	42.1 (±0.1)	0.94 (±0.04)
DI water with 2 mM SDS	26.2	35 (±0.2)	0.97 (±0.03)

Any microbubbles that are either entrained near the liquid stream plunging into the reservoir or that are generated at the pump interface, must be stopped before they enter the device. The settlement tube was previously employed to meet these requirements. However, it was found that when compared with the settlement tube the ultrasonic outgasser was quicker and more efficient for this purpose (results presented in Section 3.3).

The electrical circuit (not shown in the figure), included a TGA 1244 type arbitrary waveform generator from AIM-TTi Instruments. The signal generator was used for providing the following signals: triggering signal, a sinusoidal ultrasonic signal for UT_1, and a 39.5 kHz ultrasonic signal for transducer UT_2. A DC supply box (by HAMEG Instruments) was used for maintaining potential across two Pt electrodes located in the generation chamber, G. An ENI RF 2100L power amplifier was used for amplifying the signal provided to the UT_1 transducer by 50 dB and a B&K 2713 power amplifier was used (amplification dial set at 55 dB) for driving 39.5 kHz ultrasonic transducer UT_2.

3.2.1 Pressure measurement technique

The hydrophone used for recording acoustic pressure in the stream was a B&K 8103 hydrophone (S.No: 2261933). The external diameter of the B&K 8103 hydrophone (9.5 mm) is very close to the diameter of the stream exiting the UAS device (10 mm), as pointed out in reference [8]. If acoustic data was recorded by placing the hydrophone directly in the stream, the measured pressure could only be considered as representative of the pressure amplitude propagating through the stream. In order to have a better estimate of the pressure amplitude and to have good control over the hydrophone spatial location, a mount was employed to hold the hydrophone in the stream exiting the UAS

device in references [8, 149]). The acoustic measurements recorded using the hydrophone placed in this prismatic mount (or block) will be reported in this thesis.

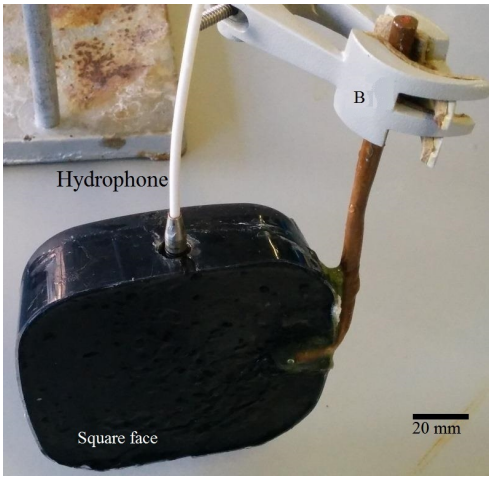

Figure 3.2: Snapshot of B&K 8103 hydrophone placed safely in a prismatic block made from the acoustic matching material (Rho-c), held rigidly by bracket B. The pressure measurements in the stream were carried out using this assembly.

The two-part polymer (Rho-c) used for manufacturing the conical chamber was used for making a rectangular prismatic block (dimensions 11 cm X 11 cm face and 4 cm deep) to hold a hydrophone. The block also consisted of an 11 mm diameter hole, drilled separately, to be used as a safe holding place for the active element of the hydrophone. The hydrophone is placed such that its acoustic centre is located at a distance of 9.5 mm from one of its square faces (see Figure 3.2). Any air gap around the hydrophone placed inside the block was filled with the working liquid to provide a continuous acoustic boundary [8]. The prismatic block (along with the hydrophone) was held rigidly with a bracket (B) and this assembly was placed in the stream path. The acoustic centre of the hydrophone was approximately aligned with the centre of the stream and was placed at a distance of 20 mm from the nozzle tip, with due care taken to the orientation of the active element. This arrangement provides a broad surface for the stream to impinge upon and a safe location for the hydrophone in the stream path [8].

The hydrophone was connected to the data acquisition system via a B&K 2635 charge amplifier, with the following settings on the dials: transducer sensitivity at 0.1 pc/m/s^2, multiplier at 0.1 mV/unitout, and upper frequency limit setting at >100 kHz. It is important to note that B&K hydrophones have a peak in their sensitivity values at approximately 130 kHz (see Figure 3.3). The hydrophone sensitivity values, as presented in Figure 3.3, can be converted to their equivalent charge sensitivities by using the capacitance of the hydrophone piezo element (including the influence of the cable), which is generally available in the calibration chart. For each measurement, the acoustic

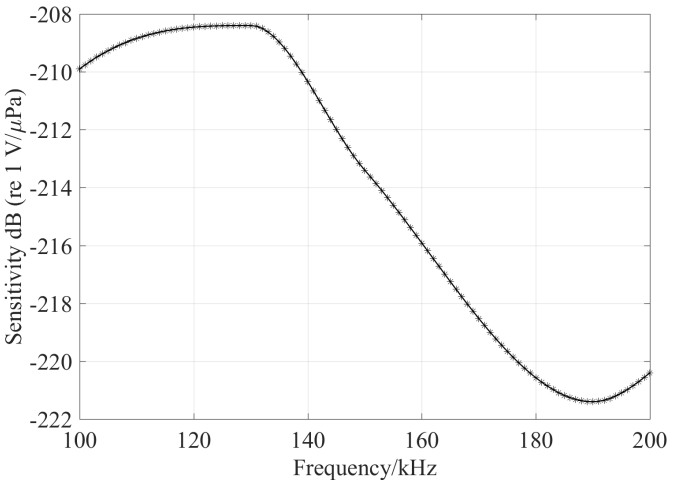

Figure 3.3: Free-field sensitivity of the B&K hydrophone in the frequency region of interest. Values interpolated at 1 kHz resolution using information taken from the calibration chart.

pressure amplitudes (and subsequently the spectral content) were evaluated by considering the sensitivity value of the B&K hydrophone at the insonation frequency provided to UT_1.

The influence of placing the hydrophone in the prismatic block for recording acoustic measurements in the stream will be discussed in Section 5.2.2.

3.2.2 Timing pattern for input signals

During the experiments, a Tektronix TDS 2024C four channel oscilloscope was used for observing and sometimes recording the: output of the flow meter, electrical current flowing across the Pt electrodes (for microbubble generation, if present), trigger signal, and hydrophone data. Figure 3.4 shows an example plot of the timing sequence used for experimental investigations. The hydrophone data and trigger signal were generally recorded using a PCI-DAS4020/12 data acquisition (DAQ) card from Measurement and Computing (maximum possible sampling frequency f_s = 20 MHz) working with an in-house written Visual Basic 6 (VB) program (see Figure 3.5 for an example of the Visual Basic (VB) front end interface). It should be noted that, in place of PCI-DAS4020/12 DAQ card, the NI BNC-2110 DAQ card was used for recording acoustic pressure reported in Section 5.4 of Chapter 5 and for Chapter 7.

A trigger signal with pulse repetition period (PRP) or t_1 at 200 ms and associated ultrasonic signal pulse length or t_2 at 20 ms recorded using the DAQ card are shown in Figure 3.4. The trigger signal was a 5 V zero-to-peak square pulse and the ultrasound signal was initiated with the rising edge of the triggering signal.

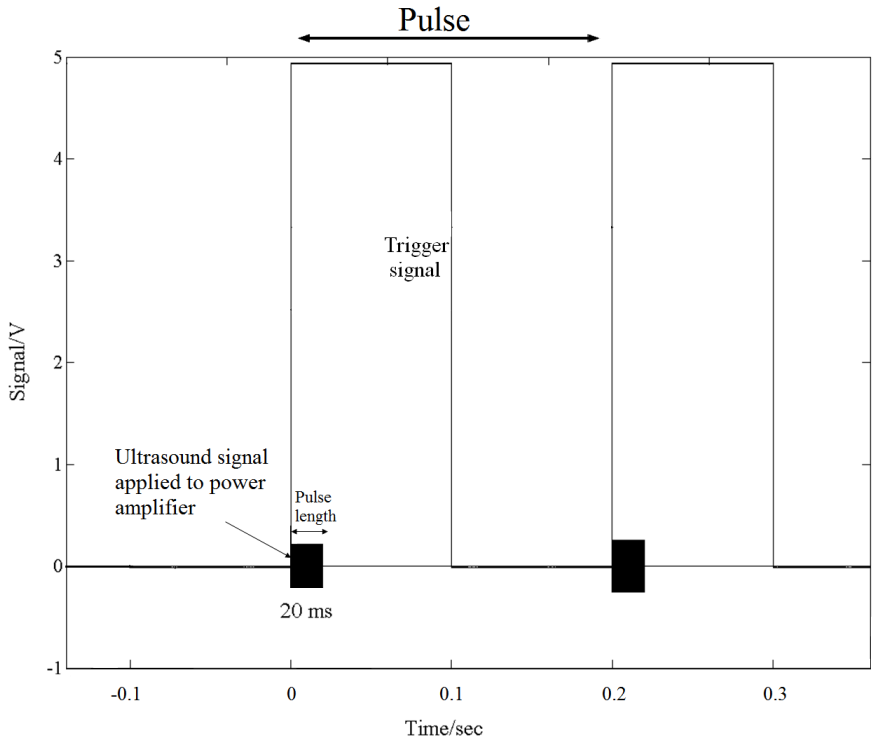

Figure 3.4: A plot showing the triggering signal (square pulse) of PRP 200 ms and the ultrasonic signal supplied to the power amplifier at pulse length t_2 of 20 ms. The frequency of the ultrasonic signal was 100 kHz.

3.2.3 Visual Basic interface

A snapshot of the user interface employed for data acquisition, designed in VB, is shown in Figure 3.5. Data acquisition was triggered by the rising edge of the trigger, and acoustic data from the hydrophone was recorded for a period of 20 ms. Once the data is acquired and saved, the frequency content of the hydrophone signal can be evaluated for all the pulses recorded by pressing the "FFT" button on the interface. For FFT evaluation, the recorded hydrophone data was windowed using a rectangular window of 16 ms in length and centred at 10 ms (where 0 ms corresponds to start of the trigger) to avoid the pressure transients. The start and end points of the rectangular window are marked in Figure 3.5 using white arrow marks. A discussion on the pressure transients recorded in the pressure-time traces, an example of which can be seen in Figure 3.5, will be presented in Section 6.4.

The individual components of the modified kit shown in Figure 3.1 are discussed in the sections below.

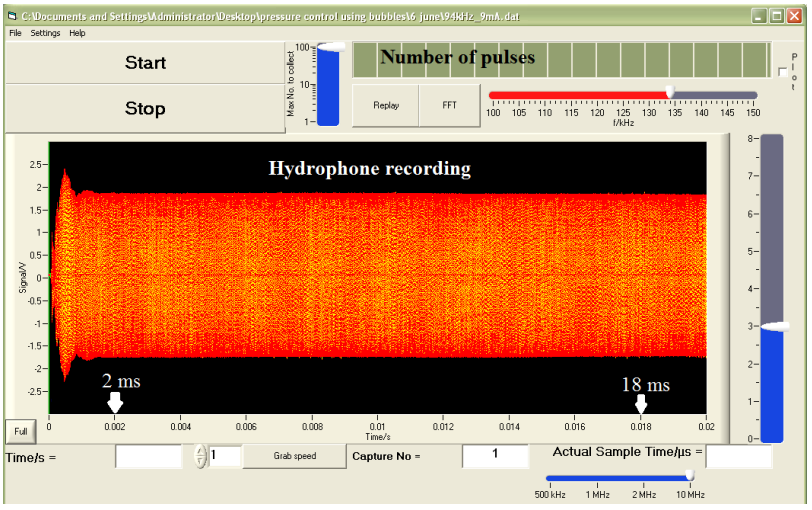

Figure 3.5: A snapshot of the Visual Basic (VB) program user interface, showing a representative recorded hydrophone signal, a counter for the pulse number, sampling frequency selector, and a button for FFT evaluation. The white arrows at 2 ms and 18 ms represent the position of the rectangular window.

3.2.4 Liquid inlet design

Earlier designs of the inlet port for the UAS device consisted of a silicone tube 8 mm inner diameter connected to a Y-junction port as shown in Figure 1.3. During preliminary tests carried out using the UAS device it was observed that this design affected the hydrodynamic stability of the cylindrical liquid stream that leaves the nozzle at flow rates beyond 2.5 litre.min^{-1}. It was also observed that any minor turbulent disturbances present at the inlet of the conical chamber were observed to develop into swirling instabilities on the stream surface. These turbulent instabilities in the stream were reduced by maintaining the flow rate at 2.1 litre.min^{-1} and by employing a new four-port inlet system. This new assembly, along with the conical chamber and the transducer UT_1 is shown in Figure 3.6.

The inlet tube (I) was manufactured using hollow glass tubes and was designed to take the liquid from the outlet of the bubble generation chamber, G, and into the broad side of the cone. The liquid flows into the conical chamber from both sides of the ultrasonic transducer UT_1. A bleed tube was attached to remove excess air trapped in the cone.

3.2.5 Bubble generation chamber

The bubble generation chamber, G, holds two electrodes which are separated by few millimetres. Three different electrode orientations were employed to evaluate their influence on the bubble size distributions (BSDs) generated during electrolysis. The results

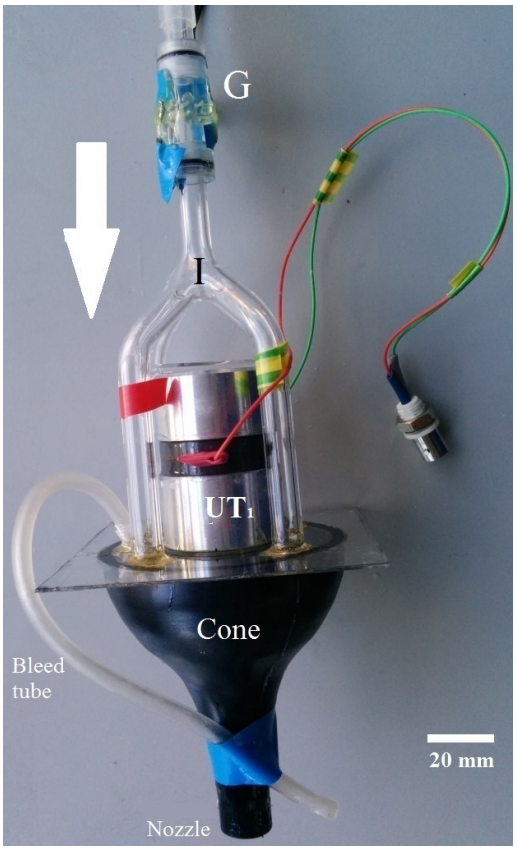

Figure 3.6: The modified liquid inlet design for the UAS device. The four-port liquid inlet (I), bleed tube (transparent), and the transducer (UT_1) were attached onto a transparent polycarbonate sheet. The bubble generation chamber, G, is also shown. The inflow direction is represented by a white arrow.

of BSD generated will be presented in Chapter 4. For the schematic shown in Figure 3.1, the two electrodes are separated by 4 mm inside the generation chamber and the direction of separation is along the flow. The bubble generation chamber can be seen in Figure 3.6.

3.2.6 Ultrasonic outgasser

In the modified experimental schematic shown in Figure 3.1 the liquid from the settlement tube was shown to enter into an ultrasonic outgasser, which was equipped with a transducer marked as UT_2. The working liquid laden with surfactant was observed to entrain bubbles in the reservoir (beneath the plunging stream of liquid) and in the pump. These microbubbles when they enter the conical chamber were found to hinder acoustic propagation. As this population of microbubbles could not be effectively controlled, it was deemed that removing them would offer improved control over the acoustic properties of the working liquid. These entrained microbubbles were termed the unwanted microbubbles.

The settlement tube was a passive system for removing unwanted microbubbles from the liquid. The liquid flows through the settlement tube and fills approximately half its volume when the tube is laid down lengthwise. Large bubbles in the liquid quickly rise up by buoyancy and are generally collected at the top of the settlement tube. However, smaller microbubbles (less than approximately 20 μm in diameter) have much less buoyancy force compared with the larger bubbles. Thus, the length of the settlement tube used (50 cm) was found to be ineffective in removing very small microbubbles. In such a case, an active technique for removing microbubbles from the liquid could be quicker and effective. The ultrasonic outgasser discussed in this thesis was previously developed and successfully demonstrated by Foley in 2014 [150] in studies related to the influence of the outgasser on hydrogen gas evolution.

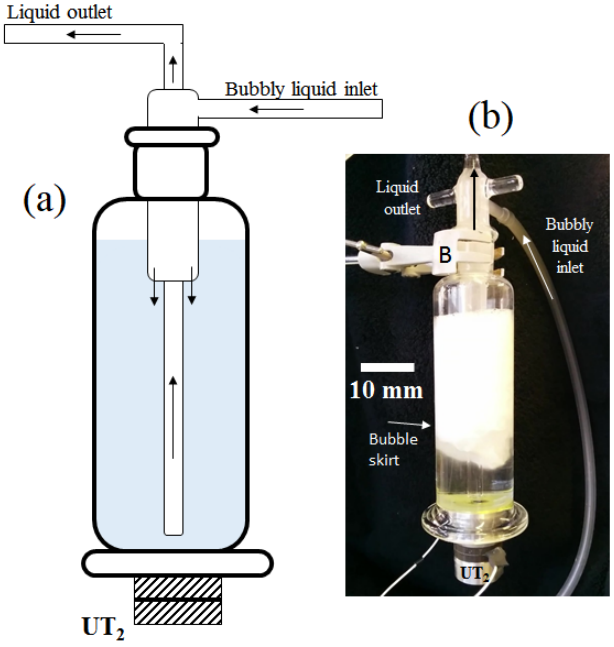

Figure 3.7: The ultrasonic outgasser used in this thesis. Part (a) is a sketch of the outgasser demonstrating its liquid flow route, and part (b) is a snapshot of the outgasser taken during its operation.

The outgasser, as shown in Figures 3.7, was constructed from a 250 ml glass Dreschel bottle. A 39.5 kHz ultrasonic transducer (UT_2) was glued onto the bottom of the bottle. The tube carrying the liquid into the outgasser empties at the top of the Dreschel as shown in Figures 3.7a. The liquid outlet is taken using a co-axial glass tube which extends up to the base of the bottle. In order to isolate and remove cavitation noise generated by UT_2 (as observed by the hydrophone held in the stream), a small silicone tube of 6 mm ID was connected in the liquid pathway between the outgasser and the generation chamber, G. It was observed that at voltage input to the power amplifier (V_{pa}) below 2 V_{pp} (or below 31.5 W measured electrical power input in transducer UT_2[2]),

[2]See Figure 5.7 for the schematic of electrical power measurement.

the outgasser was not effective at containing the unwanted microbubble population in its cylindrical column

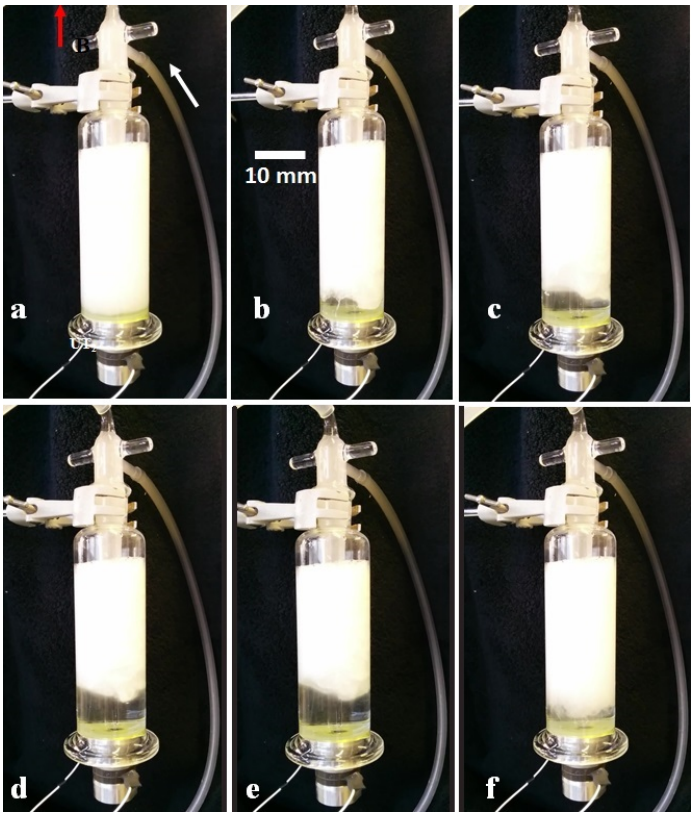

Figure 3.8: A sequence of images demonstrating the working principle of the outgasser. The scale bar in frame "b" is 10 mm long. The bubble-free liquid at the bottom of the cylindrical column can be noted in frames "d" and "e".

The liquid level in the Dreschel bottle, during experiments, was maintained such that its inlet port was completely immersed in the inflowing liquid to prevent bubble entrainment. The working principle of the outgasser is based on primary and secondary Bjerknes forces acting on bubble clouds in standing ultrasonic fields[3]. When bubbly liquid is flowing through the outgasser and when UT_2 is turned on, standing waves were set-up in the bottle and radiation forces from the standing waves lift up a cloud of bubbles. A bubble skirt was generally observed to form, depending on the size and the distribution of bubbles in the liquid, and when formed it was held up by the radiation forces (see Figure 3.7b). Bubbles then generally move to the upper part of the cylindrical column making the liquid at the bottom of the bottle bubble-free. The bubble-free liquid then exits the bottle (through the co-axial outlet tube) and proceeds towards the generation chamber, G.

As time progresses, the bubble cloud slowly moves to the top of the column and collect into a foam. Figure 3.8 presents a collage of images taken from a video recorded

[3]Influence of acoustic standing waves on bubble clouds can be found in references [83, 85].

at 29 fps demonstrating the working of the outgasser. The inter-frame time gap for the images shown in Figure 3.8 is 2 s. The liquid in the cylindrical column of the outgasser is white in colour due to the presence of a large number of microbubbles, generated by injecting air into the inlet tube of the pump using a syringe. The water inlet and outlet are marked by white and red arrows respectively in frame "a". The transducer was turned on between frames "a" and "b" (exact timing for the start of ultrasound was not recorded - as the purpose of this experiment was to demonstrate the working principle of the outgasser). Subsequent frames demonstrate the formation of a bubble skirt as bubble-free water leaves through the central tube. Transducer UT_2 was turned off in-between frames "e" and "f", and the bubbles are free to mix with the liquid and to depart with the flow. In the absence of a large bubble population in the cylindrical column of the outgasser, the formation of filamentary structures and audible cavitation noise were observed.

It is important to evaluate the effectiveness of this outgasser in removing (or outgassing) unwanted microbubble population present in the liquid and to compare its performance with that of the settlement tube under similar operating conditions. This could be carried out either using acoustical observations, or using optical observations, or a combination thereof. The next section describes these experiments and corresponding results in detail. The influence of the outgasser on the performance of the UAS device, at the resonance frequency of the transducer, is presented in Section 5.5.

3.3 Evaluating the effectiveness of the outgasser

The term effectiveness in this context refers to the potential/capability of the ultrasonic outgasser to restrict the microbubbles present in the liquid within its cylindrical column. This effectiveness can be quantified by acoustical and optical techniques and involves measurement of the time taken by the outgasser to make the liquid completely free of unwanted microbubbles. The advantage of using the outgasser over the settlement tube can be demonstrated using the acoustic measurements. Figure 3.9 shows the pressure-time plots recorded in the stream, generated when a test signal is supplied to the power amplifier to drive the transducer UT_1. The test signal was a 105 kHz sinusoidal signal with voltage to the power amplifier V_{pa} of 100 mV_{pp}, and PRP (or t_1) at 200 ms, and pulse length (or t_2) at 20ms. The pink trace in Figure 3.9 presents the pressure-time plot, recorded when employing just the settlement tube and the black trace presents the pressure-time plot recorded when employing just the ultrasonic outgasser in the liquid loop. In both experimental cases, no microbubbles were seeded in the generation chamber, G.

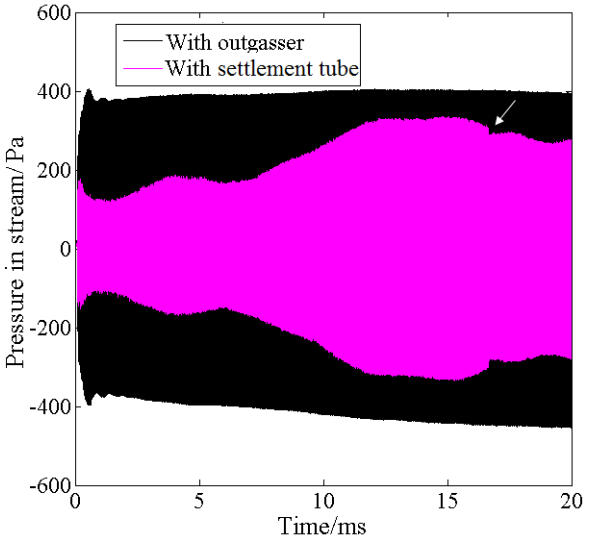

Figure 3.9: Traces of pressure measured in the steam using only the settlement tube (pink trace) and using only the ultrasonic outgasser (black trace), demonstrating the superior performance of the outgasser.

Comparing the traces in Figure 3.9, the pressure amplitude (peak-to-peak) measured in the stream while using just the outgasser is almost twice as high, relative to the same measurement using the settlement tube alone. As the system parameters and the input conditions to the transducer were unchanged in both these experiments, the improvement in the measured acoustic pressure when using the outgasser is a direct result of restraining the unwanted microbubble population in the cylindrical column of the outgasser. The pressure-time profile recording whilst using the outgasser was also observed to be symmetric about its mean value (0 Pa). The lower amplitude of acoustic pressure recorded when using just the settlement tube is attributed to a continuous stream of small microbubbles that aren't removed by buoyancy.

The pressure-time plot shown in pink in Figure 3.9 (using just the settlement tube) also consists of a series of undulations and a small spike in pressure amplitude (marked by a white arrow). The occurrence of this pressure spike coincided with a large cluster of microbubbles leaving the settlement tube and entering the conical chamber, as observed with the naked eye. In contrast, it can be observed that the recorded pressure-time plot when the outgasser was employed contains no spikes and no bubble clusters were observed leaving the outgasser (also see Section 3.3.2 for optical observations).

For settlement tube to be effective, the working liquid had to be circulated for at least 30 minutes before carrying out any acoustic measurements. However when the settlement tube was replaced with the outgasser and when the outgasser's transducer (UT_2) was turned on, the improvement in pressure output of the UAS device was observed within a few minutes. In order to quantify this response time, the following

acoustic and photographic observations were conducted.

3.3.1 Acoustic quantification

The following experiment was conducted to record the combined response times (i.e., the time required to effectively remove the microbubbles from the liquid) of the settlement tube and the outgasser. For this experiment, both the settlement tube and the outgasser were connected in series (one after another) as shown in Figure 3.1. A square trigger signal with PRP (t_1) of 5 s was used for triggering the transducer UT_1 at 100 kHz with V_{pa} at 100 mV_{pp}, at pulse length t_2 of 20 ms. The flow rate in the system was maintained between 1.8 to 1.9 litres.min^{-1} and the liquid temperature was maintained at 28.1^{o}C. No current was supplied to the two electrodes in the generation chamber, G.

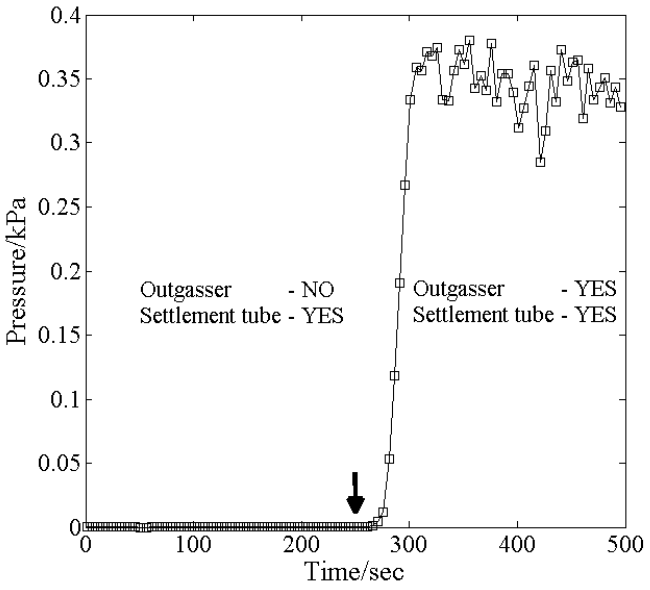

Figure 3.10: Comparing the performances of the settlement tube and the outgasser working on microbubbles generated by sucking air into the pump. The terms "YES" and "NO" refer to the active and inactive operation of respective devices.

Transducer UT_1 was turned on prior to triggering the data recording. Then, the inlet tube of the pump (located in the reservoir) was briefly lifted up above the liquid level and air sucked into the pump was allowed to mix with the working liquid. This action caused microbubbles to form in the liquid. The bubbly liquid was then allowed to flow through the settlement tube, the outgasser, and the generation chamber, G, to fill up the conical chamber. The acoustic data recording was triggered only when the bubbly liquid completely filled the conical chamber. The pressure measurements from the stream were recorded using the VB program for each pulse, and the frequency content of the recorded data was evaluated once data recording was completed. Using

the frequency content of the data recorded, it was observed that the contribution by the harmonics of 100 kHz signal to the pressure measured was negligible. The results shown below were extracted from the contribution of 100 kHz signal, evaluated per pulse.

The outgasser transducer UT_2 was only turned on at 250^{th} s (the temporal location is marked by a black arrow on X-axis in Figure 3.10). Between 0 s to 250 s, only the settlement tube was in operation and pressure could not be detected by the hydrophone. It can be observed that the settlement tube is ineffective (and slow when compared with the response time of the outgasser) in removing unwanted microbubble population from the liquid. Once the UT_2 was turned on, it took less than 75 s for the outgasser to restrain all the microbubbles from leaving its cylindrical column and for the bubble-free liquid to replace the bubbly liquid inside the conical chamber. The pressure measured in the stream slowly increases to 0.3 kPa (zero-to-peak), 100 s after starting the UT_2. The fluctuations in the pressure measured after the 400 s (around the 0.34 kPa mean value) could be attributed to the minor hydrodynamic fluctuations in the flow rate (caused by the pump). From these observations, it can be argued that the outgasser is quicker and more efficient in removing unwanted microbubbles from the liquid when compared to the settlement tube.

Subsequently, for the experiments that were carried out thereafter, the settlement tube was disconnected from the experimental set up and the outgasser was directly connected in-between the flow control valve and the generation chamber, G. Then, quantitative tests were conducted to observe the response time of the outgasser in restraining a known volume of air injected into the liquid using a syringe (at the pump inlet), in contrast to lifting the inlet tube of the pump above the water level, which draws air of unknown volume.

For this experiment, both the outgasser transducer UT_2 and the primary transducer UT_1 were turned on a few minutes prior to the start of data recording. Transducer UT_1 was driven at 100 kHz with 100 mV_{pp} as V_{pa}, PRP or t_1 at 200 ms, and pulse length t_2 of 20 ms. The acoustic recordings start at the 1^{st} pulse when both transducers have been running for a few minutes. Then the transducer beneath the outgasser (UT_2) was turned off at the start of the 10^{th} pulse (see Figure 3.11). Air of 1.8 ml volume was injected into the pump inlet at the start of the 20^{th} pulse (temporal location marked by a black arrow on the X-axis of Figure 3.11). The air mixes with water to form very fine bubbles, which then flow into the conical chamber and fill it up. Transducer UT_2 was turned on again at the 40^{th} pulse and the pressure measured outside the nozzle was allowed to recover. The time period for which the outgasser was turned off is marked using a blue rectangular box.

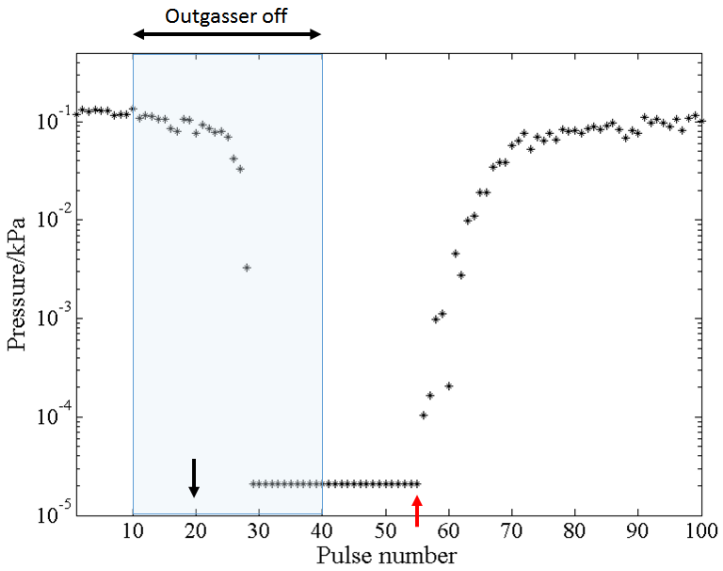

Figure 3.11: Result of an acoustic quantification experiment to determine the effectiveness of the outgasser. The outgasser was turned off between pulses 10 to 40 (marked by a blue rectangle). Air injected into the pump at the 20^{th} pulse.

The Y-axis of Figure 3.11 is plotted in logarithmic scale for a clear representation of the pressure drop as the outgasser was turned off and as air was injected into the pump. When UT_2 was turned off at the 10^{th} pulse, the pressure was observed to drop slightly from the initial amplitude, which suggests the influence of a small amount of microscopic bubbles leaving the outgasser and travelling into the conical chamber. The introduction of air into the pump reduces the acoustic pressure in the stream by four orders of magnitude. Once the outgasser was restarted, the pressure slowly recovers as the bubbly liquid present in the conical chamber was replaced with bubble-free liquid leaving the outgasser[4].

From the plot shown in Figure 3.11, two individual events could be tracked for different volumes of air injected into the pump. The first event is the starting point of the recovery curve on the pressure-pulse trace (once UT_2 is turned on, as marked by a red arrow) and the second event (or process) is the slope of the recovery curve. The slope of different recovery curves (dp/dt) was evaluated by fitting a third order polynomial curve (with least-square error) to the pressure-time plot between the red arrow mark and the plateau region recorded.

For example, a pressure-pulse plot with results similar to that shown in Figure 3.11 but generated when 2.5 ml of air is injected into the pump is presented in Figure A.1. Figure A.1 demonstrates that similar trends and reference points could be marked on Figure A.1. The influence of different volumes of air injected into the liquid on the

[4]See Section 3.3.2 for proof of bubble-free liquid leaving the outgasser, quantified using images taken by a high-speed camera.

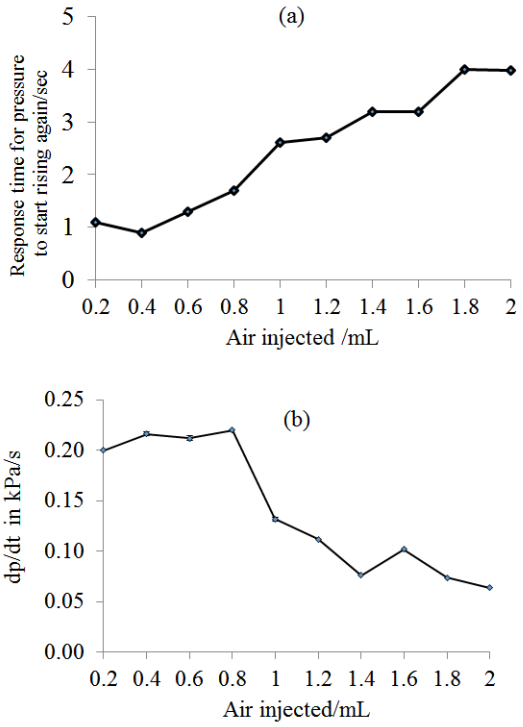

Figure 3.12: Acoustic quantification of the effectiveness of the outgasser with different volumes of air injected into the pump. Part (a) marks the location of the first point on the recovery path (marked by the red arrow in Figures 3.11), and part (b) shows the slope of the recovery curve of the pressure-pulse plot.

performance of the outgasser is presented in parts (a) and (b) of Figure 3.12. The results demonstrate a linear response of the outgasser to different volumes of air injected into the pump.

The acoustic observations reported in this section can be compared and correlated with the visual observations of the liquid leaving the outgasser. Hence, an optical quantification technique was developed to accurately measure and record the number (N) and size distribution of bubbles leaving the outgasser. The optical observations were carried out by placing a transparent observation chamber at the outlet of the outgasser and by imaging the liquid leaving it using a high-speed camera. The technique presented in Section 3.3.2 below was also extensively used in Chapter 4 to size and quantify the microbubbles electrolysed in the generation chamber, G.

3.3.2 Optical quantification

Optical observations of the bubble size distribution (BSD) of the unwanted microbubbles present in the liquid leaving the outgasser, were carried out using a Photron APXRS Fastcam high-speed camera. The experimental setup used for this task and the optical sizing to evaluate the BSD from images recorded is discussed below.

3.3.2.1 Experimental setup for measuring bubble size distribution

The experimental setup used for imaging the liquid leaving the outgasser consisted of a Totton NDP 14/2 pump and a Gems FT 201 turbine type flow meter connected in series with a flow valve. In this experiment, the UAS device (and its transducer UT_1) was not employed and only transducer UT_2 was active. An optical observation chamber was placed at the outlet of the outgasser, as shown in Figure 3.13. The liquid leaving the outgasser is allowed to flow through an observation chamber and then emptied directly into the reservoir, where its temperature was maintained.

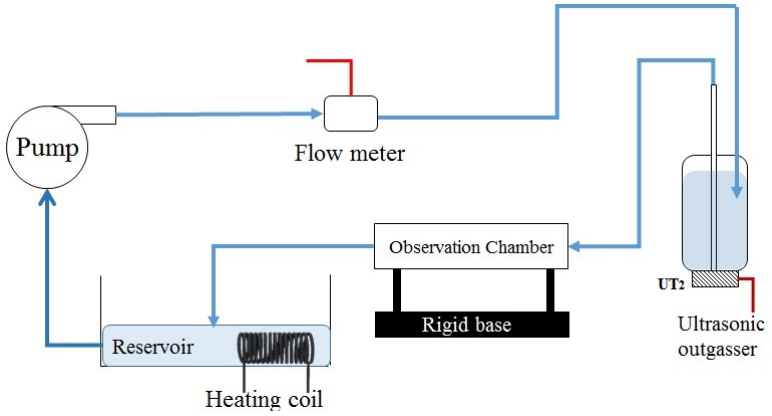

Figure 3.13: The schematic for the experimental setup used to (optically) observe changes in the BSD of microbubbles present in the liquid leaving the outgasser. Also, refer to Figure 3.14 for the details of the observation chamber.

The observation chamber was prepared by separating two microscopic glass slides (each slide was 75 mm long, 26 mm high and 0.8 mm thick) using two other similar slides as spacers. The two spacer slides were arranged, as shown in Figure 3.14, to create a channel for the working liquid to flow. The channel thus created was 60 mm long, 9 mm high and 0.8 mm deep. An L shaped 100 μm diameter steel wire was glued inside the observation chamber which was used as a reference length during image processing.

The observation chamber was held rigidly by mounting posts, which in turn were screwed into a slotted Aluminium board (Thor Labs). A Photron APXRS Fastcam (Serial No: 141714165 - Mono) high-speed camera was placed rigidly on the floor and was focused onto the centre of the observation chamber (focus area is marked by the small square with dotted lines in Figure 3.14a). A combination of 12X zoom adapter (Navitar) lens with a 2X magnification lens was attached to the high-speed camera, which provided a maximum resolution between 1 to 5 μm and a depth of field in-between 0.03 to 0.75 mm. A Hawowys ultrafine LED torch was used for illuminating. The slotted aluminium board was mounted on four rubber isolator mounts placed on the laboratory desk. The liquid in use (DI water + 2 mM SDS + 0.1 M Na_2SO_4 per litre) was filtered

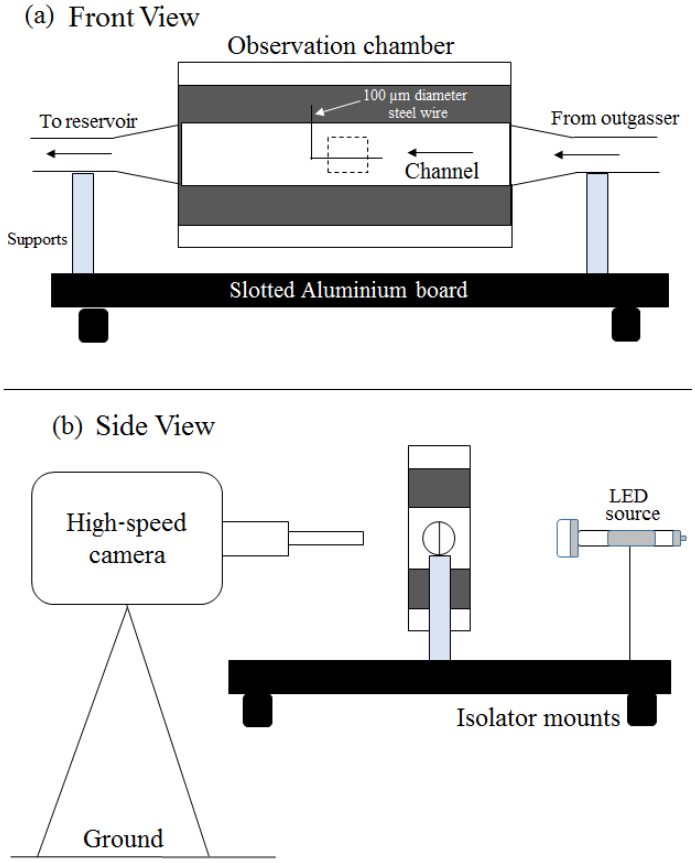

Figure 3.14: A schematic of the observation chamber for imaging the bubbles present in the liquid leaving the outgasser. Size of chamber and camera are not to scale. Part (a) shows the front view of the observation chamber. The dotted area shows the focus zone of the camera (1024x720 pixel resolution). Part (b) shows the side view of the chamber along with the location of the high-speed camera and the LED source.

using Whatman filter paper with pore size 50 μm, to remove small fibre type impurities that might obstruct imaging or liquid flow in the channel.

For this experiment, a known volume of air was injected into the pump using a small syringe a few seconds before triggering the camera. The microbubbles formed in the liquid are mixed by the pump, convect with the flow, and fill the outgasser and the observation chamber. After this, the outgasser and camera were triggered simultaneously (marked as 0 ms). Images recorded with the high-speed camera were used to track the changes in bubble population with time. Videos were recorded at 1000 fps, with an exposure time of 2 μs per frame[5]. The high-speed camera was programmed to recorded images in the time range between -0.43 s to 8.74 s, where the symbol "-" denotes acquisition before the start of the trigger and 0.43 s is 5% of the total acquisition time, which was limited by the memory available in the camera. Thus the camera

[5]At this frame rate, each image captured a fresh liquid sample with microbubbles inside them, i.e., same microbubbles were not present in subsequent frames. Also, see Section 4.2.1 for further discussion.

recorded the BSD present in bubbly liquid prior to the start of UT_2, as well as the evolution of BSD after the outgasser was turned on. During the experiments, the liquid temperature was maintained at 23.3^{o}C and flow rate was maintained at 2.1 litre.min^{-1}.

Images recorded using the high-speed camera must be processed to determine the variation in the BSD with time. The technique used for bubble size evaluation using images recorded is presented in Section 3.3.2.2. This technique was also employed for evaluation of BSDs for microbubbles electrolysed in chamber G.

3.3.2.2 Bubble size measurement using image processing

Individual frames extracted from the high-speed imaging data were used for measuring geometrical characteristics of bubbles using circle detection algorithms. In this context, it was observed that the Hough transform is employed by many image processing tools and studies [151] for detecting arbitrary, circular, and elliptical shaped objects in images (for example - counting bacterial or other cells present in an image [152]).

A Matlab based circle detection algorithm (available with its image processing toolbox) that employs the Hough transform was initially tested to detect and count the number of circles (in this case - number of bubbles N) present in an image. An initial estimate for the size of the target object has to be defined in Matlab prior to processing. However, Matlab's algorithm was observed to underestimate the number of bubbles present in an image N. This effect was prominently observed when the pictures were noisy, where the word "noise" here refers to presence of many small bubbles that are less than 5 μm in size (which is the optical limit of the lenses used). This made the BSD estimation a cumbersome process.

As an alternative, an image processing software called "ImageJ" was employed [152], which uses powerful techniques such as threshold control (for Black/White images) and watershed approach while counting or estimating object sizes and shape. These techniques, combined with the software's ability to process many images simultaneously made it best suited to the present work. The bubble sizing routine developed using "ImageJ" is presented in detail below.

The images in which the bubbles are to be counted were loaded into ImageJ (a stack of images or even a whole video could be loaded, as required). The images were then converted into an 8 or 16-bit grey-scale image (converted image shown Figure 3.15a). Then, the black/white (BW) threshold of the image was adjusted to highlight bubble outlines. Then, the background brightness of the image could be normalized i.e., it is effectively subtracted from the image if required (result shown Figure 3.15b). The

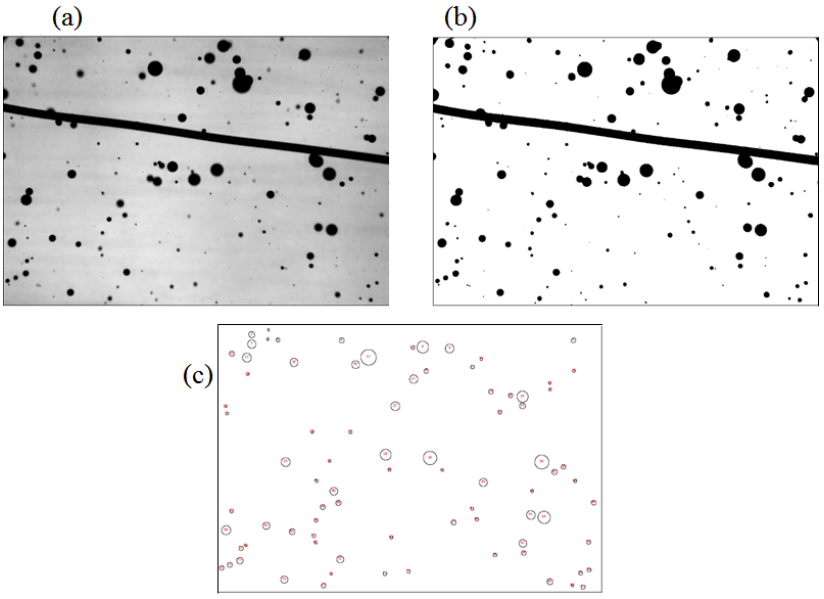

Figure 3.15: A sample set of images demonstrating the size measurement technique using the circle detection algorithm in ImageJ. Part (a) shows a snapshot from a high-speed video in 16-bit grey-scale, with the reference black line (100 μm diameter), part (b) shows the processed image, and part (c) shows the image after the circle detection.

remaining features, such as the bubble outlines and reference steel wire, were then highlighted. The highlighted features were then processed via shape detection algorithm. This algorithm consists of options for detecting a perfect circle (defined by the number "1" in the options menu) and to eliminate any straight lines in the image (defined by the number "0" in the same options menu)[6]. The circular shape present inside the bubbles was disregarded (which happens due to light refracting from the edges of the bubble and therefore resulting in its centre sometimes being illuminated as a bright spot). Once this process was completed, the outlines of bubbles which are perfectly circular were detected. Non-circular outlines may either refer to overlapping bubbles or to bubbles that were obstructed by the reference wire (both of which were rejected). Refer to part (c) of Figure 3.15 for an example of bubble outlines detected from a given image. The red marker inside each bubble in part (c) shows the bubble count in that particular image. The outlined bubbles were then measured (with the scale earlier defined using the 100 μm steel wire) and the measurement parameters (area, perimeter, location of bubble in the frame, and centroid) were recorded into a Microsoft Excel file. These results were processed and plotted to present the variation of BSD with time.

[6]If a number below "1" is used (for example, "0.8"), then that number refers to an ellipse whose minor axis is 80% smaller than the major axis.

3.3.2.3 Variation of bubble size distribution with time

The response time of the outgasser, in restraining a known volume of air injected into the pump, can be understood by observing the snapshots extracted from the high-speed images. One such example is shown in Figure 3.16. Frame "a"' (430 ms before trigger) displays the bubble population present in the liquid, generated by injecting 2.5 ml of air into the pump. The outgasser transducer UT_2 and the high-speed camera were simultaneously triggered at 0 ms. Frames from "b" to "i" are spaced 1 s apart, starting at 1 s for frame "b". The dark line across each frame in the figure is the reference wire (of 100 μm diameter). The liquid flow direction in the images is from right to left as pointed by the arrow in frame "i". The bubble population present in the liquid before the outgasser was turned on (as shown in plot "a") was observed to decrease with time after the outgasser was turned on. After frame "d" (i.e., 3 s after the start of the outgasser) very few microbubbles could be seen in the liquid exiting the outgasser. This implies at a flow rate of 2.1 litre.min^{-1}, and at power input to UT_2 at 31.5 W, the radiation forces generated in the outgasser on the bubble population were strong enough to withhold the microbubbles from the liquid leaving the outgasser.

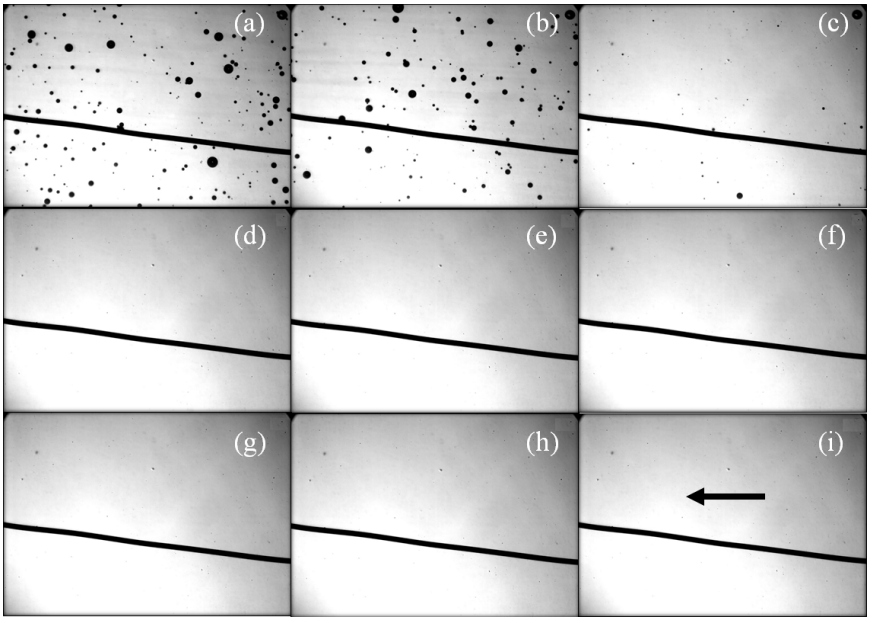

Figure 3.16: Observations from the high-speed camera demonstrating the effectiveness of the outgasser working on microbubbles, generated by injecting 2.5 ml air. Transducer UT_2 was triggered at 0 s and the reference wire in each frame is 100 μm wide.

To evaluate the parameter N and the size distribution of bubbles (BSD) that are recorded in the observation chamber, the high-speed images (shown in Figure 3.16) were processed using the circle detection algorithm of ImajeJ software. The results were shown in the form of a bar chart in Figure 3.17(i) for N and Figure 3.17(ii) for variation of BSD. Note that in Figure 3.17(ii), the X-axis shows the bubble radii starting from 5

μm, which takes into account the optical limit for the imaging system. The width of each bar in Figure 3.17(i) is 500 ms, except for the first bin which covers the time window between -430 ms to 0 ms. The height of each bar shows the number of bubbles (N) detected in that time window. It was observed that the spatial location of the camera focus region on the observation chamber had very little influence on either the value of N or the BSD values.

The individual bin divisions marked in Figures 3.17(i) are A (-0.43 to 0 s), B (0.5 to 1 s), C (1.5 to 2 s), and D (5 to 5.5 s). The higher value of N recorded in the second bin (i.e., time window 0 ms to 500 ms), immediately after turning on the UT_2, can be understood if we observe the evolution of BSD with time. As the outgasser is turned on, it can be seen that the number of bubbles recorded above 10 μm radius increases (BSD of bin B). This increase in bubble number (in time window 0 ms to 500 ms) is possibly due to fragmentation of larger bubbles in the cylindrical outgasser chamber as a result of strong acoustic radiation forces, driven by the pressure field generated by UT_2. The fragmentation of microbubbles in the cylindrical column of the outgasser was also observed by Foley [150].

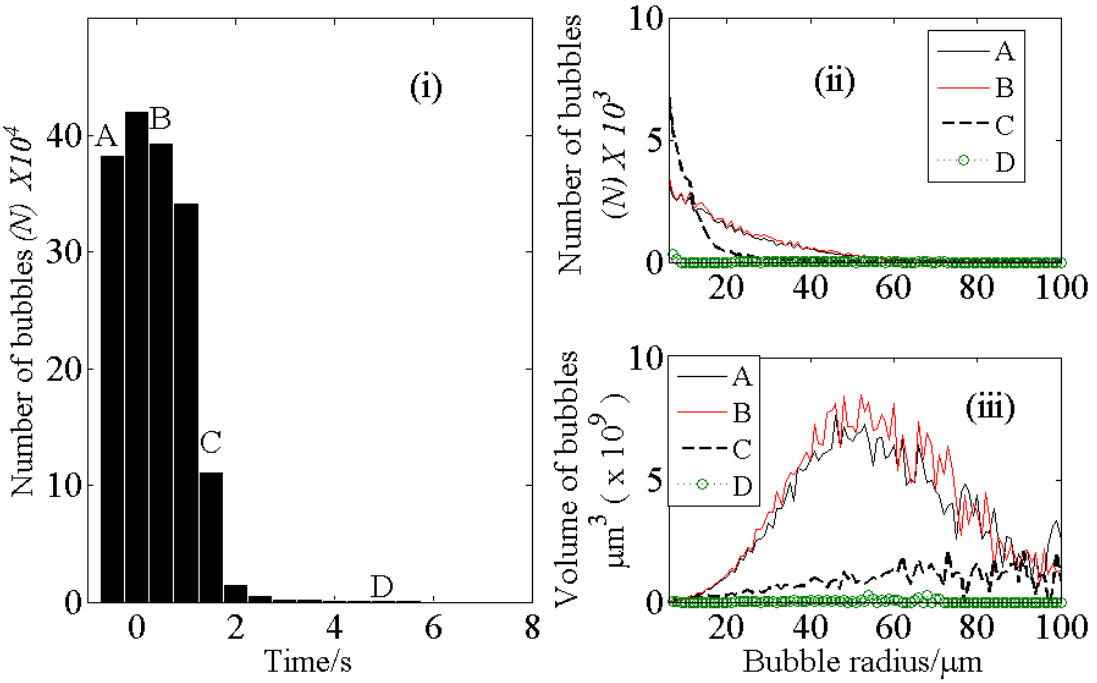

Figure 3.17: Variation of N and NV with time as outgasser works in restraining microbubbles generated by injecting 2.5 ml air into the pump. Part (i) Variation of N with time, part (ii) variation of BSD with time, and part (iii) variation of NV with time. More details in the text.

Another way to look at the data presented in Figure 3.17(i) and Figure 3.17(ii) is to observe the variation in the total observed volume of the gas NV (recorded in the observation chamber) with time. In this case, as circular shapes are extracted from

the image processing software (to represent the microbubbles), the volume of a bubble detected (V) can be evaluated using

$$V = \frac{4}{3}\pi R^3, \tag{3.1}$$

where R is the instantaneous radius of each bubble detected. This variation of parameter NV with time was calculated and is shown in Figure 3.17(iii). The Y-axis of this subplot records the parameter NV present in each time window for bubble radii bins shown on X-axis (bins are 1 μm wide).

It can be observed from Figure 3.17(iii) that, even though the number of bubbles at smaller radii (at the start) were generally higher, the contribution to the total gas volume by these bubbles is very small. The major contribution to the volume of microbubbles generated by injecting air into the pump is provided by microbubbles approximately at a radius of 50 μm. As observation time reaches 7 s, the volume of air recorded in the observation chamber drops, as is obvious by the green traces in Figure 3.17. Although there is rare evidence for a few stray bubbles leaving the outgasser, the overall contribution by these stray bubbles is very small, when compared with the original volume of air (curves marked by "A") present in the bubbly liquid. Similar observations for NV and BSD were also made when different volumes of air were injected into the pump, as evident from additional results shown in Figures A.4 and A.2.

These optical observations can be used to interpret the acoustic observations presented in Figure 3.11 (and additional Figure A.1). From Figure A.1 it can be observed that 7 seconds after the outgasser is turned on (approximately at pulse number 75), the pressure measured in the stream recovers to its earlier bubble-free value. The complete recovery of pressure amplitude to its bubble free value was observed to take a total of 12 s, which (it is proposed) is proportional to the time taken by the bubble free liquid to exit the outgasser, to flow into the conical chamber and to replace the bubbly liquid present inside the chamber.

The addition of surfactant to the working liquid increases the possibility for formation of microbubbles in large numbers. The effectiveness of the outgasser working on microbubbles (generated by injecting air into the pump) in surfactant-free and surfactant-laden liquids was also investigated, keeping in mind that the UAS device generally employs surfactant-laden liquid. For this experiment, two different versions of the working liquid were prepared, one with SDS and one without SDS. Air of volume 2.5 ml was injected into the pump in each case. The outgasser and the camera were simultaneously turned on (temporal location marked by a black arrow in Figure 3.18), with the transducer pulsing similar to that reported in conjunction with the result shown in Figure 3.17. The results are presented in Figure 3.18 (also, see Figure A.4 for 10

ml result). In these figures, each point represents the measured value of parameter N for a time span of 500 ms (for example, a point at 0 ms in Figure 3.18 represents N recorded from 0 ms to 500 ms, the exception being the first point which covers a time span between -430 ms to 0 ms).

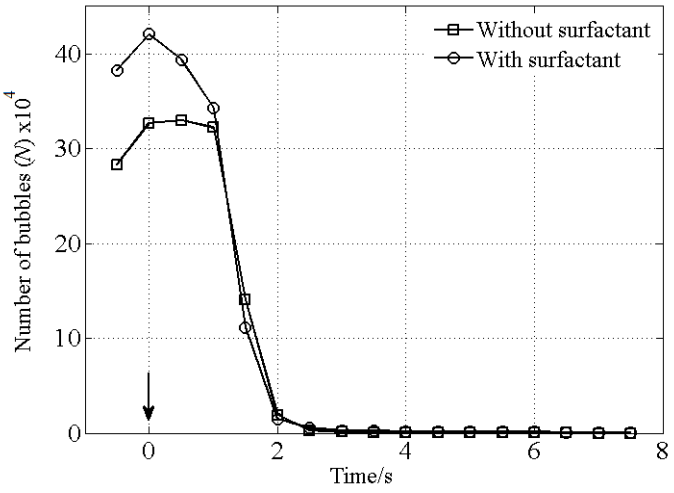

Figure 3.18: Optical quantification of the effectiveness of the outgasser working on 2.5 ml of air injected into the pump. The temporal location when the outgasser and the camera were simultaneously triggered is marked by a black arrow.

The number of bubbles N in Figure 3.18, recorded before the start of the outgasser when using surfactant laden liquid (marked with "o") is higher than the N recorded when using surfactant-free liquid (marked with "□"), as expected. Interestingly enough, the BSDs generated are very similar, when using either liquids (see Figure A.2). This suggests that the pump mixes injected air with the working liquid irrespective of the surfactant concentration. Observing Figure A.4 (and associated Figure A.3), in which the outgasser was working on 10 ml of injected air, it is interesting to note that the times taken by the outgasser are very similar irrespective of surfactant concentration.

These results conclude the development of experimental kit and the investigations on the performance of the outgasser. With the successful demonstration of the ability of the outgasser to make the liquid free of unwanted microbubbles, the conclusions of this chapter can be presented.

3.4 Conclusions

This chapter introduced the modified experimental kit that was employed during the experiments carried out to investigate the performance of the UAS device. The individual components of the kit were designed to attain control over the working parameters.

These components include a four-port liquid inlet tubing to reduce turbulence, an active technology called the ultrasonic outgasser to remove unwanted microbubbles, and a bubble generation chamber to add microbubbles to the bubble-free liquid. In addition to these components, an immersion heater was placed into the reservoir to maintain the temperature of the working liquid. An established technique to measure acoustic pressure in the stream leaving the UAS device was summarized.

The presence of unwanted microbubble population negatively influenced the performance of the device. The settlement tube was previously employed in the liquid loop (see Figure 1.1) to remove the unwanted microbubble population. It was shown in this chapter that the settlement tube was slow in its performance when compared with the active ultrasonic outgasser (see Figures 3.9 and 3.10). By activating the outgasser transducer (UT_2) at 39.5 kHz with 31.5 W measured power input, the liquid leaving the outgasser was acoustically (see Figure 3.11) and optically (see Figure 3.16) investigated and demonstrated that it is bubble-free. By using the modified experimental setup and by maintaining the operating liquid temperature at approximately 28.5^{o}C, improvement in the reliable performance of the device was targeted. The new experimental setup is suggested as a replacement for the existing experimental kit.

With the liquid leaving the outgasser bubble-free, its acoustic properties could be precisely modified by adding a known quantity of microbubbles using electrolysis. The next chapter uses the optical technique introduced in Section 3.3.2.2 for measuring the size distribution of microbubbles electrolysed in the generation chamber, G. The variations in the BSDs generated will be influenced by the flow parameters, electrode current, and triggering signal provided to the electrodes. Hence, the aim of the next chapter is to study these bubble size distributions and to select the right combination of working parameters which supplies bubbly liquid of required void fraction to fill the conical chamber. The influence of bubble-free liquid on acoustic propagation in the UAS device are presented in Chapter 5 and the influence of bubbly liquid (taken from the outlet of generation chamber, G) are presented in Chapter 6.

Chapter 4

Electrolytic microbubble generation in tubular flows and optical sizing

4.1 Introduction

In Chapter 3, a modified version of the experimental setup was introduced, which was developed with the aim of achieving improved control over the working variables such as liquid flow rate, unwanted microbubble population, liquid temperature, etc. Compared to the original experimental setup (presented in Figure 1.1), the new setup contains: a new inlet port into the conical chamber, an ultrasonic outgasser, water heater, and a generation chamber, G. The ultrasonic outgasser, an active method to remove unwanted microbubble population from the liquid, replaced the settlement tube. It was shown that the outgasser is quicker and more effective at reducing the unwanted microbubble population in the liquid.

This chapter deals with just the bubble generation chamber, G. This chamber was placed in the liquid path (see Figure 3.1) between the ultrasonic outgasser and the conical chamber with the aim of electrolytically generating microbubbles and adding them to the bubble-free liquid leaving the outgasser. The experimental investigations reported in this chapter were focused on evaluating the influence of working parameters such as liquid flow rate, surfactant concentration, and current through the electrodes. The experimental work and results detailed in this chapter were thus directed at generating, controlling, observing, and sizing these microbubbles.

Electrochemical microbubble generation is generally studied for its varied applications in different scenarios such as in microgravity (in a drop shaft [153]), for hydrogen gas evolution under Galvanostatic conditions at a microelectrode tip [154], and even under simple sonication [147]. Extensive works can be found in the literature that include sizing of naturally occurring gas bubbles and studies on experimentally generated microbubbles. Some of these works are summarized in reference [26]. Widely reported works include sizing techniques of naturally occurring bubbles formed beneath breaking waves [92] and investigations on bubble generation techniques such as ultrasonic irradiation close to the face of the transducer [147], bubbles generated by means of air injection using nozzles [90], and electrolytic methods for generating gas bubbles at electrode tips [153, 154]. The practical applications of these microbubbles span a wide range of research fields, such as quantifying the greenhouse gases produced or trapped in the ocean waters [26], drug delivery using encapsulated bubbles aided by ultrasonic energy [147], use of ultrasonic contrast agents during acoustic imaging [143], and aiding the cleaning process in ultrasonic cleaning baths or allied industries [34]. Accurate size determination of microbubbles in all these scenarios could be undertaken using different techniques (listed below) depending on the accuracy required, experimental operating conditions, and techniques suitable for the respective studies.

The size of the microbubbles was generally measured either using optical methods (including high-speed photography) [20], or using acoustical techniques such as scattering and absorption of propagating acoustic signals in bubble clouds [102, 146], or by studying the harmonic content generated in bubbly liquid excited with acoustic energy [97, 155]. Each method has its own set of advantages and drawbacks. For example, optical methods are useful for experiments carried out in a laboratory (for example, bubbles held in a small channel using a microscope [147]), or when the depth of field of the target area is narrow. On the other hand, acoustical methods are sometimes more suitable (for example, counting bubbles in the ocean) because of the strong acoustical scattering and absorption cross-section of microbubbles [75, 92].

The objectives of this chapter are to detail an experimental setup for generating electrolytic microbubbles (using two Pt electrodes) and the results of size determination using images captured from a high-speed camera. Optical sizing was chosen partly due to the availability of accurate sizing technique developed (as detailed in Section 3.3.2.2), and partly due to the advantages offered by imaging techniques over acoustical techniques in fast flowing liquids.

A description of the experimental setup employing the generation chamber, G, and an optical observation chamber is given in Section 4.2. This setup is very similar to the one presented in Figure 3.13. For experiments reported in this chapter the ultrasonic

transducers (UT_1, UT_2) were not employed, as neither the UAS device nor the outgasser was needed for optical sizing. The discussion and results on BSD generated are presented in Section 4.4. The conclusions of this chapter are presented in Section 4.5 and will be revisited in Chapter 6. Some additional results and figures supporting the discussions in this chapter are given in Appendix B.

The next section provides a brief discussion on void fraction and its influence on the speed of sound in liquids (with reference to equations developed in Section 2.1.5).

4.1.1 Void fraction and Wood's equation

In Section 2.1.5, the relationship between the speed of sound in bubbly liquid c_m and the void fraction β was presented in equation 2.20. If the void fraction in the working liquid is known, and when the microbubbles are undergoing linear isothermal (breathing mode) oscillations about their mean position, then the value of c_m could be estimated. The value of c_m evaluated at different void fraction values (β) increasing from 10^{-6} to 10^0 using equation 2.20, results in a well-known graph, shown in Figure 4.1.

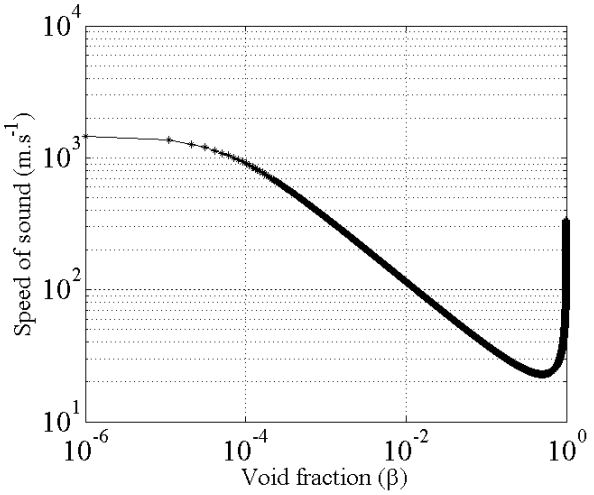

Figure 4.1: Variation of speed of sound in a bubbly liquid c_m at different void fraction β values, evaluated using equation 2.20.

The electrode current I that is used to generate the microbubbles in chamber G can be used to evaluate (using Faraday's law) the volumes of the hydrogen and oxygen gas that evolve at the electrodes. The total gas volume evolved can be used to interpret the void fraction of bubbles present inside the conical chamber. If a current I passes through the liquid for t seconds, then charge Q flowing into the liquid and the number of moles of gas M that evolve at the electrodes are related by

$$It = Q = nMF, \tag{4.1}$$

where F is the Faraday's constant (magnitude of charge per one mole of electrons) at 96485.33 C/mol and n is the number of electrons consumed by the electrolyte. Electrolysis of water requires 2 electrons to produce 0.5 moles of oxygen for every 1 mole of hydrogen, implying that 3.52 μM of hydrogen gas and 1.73 μM of oxygen gas evolve at the electrodes when they consume 1 C of electric charge. The molar volume of an ideal gas at atmospheric pressure (0.1 MPa) and room temperature (25^{o}C) is 24000 cm^3.M^{-1}. These values can be used to calculate the total volume of gas evolved at the electrodes. For example, if a current (I) of 200 mA is passed into the electrolyte[1] for 3.63 s, it implies a charge of 0.726 C (assuming no other losses). The volume of the conical chamber is 120 cc, so the void fraction β is

$$\beta = \frac{(24000)(3.76\text{x}10^{-6})}{120} = 7.52\text{x}10^{-4}. \tag{4.2}$$

Here the symbol "x" denotes arithmetic multiplication. Note that the result shown in equation 4.2 is valid for electrolysis in a stationary water reservoir and will only be considered as a guideline. An accurate estimate of the speed of sound in the conical chamber can be attained using experimental measurement. The results of experimental measurements of c_m at different electrode currents will be presented in Section 6.1.

It is also known that the value of c_m in cylindrical streams will be different to that estimated by using approximated free field conditions [156]. The boundary constraints on the waveguide could play an important role and a few studies were directed towards investigating the influence of bubbly liquid in pipes [142, 156]. Equation 4.3 provides a slightly modified version for evaluating speed of sound c_m in a pipe with constant diameter having flexible (non-rigid) walls[2], with microbubbles undergoing isothermal oscillations, and when the liquid surface tension is neglected,

$$c_m = \left[\left(\beta\rho_a\left(\frac{p}{P_0}\right) + (1-\beta)\rho_0\left(1+\frac{1}{K}(p-P_0)\right)\right)\left(\frac{\beta}{p}+\frac{1-\beta}{K}\right)\right]^{-\frac{1}{2}}. \tag{4.3}$$

Equations 2.20 and 4.3 were used to calculate c_m and a comparison is presented in Figure B.1 for void fraction values varying from 10^{-6} to 10^0. This figure shows that, near the void fraction of interest to this study (approximately 4.88 x 10^{-5} generated when using 13 mA electrode current and a DC control pulse), the speed of sound estimates are very similar. Hence equation 2.20 can be used in place of equation 4.3 in the present study to estimate the value of c_m in the UAS device.

[1] At 2.0 litre.min^{-1} the bubbly liquid takes 3.63 s to replace the (bubble-free) liquid already present in the conical chamber.

[2] Equation 4.3 is a variation of equation 34 from reference [156], by replacing the material properties of the pipe walls with acoustic properties of water.

With the relationship between c_m and β determined, the next section describes the experimental setup used for generating microbubbles in the chamber, G, and the results of optical sizing using observations from the high-speed camera.

4.2 Experimental setup

The experimental setup used for microbubble generation and subsequent imaging is shown in Figure 4.2, which is similar in construction to the setup shown in Figure 3.13. The setup consists of a Totton NDP 14/2 water pump for circulating the working liquid in a closed loop. A GEMS FT201 turbine type water flow meter was used to measure the flow rate. The flow rate could be controlled by using a manual screw type flow control valve. A glass jar that holds approximately 1.5 litres of liquid was used as a reservoir. The working liquid passes through a metal mesh water filter to restrain any small fibre type impurities. The liquid flow path includes the bubble generation chamber G (see Figure 4.3 for a detailed schematic of G) which holds two 99.9% pure 100 μm diameter Pt wires (or electrodes) purchased from Advent Research Materials and used as received. The position and orientation of the electrodes could be chosen from the three different designs (see Figure 4.16 for the designs) and in the schematic Figure 4.2 the two electrodes were separated by 4 mm inside the pipe with the direction of separation along the flow.

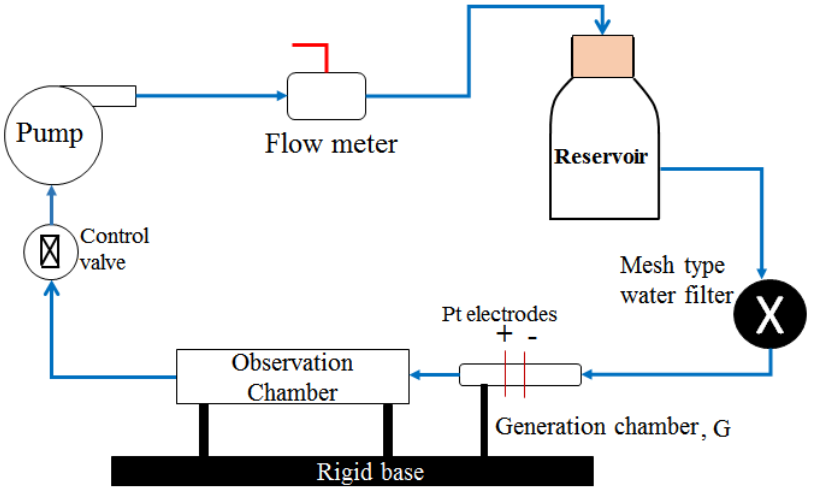

Figure 4.2: Schematic of the experimental setup used for generating microbubbles in chamber G. Bubble sizing was determined using recordings from a high-speed camera focused onto the observation chamber. Also, see Figures 4.3 and 4.16.

The generation chamber, G, was constructed from a hollow plastic pipette pipe of internal diameter 8 mm. The outlet of the chamber G was connected to an optical

observation chamber that is 75 mm long, 26 mm high, and 3.6 mm thick. The observation chamber was made by separating the two microscopic glass slides by 2 mm thick double sided tape (each slide has is 75 mm long, 26 mm high, and is 0.8 mm thick). A 100 μm diameter steel wire was placed inside the observation chamber and both ends of the steel were attached to the double sided tape, to be used as a reference during image processing. Both the bubble generation and observation chambers were screwed onto mounting supports, which were in turn screwed into a wooden plank with evenly spaced holes to aid mounting at convenient locations. A Phantom V5.1c high-speed camera was screwed onto the same wooden plank and was focused onto the centre of the observation chamber (as marked by the small square with dotted lines at 768 X 768 pixel resolution, see Figure 4.3a). In Figure 4.3b, two electrodes (in red) on either side of the reference wire (in black) are marked. A combination of 12X zoom adapter (Navitar) lens with a 2X multiplier lens was attached to the high-speed camera, which provided a lower resolution limit (in between) of 1 to 5 μm at a depth of field 0.03 to 0.75 mm. A Hawowys ultrafine LED torch was used for illuminating the observation chamber. The wooden plank was rigidly secured on 4 rubber isolation mounts. A Digitron Instrumentation digital thermometer was used for measuring liquid temperature in the water reservoir. The electrodes shown in Figure 4.3 are separated by 4 mm, with their separation direction perpendicular to the flow.

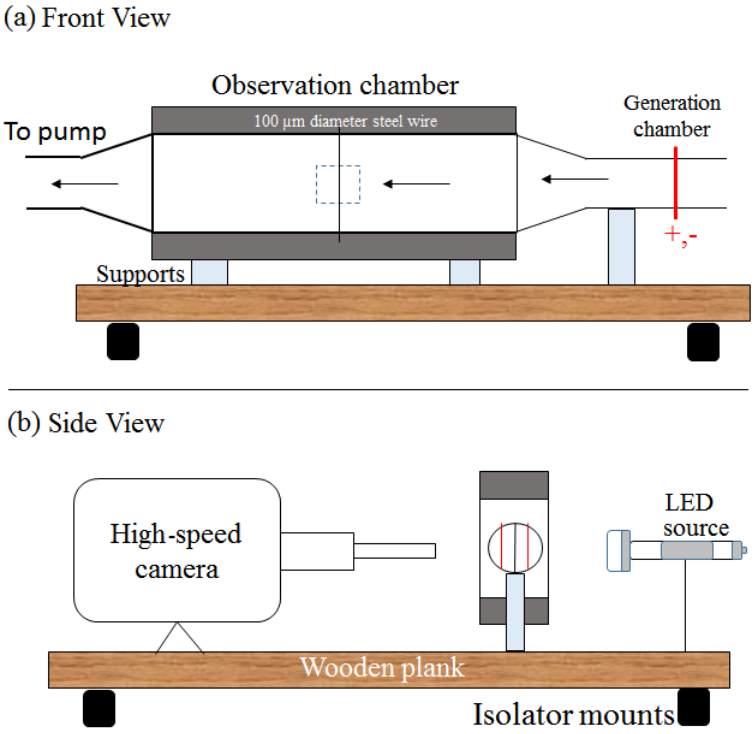

Figure 4.3: A line sketch of the bubble generation and observation chambers (not to scale). Part (a) shows the front view of both the chambers. Part (b) shows the side view of the chambers with the location of the camera and the LED source. The water flow direction in (a) is marked by arrows and in (b) is into the paper.

The two electrodes in the generation chamber were powered by a home-built control box (see Figure 4.4). A TGA 1244 type arbitrary waveform generator (AIM-TTi Limited) was used for generating either square pulses to control the "ON" and "OFF"' timing for bubble generation (also see Figure 4.5) or a DC signal which generates bubbles all the time (i.e., always "ON"). The potential difference across the two electrodes was maintained by HAMEG Instruments DC power supply box. The signals from the function generator and the DC power supply box were connected into a home-built control box which was designed to sum up the signals before transferring it to a relay. The amplified signal was then supplied to the electrodes for microbubble generation. The control box also has a provision for measuring the current flowing across the electrodes (which was measured as a voltage drop over a 1 Ω resistor).

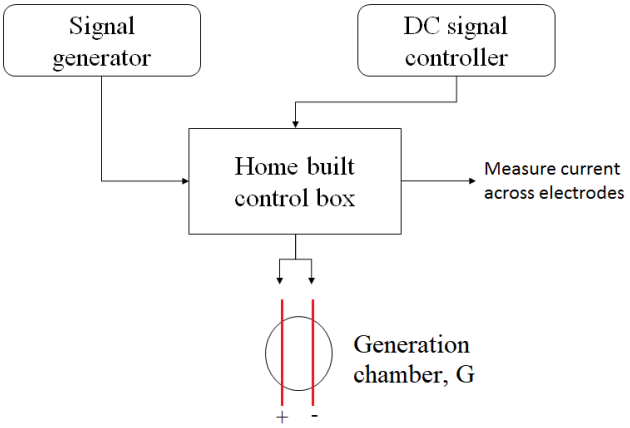

Figure 4.4: Schematic for the home-built electronic circuit used for controlling the pulse length and the electrode current. Note the provision for measuring the current flowing across the electrodes. The electrode orientation demonstrates a separation of 4 mm with their direction perpendicular to the flow.

Figure 4.5 shows an example of a square shaped current pulse across the electrodes (recorded and averaged over 128 cycles using the Textronix TDS 2024C oscilloscope), with a pulse length of 5 ms and current strength of 200 mA. In the figure, the term "ON" refers to the time period when bubbles were generated in chamber G and the term "OFF" refers to the time period when the bubble generation was turned off.

The electrolyte for bubble generation experiments was prepared using DI water taken from PUR1TE select water system and was mixed with 0.1 M Na_2SO_4 (14.2 g per litre). Since the surfactant concentration present in the liquid will change its surface tension value (see Table 3.1) in turn influencing the size and distribution of bubble population generated, different concentrations of surfactants (varying from 500 μM to 2 mM) were used. The electrolyte was initially filtered using Whatman filter paper (with 50 μm pore), prior to introducing it into the experimental setup.

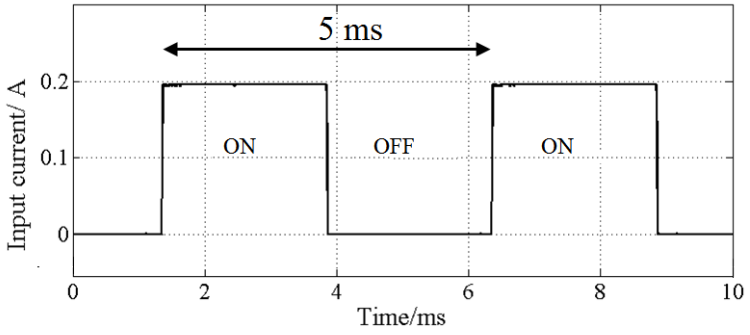

Figure 4.5: A sample recording showing the shape and the strength of the current signal (averaged over 128 cycles in the oscilloscope) flowing across the electrodes, generated using the control box shown in Figure 4.4.

The frame rate for imaging was maintained at 2100 fps. Exposure time for each image was found to have an important role in capturing sharp outlines of bubbles. A 10 μs exposure time per frame was found to be enough for producing images with sharply defined bubble edges when using flow rates of up to 1 litre.min^{-1} (using the Phantom V5.1C). However, at 2 litre.min^{-1}, exposure times of around 4 μs were needed. Flow rates at or above 3 litre.min^{-1} might need exposure rates of approximately hundreds of nanoseconds which were not available either with the Phantom V5.1C camera or the Photron APXRS Fastcam camera available in the laboratory.

Once bubbles were generated, they were imaged in the observation chamber and the captured images were used to infer the bubble size distribution. The relationship between the variation in the BSD with the system parameters will aid in the deciding the best combination of working parameters needed to study the UAS device. The next section briefly presents the image processing technique used for evaluating BSD, which is similar to the analysis presented in Section 3.3.2.2.

4.2.1 Bubble sizing using image processing

An example of high-speed images recorded from the observation chamber is shown in Figure 4.6. The black line across the frames of Figure 4.6 is the reference steel wire of 100 μm diameter. For this experiment, the system parameters used for bubble generation were: 126 mA current across electrodes with a square pulse of length 0.5 ms, liquid flowing at 0.5 litre.min^{-1} (no surfactant). In Figure 4.6 the flow direction is from right to left in each image. This flow direction can be observed by tracking a single bubble across the frames (i.e., by following the white arrow). A bubble that enters into the frame "a" takes approximately 2.8 ms to flow across the observation window and then out of the frame "f".

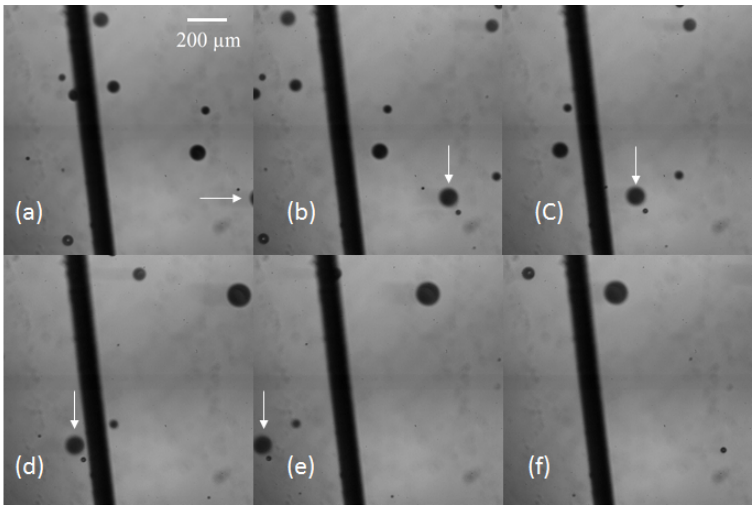

Figure 4.6: Five consecutive frames recorded at 2100 fps with 10 μs exposure showing the flow of bubbles generated in chamber G across the observation window. The black line across the individual frames is the reference steel wire 100 μm diameter.

The time taken for a single bubble to move across a given observation window is dependent on the flow rate (when imaging at a fixed frame rate). For example, it was observed that in a video recorded at 2100 fps with liquid flowing at 2.0 litre.min^{-1}, every successive frame captured a new population of bubbles flowing through the observation chamber. However at lower flow rates, such as 0.7 litre.min^{-1}, a bubble entering the optical window takes 5 successive frames to leave it. This time gap increases to 13 frames at a flow rate of 0.2 litre.min^{-1}. This variation was taken into consideration while selecting the images from a video to avoid multiple counting of the same bubble.

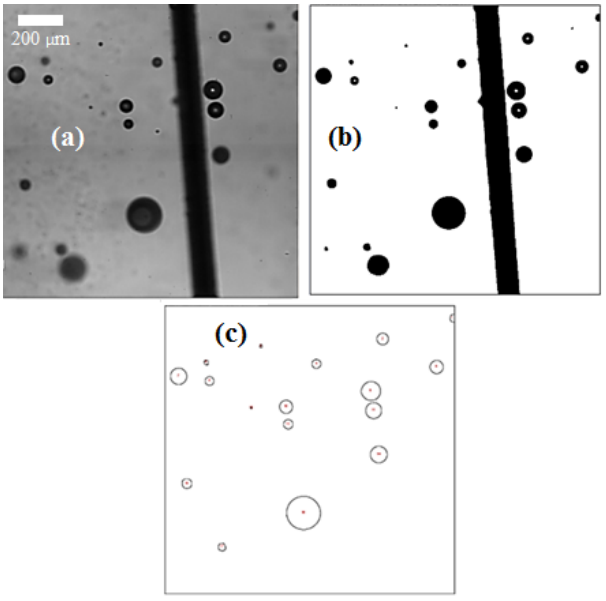

Figure 4.7: A series of images demonstrating different steps in bubble sizing using ImageJ circle detection algorithm for bubbles electrolysed in chamber G.

After the individual frames were extracted from a selected high-speed video, the bubbles present in each image were counted using the circle detection algorithm in ImageJ. Figure 4.7 demonstrates an example set of images for bubble size detection evaluated using ImageJ in three steps: (i) selecting the original image in grey-scale, (b) adjusting the threshold for the BW image and removing optical noise, and (c) detecting the circular objects. For each BSD measurement, 100 images extracted from the high-speed video were used to record, evaluate and present the information. Once the circles were detected, they were counted and sorted into a histogram and plotted.

During the experiments carried out, the variables were limited to:

- surfactants - Sodium Do-Decyl sulphate (SDS) between 500 μM to 10 mM and Triton-X100 (TX100) between 1 mM and 2 mM,
- flow rate between 0.2 to 2.0 litre.min^{-1},
- current across electrodes between 0 mA to 250 mA,
- control pulse signal length between 500 μs to 50 ms for square pulses, and a DC signal.

The results section start with a preliminary discussion about bin size selection for histogram display and comments on the experimental reproducibility.

4.3 Preliminary results and discussion

The preliminary results of microbubble generation and subsequent size detection using the circle detection algorithm are presented in Figure 4.8. This figure presents the measured BSD (in the form of a histogram distributed evenly between 0 to 40 μm radius bins on the X-axis, with bin size of 0.1 μm) generated using 0.5 ms square pulse at 176 mA current and using two different flow rates (a) 0.7 litre.min^{-1} and (b) 0.2 litre.min^{-1}. The electrolytic solution was made by mixing 0.1 M Na_2SO_4 and 1 mM SDS in 1 litre of DI water. The Y-axis of the plots in Figure 4.8 presents the number of bubbles detected (N) normalized to the bin size of 0.1 μm (i.e., N/μm). In both parts (a) and (b) of Figure 4.8 bubbles were not detected at radii below 2.5 μm, which is due to the post processing filter applied in ImageJ (based on the optical limit for the lens combination). The measured bubble radii in both cases vary from 2.5 μm to 50 μm, although very few bubbles were recorded beyond the radius of 40 μm.

An important feature observed from both these results is at the start of the graphs (at around 2.5 μm) as marked by black arrows in Figure 4.8. A disproportionately large number of bubbles (or in this case circles) were detected in these bins when compared

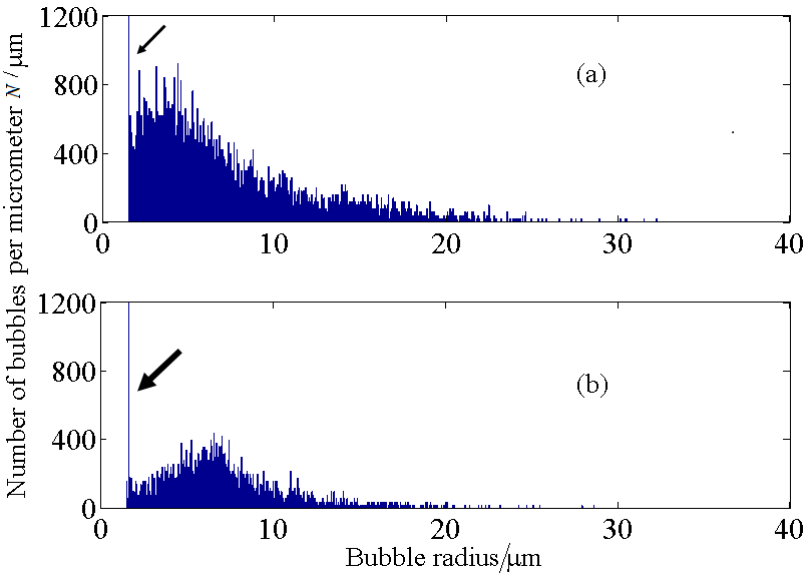

Figure 4.8: Preliminary results of bubble size distribution (BSD) measured using circle detection algorithm and presented as a histogram. Part (a) shows the BSD at flow rate 0.7 litre.min^{-1} and part (b) shows BSD at 0.2 litre.min^{-1}. The black arrow mark represents unwanted noise pixels in the distribution.

with the rest of the distribution. Upon comparing the original images with the distributions, this artefact was found to be the (optical) noise pixels that were detected by the image processing technique (even after employing the post-processing filter at 2.5 μm). Because the optical limit of the combination of lenses is quoted to be between 1 to 5 μm by the manufacturer, it was decided to present the BSD results in the radius range from 5 μm and up to a maximum of 100 μm.

Bubble generation using electrolysis of liquids is known to be a stochastic process [157]. This implies that tiny random fluctuations in electrode current might influence the mean and standard deviation (SD) values for the measured BSDs. To observe the reproducibility of the bubble generation process, three bubble generation tests were conducted on each day for three different days under similar operating conditions. The electrolytic solution was prepared by adding 0.1 M Na_2SO_4, 2 mM of SDS to 1 litre of DI water (freshly prepared and filtered each day). The flow rate in the system was maintained (for the result shown in Figure 4.9) at 0.7 litre.min^{-1}, a 10 ms square pulse was used as the control the signal, with 176 mA current across the electrodes. The results were normalized to the bin size (in this case, and from here on, 1 μm). The solid dark curve in Figure 4.9 shows the mean of all the measurements and the dotted outer lines present the region of standard error. The BSD measured was observed to have a maximum around 7.5 μm each day. The distribution tapers off both sides of 7.5 μm and the largest single bubbles detected were between 55 μm and 65 μm (not shown). Additional results are shown in Appendix B, in Figure B.2,

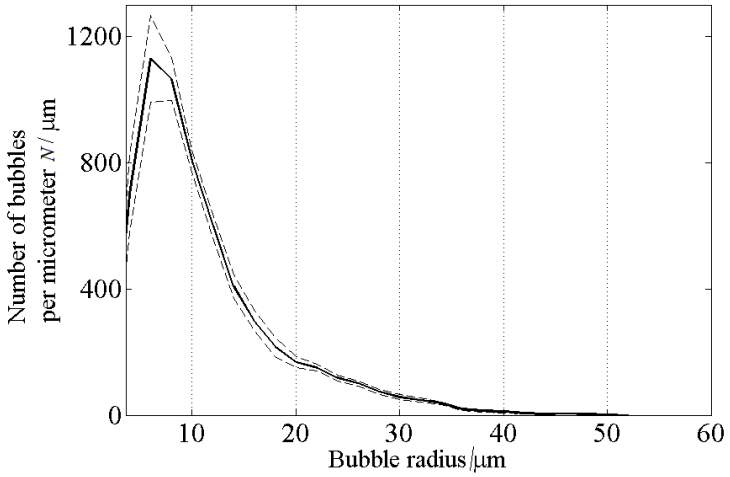

Figure 4.9: Graph presenting the mean curve and standard error curves of the BSD generated and detected using electrolysis demonstrating the repeatability of the generation process. The experimental conditions are in the text.

For experiments involving microbubble generation the statistical mean and the standard error of the distributions (as shown in Figures 4.9 and B.2) or the percentage ratio of mean to the standard deviation of the measured distribution called the polydispersity index are generally reported [147]. In contrast, for acoustical pressure measurements, depending on the type of survey the statistical quantities mean, standard deviation, percentiles, and quantiles of the measurements in different octave bands are recommended for reporting [158]. The use of polydispersity index (or more accurately the percentage dispersity index) for reporting BSDs recorded makes it easy to compare BSDs generated using different microbubble generation techniques [147]. Hence, the dispersity index was chosen as the statistical metric for reporting the BSDs electrolysed in chamber G.

A series of experiments were carried out for observing the bubble size distribution generated whilst using a combination of system parameters to find the influence of these individual variables on the BSDs generated. The results and relevant discussions are organized and presented below.

4.4 Influence of system variables on size distribution

This section is divided into six sub-sections. Each section presents a few examples of the influence of an individual parameter on the bubble size distribution generated in chamber, G. The influence of surfactant concentration is presented in Section 4.4.1, the influence of flow rate is discussed in Section 4.4.2, the variation of BSD with electrode

current in Section 4.4.3, the influence of using different pulse length in Section 4.4.4, and the influence of electrode position in the generation chamber, G, in Section 4.4.5.

4.4.1 Influence of surfactant

4.4.1.1 Surfactant concentration

This section discusses the influence of the surfactant content present in the electrolyte on bubble size distribution generated. It is known that the presence of surface active molecules in water reduces its surface tension. When the working liquid was mixed with SDS surfactant at 2 mM concentration per litre, the measured value of the surface tension dropped to 35.1 mN.m^{-1} from 72.1 mN.m^{-1} (see Table 3.1). As a result of the reduction in surface tension, the BSDs and the number of bubbles generated in chamber G will be strongly influenced. This is evident from the BSDs reported in Figure 4.10 which presents the influence of SDS at different concentrations in the working liquid SDS, increasing from 0 mM (i.e., no surfactant in the liquid) to 2 mM (0.576 g.litre^{-1}). Note that the Y-axes (in logarithmic scale) were normalized to the bin size used for plotting (1 μm) and the X-axis is drawn between 5 to 80 μm. The operating conditions for all the results presented in Figure 4.10 were - flow rate of 0.71 litre.min^{-1} with 250 mA across electrodes using a square control pulse length of 1 ms. Note that, a lower flow rate was chosen in this experiment to aid effective demonstration (for additional result see Figure B.3 reporting the BSD generated when using 1 mM of SDS, at a flow rate of 2.0 litre.min^{-1}).

From Figure 4.10, it can be observed that in the absence of surfactant (i.e., at 0 mM), the bubbles generated vary widely in their radii from 10 μm to 80 μm. The number of bubbles detected was also very small (with less than 10 bubbles in most bins) and there are some bins with no bubbles. Discontinuities in the distribution (for example, in bin 46-48 μm at 2 mM curve) represents the absence of bubbles observed. In the case of 0 mM SDS, inferring a mean value of the distribution would not be meaningful. However, as the surfactant concentration increases up to 2 mM, the mean value of the BSD settles between 6 to 8 μm, with the number of bubbles recorded at these radii approximately 900 (for 2 mM distribution). No bubbles were detected beyond 64 μm at a surfactant concentration of 2 mM or above[3]. The standard deviation value of the distribution is 7.17 μm for 2 mM SDS concentration and increases as surfactant concentration reduces.

[3]Surfactant concentrations beyond 2 mM per litre such as 3 mM and 4 mM were also used, but the bubble size distributions generated at these concentrations were very similar in number and shape to the 2 mM curve. The value of the measured surface tension of the liquid beyond 2 mM was observed to be stable around 35.1 mN.m^{-1}.

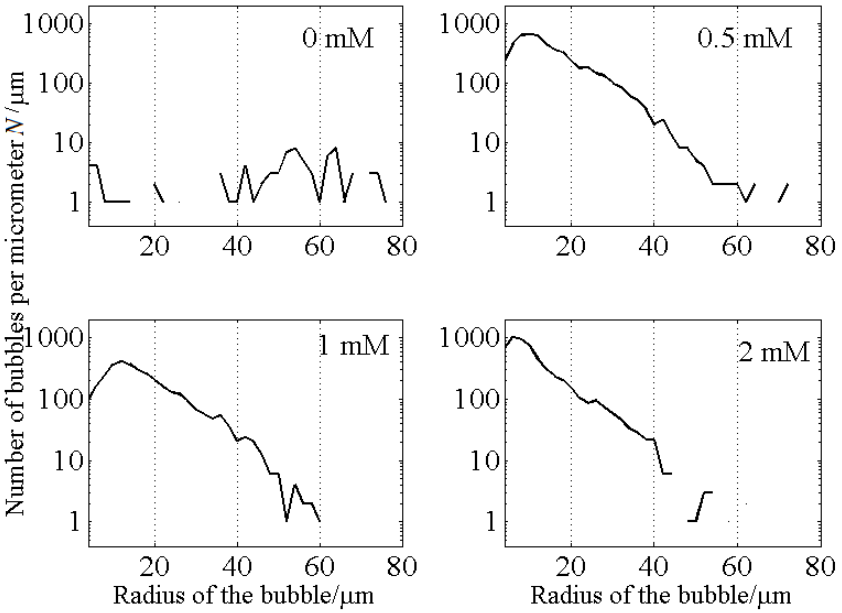

Figure 4.10: Bubble size distribution generated using different concentrations of surfactant SDS increasing from 0 mM to 2 mM. The Y-axis is in logarithmic scale and subsequently, any radius bin where no bubbles were detected was shown to be empty.

As surfactant concentration increased, bubbles with smaller radii were observed to form in larger numbers. This demonstrates that a larger value for surface tension promotes bubble formation with larger diameters at the electrodes, but with high variability in the radii that were electrolysed.

At a flow rate of 2.0 litre.min^{-1} and at SDS concentration of 2 mM per litre of liquid (operating conditions generally used in the UAS device), the increase in the shearing forces in the liquid assist in reducing the mean radius of the microbubbles generated further (discussions in Section 4.4.2).

The surfactant Triton-X100 (TX-100) is generally used in place of SDS in laboratory experiments. SDS is an anionic surfactant [159] whereas TX-100 is a non-ionic surfactant [160] (non-ionic surfactants are not known to lather in liquids compared with ionic surfactants). In order to observe the influence of the two different surfactants on the BSDs generated, experiments were carried out while using TX-100 (procured from Sigma-Aldrich Limited, 0.5 mM TX-100 implies 0.32 g.litre^{-1}), under different working conditions. A comparison of results is reported in Figure 4.11, recorded when the flow rate was 0.5 litre.min^{-1}, a square pulse of 10 ms was used, and electrode current fixed at 100 mA.

Comparing the two curves shown in Figure 4.11, the N in each bin when using TX-100 is smaller than the value of N per bin generated when using SDS. This can be

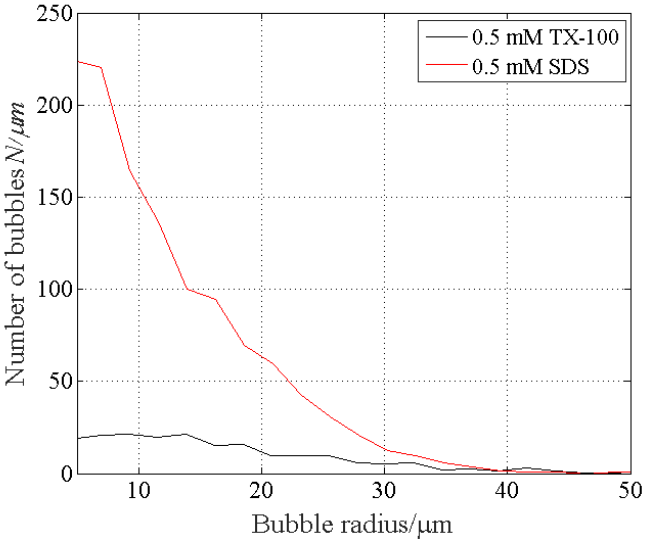

Figure 4.11: Comparing the BSDs electrolysed when using either 0.5 mM of SDS as the surfactant (red line) or 0.5 mM of TX-100 as the surfactant (black line).

attributed to the difference in the values of liquid surface tension recorded when using similar concentrations of the two different surfactants. When using 0.5 mM SDS per one litre liquid, the measured value of surface tension was 56.1 mN/m, whereas the surface tension value when using 0.5 mM to TX-100 was 62.2 mN/m (measured using a DuNoy Tensiometer). In this context, it can be easily understood (by using Figure 4.11) that, when employing different concentrations of TX-100 and SDS which achieve similar surface tension values in the working liquid, the BSDs generated would be very different. This could probably be attributed to the different micelle sizes of the two surfactants employed [161], which determines the size of the surfactant molecules.

Although the use of SDS is more common place, it is also a known harsh surfactant, when compared with TX-100, which is more gentler [161]. SDS is known to precipitate at lower liquid temperatures [161]. So, the choice of surfactants for microbubble generation depends on the BSDs required, the temperature of the liquid in operation, effectiveness of the surfactant when the UAS device is used for cleaning, ease of use, and ease of liquid disposal after use.

4.4.2 Influence of flow rate

The shearing forces increase at every point as the liquid flow rate increases. This implies that larger shear forces cause bubbles to pinch-off from the electrodes at a faster rate, resulting in the formation of a large number of smaller sized bubbles. Conversely, at lower flow rates, the shear forces in the liquid are smaller and therefore a smaller number of large radius bubbles should be expected.

This effect can be observed using the example result shown in Figure 4.12, which shows the number of bubbles generated per micrometre bin ($N/\mu m$) in the radii range from 5 μm to 50 μm. The working parameters used were: 10 ms square pulse, 176 mA electrode current and electrolytic liquid with 2 mM SDS. The three curves shown in Figure 4.12 present the results of BSD observed when using flow rates of 2.0, 0.7, and 0.2 litre.min^{-1} respectively as marked. It was observed that, as the flow rate reduces, the mean of the distribution increases from 7 μm to 12 μm.

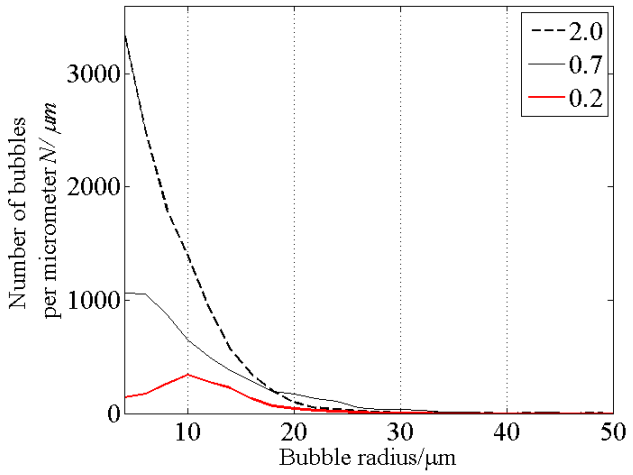

Figure 4.12: Influence of different flow rates on the BSD generated in the chamber, G, under similar operating conditions.

Because of the presence of a large concentration of surfactant (2 mM of SDS per litre of liquid) during the experimental results reported in this section, very few bubbles were generated (and detected) beyond 50 μm radius. Also, see Figures B.4 and B.5 in Appendix B to observe the combined influence of changes to surfactant concentration and flow rate on BSDs generated.

The next section presents the influence of electrode current on the BSDs.

4.4.3 Influence of electrode current

This section presents the influences of increasing the electrode current across the electrodes and subsequent changes to the BSD recorded. An increase in the current flowing through the electrodes implies a possibility for a larger volume of gas to evolve. This means that at a fixed concentration of surfactant in the liquid, as the current across the electrodes increases, the number of bubbles per micrometre bin will increase whilst the shape of the BSD is retained. This effect can be observed in Figure 4.13. Figure 4.13(a) shows the BSD recorded at a flow rate of 2.0 litre.min^{-1} as the current increases from 100 mA to 176 mA and Figure 4.13b shows the BSD recorded at 0.5 litre.min^{-1}. The

working conditions for these experiments were - electrolytic liquid with 0.5 mM SDS, with a square pulse length of 10 ms.

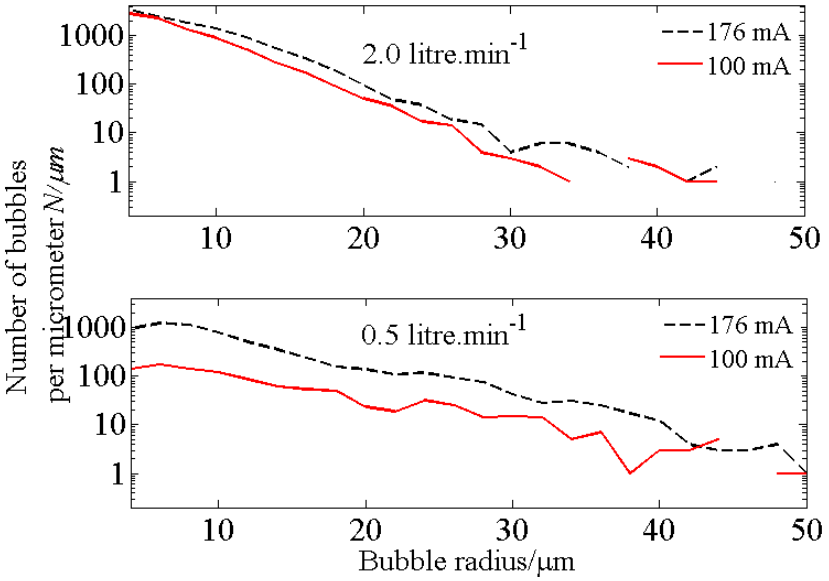

Figure 4.13: Influence of BSD with increasing current across the electrodes, at two different flow rates. Note that Y-axis is in logarithmic scale.

As discussed in Sections 4.4.1 and 4.4.2, the shape of the BSD is influenced by flow rate and surfactant concentration. As the electrode current increases from 100 mA to 176 mA, the number of bubbles registered in each bin when using a 0.5 litre.min^{-1} flow rate increases by 4 to 5 times. However at a flow rate of 2.0 litre.min^{-1} (i.e., Figure 4.13a) there appears to be little difference between the maximum number of bubbles generated at radii between 6 μm to 8 μm. The relatively larger liquid velocity around electrodes in the generation chamber, G, when using a flow rate at 2.0 litre.min^{-1} might be the contributing factor.

The result in Figure 4.13 shows that; at a fixed flow rate and surfactant concentration, the shape of the distribution could be maintained and the N of microbubbles generated using electrolysis could be controlled by changing the electrode current. This argument will be revisited in the conclusions section of this chapter.

4.4.4 Influence of electrolytic signal pulse length

The ON-OFF timing of the square shaped control signal used for bubble generation was one of the controlling factors during microbubble generation. The influence of using different lengths for triggering pulses on microbubble generation, with pulse length starting from 0.5 ms and increasing up to 50 ms, were observed under different working conditions. As an example, the BSD generated using different pulse lengths between

0.5 ms to 10 ms with electrode current held at 176 mA is shown in Figure 4.14. The working parameters used were - flow rate at 0.7 litre.min^{-1} and an electrolytic liquid with 2 mM SDS as an additive.

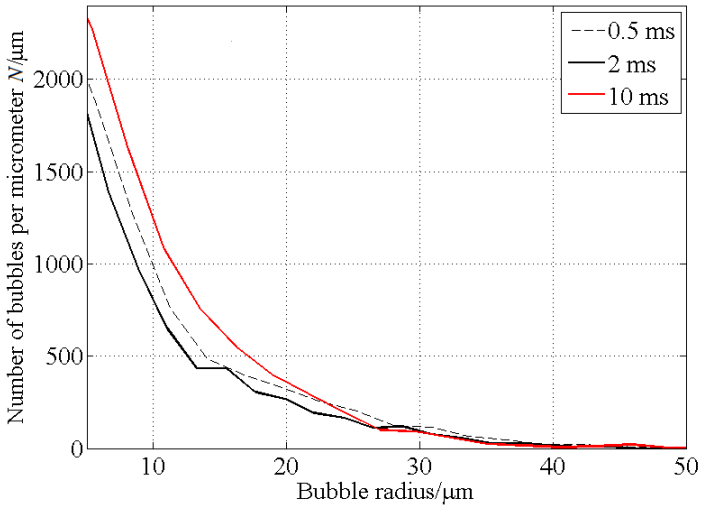

Figure 4.14: Variation in the BSD when using different pulse lengths for bubble generation, with electrode current kept constant at 176 mA.

From Figure 4.14, it can be clearly reported that using different pulse lengths during electrolysis of liquid had a minor influence (within the experimental error limits) on the shape of the BSD or on the number of bubbles recorded per bin. This effect could be understood by considering the flow rate in the system and liquid velocity in the channel. At a flow rate of 0.7 litre.min^{-1}, the liquid travels from the electrodes in the generation chamber to the observation window in approximately 2 s. During this time, at a pulse length of 10 ms (implying that the microbubble generator was ON for 5 ms and was OFF for the next 5 ms), the electrodes were turned on and off approximately 200 times. Although the diameter of the generation chamber is very similar to the piping used in the UAS device, the observation chamber is very narrow. This implies that the influence of pulse length on the variation of BSD generated would be averaged out during imaging unless the pulse lengths are as large as 2 s. The strongest contributors to N recorded and the BSDs are flow rate and the surfactant concentration. This could further be illustrated using Figures B.6 and B.7, which present the influence of a rectangular type control signal on BSD recorded.

Based on this result, the use of DC pulse as a control signal in place of the square pulse was considered. The DC control pulse would offer an advantage of providing a continuous stream of microbubbles (rather than an intermittent stream) to fill the conical chamber of the UAS device. The BSD generated when using a DC control pulse was investigated, whilst slowly increasing the electrode current from 1 mA. During these observations, it was observed that the minimum electrode current required to initiate

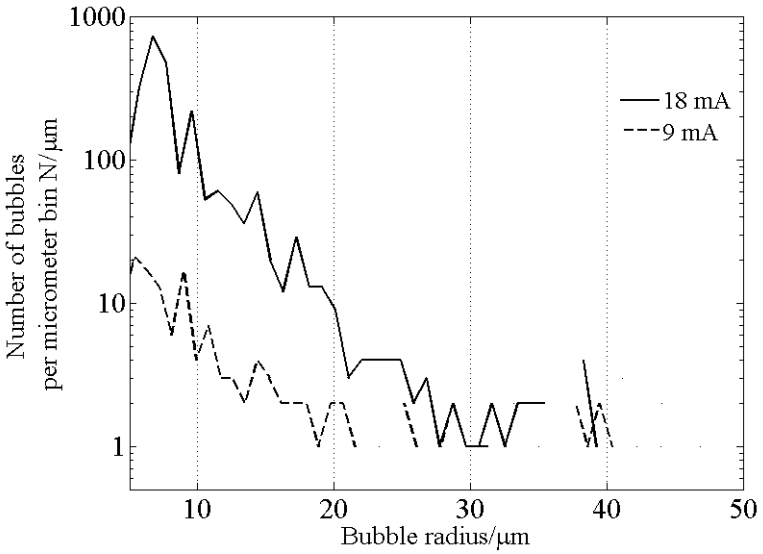

Figure 4.15: Bubble size distribution generated when using a DC signal as the control pulse at 9 mA and 18 mA electrode currents. The Y-axis is in logarithmic scale.

electrolysis in the working liquid was 3 mA. Subsequently, no bubbles were detected in the observation chamber at currents between 1 mA and 3 mA.

Figure 4.15 presents the BSD generated when using electrode currents of 9 mA and 18 mA (with the DC pulse as the control signal), with a liquid flow rate at 2 litre.min^{-1} and 2 mM SDS as the surfactant, conditions which are similar to the working of the UAS device. The results follow the trends, values, and shape of the BSDs reported in earlier sections, as expected.

The next section details the influence of electrode orientation and their spatial positioning in the generation chamber, G, on BSDs generated. Two of these positions were represented earlier in Figures 4.2 and 4.3 and the third position is shown as part of Figure 4.16.

4.4.5 Influence of electrode orientation

The BSD presented in the above sections was evaluated by placing/separating the electrodes by a small distance in the radial direction of the generation chamber. This configuration is shown, as a schematic, in Figure 4.16a. The orange region in Figure 4.16 indicates the electrically active area around the electrodes in the generation chamber. Two other electrode orientations were also tested to investigate the influence on the BSDs. These two orientations are illustrated in of Figures 4.16(b) and (c).

The velocity profile in the generation chamber (or in a circular pipe) in laminar conditions is termed the Hagen-Poiseuille flow or also called the parabolic flow profile,

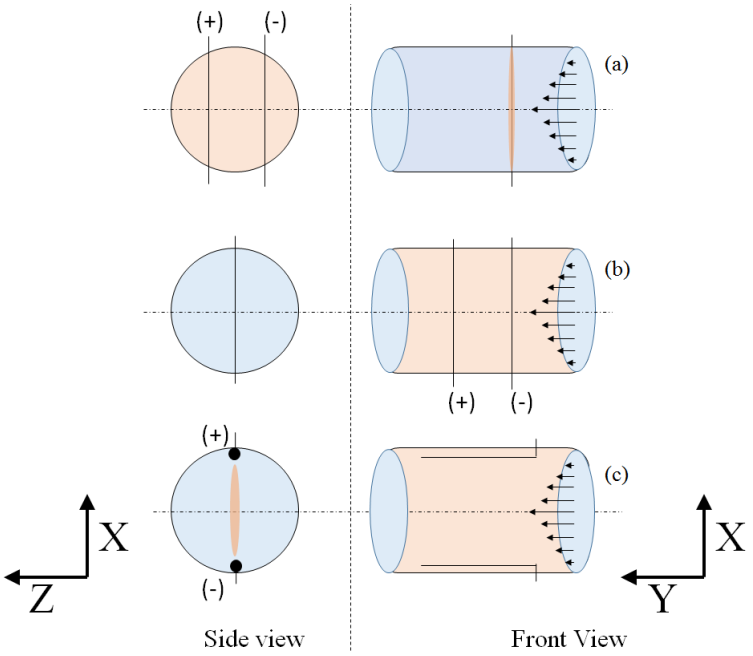

Figure 4.16: Line sketches of three different orientations for electrodes used in the generation chamber. The liquid flow direction is along the positive Y-axis. The electrodes are shown by solid lines and the axes of rotation or symmetry are shown by dotted lines. The diagram is not to scale.

that varies across the radius (represented by a series of arrow marks in the front views of Figure 4.16). This implies that the velocity of liquid at the pipe walls is very small compared with velocity at the centre of the pipe. Configuration (c) was designed with the target of generating BSD with larger mean values when compared with the BSD generated under similar operating conditions when using either configuration (b) or (a).

In configuration (a) the electrodes are parallel to the X-axis and are separated by few millimetres in the Z-direction (also shown in Figure 4.3). In configuration (b) the electrodes are parallel to the X-axis but are separated by a few millimetres in the Y-direction, and in configuration (c) the electrodes are parallel to the Y-axis and are glued at the two ends of the generation chamber (separated by 8 mm in the X-direction). Ideally, configuration (b) should generate BSD with a wider deviation from the mean values when compared with configuration (a) due to the placement of electrodes.

An increase in the mean value of the BSD was indeed observed when using electrode configuration (c) but only at flow rates below 1.0 litre.min^{-1}. Figure 4.17 presents a comparison of BSD generated using all three configurations at working conditions: 2.0 litre.min^{-1} flow rate, 1 mM SDS per litre, and 5 ms pulse length. It can be observed that (within the experimental error), the three curves represent similar BSD trends. At flow rates and surfactant concentration used for the UAS device, it was found that all three

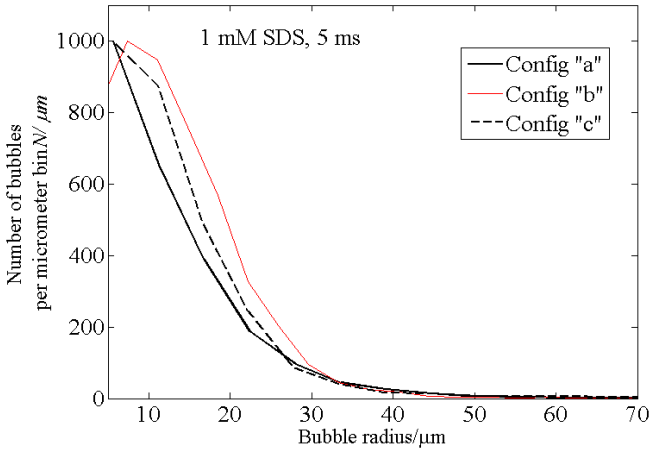

Figure 4.17: Number of bubbles per micrometre generated between 5 and 70 μm radius bins, when using three different electrode configurations of Figure 4.16.

configurations for electrode position did not yield any statistically significant changes to either the maximum values of N or in the BSD trends.

These results (along with additional plots located in Appendix B) provide some examples of the influence of various working parameters on the bubble size distribution generated in chamber, G. A summary of these results, the related discussions on choosing the right combination of system parameters required for studies reported in Chapter 6, and the conclusions of this chapter are presented below.

4.5 Discussion and conclusions

This chapter presented the optical observations and sizing of microbubbles generated by electrolysis of the working liquid in a pipe (or in the generation chamber, G). The chamber is designed to be placed prior to the inlet of the UAS device and receives bubble-free liquid from the outlet of the ultrasonic outgasser (as represented in Figure 3.1). Microbubbles were generated by using two Pt wires as electrodes embedded into the generation chamber. The working liquid has 14.2 g.litre^{-1} of salt (Na_2SO_4) added to make it electrically conductive and it was observed that at this concentration a minimum electrode current of 3 mA was required to electrolyse the liquid and to generate microbubbles. The electrical current was supplied, measured, and controlled using a home built electronic circuit. The bubbles generated in the chamber were photographed in an optical observation chamber and were sized using the circle detection algorithm.

The variables that influenced the bubble generation mechanism, their individual sizes and distribution were identified as the current across the electrodes, liquid flow rate, surfactant concentration, electrode positioning, and triggering pulse length controlling

the ON/OFF time. A large set of experiments with different combinations of working parameters were conducted. However, the results shown in this chapter were fine tuned to present the influence of each working parameter individually, with the eventual aim of demonstrating their influence on the bubble generation in the chamber, G. Only a few selected combination of these system parameters was eventually chosen, based on the BSD trends observed.

In this chapter, it was shown using Figures 4.10 and 4.12 that surfactant concentration and flow rate were the dominant parameters that influence the number of bubbles generated (N) in each micrometre sized bin. These parameters also strongly impact the shape of the distribution. At a flow rate of 2.0 litre.min^{-1} and 2 mM surfactant concentration (which was generally employed in the UAS device), any increase in electrode current translates into an almost proportional increased in the value of N, with a peak value in BSD between 7 to 10 μm (results presented in Figures 4.13a). It was also observed that at a fixed flow rate and fixed surfactant concentration in the liquid, neither the length of the control pulse signal nor the spatial orientation of the electrode had a major influence on the BSDS generated.

The average value of percentage dispersity index for microbubbles generated in the chamber, G, when the operating conditions are similar to that of the UAS device was 235%. This value is larger than the associated dispersity indices reported when either using sonication (≈150%) or using electrohydrodynamic force based atomization of liquids (≈30%), reported in reference [147]. The value of percentage dispersity index of the BSDs generated (using electrolysis of working liquid in the generation chamber, G) can be altered by changing the working parameters. For example, a percentage dispersity index of 99% was recorded when using a flow rate of 0.5 litre.min^{-1} with no surfactant in the working liquid.

Using the results presented in this chapter, the following combination of variables was chosen for microbubble generation, to be employed for investigating the response of the UAS device to bubbly liquid: DC control pulse signal with electrode current above 3 mA, electrode placed in either configuration (a) or (b) of Figure 4.16. These working variables along with the parameters generally employed in the UAS device (2.0 litre.min^{-1} flow rate, 0.1 M Na_2SO_4 salt, and 2 mM SDS surfactant) would generate a BSD with maxima between 7 to 10 μm (similar to BSD shown in Figure 4.15) with consistent reproducibility.

The ultrasonic transducer UT_1 (used in the UAS device) is resonant at 135 kHz, implying a resonant bubble radius at approximately 25 μm. It was discussed in Sections 2.1.5 and 4.1.1, that equation 2.20 is an approximation valid only under linear

acoustic propagation for bubbly liquids. Successful implementation and use of microbubbles generated in chamber G in the UAS device implies that the majority of the microbubbles present should be below a radius of 25 μm and the pressure amplitude in the liquid should be below the cavitation threshold (see Section 2.1.2.1). The first part of this requirement was investigated and reported in this chapter, and the second part of the requirement implies that the UAS device operates in the linear regime (where pressure recorded in the stream is below 100 kPa zero-to-peak).

The next chapter presents the response of the UAS device at 135 kHz when employing bubble-free liquid. The response of the UAS device when using electrolysed microbubbles, at resonance and off-resonance frequencies, will be reported in Chapter 6.

Chapter 5

Response of the UAS device

5.1 Introduction

The working principle of the UAS device was introduced in Chapter 1. Literature on acoustic cavitation and relevant phenomena, encountered when a liquid is insonated with large pressure amplitudes, was presented in Chapter 2. The benchtop version of the experimental setup that was previously employed for the UAS device was upgraded to attain control over the working parameters. The new experimental setup and the equipment introduced into the setup were discussed in Chapter 3. A large portion of Chapter 3 was dedicated to the results of investigations on the ultrasonic outgasser and its effectiveness in removing unwanted microbubbles. Using acoustical and optical observations, the liquid leaving the outgasser was demonstrated to be free of these unwanted microbubbles. The generation chamber G which was connected after the outgasser, takes the bubble-free liquid and adds microbubbles of known size and distribution (optical sizing results were presented in Chapter 4) and feeds the bubbly liquid into the conical chamber.

In order to investigate the response of the UAS device to bubbly liquid (either at resonance or at off-resonance frequencies of the transducer), a knowledge of the response of the UAS device filled with bubble-free liquid is vital. This response includes the response of the ultrasonic transducer UT_1 and the influence of attaching this transducer to the conical chamber. Hence, this chapter presents the results of experimental investigations on the performance of the UAS device at the resonance frequency of the transducer (135 kHz), when no electrical power was supplied to the electrodes in the generation chamber, G.

The response of the UAS device, as quantified by the pressure measured in the stream, combines the response of the ultrasonic transducer UT_1 and the response of the

liquid inside the conical chamber. The piezo based ultrasonic transducer employed in the present thesis is a tonpilz type transducer. The response of a tonpilz type transducer to different input voltages and loading conditions was extensively studied and reported for sonar applications [162]. Some of the important characteristics of a tonpilz type transducer include a highly resonant type response, presence of linear and non-linear regimes, saturation effect, and loss of electrical energy via dielectric heating. This chapter discusses these characteristics and then presents the performance of the UAS device. This chapter also discusses the relationship between the pressure output (as measured in the stream) and the electrical power dissipated in the transducer during its operation.

Individual sections in this chapter are organized as follows:

- Section 5.2 will present the pressure output of the UAS device as measured in the stream,
- Section 5.3 will discuss the response of the transducer, its non-linearities, saturation effect, and the electrical power dissipated in the transducer under different loading conditions,
- Section 5.4 presents the variation of acoustic pressure in the stream at different distances from the nozzle tip,
- Section 5.5 presents the observed improvement in the pressure output when the outgasser is employed, and
- the conclusions of this chapter will be presented in Section 5.6.

5.2 Pressure output of the device

Hydrophones are generally calibrated under free field experimental conditions (or as close to free field conditions as possible) when the active element is completely immersed in water (for example, see the latest standard for calibration [163]). In free field experimental conditions (and under linearised assumptions) the loss of energy as the acoustic signal propagates from a source location to the receiver location is only attributed to spreading and fluid absorption losses. Hence, the distance between the transducer face and the acoustic centre of the hydrophone plays a vital role. When acoustic measurements are carried out in a tank, the received data is generally gated to only take into account the direct path and avoids recording of the reflected or the reverberant acoustic field (based on experimental requirements).

The UAS device, however, is a reverberant waveguide and the internal diameter of the nozzle (10 mm) restricts the entry of the B&K 8103 hydrophone into the conical chamber. Acoustic pressure from the UAS device is generally measured in the stream

as demonstrated in reference [8] and the distance is generally quoted from the nozzle tip to the acoustic centre of the hydrophone. The best location to hold a specimen for decontamination was observed to be at a distance of 20 mm from the nozzle tip. Hence it is reasonable to place a hydrophone in the stream to record acoustic pressure, with the acoustic centre at a distance of 20 mm from the nozzle tip. As the distance between the nozzle tip and the acoustic centre of the hydrophone increases, the recorded pressure should be expected to reduce. However, at some working conditions of the UAS device, the capillary stability of the stream (exiting the nozzle) comes into play and has a prominent impact on the time averaged acoustic pressure recorded (in the stream) at distances beyond 40 mm from the nozzle tip. The measurements of acoustic pressure in the stream at different distances from the nozzle tip will be presented in Section 5.4 and the investigations of capillary instability formation on the stream will be presented in Chapter 7.

This section is dedicated to the reporting of the pressure output of the UAS device as measured in the stream (at distance of 20 mm from the tip). This requires an introduction to the measurement technique (Section 5.2.1), quantifying the influence of the prismatic block (Section 5.2.2), the measurement of the voltage across transducer terminals (Section 5.2.3), and finally the measured pressure output (Section 5.2.4).

5.2.1 Pressure measurement technique

Experimental results reported in this chapter were recorded using the schematic shown in Figure 3.1. For example, Figure 5.1 presents a sample acoustic pressure vs time plot recorded from the hydrophone placed in the prismatic block (Figure 3.2), after suitable amplification. Figure 5.1 also shows a trigger trace (in light yellow) and a trace of the input signal supplied to the power amplifier. The time delay between the rising edge of the trigger signal and the hydrophone data relates to the speed of sound of the liquid present in the conical chamber. The outgasser was not present for this measurement and the influence of unwanted microbubbles in the liquid can be noted.

It is important for the acoustic measurements recorded using the assembly shown in Figure 3.2 to take into consideration the influence of the prismatic block. The acoustical response of the prismatic block could be evaluated by approximating it as a rectangular room (along with appropriate boundary conditions). Placing an acoustic source on the square face of the prismatic block, where liquid jet impinges, and by placing the receiver at the acoustic centre of the hydrophone, the influence of the prismatic block (represented by the rectangular room model) can be estimated using normal mode analysis [164]. The result of this study is presented in Section 5.2.2.

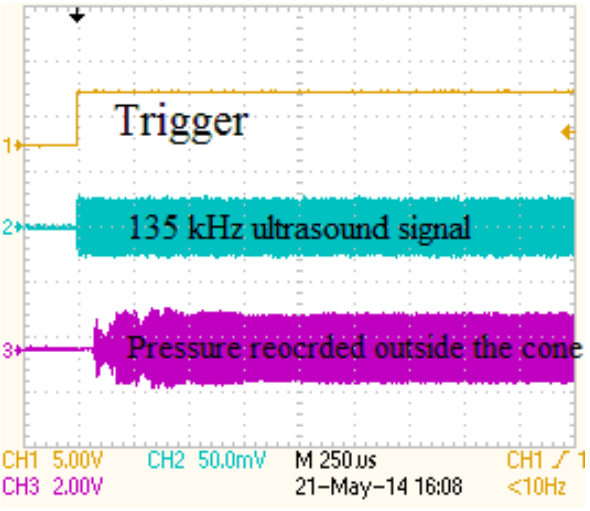

Figure 5.1: A plot of sample data captured using Tektronix TDS 2024C oscilloscope. Trace 1 is the trigger signal, trace 2 is the 135 kHz ultrasonic signal to the power amplifier, and trace 3 is the pressure measured in the stream using the B&K hydrophone placed in the prismatic block.

5.2.2 Influence of the prismatic block

The sound field distribution inside a rectangular room can be evaluated as a solution to the linearised Helmholtz equation, solved for the Cartesian coordinates. Assuming that the decay constants of the Rho-c polymer in the frequencies of interest to this study are approximately constant[1] and have values similar to that of water, the steady state pressure field P_ω generated at a point $\boldsymbol{r}_1$ inside the rectangular room due to a source located at $\boldsymbol{r}_0$ can be calculated using the eigen solutions. This pressure, P_ω, which is a function of frequency, can be considered as the transfer function of the rectangular room. The parameters $\boldsymbol{r}_0$ and $\boldsymbol{r}_1$ are the corresponding 3D vector coordinates of the source (taken as the location where the stream impinges on the block's square face) and the receiver (acoustic centre of the hydrophone) respectively. The boundary condition for the sound field within the prismatic block made from Rho-c polymer can be considered as soft boundary or a pressure release boundary. The transfer function is given by [165]

$$P_\omega = K_1 \rho_1 c_1^2 \sum_{nb} \frac{P_n(\boldsymbol{r}_1) P_n(\boldsymbol{r}_0)}{\omega^2 - \omega_n^2 - 2j\delta_n \omega_n}. \tag{5.1}$$

In this equation, parameters ρ_1, c_1 are the density and the speed of sound of the Rho-c material and the parameter K_1 is a proportionality constant [165]. Variable ω_n represent the series of nb eigen frequencies of the room. The pressure distribution within the block at the hydrophone location $\boldsymbol{r}_1$, is given by $P_n(\boldsymbol{r}_1)$ and the incident pressure from the stream impinging on the block surface is given by $P_n(\boldsymbol{r}_0)$. From the eigen

[1] Frequencies of interest were 120 kHz to 145 kHz (0.2 octave around resonance frequency 135 kHz).

solution, the value of $P_n(\boldsymbol{r}_0)$ is calculated as

$$P_n(\boldsymbol{r}_0) = C.sin(\frac{n_x \pi x_0}{L_x}).sin(\frac{n_y \pi y_0}{L_y}).sin(\frac{n_z \pi z_0}{L_z}), \tag{5.2}$$

where L_x, L_y, L_z are the dimensions of the equivalent sized room; n_x, n_y, n_z are numbers for the nodal planes in respective directions; and C is an arbitrary constant. The equation representing $P_n(\boldsymbol{r}_1)$ is obtained by replacing the vector co-ordinates of $\boldsymbol{r}_0$ in equation 5.2 with the co-ordinates of $\boldsymbol{r}_1$.

The parameter δ_n in equation 5.1 represents the decay constant, which are dependent on the medium in the room. The values of δ_n, which are generally smaller than that of ω_n [165], and can be obtained from reference [165]. Although the Rho-c polymer used for making the prismatic block mimics acoustic properties of water, the polymer could also possibly transmit shear waves when acoustic pressure is incident upon it. In addition, the polymer material might offer higher damping to propagation of the pressure waves within it, when compared to water. This implies that investigations into the response of the prismatic block to incident acoustic signals should also include different possible estimates for δ_n.

Assuming that the stream diameter and hydrophone active element are point source and point receiver objects, the pressure measured at the receiver location within the rectangular room ($\boldsymbol{r}_1$) can be evaluated for a normalized unit amplitude of acoustic pressure propagating in the stream at each frequency. This value of P_ω was evaluated between 100 kHz and 150 kHz (at a frequency resolution of 100 Hz) and is shown in Figure 5.2. This figure contains four subplots highlighting the influence δ_n on equation 5.1, starting from a value that is equivalent to that of water, to the estimated high value (whilst satisfying the constraint $\delta_n \ll \omega_n$). From Figure 5.2 it can be observed that the pressure measured inside the block is generally greater than the acoustic pressure amplitude incident from the stream, and the strong influence of δ_n is also evident. However, as expected δ_n only alters the overall damping in the system but not the frequency characteristic response of the room.

Reverting back to equation 5.1, the assumption that the stream and the active element of the hydrophone are point objects, and the use of $P_n(\boldsymbol{r}_1)$ and $P_n(\boldsymbol{r}_0)$ represents consideration of spatially averaged pressure amplitudes at these locations. It is known that spatial averaging of acoustic signals in (free-field) hydrophones is known to cause error in estimation of peak amplitudes [166] if the hydrophone size (in this case 9.5 mm wide) and the minimum wavelength of interest (in this case 6.9 mm at 145 kHz in 1000 $\mathrm{m.s^{-1}}$ c_m in the UAS device) are similar. However, the errors are very minimal (and only up to 4% [166] at peak amplitudes) at the frequencies of interest to this study

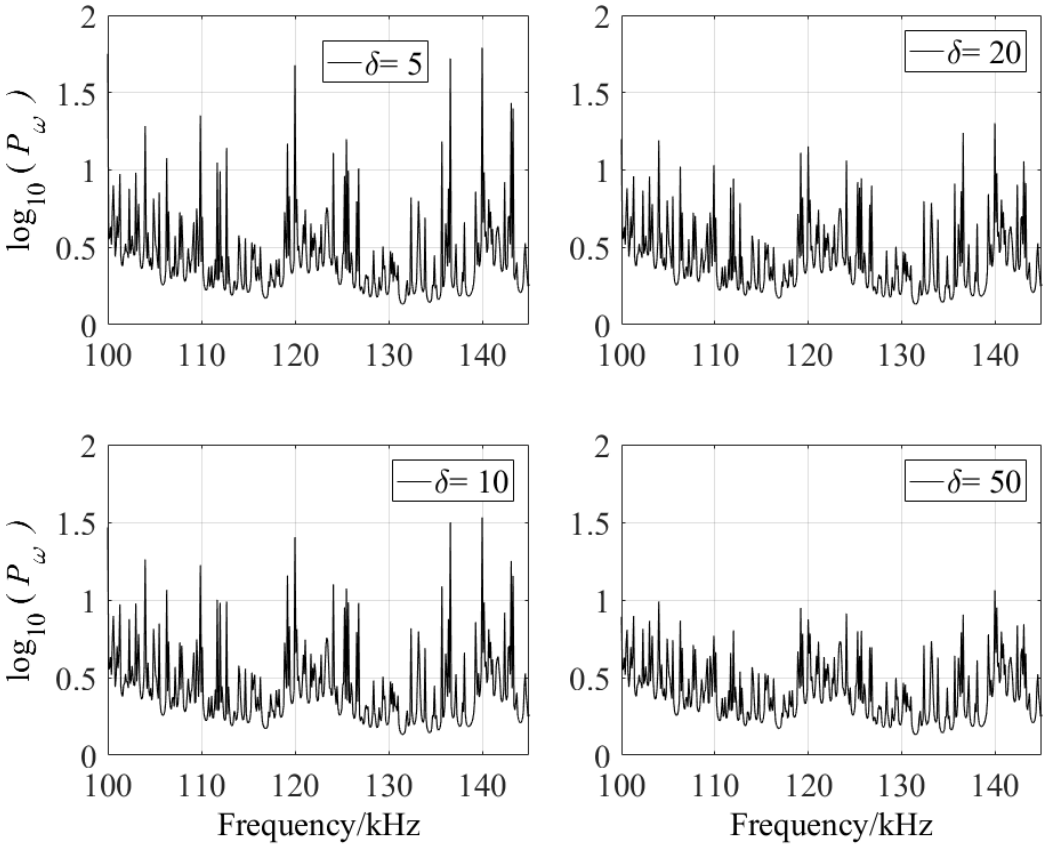

Figure 5.2: Predicted, frequency dependent, acoustic pressure amplitude at the receiver location within a rectangular room (representing the prismatic block) for different values of δ_n. Evaluated using equation 5.1.

using B&K 8103 hydrophone. Nevertheless, to estimate the influence of a finite sized source and receiver on the transfer function of the room, the spatial location of both the source point ($\boldsymbol{r}_0$) the receiver point ($\boldsymbol{r}_1$) were moved around within a 10 mm sized square region (centred around the earlier location of the point object). The equation 5.1 was re-evaluated between 120 kHz and 145 kHz (at 1 kHz resolution) in each case and the result is presented in Figure 5.3.

Figure 5.3 contains a mean curve (shown in black) and two limiting curves representing the estimated variation in the P_ω value when using different geometrical locations of source and receiver points. This figure demonstrates that the model is robust and consideration of point objects representing spatial averaged amplitudes is a valid approximation for the prismatic block. The mean curve presented in Figure 5.3 will be used to estimate the acoustic pressure in the stream using the hydrophone recordings carried out using assembly shown in Figure 3.2.

At this stage, the limitations of the model employed in this section have to be considered and appreciated. First, the prismatic block used for holding the hydrophone cannot exactly be represented by a rectangle due to the rounded edges of the prismatic

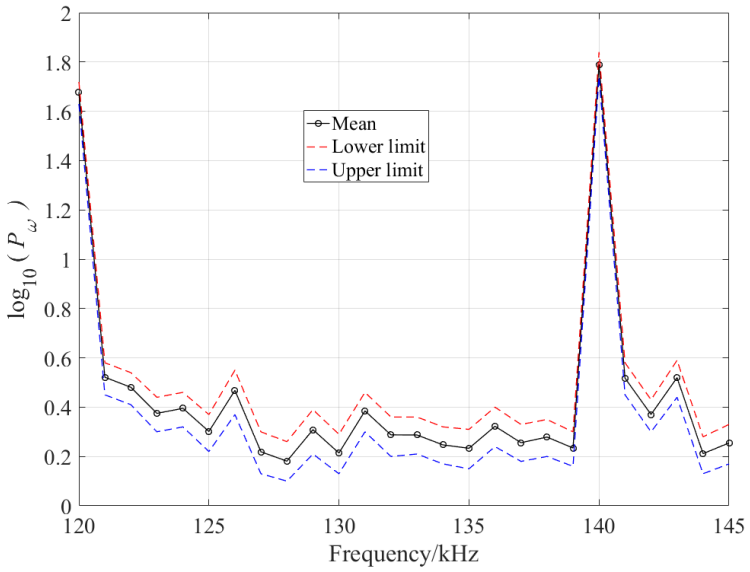

Figure 5.3: Predicted variation of acoustic pressure amplitude with frequency (at 1 kHz resolution) evaluated using equation 5.1 with both the source and receiver locations distributed over a 10 mm square.

block. The acoustical study of non-rectangular rooms is generally carried out using finite element [165] or other numerical methods [164]. In addition to that, the equation 5.1 considers the source emitting signal at a single frequency ω, whereas the pressure amplitude measured in the stream of the UAS device (in the non-linear regime) contains sub and ultraharmonics of the driving frequency (see results in Section 5.2.4). The (unknown) damping constants of the Rho-c material are assumed to be closer to that of damping properties of water.

It is assumed that the errors introduced by these approximations are smaller than the random errors associated with measurement of acoustic pressure (quantified using the standard error estimation during measurements) within the prismatic block. In addition, it will be shown in Section 5.2.4 that the contribution to the pressure amplitude at the sub/ultra harmonics of the driving frequency is generally small when compared to the pressure amplitude measured at the insonation frequency.

The next Section 5.2.3 discusses the measured values of the voltage across the transducer terminal (V_t) in relation to increasing V_{pa}, which is set to act as a precursor to the pressure measurements recorded in the stream (see, Section 5.2.4).

5.2.3 Voltage across transducer terminals

The value of V_t (voltage supplied to the transducer terminals) is an important parameter in quantifying the response of any ultrasonic transducer. Tracking the variation of V_t

in time and frequency domains tells us information about the occurrence of potential non-linear phenomena (such as distortion, hysteresis, appearance of harmonics [167]), demonstrates the response of the transducer at different loading conditions, and in the case of UAS device it can be used to correlate the acoustic pressure output from the device. The response of the UAS device (both in the laboratory and in commercial situations) is controlled by changing the input voltage supplied to the power amplifier (V_{pa}). The measured RMS value of V_t recorded for increasing V_{pa} was measured using an oscilloscope and the results are presented in Figure 5.4.

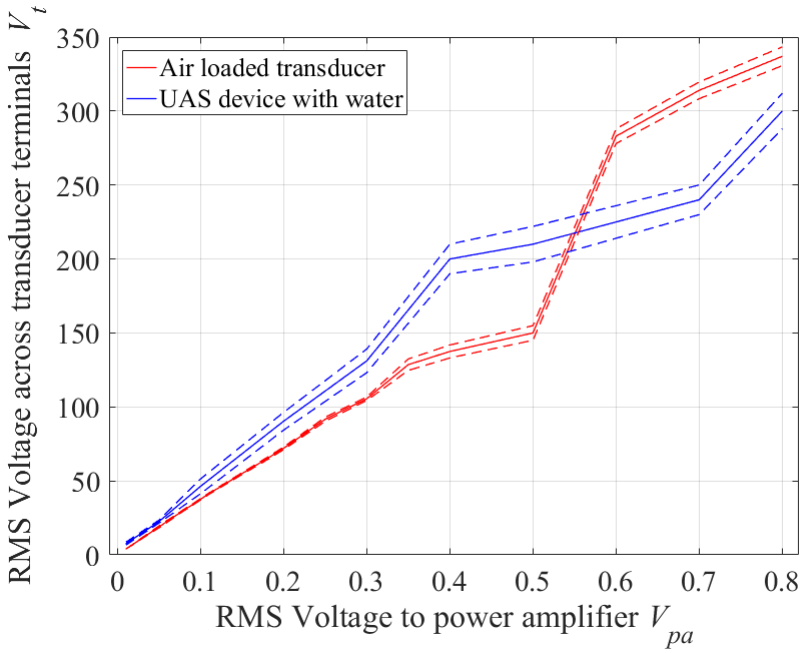

Figure 5.4: The variation of measured value of V_t with increasing V_{pa}. The solid lines demonstrate statistical mean and the dotted lines represent standard error bands.

Figure 5.4 presents two curves which correspond to the RMS value of V_t when the transducer is radiating either into air (i.e., no acoustic load, red curves) or when the transducer is connected to the UAS device filled with flowing bubble free liquid (blue curves). The linear response of the transducer can easily be observed at V_{pa} values below 0.1 V_{rms}. As V_{pa} increases further the influence of different loading conditions changes the shape of the response curves. The standard error bands increase as the V_{pa} increases in both cases, probably due to the non-linear response of the transducer and increased loss of energy via dielectric heating. The values of V_t as V_{pa} extends beyond 0.6 V_{rms} are also different for air loaded transducer and UAS device loaded transducer, probably due to the changes in the contributions to the electrical power dissipated in the transducer (see Section 5.3).

The transition between the apparent linear and the non-linear shape of V_t vs V_{pa} curve in Figure 5.4, approximately beyond 0.3 V_{rms} is of primary importance during

evaluation of the performance of the UAS device. Coupled with measurements of power dissipated in the transducer, the transition region or the transition point between the linear and non-linear regimes helps in understanding and classifying the characteristics non-linear pressure output of the UAS device[2], as will be demonstrated in Section 5.2.4). The value of V_t at which the linearity of ultrasonic transducer breaks down (as evidenced by the appearance of harmonic distortion in V_t, see Section 5.3.1) is said to be dependent on piezo material used [168] for transducer manufacturing, and the pre-stressing applied to the transducer [167]. The non-linear regime is known to demonstrate strong hysteresis phenomenon (see Figure D.1). The relationship between V_t and V_{pa}, as shown in Figure 5.4, was employed during discussions in this chapter. However, to keep consistency with the historical and the future works on the UAS device, the value of V_{pa} is used or quoted throughout this thesis.

With these results at hand, the acoustic pressure emitted from the UAS device as measured in the stream will be presented and discussed in the section below.

5.2.4 Pressure measured in the stream

The primary driving factor of this thesis is the study of acoustic pressure in the stream of the UAS device. Figure 5.5 presents the variation of pressure recorded in the stream (using the hydrophone placed in the block) at 135 kHz, when the voltage to the power amplifier (V_{pa}) was gradually increased from 0.0 V_{rms} to 0.8 V_{rms}. The operating conditions were 20 ms pulse length (or t_2) and PRP value of 100 ms. During these observations, the liquid flow rate in the system was maintained at 2.2 litre.min^{-1} and the liquid temperature was held at 29.1^{o}C. Input conditions to the power amplifier were limited to a V_{pa} of 0.8 V_{rms} to avoid overloading. The acoustic data recorded in this experiment was averaged over 50 measurements and the standard errors evaluated at each input voltage were drawn in Figure 5.5 at respective input voltages. The outgasser was turned off to simulate the working of the UAS device in a commercial setting. Similar pressure-output vs input-voltage plots were reported when experimental observations were carried out using the 121.5 kHz ultrasonic transducer [13] (the 121.5 kHz transducer was not used in this thesis).

Figure 5.5 demonstrates a non-linear relationship between the pressure measured in the stream with a linear increase in the value of V_{pa}. Cleaning of contaminants on a specimen held in the stream was generally observed when pressure in the stream was above 200 kPa (i.e., at V_{pa} values above 0.6 V_{rms}). A sudden jump in the pressure output can be observed as V_{pa} increases from 0.3 V_{rms} to 0.4 V_{rms}. To gain a better

[2]The non-linear pressure output vs V_{pa} trend was also reported earlier, see [11, 13].

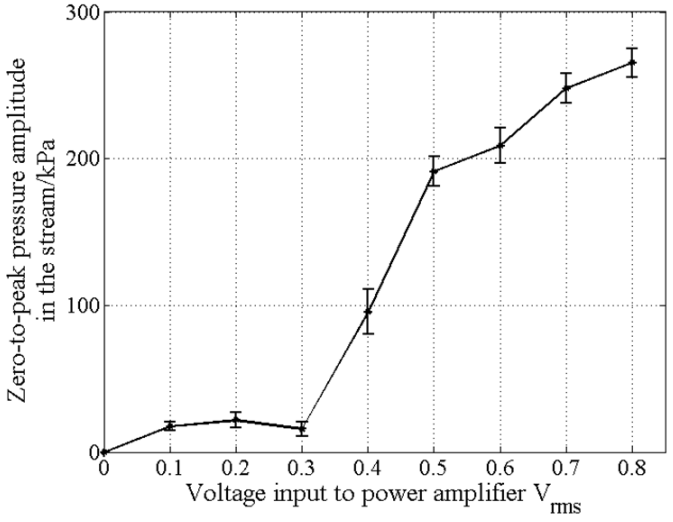

Figure 5.5: Acoustic pressure measured in the stream at a distance of 20 mm from the nozzle tip with increasing input voltage to power amplifier (V_{pa}). Also, see Figure 7.7 for associated capillary instability.

understanding of this non-linear shape of the response curve (shown in Figure 5.5) considerations towards electrical power dissipated in the transducer (W_e) under similar working conditions are very important. The discussions on electrical power will be presented in Section 5.3.

This result shown in Figure 5.5 should be considered along with the result presented in Figure 5.6, which presents the frequency content (in power spectral density or PSD estimate) of the acoustic signal recorded in the hydrophone. The red curve in Figure 5.6 presents the frequency content at V_{pa} of 0.1 V_{rms}, which demonstrates strong contributions to acoustic signal from the f component (135 kHz) and a minor contribution from the *2f* component. On the other hand, at V_{pa} of 0.8 V_{rms}, the contributions to the acoustic pressure include the fundamental f, its higher harmonics, and a 20 dB increase in the noise floor when compared with the 0.1 V_{rms} plot. The presence of harmonics of the driving signal in the acoustic pressure spectrum and the overall increase in the noise floor demonstrates non-linear acoustic propagation in the liquid when V_{pa} was 0.8 V_{rms}. On the other hand, when employing V_{pa} values as small as 100 mV_{pp}, the contribution to pressure amplitude was observed to be predominantly from the insonation frequency alone[3] (pressure-vs-time result presented in Figure 5.15).

The spectra shown in Figure 5.6 can be compared with the spectra reported in the literature to gain an insight into the nature of non-linear acoustic propagation within the UAS device. For example, Figure 3a in reference [169] by Tung et al. (2010) presents

[3]A PSD estimate of acoustic pressure in the stream when using V_{pa} of 100 mV_{pp} at 135 kHz was placed in Chapter 6 along with the discussions on the linear response of the UAS device and the influence of the bubbly liquid.

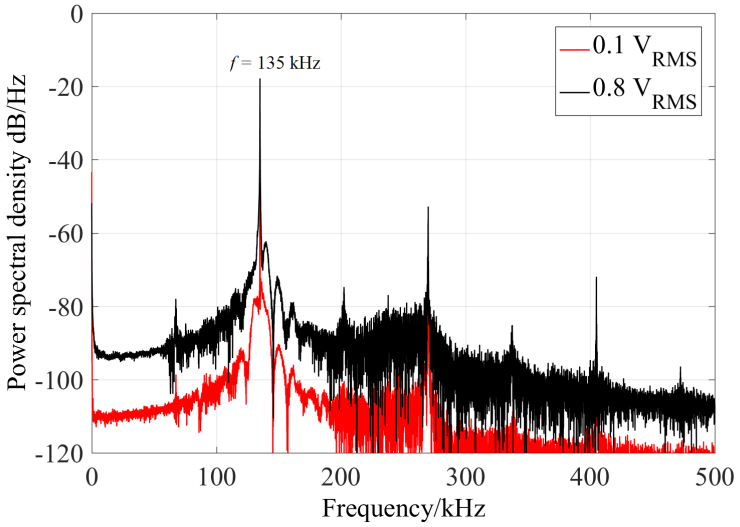

Figure 5.6: Power spectral density plot of the pressure amplitude measured in the stream when V_{pa} was 0.1 V_{rms} and 0.8 V_{rms}.

the influence of pressure amplitude on initiation of inertial cavitation, by observing the FFT amplitude of the acoustic data recorded in a vessel when employing a focused ultrasonic transducer. However, it is easier to compare the results shown in Figure 5.6 with the results presented Figure 2 of reference [78] by Frohly et al. (2012). Using the results reported in reference [78] as a comparison, the broadband nature, and the sub, ultraharmonic content of the acoustic signal shown in Figure 5.6 can be highlighted. The black curve in Figure 5.6 demonstrating an increase in the contribution to the noise floor indicating non-linear acoustic propagation and probably even inertial cavitation of the liquid inside the UAS device. However, the amplitude recorded at 270 kHz is much smaller than the amplitude recorded at 135 kHz (for the black curve in Figure 5.6). This is due to the sensitivity value used for conversion (-209 dB re 1 V/μPa at insonation frequency of 135 kHz), and it is expected that sensitivity of the hydrophone reduces as frequency increases beyond 200 kHz. Investigations on the evolution of the pressure amplitude at the insonation frequency as V_{pa} increases demonstrated a sudden jump as V_{pa} increases beyond 0.4 V_{rms}. This demonstrates sudden onset of cavitation and initiation of probable cavitation related transient events such as bubble collapse which creates white noise [78].

These acoustic spectra must be correlated to the spectra of the electrical signal supplied to the transducer and to the electrical power dissipated in the transducer. The next section reports the measurement of electrical power dissipated in the transducer at different V_{pa} values and compares them with the results presented in Figure 5.5. The spectra observed in the measured electrical signals across the transducer terminals are reported in Section 5.3.1.

5.3 Power dissipated in the transducer

The total electrical power dissipated in a piezo based ultrasonic transducer (W_e) is generally divided into three components: W_d the dielectric power dissipated in the transducer material, W_m the power towards the mechanical losses of the transducer, and W_a the power radiated into the fluid medium. The overall electroacoustic efficiency of the transducer is thus made up of two parts, the electromechanical efficiency and mechanoacoustical efficiency [168].

Acoustic power radiated into the working fluid is in turn related to the radiation resistance R_r offered by the fluid to the transducer by

$$W_a = \frac{1}{2} R_r u_t^2, \tag{5.3}$$

where u_t is the absolute value of the vibrational velocity at the face of the transducer. A large value of R_r (along with low mechanical losses in the transducer), which increases the mechanoacoustical efficiency [168], is desired for effective radiation of acoustic energy into the fluid.

The fluid loading on the transducer face can be altered to change the value of R_r. Two fluid loading conditions that are generally employed to characterize the performance of the transducer are in-air loading and in-water loading [170]. In-air characterization involves evaluating the input electrical admittance Y and the power dissipated in the transducer (W_e) as a function of frequency when the transducer is radiating into air. In-water characterization involves placing the transducer in a large water tank with one or both of its faces completely immersed, to evaluate Y and W_e. When the transducer is submerged in water, the effect of increased load on the transducer face is quantified using changes to the radiation impedance. The changes to the input electrical impedance of the transducer under different loading conditions, the influence of different frequencies of operation, and the variation of R_r at different loading conditions will be presented in Chapter 6. In this chapter results from measurement of W_e for transducer under different loading conditions are reported.

During no loading or air loading condition, where radiated acoustic power W_a = 0, the electrical power dissipated in the transducer provides us with an estimate of electrical power lost to mechanical and dielectric sections of the transducer [168]. When the transducer is placed in a water tank, with one of its faces completely submerged (i.e., $W_a \neq 0$), the value of W_e provides us with the power dissipated under a known loading condition. Then, the measurement of W_e when the UT_1 transducer is connected to the UAS device with bubble-free liquid provides us with a third loading condition which

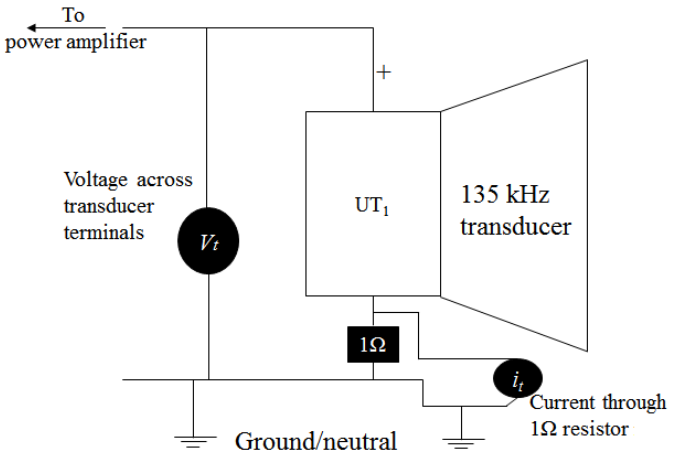

Figure 5.7: Simplified diagram demonstrating the technique used for measuring power dissipated in the ultrasonic transducer UT_1, using voltage and current measurements.

is relevant to the present study. The result of the third loading condition can then be compared against the other two loading conditions.

Experimental measurement of electrical power dissipated in a transducer turned on for a length of t_2 seconds is given by [171]

$$W_e = \frac{1}{t_2}\int_0^{t_2} V_t(t) i_t(t) dt, \tag{5.4}$$

where $V_t(t)$ and $i_t(t)$ are the voltage applied across the transducer terminals and the current flowing into the transducer. Figure 5.7 presents the measurement technique used for evaluating W_e. Voltage $V_t(t)$ was recorded across transducer terminals and the current $i_t(t)$ was recorded as a voltage drop across a small 1 Ω or 1.2 Ω resistor (as shown in Figure 5.7). For evaluating the power dissipated in the transducer in the air loading condition, the transducer UT_1 was placed on a styrofoam block to isolate it from the surroundings, with care taken so that the active faces of the transducer were radiating into air and power consumption was recorded. The transducer was then placed carefully in a large water tank (73 cm X 46 cm X 30 cm, water filled up to 25 cm height) with one of its faces completely immersed in water. The transducer was rotated slightly to avoid reflections either from the tank bottom or from the air-water interface, and power consumption was recorded. Results are presented in Figure 5.8.

Figure 5.8 contains three different plots showing the amount of electrical power dissipated in the transducer under the three different loading conditions. The red curve presents the measured value of W_e when the transducer is running free (i.e., air loaded) and the dotted black curve presents the measured value of W_e when the transducer was placed in the water tank. The solid black curve in Figure 5.8 represents the power dissipated in the ultrasonic transducer when it is attached to the conical chamber filled

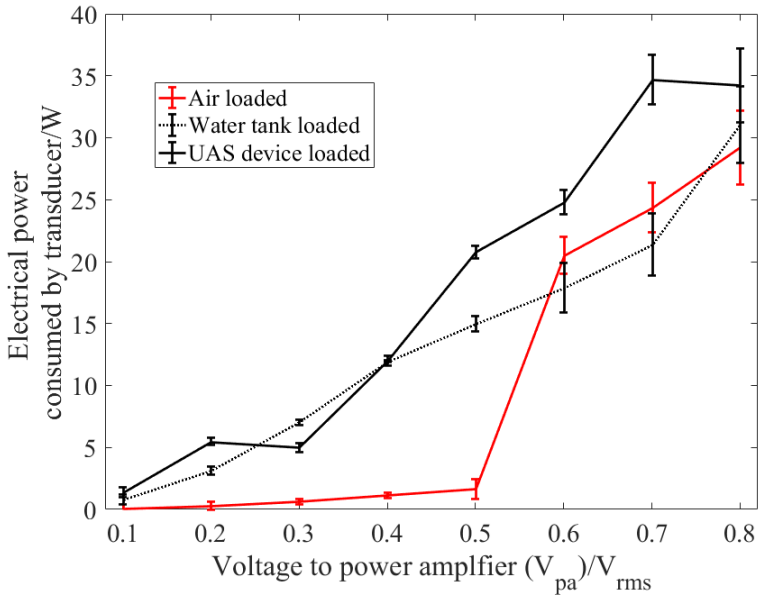

Figure 5.8: Power dissipated in the transducer (at 135 kHz) at different loading conditions, as V_{pa} increases.

with bubble-free liquid. For each measurement, the standard error values drawn were evaluated from 128 measurements at each value of V_{pa}. The pulse length for which the transducer was turned on in each case (t_2) was 20 ms and PRP was 100 ms. The water present in the tank was at room temperature (21^{o}C) and the temperature of the liquid in the UAS device was 28^{o}C. The outgasser was turned off during the electrical power measurements carried out for the UAS device and liquid was flowing at 2.1 litre.min^{-1}.

When the transducer is radiating into air, the trend of W_e with V_{pa} presents clear demarcations (see Figure 5.8) with three different slopes in the W_e vs V_{pa} plot. A non-linear increase in power consumption with an increase in the value of V_t is caused by field dependent non-linearities [172] in the dielectric, piezo, and elastic properties of the transducer material [167] (also see Section 5.3.1). The dielectric loss of electric energy in the transducer is emitted as heat and it can be observed that this loss is very high in the non-linear regime (red trace in Figure 5.8 beyond V$_{pa}$ of 0.5 V$_{rms}$). However, the sudden jump in the W_e value measured when the transducer is radiating into air is not as prominent when the transducer is placed in the water tank.

When the transducer is working in a fluid acoustic medium and in its linear regime of operation, the influence of the medium is generally taken into account by using its specific acoustic impedance (ρc). By considering the radiative medium as homogeneous, isotropic, and non-viscous [168], the radiation impedance (Z_r) encountered by the transducer can be evaluated by taking into account the shape and the size of the transducer.

This radiation impedance is generally made of two parts

$$Z_r = R_r + jX_r, \tag{5.5}$$

where R_r is the resistive part, and X_r is the reactive part. The radiation reactance X_r may be regarded as an additional vibrating mass (M_r) attached to the transducer, as a result of increased fluid loading. The value of M_r is defined as

$$M_r = \frac{X_r}{\omega}. \tag{5.6}$$

In water loaded condition, the power dissipated in radiation resistance R_r represents the far-field acoustic power emitted by the transducer and energy stored in M_r represents the near-field acoustic energy contribution [170]. Hence, based on the size, shape, and the design of the transducer, the radiation impedance value changes. The piezoceramic material used and the construction of the transducer would also influence its linear and non-linear performance [168]. These discussions could be used to explain the absence of sudden jump in the plot of W_e vs V_{pa} under water loaded condition (dotted black trace of Figure 5.8).

With a change in the value of Z_r as the transducer is placed in the water, the contribution to W_m and W_d change [168] and some portion of W_e goes into W_a. As the voltage supplied to the transducer terminals increases, the transducer starts behaving non-linearly [173]. As cavitation is initiated in the liquid, the real and the imaginary parts of Z_r decrease [174, 175] and increase [176] respectively. As the real and imaginary parts of the Z_r are related to near field and far field radiation from the transducer, they are altered and this changes W_a and eventually W_e also changes [176].

The dotted black line in Figure 5.8, which represents the power dissipated in the transducer under water loaded condition, shows a significant change in the slope in the W_e vs V_{pa} curve only after V_{pa} exceeds 0.7 V_{rms}. The contributions to different loss parameters also change in the non-linear regime [177] and alter the acoustic power emitted by the transducer. When the transducer is placed in the water tank, audible cavitation noise was observed as V_{pa} exceeds 0.4 V_{rms}.

The solid black curve in Figure 5.8 which corresponds to the W_e of the UAS device filled with bubble-free water is also different to that of the dotted black line (transducer radiating into water tank) due to differences in the value of R_r faced by the transducer as mounting changes. Further discussions on the estimation of R_r under different loading conditions is reported in Section 6.3.3 in Chapter 6.

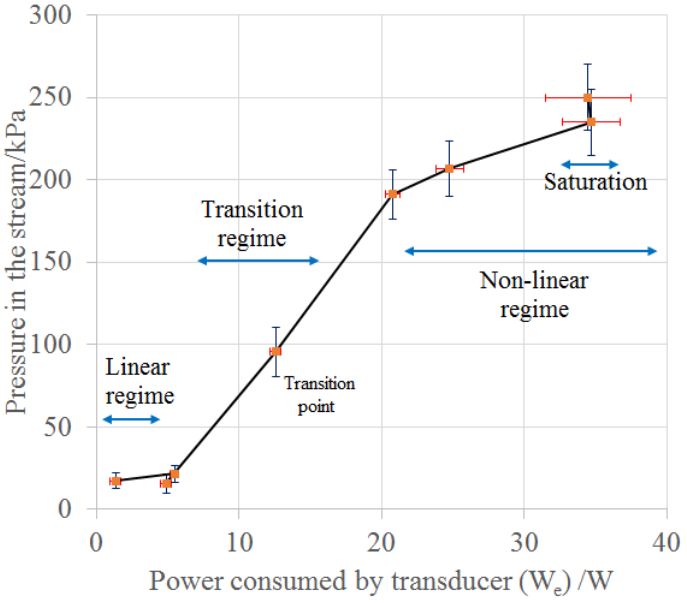

Figure 5.9: Variation of pressure recorded in the stream with electrical power dissipated in the transducer, when connected to the UAS device with bubble-free liquid. Different regions marked in the plot are discussed in the text.

The solid black line from Figure 5.8 and the pressure-vs-voltage plot of Figure 5.5 were compiled together and are presented in Figure 5.9, i.e., when the transducer UT_1 is connected to the UAS device and operating on bubble-free liquid. In this figure, the red coloured error bars represent the standard error in the measurement of W_e and the blue error bars represent the standard error in the measurement of acoustic pressure amplitude in the stream. Figure 5.9 is (approximately) marked with different regimes of operation of the UAS device. In the linear regime, generally occurring below 0.1 V_{rms} the pressure output and the power dissipated in the transducer increase linearly with increasing V_{pa}. The pressure recorded in the stream is below 50 kPa (zero-to-peak) and the power dissipated is below 10 W. After this stage, the slope of the power-pressure plot changes suddenly and the recorded pressure amplitude increases to approximately 100 kPa. The region between 5 W and 20 W in Figure 5.9 is termed as the transition regime. The existence of "transition regime or threshold regime" in piezoelectric transducers is well documented [178], which is marked by sudden jumps in the power dissipated in the transducer [173]. The transition point in Figure 5.9 also corresponds to the V_{pa} value where capillary instabilities on the stream are initiated.

Beyond the transition point, the pressure measured in the stream was associated by audible cavitation noise, sonoluminescence inside the conical chamber (and in the stream) [179], and lateral ejection of liquid droplets from the stream (discussed in Chapter 7). The non-linear regime is when the pressure in the stream exceeds 200 kPa and most vigorous cleaning action on target surfaces was observed (also see Figure 5.18).

The saturation regime is marked at the end of the plot as W_e reaches 35 W. Care must be taken when comparing the results reported in Figure 5.8 with those available in literature [167, 171] as the power consumption trends are known to change with loading and working conditions [180].

The location of the transition point (or the initiation of capillary disturbances) with respect to V_{pa} was found to be influenced by the following factors: transducer loading conditions (Figure 5.8), the pulse repetition period (PRP), changes to liquid temperature, the presence of additives to the liquid such as glycerol (Figure D.1), and the presence of microbubbles in the liquid (either deliberately introduced, Figure 6.4 or unwanted, Figure 7.13). These are further discussed in Chapter 7.

It is important to note the apparent large size of the transition regime in Figure 5.9, when compared with the linear and non-linear regimes. This is due to the fact that the transition regime consists of only one measurement point and any intermediary values are linearly interpolated. The resolution of measurement points used for quantifying the pressure output of the device, as shown in Figure 5.5 is 0.1 V_{rms} in V_{pa}. This choice of this resolution is evident both in the historical reports compiled when using the UAS device and in this thesis. A finer resolution in V_{pa}, particularly between 0.3 V_{rms} and 0.4 V_{rms} quantifying the response of the device, is reported in Figure D.1 in relation to the initiation of capillary instability phenomenon.

The classification of the three regimes reported in Figure 5.9 was aided by the investigations into the frequency content of the voltage signal measured across the transducer terminals (V_t). The next section continues the discussions on the non-linear response of the UAS device in the context the electrical non-linearities observed during measurement of electrical power.

5.3.1 Influence of transducer non-linearities

The linear behaviour of a piezo transducer, along with its elastic and piezoelectric relationships could be understood by using the standard piezoelectric constitutive equations [173], which are independent of the applied electric field. However, the non-linear relationship between piezoelectric and elastic properties of a transducer, generally noticed above a certain threshold value of electric field amplitude, are known to involve field dependent coefficients [173], cannot be analysed using simplified equivalent circuits [181], and the models are generally complicated by their necessity to include the saturation phenomenon [177].

In that sense, the non-linear properties of the transducers are different from their linear counterparts [178]. The change in dielectric coefficients, as electric field increases, results in strong hysteresis and saturation phenomenon [173], which causes transducer heating by dielectric losses [182]. The well established non-linear behaviour of a piezo-ceramic element includes the presence of multiples of the insonation frequency in the voltage and current amplitudes [173, 178]. Experimental investigations, similar to those reported in this section, are generally employed [167, 177] to investigate the non-linear response of transducers.

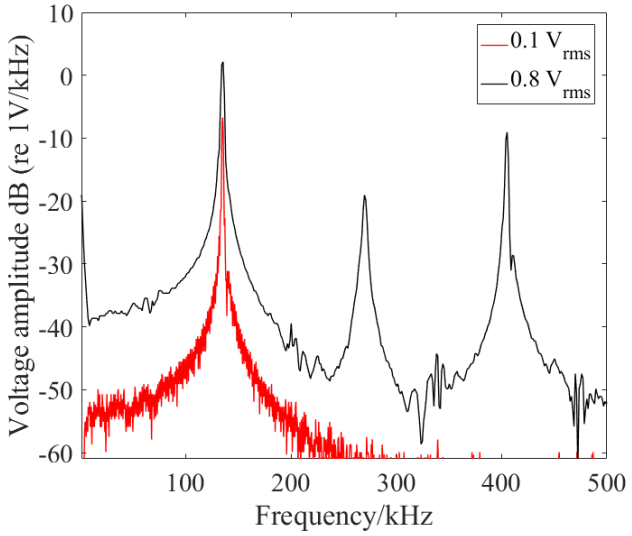

Figure 5.10: Averaged frequency spectrum of the voltage-time data recorded across terminals V_t (normalized to the bin width) for the air loaded transducer at two different V_{pa} values (f_s was 1 MHz). Data is averaged over 128 cycles.

Evidence for the non-linear response of the air loaded UT_1 transducer can be seen in Figure 5.10, which compares the averaged frequency spectrum of the voltage-time data recorded across transducer terminals (V_t) at V_{pa} of 0.8 V_{rms} (black curve) and 0.1 V_{rms} (red curve). The contributions to the voltage signal V_t at the harmonics of the insonation frequency at V_{pa} of 0.8 V_{rms} are obvious. Voltage-time data recorded at f_s value of 2.5 MHz showed that the harmonics in the voltage signal (for V_{pa} of 0.8 V_{rms}) extended further and up to 1 MHz above the noise level.

Spectra similar in amplitude to those shown in Figure 5.10 were also observed from the voltage-time data, both when the UT_1 was placed in the water tank and when the UT_1 was connected to the conical chamber filled with bubble-free water. Similar trends were also observed when investigating the frequency content of current-time data recorded at transducer terminals (results not shown).

The non-linear response of the transducer can be clearly observed by tracking the contributions of the fundamental and the higher harmonic components in the spectra of

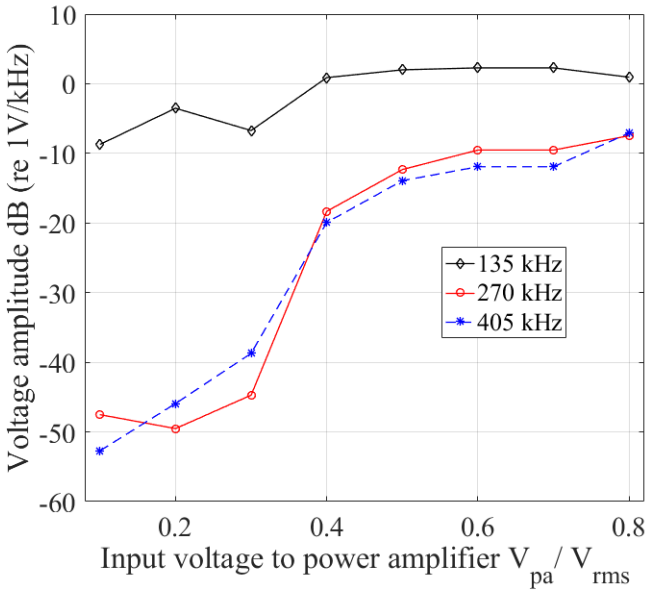

Figure 5.11: Trends in the mean values at the insonation frequency (f = 135 kHz) and its higher harmonic components taken from V_t spectra as V_{pa} increases, when transducer was connected to the UAS device with bubble-free liquid

voltage-time data recorded at transducer terminals (V_t) as V_{pa} increases. The relevant result, when the transducer was connected to the UAS device, with PRP at 100 ms and pulse length (or t_2) of 20 ms and averaged over 128 cycles is shown in Figure 5.11. In the designated linear regime (V_{pa} below 0.1 V_{rms}) the amplitude of 135 kHz component is around -9 dB. The amplitudes of 270 kHz and 405 kHz components at these V_{pa} values were very close to the noise floor. At V_{pa} value of 0.3 V_{rms}, a reduction in amplitude was recorded at the insonation frequency, whereas contributions by the harmonics are on an increasing trend. The saturation in the amplitude of the fundamental component of V_t can be observed as V_{pa} increases beyond 0.6 V_{rms}. The saturation phenomenon in ultrasonic transducers is generally caused by a drop in the mechanical quality factor Q_m in the non-linear regime [178]. The harmonic content in the voltage (and the current) signal in the transducer also contributes to the pressure amplitude.

With the non-linearities in the response of the UT_1 transducer reported, the next section will discuss the results of the pressure measurements in the stream as the distance between the hydrophone acoustic centre and the nozzle tip increases. These results are presented with due importance attached to the cleaning distance, which is generally quoted to be between the nozzle tip and the target location.

5.4 Influence of measurement distance

When employed for cleaning operations, the UAS device is designed to exploit the large pressure amplitudes (around 250 kPa) and subsequent cavitation related phenomena generated in the working liquid. Large pressure amplitudes are generally produced within the liquid when the device is operating in its non-linear regime. As observed during the preliminary experimental observations [11], the optimal cleaning distance was at 20 mm from the nozzle tip. However, it is also important to record and quantify the variation in pressure amplitude as the measured distance from the nozzle tip increases.

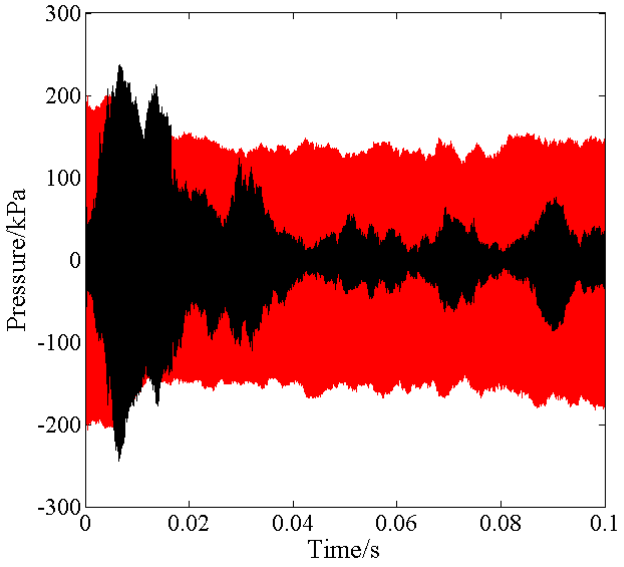

Figure 5.12: Pressure-time profile recorded in the stream, measured at a distance of: (a) 5 mm (red trace) and (b) 25 mm (black trace). Distance measured is between the nozzle tip and the outer surface of the prismatic block.

Figure 5.12 presents two instantaneous pressure-time profiles recorded in the stream when the acoustic centre of the hydrophone is located in the prismatic block at a distance of (a) 14.5 mm from the nozzle tip (red trace) and (b) at 34.5 mm from the nozzle tip. The power amplifier was supplied with a V_{pa} of 0.7 V_{rms} at 135 kHz for both the cases. The traces show the pressure-time profiles recorded in the absence of the outgasser in the liquid loop and are characterised by undulations which are caused by the unwanted microbubble population. The black trace, however, demonstrates undulations that are peculiarly larger in amplitude when compared to the red trace, particularly after the 20 ms mark. These undulations are caused by the formation of capillary instabilities on the stream. These capillary instabilities are varicose type radial oscillations formed on the surface and cause variations in the pressure amplitude at distances larger than 20 mm, measured between the nozzle tip and the outer surface of any target. The

non-linear capillary instability formation was investigated using optical imaging of the stream surface and the results are reported in Chapter 7.

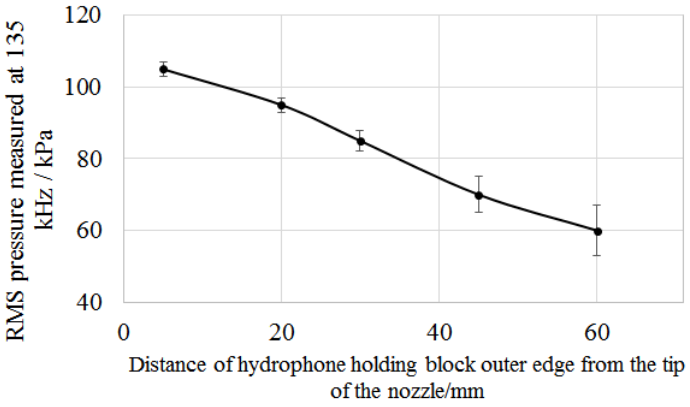

Figure 5.13: RMS value of the pressure measured in the stream as distances between the nozzle tip and prismatic block outer surface increases. Also, see Figure 5.14.

The presence of these undulations implies that the time averaged acoustic pressure measured in the stream would be strongly influenced as the measurement distance increases. To evaluate this trend, pressure measurements were recorded with the device operating in the non-linear regime at a few selected locations in the stream, starting at a distance of 5 mm from the nozzle tip and increasing up to a distance of 60 mm. The RMS value of the pressure recorded from these measurements, along with the corresponding standard error bars (evaluated from 50 recordings) is shown in Figure 5.13. At distances smaller than 20 mm, the RMS pressure measured in the stream is approximately 100 kPa with (relatively) very little error. As the distance increases, the RMS value of pressure drops to 60 kPa with a relatively larger error bar at the 60 mm location.

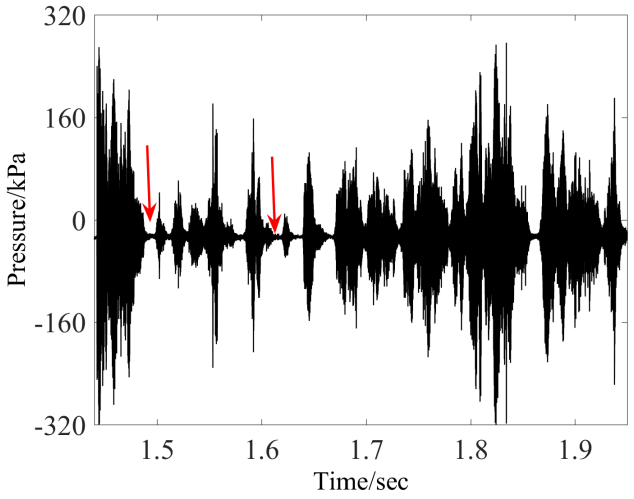

Figure 5.14: Pressure-time plot, measured in the stream with hydrophone centre placed at a distance of 50 mm from the nozzle tip.

This result demonstrates the extent to which the capillary oscillations on the stream influence the pressure amplitude. For example, Figure 5.14 presents a 0.6 s portion of the pressure-time plot recorded in the stream, when the hydrophone acoustic centre was at a distance of 50 mm from the nozzle tip. In this plot, regions with a pressure amplitude between 200-300 kPa zero-to-peak, are interspaced with regions of 0 kPa, as marked by red arrow marks. At this distance, it was observed that the radial amplitude of capillary oscillations is large enough to breakup the stream. Hence, no pressure was recorded when the stream was broken down and ultrasound cannot propagate beyond the broken stream tip. This increases the size of the error bars, as seen in Figure 5.13. Obviously, it would serve no purpose to place the hydrophone for pressure measurement at distances beyond the stream breakup length (L). The optical measurements of L and the temporal evaluation of stream breakup phenomenon are presented in Section 7.2. Figure 5.12 is used again in Figure 7.9 to temporally correlate the optical observations of capillary wave formation with the pressure undulations reported here.

Measurements of the pressure output of the UAS device presented in this chapter up to here are recorded in the stream when the outgasser transducer was inactive, although care was taken to reduce the unwanted microbubble population by the keeping the pump running for 30 min before measurements. In Chapter 3, the outgasser was shown to be effective at improving the pressure output from the UAS device at off-resonance frequencies. The next section will present the influence of the outgasser at the resonance frequency of the transducer as V_{pa} increases.

5.5 Pressure output when using the outgasser

This section will demonstrate the significance of the outgasser when UT_1 was operating at 135 kHz. When V_{pa} was held at 100 mV_{pp} (i.e., in the linear regime of operation) and when the outgasser was active, the recorded pressure-time trace shown in Figure 5.15 demonstrates consistency in the performance of the UAS device over the recorded time. Note that, even though the spectrogram[4] of the recorded data demonstrates contributions from the higher harmonics of the insonation frequency, their contribution is very small. A very small ring-up time, in the order of 1 ms, and no overshoot can be observed in the pressure-time plot shown in Figure 5.15. This observation will be revisited in Chapter 6, when the ring-up time of the device at off-resonance frequencies will be discussed.

[4]Spectrogram options: Hamming window of size 1024 samples, overlap of 16 samples, and 8192 points of Discrete Fourier Transform. Parameters are chosen based on best representation.

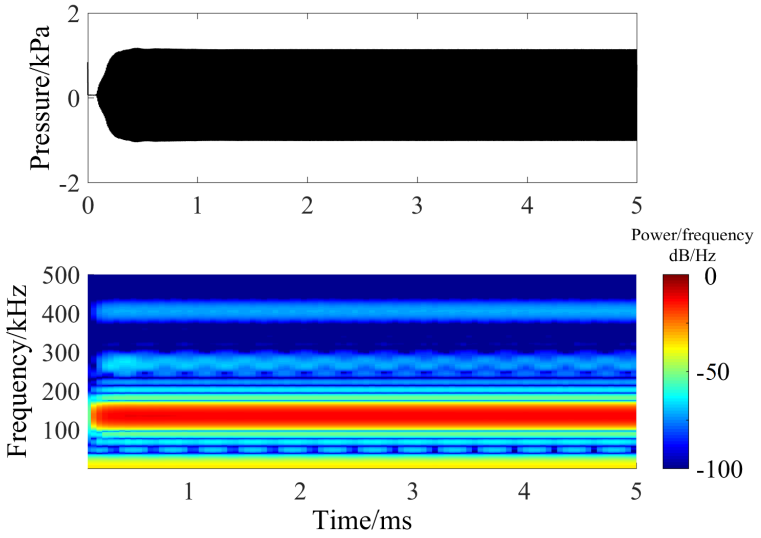

Figure 5.15: Pressure-time plot of acoustic data recorded in the stream with the outgasser active. The spectrogram of the recorded data is shown in the subplot below.

When using the UAS device importance must be attributed to the duty cycle used during experiments, as it was observed to play an important role in the pressure amplitudes recorded. During investigations of electrical power dissipated in the transducer, it was observed that the averaged values of W_e for different duty cycles (starting from 2% and up to 20%) were statistically very similar. In the absence of the outgasser in the liquid loop and when using a fixed pulse length (t_2) of 20 ms, as PRP value increases from 0.1 s to 5 s, the location of threshold point was observed to drop. This can be attributed to the relative resting time available to the transducer between pulses, as duty cycle increases. These results can be seen in Figures 5.16, C.1.

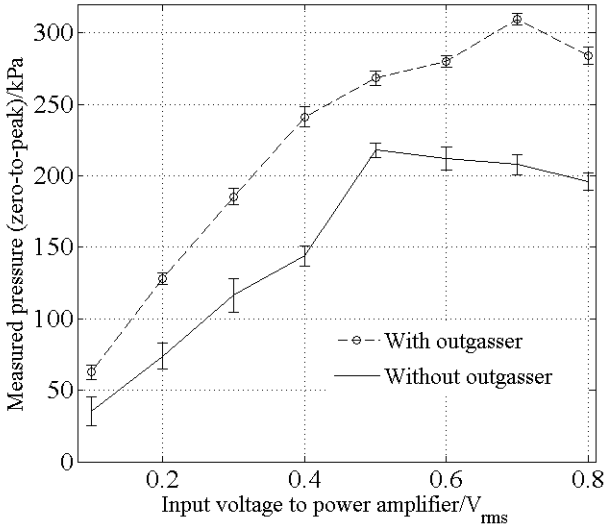

Figure 5.16: Pressure measured in the stream with increasing V_{pa} when using the outgasser (2.0 litre.min^{-1} flow rate, PRP value of 5 s, and liquid temperature at 28.3^{o}C).

The use of the outgasser demonstrates an improvement in pressure at all drive levels (both in the linear and non-linear regimes) with no statistically significant changes to the electrical power dissipated in the transducer. A 50 kPa improvement in zero-to-peak pressure amplitude in the non-linear regime (at V_{pa} between 0.7 to 0.8 V_{rms}) and up to 30 kPa improvement in pressure amplitude in the linear regime were observed (see Figure 5.16). The smaller error bars in the pressure amplitude recorded when using the outgasser demonstrate an improvement in repeatability of the UAS device.

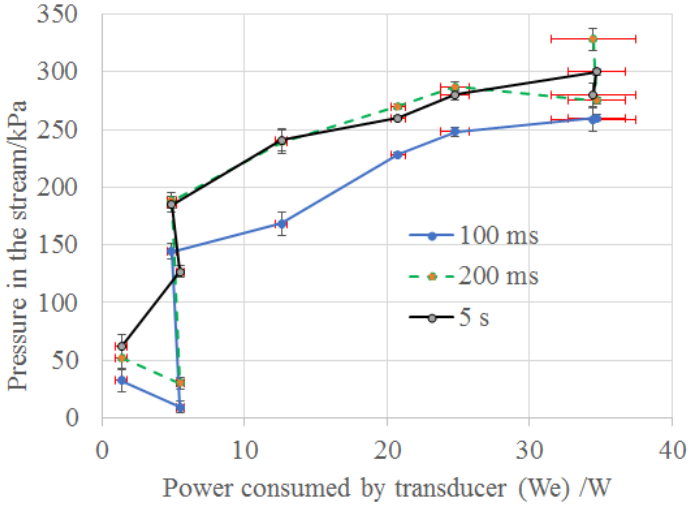

Figure 5.17: Pressure recorded in the stream vs electrical power dissipated in the transducer when using outgasser in the liquid loop, at different values of PRP.

A graph similar to the one shown in Figure 5.9 can now be drawn using the pressure amplitudes recorded in the stream when using the outgasser and when employing different PRP values. This result is shown in Figure 5.17. The existence of transition point, non-linear regime, and saturation regimes from Figure 5.17 can still be pointed out. However, the demarcation for the linear regime becomes ambiguous due to the improvement in pressure output from the UAS device by the use of the outgasser. The 0.1 V_{rms} resolution in the value of V_{pa} employed during the experiments carried out should also be remembered here, as it influences the shape of the curve reported in Figure 5.17 and the exact demarcations of the three different regimes. Hence in Chapter 6, when the linear response of the transducer under different loading conditions are reported, the value of V_{pa} was chosen so as to work as far away as possible from non-linearities (using Figures 5.4 and 5.11 as a guideline).

These discussions complete the study of the UAS device at the resonance frequency of the transducer when using bubble-free liquid. The next section presents the conclusions of this chapter and will lead to the objectives of the next chapter.

5.6 Conclusions

This chapter began with a discussion on the acoustic pressure from the UAS device, as measured in the stream. The influence of the prismatic block used for holding the hydrophone was quantified by considering acoustic propagation in an equivalently sized rectangular room, and the result was presented as a function of frequency at the hydrophone location.

The response of the UT_1 transducer at its resonance frequency (135 kHz) was quantified when the voltage input to the power amplifier V_{pa} increased linearly from 0.1 V_{rms} to 0.8 V_{rms}, under different loading condition (air loaded, water loaded, UAS device loaded). The trend in V_t vs V_{pa} (shown in Figure 5.4) at different loading conditions on the transducer helped in the evaluation and classification of its non-linear response. The electrical power dissipated in the transducer under these different loading conditions was investigated. The harmonic content in the voltage amplitude measured across transducer terminals further highlighted the non-linearities in the piezoelectric transducer employed, as drive increases.

From the results presented in Figures 5.5 and 5.8, the non-linear relationship between of the pressure output of the UAS device and the power dissipated was demonstrated. This result shown in Figure 5.9 was divided into different regimes: linear, transition, non-linear, and saturation, to identify or mark different characteristics in the response of the UAS device.

Along with these experimental observations, discussions were also presented on the influence of using different PRP values on the pressure amplitude recorded and the influence of distance between the acoustic centre of the hydrophone and the nozzle tip. The advantage of employing the ultrasonic outgasser in the liquid loop was also reported. These studies thus cover the influence of region "A" of Figure 1.3, i.e., the power input to the transducer, on the performance of the UAS device.

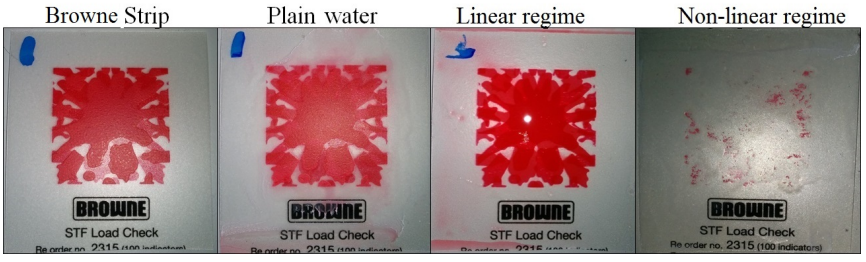

Figure 5.18: A demonstration of cleaning performance of the UAS device on a Browne strip. The images from left to right present influence of different process on four different strips: a clean specimen (Browne strip), a specimen cleaned with plain running water for 20 s, a specimen cleaned with pressure generated in the linear regime for 20 s, and a specimen cleaned with pressure generated in the non-linear regime for 20 s.

Of the different regimes demonstrated by the UAS device, the non-linear and the saturation regimes are better suited to the cleaning operations, due to the large pressure amplitudes generated in the stream. Cleaning achieved on a target substrate could be evaluated using different techniques [183], and in the present study, the optical imaging technique offers an advantage. To demonstrate the practical implementation of the non-linear regime of the UAS device on the cleaning performance, four Browne STF load check strips from Isopharm Ltd were used. The strips were exposed to either plain water (transducer turned off), or ultrasonic pressure from the linear regime (V_{pa} of 0.1 V_{rms}), or ultrasonic signal pressure from the non-linear regime (V_{pa} of 0.7 V_{rms}) each for 20 s. Figure 5.18 presents a demonstration of the cleaning effectiveness of the UAS device using these test strips. It is obvious from Figure 5.18 that the linear regime of the device (or even the plain water) does not aid in cleaning, whereas the pressure generated from the device in the non-linear regime aids the cleaning operations.

With the response of the UAS device when using bubble-free liquid quantified, the discussions can now proceed towards the investigation of the response of the UAS device to bubbly liquid generated from chamber G. These investigations were carried out at resonance and off-resonance frequencies. A complete investigation, in this case, requires knowledge of the: radiation impedance on the face of the transducer, response of the transducer at different frequencies, and acoustical properties of the bubbly liquid inside the chamber. The relevant analysis, experiments, and discussions will be presented in Chapter 6.

Chapter 6

Response of the device to bubbly liquid

This chapter presents the experimental observations and related discussions on the response of the UAS device to bubbly liquid. Microbubbles generated in the chamber G, which was connected in series between the ultrasonic outgasser and the UAS device, were employed for this purpose. The generation chamber takes bubble-free liquid from the outgasser and adds microbubbles to it by means of electrolysis. The size and distribution of the bubbles electrolysed were studied and it was shown that the BSD generated is influenced by changes to the working parameters and the current strength across the two Pt electrodes. In this context, the addition of microbubbles to the working liquid will have an influence on the region "B" of Figure 1.3 and subsequently on the performance of the device.

Addition of microbubbles to bubble-free water is known to influence its elastic properties [102], which influences both the phase speed of sound (c_m) and attenuation of acoustic disturbances propagating within it. Microbubbles are known to be strong absorbers and scatterers of acoustical signals [47, 93, 184]. The propagation of acoustic pulses in bubbly liquids is influenced by parameters such as frequency of insonation, amplitude of pressure pulses, void fraction, and the size of individual bubbles in a cloud. Considering these parameters, this chapter attempts to quantify the response of the UAS device when employing microbubbles of known size and distribution at different insonation frequencies.

In order to investigate the response of the UAS device to bubbly liquid, its response to bubble-free liquid should be quantified. Results presented in Chapter 5 (particularly in Section 5.5) were directed towards gaining an understanding of the resonant response of the UAS device in bubble-free liquid. The non-linear shape of the pressure output

curve was discussed in detail, and was aided by the observations of power dissipated in the transducer. It was shown that this non-linear pressure output is driven by the inherent non-linear response of the piezoceramic used in the transducer.

The linear regime of the operation of the UAS device is characterised by contributions primarily from the insonation frequency, whereas the non-linear regime has additional contributions from the harmonics of the insonation frequency (along with an increase in the broadband noise floor). The non-linear regime of the UAS device was shown to be effective at decontaminating target surfaces. With the help of the ultrasonic outgasser in the liquid loop (whose performance was quantified using acoustical and optical techniques, as presented in Chapter 3), the pressure output of the device increased by up to 50 kPa in the non-linear regime.

With these results at hand, the discussions can progress towards the response of the UAS device to bubbly liquid. Propagation of acoustic energy in waveguides containing bubbly water was recently studied [185] with the aim of understanding the acoustic attenuation in pipes [142]. Acoustic energy was used to estimate the size of bubbles present in pipes [102], by employing active acoustics and to aid in diminishing the destructive nature of cavitating microbubbles [186]. However, the primary focus of the results presented in this chapter is directed towards understanding the linear response of the UAS device when using bubbly liquid, under pressure amplitudes sometimes as large as 0.1 kPa.

This chapter begins with the results of using microbubbles in the UAS device when the transducer was running at 135 kHz (Section 6.1) and then moves onto the results of using microbubbles in the UAS device when the transducer was running at frequencies outside its resonance (Section 6.2). The observed off-resonant response will be explained with the help of changes to the input electrical admittance of the transducer (Section 6.3). This input electrical admittance of the transducer was also estimated using lumped parameter modelling and compared with the admittance plots gathered using an impedance analyzer. Then, the relevant discussions on the acoustic pressure measured in the stream at off-resonance frequencies, and investigations on the transients observed in the pressure output will be presented in Section 6.4. The conclusions are presented in Section 6.5.

6.1 Influence of microbubbles at 135 kHz

To start with, a discussion on the speed of sound c_m in the bubbly liquid when employing electrolytic microbubbles in the UAS device, is important. The speed of sound in the

UAS device when using the bubble-free liquid, c, was measured at 1480 m.s^{-1} ($\pm$ 37 m.s^{-1}). As microbubbles seeded from the generation chamber, G, mix with the working liquid and fill up the conical chamber, the measured speed of sound would reduce from its bubble free value. The value of c_m is generally dependent on the void fraction present in the liquid, as demonstrated in Figure 4.1. However, in this chapter, it is practical to estimate the values of c_m in the UAS device when employing microbubbles generated at different electrode currents. For this study, the DC potential across the Pt electrodes was gradually increased, while measuring the speed of sound in the device using the time of flight method. As stated in Chapter 4, a minimum electrode current of 3 mA was required to electrolyse the working liquid, and the subsequent variation of c_m with increasing I is presented in Figure 6.1. The standard error bars drawn in Figure 6.1 were evaluated from 128 individual measurements at each value of I.

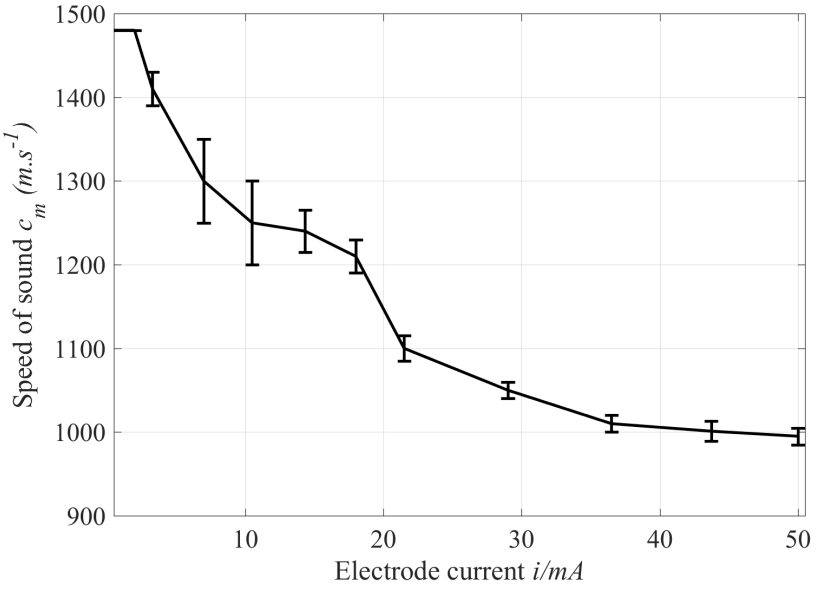

Figure 6.1: Experimental measurement of the speed of sound c_m in the UAS device when using bubbly liquid, with increasing electrode current.

As expected, the value of c_m decreases as electrode current gradually increases beyond 3 mA, with a mean speed of sound of 1250 m.s^{-1} and a standard error of $\pm$ 50 m.s^{-1} at an I of 10.5 mA. This standard error drops to $\pm$ 10 m.s^{-1} as the current across the electrodes increases beyond 30 mA. This drop could be attributed to a general increase in the reliability of the number of bubbles (N) electrolysed as electrode current increases. The observations of c_m, as presented in Figure 6.1, were restricted to a maximum electrode current of 50 mA, beyond which the estimation of c_m became difficult.

In the linear regime of operation of the UAS device and at the resonance frequency, the primary contribution to the acoustic pressure (measured in the stream) is from the

fundamental frequency (see Figure 5.15). Although there are minor contributions to the acoustic pressure by the other harmonic components in this regime, their amplitudes are relatively small. To investigate the influence of microbubbles on the response of the UAS device, a test was carried out at 135 kHz when using V_{pa} value of 100 mV_{pp} and with the electrode current (I) held at 13 mA. The pressure in the stream was recorded before and after the bubble generation was triggered, with a time gap of at least 5 s between the individual measurements. This was done to ensure that the bubble-free liquid in the conical chamber was completely replaced with bubbly liquid, which at a flow rate of 2.0 litre.min^{-1} takes 3.63 s. The power spectral density (PSD) of the averaged pressure measured in the stream in both cases is presented in Figure 6.2 (data averaged over 100 cycles).

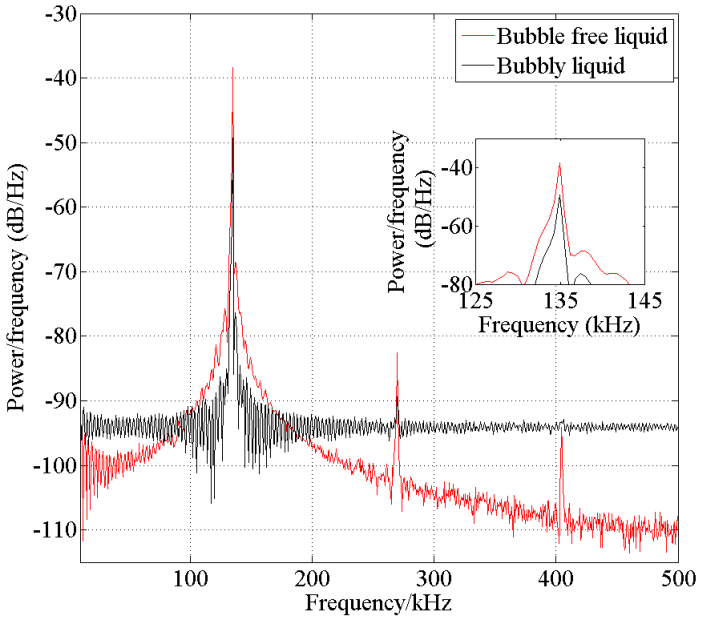

Figure 6.2: Comparison of PSD content of the averaged acoustic pressure measured in the stream when using bubble-free and bubbly liquids. See inset for more detail.

As expected, when using bubble-free liquid the contribution by the fundamental frequency dominates the pressure measured in the stream. The harmonic components are also present, albeit at smaller amplitudes, and the contribution by the broadband component drops with frequency (after 135 kHz). When using bubbly liquid, there is a reduction in the amplitude of the fundamental component (see inset in Figure 6.2), the contribution by harmonic components is almost non-existent, and the amplitude of the broadband component was noise limited to -92 dB. This could be attributed to an increase in the acoustic absorption of the bubbly liquid. This result presents evidence to suggest an absence of non-linear bubble dynamics inside the liquid during this experiment and suggests that at the resonance frequency (and at averaged pressure

amplitude in the stream measured at 1 kPa zero-to-peak) the microbubbles injected into the UAS device are undergoing only breathing mode oscillations.

When using the UAS device in its linear regime, i.e., when the value of V_{pa} was smaller than 0.1 V_{rms} (i.e., in the linear regime, see Figure 5.4), with a PRP of 100 ms and pulse lengths of 20 ms, an increase in the electrode current implied a subsequent decrease in the acoustic pressure amplitude measured in the stream. It is important to restrict the experimental investigations (evaluating the response of the UAS device to bubbly liquids) to the linear regime of operation, as operating in the non-linear regime can trigger non-linear bubble dynamics which cannot be easily examined using simplified models at different frequencies of interest. This is particularly important if the simplified models are employed to understand the response of the transducer under different operating conditions, such as when using bubble-free and bubbly liquid. Examples of transducer modelling under different loading conditions, such as the lumped parameter modelling, was discussed in reference [181] and will be discussed in detail in Section 6.3.

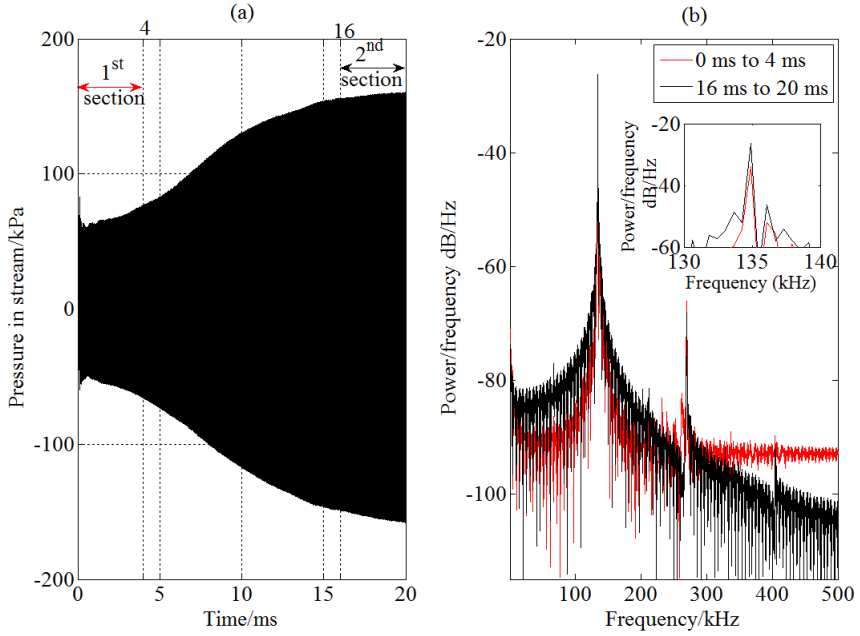

Figure 6.3: Response of the UAS device operating in the non-linear regime when using bubbly liquid at I of 10 mA. Plot (a) pressure-time plot and plot (b) estimated PSD from different portions of the pressure-time plot shown in (a). See inset in plot (b) for more detail.

However, it is important to quantify the response of the UAS device operating in the non-linear regime to bubbly liquid. The influence of microbubbles in this regime can be understood with the aid of Figure 6.3. In Figure 6.3a, a 20 ms long recording of a pressure-time plot, observed when V_{pa} was held at 0.7 V_{rms} and when the electrode

current was held at 10 mA is presented. From the recording, it seems that the peak-to-peak amplitude registered between 0 ms to 4 ms (approximately at 160 kPa), almost doubles by the time recording reaches 16 ms and stays at that value up to 20 ms. At first glance, this result might lead to the misleading conclusion that microbubbles improve the pressure output in the non-linear regime. However, a look at the frequency content of this data recording provides a better insight. The power spectral density of the acoustic data shown in Figure 6.3a was evaluated in two sections, with the first section from the first 4 ms of the recording (result shown as a red trace in Figure 6.3b) and the second section is from the last 4 ms of the recording (shown in black).

The frequency content of the acoustic data between 0 to 4 ms (red trace) has remarkable similarities to the black trace shown in Figure 6.2, which is the response of the device to bubbly liquid. The dominant contribution to the acoustic pressure in this time window (red trace of Figure 6.3b) is from the fundamental (135 kHz) and the noise floor is limited to an amplitude of approximately -90 dB. However, 16 ms after triggering the transducer (trigger at 0 ms), the pressure contribution at the fundamental has increased (see inset for detail) and the black trace of Figure 6.3b demonstrates that the device has reverted back to the operation relevant to its non-linear regime. The black trace demonstrates strong contributions from the fundamental, and an increase in the broadband component (below 135kHz), albeit at amplitudes smaller when compared to their bubble-free counterparts (see Figure 5.6).

This demonstrates that in the non-linear regime the microbubbles can influence the acoustic pressure amplitude only for a short period of time ($\leq$15 ms). After 15 ms the microbubbles are probably undergoing non-linear oscillations (due to building up of pressure amplitudes in the liquid above 100 kPa zero-to-peak). A graph similar to Figure 5.5 drawn when the UAS device employs bubbly liquid, showed smaller pressure amplitudes in the linear regime and disproportionately large pressure amplitudes in the non-linear regime. In such a case, a plot presenting the RMS value of acoustic pressure measured in the stream might be more accurate. However, it is more important to consider changes to the transition point in the pressure-vs-V_{pa} plot as microbubbles are introduced into the conical chamber (associated with the initiation of capillary disturbances).

The threshold point in the pressure-output vs V_{pa} plot can be influenced by the presence of microbubbles. The supporting result can be seen in Figure 6.4. As electrode current increases, the mean threshold voltage changes from V_{pa} of 0.2 V_{rms} (at 0 mA) to 0.3 V_{rms} (at 10 mA) and 0.4 V_{rms} (at 15 mA), when using PRP of 100 ms and pulse length of 20 ms (outgasser was on). Beyond 15 mA the transition region was observed

to be less pronounced and choosing a value of V_{pa} that marks the transition region was found to be difficult.

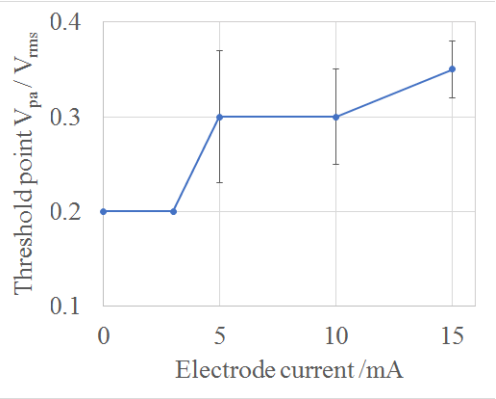

Figure 6.4: Trends in the location of the threshold point at different electrode currents.

These results imply that microbubbles generated by electrolysis could be used to reduce the pressure output of the UAS device, operating at the resonance frequency, in the linear regime but not in the non-linear regime. Hence, guided by the result shown in Figure 6.2, the UAS device with bubbly liquid could be employed where non-linear effects of microbubbles are unwanted.

With the resonant response of the device working in bubbly liquid quantified, the next step is to present the results on the response of the device operating at off-resonance frequencies. This requires a knowledge of electrical characteristics of the transducer at off-resonance frequencies, pressures generated in the stream, and the influence of bubbly liquid on these parameters. These results are presented in Sections 6.2 and further discussed in Sections 6.3 and 6.4.

6.2 Influence of microbubbles at off-resonance frequencies of the transducer

To understand the response of the UAS device (in terms of pressure output) at off-resonance frequencies and in presence of bubbly liquid, investigations towards the response of the transducer UT_1 at these frequencies must be quantified. If a transducer is run at the resonance frequency (rather than at off-resonance frequencies), the energy conversion is generally more efficient, because the electrical impedance Z_e offered by the piezoceramic element is very small. At resonance, the output velocity generated by the transducer face is aided by a higher value of electroacoustic efficiency and is assisted by the electrical quality factor Q_e. Hence, for a fixed value of V_t a transducer can generate

large vibration amplitudes at its resonance [168]. For transducers driven by an electrical field (such as the tonpilz transducer used in the present thesis), the electrical input power is given by

$$W_e = \frac{1}{2} G V_t^2. \tag{6.1}$$

Here, G is the total input electrical conductance (the real part of admittance Y) of the transducer. The value of G can be gathered either using an impedance analyzer (such as the 4192A LF Impedance Analyzer by Hewlett Packard) or can be estimated from simplified electrical equivalent models. The variation of G with frequency (around resonance) generally resembles the resonant response of a single degree of freedom system. The ratio of the susceptance B to the conductance G of the transducer can be used to obtain the electrical quality factor Q_e, a high value of which is a design criterion for single resonant systems [168].

The piezoceramic element used in tonpilz type ultrasonic transducers is generally a single frequency highly resonant type design. This implies that the value of G is generally very high at the resonance frequency and is comparatively smaller at frequencies around it. However, these frequencies of investigation have to be limited, to avoid exciting any lateral or radial vibrational modes of the ceramic [180].

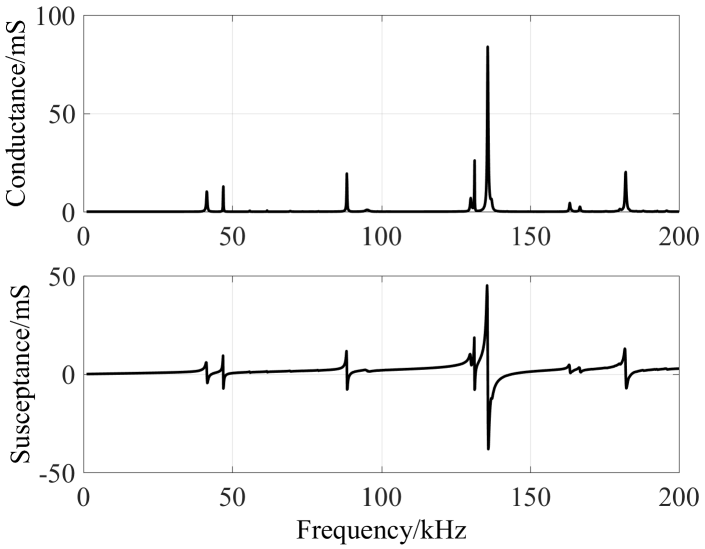

Figure 6.5: Measured values of real and imaginary parts of electrical input admittance plotted as a function of frequency with UT_1 radiating into air.

To understand the response of the UT_1 transducer at different operating conditions, a knowledge of the relevant input electrical admittances is required. The different operating conditions can be referred to as "loading conditions", because change in the acoustic impedance of the medium influences the radiation load on the transducer. These loading conditions are:

- transducer radiating into air,
- transducer radiating into a large water tank,
- transducer coupled to the UAS device and radiating into bubble-free liquid,
- transducer coupled to the UAS device and radiating into bubbly liquid.

The electrical admittance value of the UT_1 transducer for frequencies between 1 kHz and 200 kHz, radiating into air, was measured using the 4192A LF Impedance Analyzer and is shown in Figure 6.5. This plot demonstrates that the resonant frequency of the transducer is approximately at 135 kHz, as determined by the location where susceptance vanishes [168] around a maximum in the conductance plot. A frequency range covering 0.2 octave band on either side of the resonance frequency is generally considered [162] to be appropriate for modelling the response of the transducer using simplified approximations. This implies a working frequency range between 120 and 145 kHz. The discussions on Figure 6.5 and the influence of other minor resonances seen around 130 kHz in Figure 6.5 will be presented in Section 6.3. Portions of information present in Figure 6.5 within the frequency range of interest will be presented in Figure 6.7.

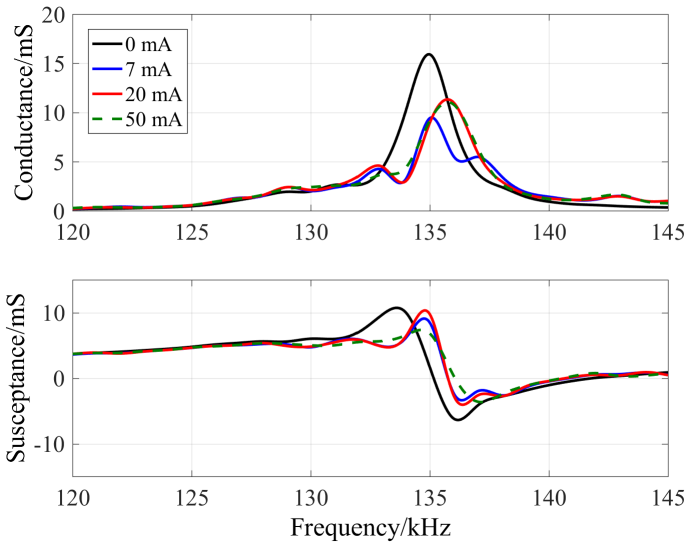

Figure 6.6: Mean values of the real and imaginary parts of the electrical admittance measured on the transducer when the UAS device was loaded with either bubble-free liquid (at I of 0 mA) or bubbly liquid (at other values of I).

It is important to compare the result shown in Figure 6.5 with the variations in the admittance values of the UT_1 transducer connected to the UAS device under different loading conditions. Microbubbles generated in chamber G (at different values of I) were used to create bubbly liquid and this liquid was fed into the conical chamber. Then, the electrical admittance of the transducer (when using different values of I) was measured using the Impedance Analyzer, in each case. The averaged values of the admittances are shown in Figure 6.6. It can be clearly seen that the minor resonances present around

130 kHz (when the transducer was radiating into air, as seen in Figure 6.5) are minimal in the measurements shown in Figure 6.6.

It should be remembered that the electrolytic microbubble generation process has inherent variability associated with the BSDs generated due to its intrinsic chaotic nature, as demonstrated using example Figures 4.9 and B.2. This implies that the measured values of input electrical admittance would also demonstrate minor variations. These variations can be quantified by repeated measurements of the admittance values of UT_1 connected to the conical chamber. The standard error bars associated with the mean values shown in Figure 6.6 are shown in Figures C.2 and C.3. The standard error in the measurements of admittance values when the device is using bubble-free liquid could be attributed to the variability in the flow rate of the liquid. The discussions related to Figures C.2 and C.3 will be presented in Section 6.4.

Reverting back to Figure 6.6, it is interesting to observe the locus of G at the resonance frequency (135.7 kHz, when I=0) as microbubbles are introduced into the liquid. For example, when I is 7 mA the value of G (the conductance) drops to 6.4 mS but increases to 11 mS as I increases to 20 mA and then drops again to 10.75 mS when using I of 50 mA (resonance frequency for 50 mA plot shifts to 136 kHz). The susceptance plot provides information on the shift in the location of the resonance frequency when using bubbly liquid. When using an I values of 20 mA and 50 mA, the plot of G demonstrates remarkably similar trends. This correlates with the plateau region in c_m measured at these values of I (shown in Figure 6.1).

To understand these trends, a detailed knowledge of the response of the transducer must be known. Once the response of the transducer is quantified, then the influence of different loading conditions on the values of Y can be understood. Subsequently, by use of equation 6.1, the electrical power dissipated in the transducer W_e can be quantified. Section 6.3 presents a lumped parameter equivalent model to investigate the response of UT_1 transducer under these different loading conditions.

6.3 Lumped parameter model

An electroacoustic device (such as a piezoceramic tonpilz transducer) is designed to convert input electrical energy to acoustic energy, and as such can be cited as an example of a coupled electro-mechano-acoustic transducer. Modelling the response of this transducer must consider the electro-mechanical and mechano-acoustic transduction principles. The lumped parameter model offers flexibility to bring together the electrical, mechanical, and acoustic radiative components in the transduction mechanism into a

single system, which can be solved under linearised assumptions. Other transducer modelling techniques such as either the distributed parameter models [162, 168], or FEM (finite element modelling) of the transducer face [187, 188], or FEM of PZT composites [189] are also well known and can be used depending on the requirement. However, in this study we restrict ourselves to lumped parameter modelling to satisfy the following criteria:

- the ability to include radiation impedance of the fluid medium under different working conditions (air, water, and bubbly liquid),
- the ability to represent all acoustoelectromechanical components by use of simple electrical analogy,
- ease of understanding and discussion, particularly when requirement demands an extension to the existing model,
- computation time.

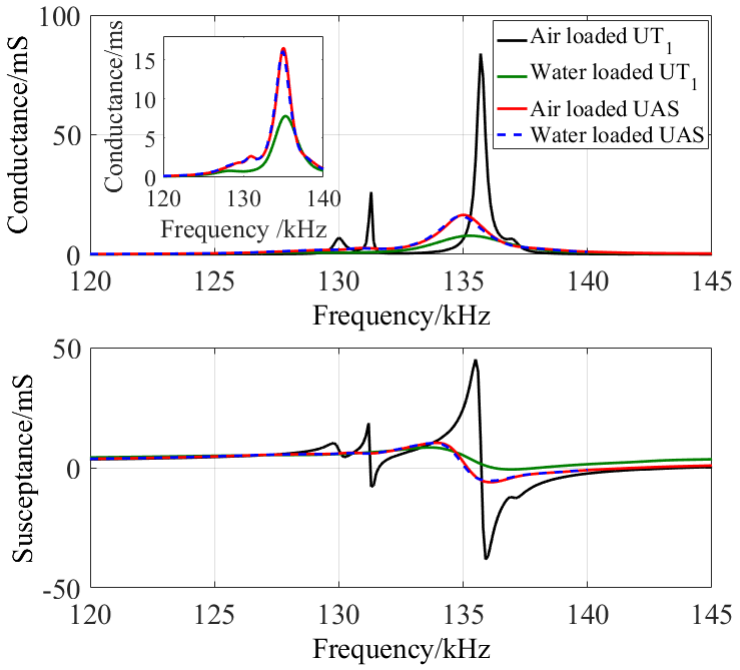

Figure 6.7: Variation of electrical input admittance of the UT_1 transducer under different loading conditions, taken from the observations of an impedance analyzer. The inset shows more detail on the variation of G with frequency. For sake of clarity, the inset does not include the variation of G for air loaded UT_1.

The lumped parameter modelling requires the measurement of G and B of the transducer at different loading conditions. The transducer is generally connected in parallel configuration to the impedance analyzer for measurements. Results may be used to determine resonance and anti-resonance frequencies of piezoceramic transducers and are usually accurate under air-loaded conditions if the mounting does not introduce significant stiffness or damping [168]. Under water loading conditions where the mechanical

and electrical quality factors, Q_m and Q_e, are not high [162], the frequency at maximum conductance may be used to obtain mechanical resonance ω_r, and the frequency of maximum resistance may be used to obtain antiresonance, ω_a.

When using lumped parameter modelling, the transducer instead of being described using complex differential equations is represented using lumped electrical equivalent circuit elements which are physically representative of mass, stiffness, capacitance, and damping characteristics of the transducer [181]. Assumptions considered for the validity of a lumped parameter model include the linearised response, sinusoidal input, and individual elements in the equivalent electrical circuit to completely represent their equivalent mechanical counterparts [162]. As long as these assumptions are valid, the equivalent circuit can be considered to be an exact representation of the transducer [181] and the circuit can further be used to investigate the influence of connecting subsystems, or to make further modifications, or to investigate transient response [181].

The admittance of the transducer under air loading and water loading conditions is shown as part of Figure 6.7, from which the differences are immediately obvious. The differences in the value of Y observed when the transducer is in UAS configuration (compared with placing the transducer in a water tank) include the influences of:

- reverberation inside the conical chamber,
- area of the transducer face in contact with the working liquid,
- the minor influence of epoxy glue (used between transducer, PTFE sheet, and the conical chamber).

With these important points in mind, the next section will discuss the electrical analogy model that is generally employed when designing or evaluating the electrical response of an underwater transducer. The modelling results will be compared with the experimental observations shown in Figures 6.6 and 6.7. The discussions lead towards understanding the influence of bubbly liquid on the working of the UAS device.

6.3.1 Transducer in air

An equivalent circuit used for evaluating the electrical impedance Z_e (or its inverse, the Admittance Y) of a PZT transducer in a tonpilz type arrangement is well established and is discussed in different references [168, 188, 190]. This model is often employed in circumstances that require: designing a new transducer or an array, designing a matching transformer to an existing transducer [191], and to estimate the performance of an existing transducer. The model for a tonpilz (or singing mushroom) type transducer with a single resonance frequency, containing equal head and tail masses, glued to a

PZT stack, and is tightened with a pre-stress rod [162, 168] is represented using the circuit diagram shown in Figure 6.8. This model, also known as the Van-Dyke equivalent circuit, allows the determination of important performance parameters of the transducer at frequencies around the resonance frequency. The resistance R_1 and capacitance C_1 in Figure 6.8 represent the electrical loss resistance and the dielectric clamped capacitance of the transducer respectively [162]. The motional arm of the transducer model (represented by parameters with suffix e, equivalent mechanical components of the transducer) consists of C_e the motional capacitance (or mechanical compliance), L_e the motional inductance (which includes the influence of head mass, tail mass, mass of the tightening bolt, stack etc.), and R_e the motional resistance of the transducer elements.

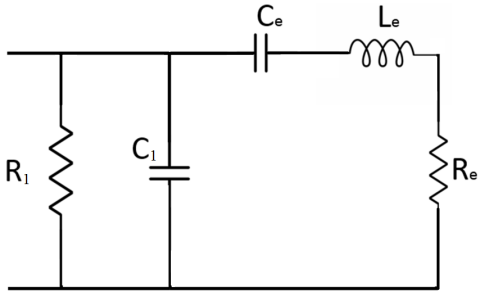

Figure 6.8: A simplified lumped element model for an air loaded piezoelectric transducer, used to represent UT_1.

The motional arm defines the resonance frequency of the single degree of freedom system electrical circuit as

$$\omega_{tr} = \frac{1}{\sqrt{(L_e C_e)}}. \tag{6.2}$$

The model in Figure 6.8 represents the transducer radiating into air. The influence of radiation resistance offered by air on the operation of the transducer is generally neglected. The input electrical admittance of the circuit shown in Figure 6.8 with frequency $(\omega/2\pi)$ can be calculated using the equation

$$Y = \frac{1}{Z_e} = \frac{1}{R_1} + j\omega C_1 + \frac{1}{R_e + j\omega L_e + \frac{1}{j\omega C_e}}. \tag{6.3}$$

An idealised response expected from this single resonant transducer and the information that can be extracted from this response curve is discussed in detail by Stansfield (1991) [162] and is followed here. To input useful information to this model, the experimentally measured admittance (Y) plotted as a motional admittance loop is generally employed. The admittance loop is generated by plotting the real and imaginary parts of admittance on X-axis and Y-axis respectively, as shown in Figure 6.9 (frequency parameter moves clockwise around the loop). From the admittance loop, the numerical values for the electrical elements of the model were evaluated by employing equations

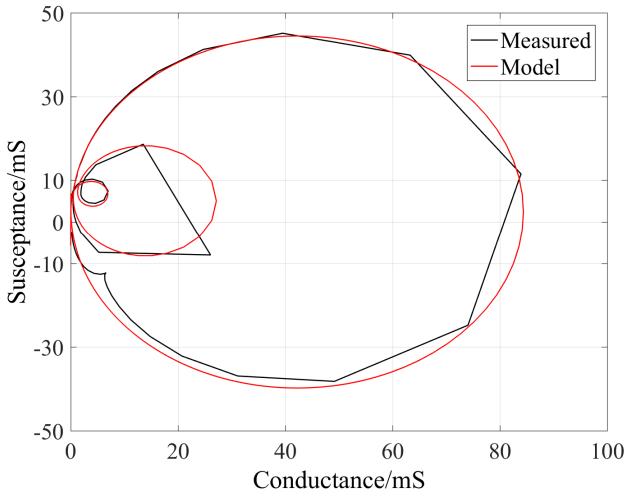

Figure 6.9: Motional admittance loop for the UT_1 transducer evaluated when radiating into air, measured (black curve) and modelled (red curve).

4.6 to 4.13 from reference [162]. The value of C_1 was evaluated at 3.28 nF and the value of R_1 is a function of frequency, which generally reduces as frequency increases. The numerical values for the motional arm for the UT_1 transducer are shown in Table 6.1. These model values are then used to generate (using equation 6.3) the conductance and susceptance values for the equivalent circuit to represent air loaded transducer UT_1.

Table 6.1: Values of motional arm parameters evaluated for the lumped parameter model on air loaded UT_1, using Figure 6.9.

	Frequency of local resonance		
Motional arm parameters for simulation	Primary resonance (135 kHz)	Second peak (131 kHz)	Third peak (130 kHz)
C_e	291.5 pF	27.058 pF	38.169 pF
L_e	4.7 mH	54.3 mH	39.3 mH
R_e	11.85 Ω	37.53 Ω	148.03 Ω

A comparison of the modelled and experimentally measured admittance plots for UT_1 radiating into air is shown in Figures 6.9 and 6.10. It is important to note that, in addition, to the primary resonance 135.7 kHz, the experimental measurements also indicate a presence of two minor peaks[1] at 131 kHz and 130 kHz in G. In order to estimate the modelling capability of the lumped parameter model to simulate the two minor resonances, two additional motional arms can be added to the 1D model (shown in Figure 6.8).

The numerical values for the motional arm parameters for the two minor resonances were evaluated by following the procedure mentioned in the previous paragraphs.

[1]For sake of simplicity the two peaks are also referred to as minor resonances.

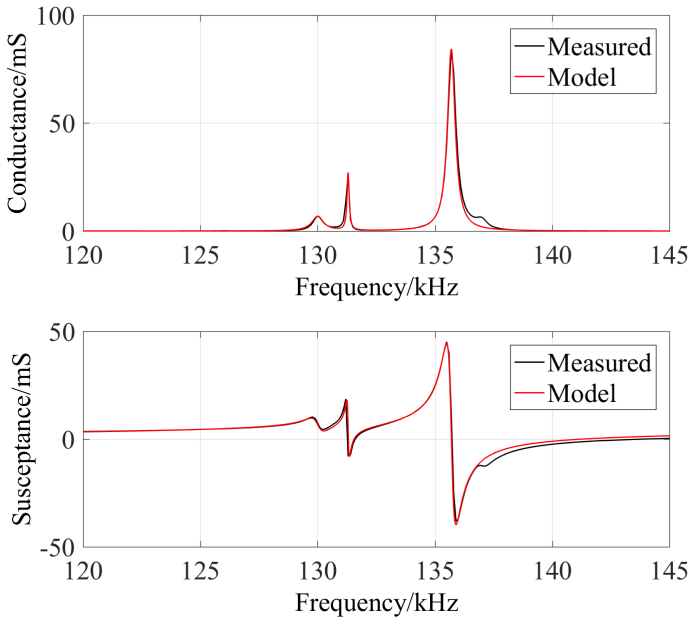

Figure 6.10: Comparison of measured and modelled curves of input electrical admittance curve for UT_1 transducer operating in air. The model results consider all resonant frequencies in the range of interest.

However, it was observed that, owing to the smaller amplitudes of conductance and susceptance values recorded at the minor resonance frequencies, the corresponding numerical values for the inductance (L_e) and resistance (R_e) of the additional motional arms are comparatively larger and the values of C_e are comparatively smaller (see Table 6.1).

The lumped parameter model is designed to simulate only one resonance frequency. Other resonances can be considered if they are independent of each other [192], are far apart, and if they demonstrate similar amplitudes in conductance. From Figure 6.7 it can be observed that, when the transducer is either placed in a water tank or is attached onto the conical chamber, the contributions by the minor resonances are very small.

When the minor resonances were excluded from the free field model, the simulated results at resonance were very similar to the experimentally measured counterparts. Hence, the contribution from these minor resonances was excluded from the modelling. The modelled 1D admittance curves, compared with the corresponding experimental observations are shown in Figure 6.11.

Once the air loaded (or free field) model for the UT_1 transducer is validated, the simulations can progress onto estimating the influence of placing the transducer in a water tank. An impedance test for a transducer when employing water as the radiating fluid is generally carried out in a large tank. The dimensions of the tank should be larger than the wavelengths in operation and reflections from the tank walls travelling back to

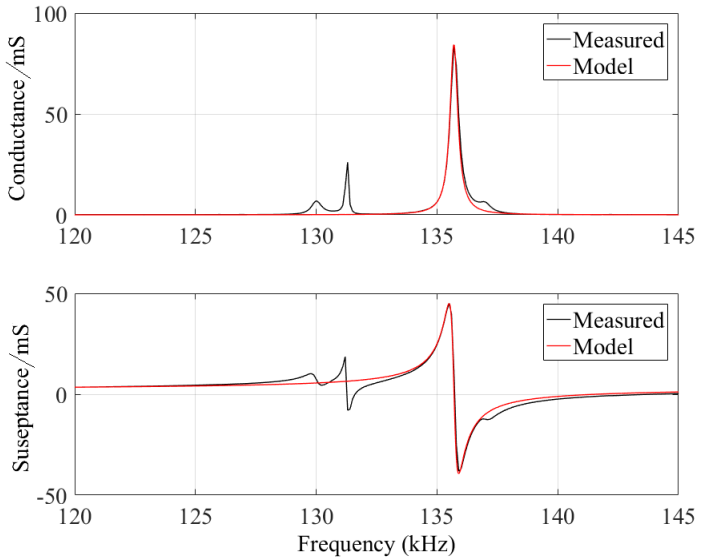

Figure 6.11: Comparison of modelled and experimental admittance of the transducer using only one motional arm in the lumped parameter simulation.

the transducer should be minimised or avoided. The influence of water loading on the transducer is well documented [162, 168], and the results of the simulations carried out on the equivalent circuit representing the UT_1 will be discussed in the next section.

6.3.2 Transducer in a water tank

The transducer was carefully placed in a large water tank with dimensions 73 cm X 46 cm X 30 cm, and filled to a height of 25 cm with one of its faces completely immersed in water. The transducer was tilted away from the bottom to avoid reflections from either the air-water interface or the bottom of the tank. When the transducer is radiating into a large water reservoir, the increase in the load on the transducer face should be included [170] in the evaluation of the impedance model. The value of L_e and R_e of the motional arm are expected to take this change in the radiation impedance (Z_r) into account. Radiation impedance estimates on a loaded transducer generally consider acoustic plane wave propagation in the medium [113]. During modelling, the additional mass M_r and additional resistance R_r encountered by the transducer in the tank (see Section 5.3) can be converted into their corresponding electrical counterparts [162] by using the electrical-to-mechanical transformer ratio of the transducer (1:N_{em}). The electrical equivalents for M_r and R_r are given by,

$$M_{er} = \frac{M_r}{N_{em}^2}, \tag{6.4}$$

and

$$R_{er} = \frac{R_r}{N_{em}^2}, \tag{6.5}$$

and the ideal electromechanical transformer ratio (N_{em}) is estimated as [190]

$$N_{em} = \frac{n_p d_{33} A}{S_{33}^E L_s}. \tag{6.6}$$

In this equation, n_p is the number of piezo elements in the stack, A is the cross sectional area of a piezo element, L_s is the total length of the stack, d_{33} and S_{33}^E correspond to short-circuit compliance coefficient and piezoelectric strain coefficient respectively [168, 190]. The values of d_{33} and S_{33}^E can be approximated from manufacturers data sheets or can be taken from reference [162] as a guideline. The value of N_{em} is generally independent of frequency. Figure 6.12 presents the updated equivalent circuit of a water loaded transducer, which shows the influence of fluid radiation impedance faced by the transducer using elements M_{er} and R_{er}.

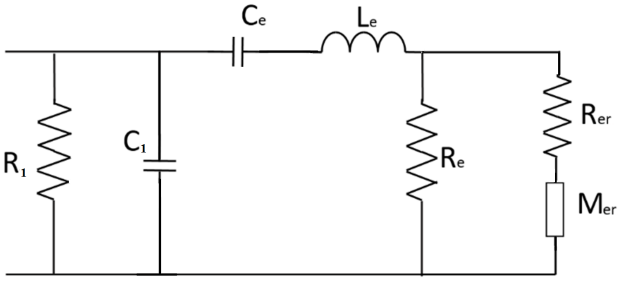

Figure 6.12: Equivalent lumped parameter circuit of UT_1 with influence of acoustical loading (shown on the far right side of the motional arm).

The values of radiation impedance Z_r for a transducer under water loading condition can be easily evaluated for simple shapes such as spherical and cylindrical pistons [162, 168, 170]. The values of R_r and X_r for a cylindrical piston placed in an infinitely large baffle and radiating into water, are available in standard acoustic books (for example [113]).

It was thought [162] that, for a tonpilz transducer the values of Z_r evaluated by considering the transducer as an unbaffled piston radiating into water [193] might be more practical. However, in the present case estimating the value of Z_r by considering the transducer as a finite baffled piston provided results closer to the experimentally measured admittance values. The following numerical values were used for different parameters in the simulation: radius of piezo stack at 15 mm, radius of the transducer face in contact with the liquid a_t at 15.5 mm (diameter of the transducer ≈31 mm), d_{33} at 245 pm/V, and S_{33}^E at 24 pm/V (both values were estimated based on guidelines given in [162]). Using equation 6.6 this implied a N_{em} value of 1.25 N.V^{-1}.

A comparison plot of experimental and simulated G and B for a water loaded transducer, as shown in Figure 6.13, demonstrates that the simulated values are closely

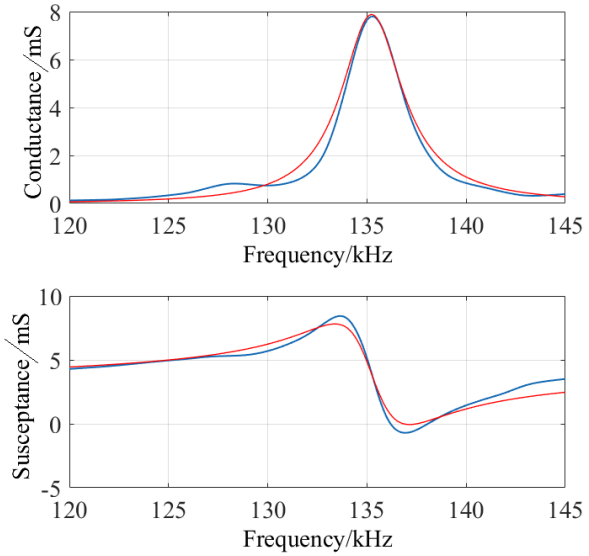

Figure 6.13: Comparison of experimental (blue) and modelled (red) admittance curves for UT_1 loaded with water on one of its faces (placing UT_1 in a large water tank).

matched at resonance. However, there is a slight mismatch at off-resonance frequencies and it will be shown that these discrepancies will reduce as the modelling progresses to the next stage where the influence of the UAS device connected to the UT_1 transducer is presented.

6.3.3 Transducer connected to the UAS device

Estimating the electrical input admittance of the UT_1 transducer connected to the UAS device operating either with bubble-free or bubbly liquid requires changes to the electrical circuit shown earlier in Figure 6.12. In this regard, some additional approximations are necessary. The approximations considered here are guided by the research works on the input impedance of acoustical waveguides. The shapes of waveguides which are similar to that of the conical chamber in the UAS device include musical instruments [194] and horns [119]. However, it is generally customary (and practically relevant) for studies on acoustic horns to evaluate the neck impedance[2] by considering the impedance value at its mouth (the larger opening) to be similar to that of a cylindrical piston mounted on an infinite rigid baffle [195]. When loaded onto the UAS device, the transducer cannot be considered as a piston mounted on an infinite sized baffled. A finite baffle mounted piston radiating into the working fluid is a better approximation.

The lumped parameter model for the transducer connected to the conical chamber should also take into account the influence of glue bonds [168] used between the

[2]The input for an acoustic horn is provided by the transducer at its neck.

transducer and the PTFE sheet. The presence of glue might affect both the low frequency capacitance C_{LF} and the transformer ratio N_{em} [190]. In addition, the length of the BNC cable used for connecting the transducer to the impedance analyser had to be increased by 1 meter for the experiments carried out using the UAS device. The capacitance of a BNC cable (which can be easily compensated [168]), generally quoted [196] for a 50 Ω cable connectors is 80 to 90 pF/m. This capacitance value of the BNC cable, however, is very small when compared to the value of C_1.

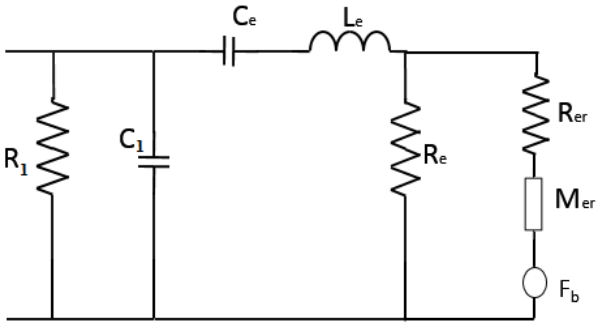

Figure 6.14: Modified electrical circuit representing the lumped parameter model used for the UT_1 transducer mounted on the UAS device. Notice the addition of new element F_b to the circuit.

As the conical chamber is a reverberant environment, acoustic signals emitted from the transducer (considering a simple ray propagation analogy) could bounce off the chamber walls in different directions. Then, there exists a possibility for some of these rays to return back to the transducer. The transducer being a reciprocal electromechanoacoustic sensor considers the average sound pressure on its face in the near field as the radiation mass it encounters. If the piezo element was acting as a hydrophone, the average pressure on the transducer face P_t is considered as the driving force during the evaluation of electrical admittance [168]. In this regard, the circuit diagram shown in Figure 6.12 will require an additional force element F_b that corresponds to the increased (or decreased) value of the average acoustic radiation impedance due to the reverberant nature of the conical chamber. It is known that loading effects on the transducer can also influence the location of resonance and anti-resonance frequencies [180]. This loading can be represented by

$$F_b = A_a P_t, \tag{6.7}$$

where A_a is the active contact area. The updated circuit diagram is shown in Figure 6.14. In the case of an acoustic projector radiating into air or a large water tank, the value of F_b can be considered zero, as represented in Figure 6.8 and 6.12. In the case of using bubble-free liquid in the conical chamber, the value of F_b in the electrical circuit can be considered as a representative of the chamber response (which varies with incident frequency). On the other hand, the value of F_b when using bubbly liquid represents the response of the conical chamber at the specific void fraction present in the liquid.

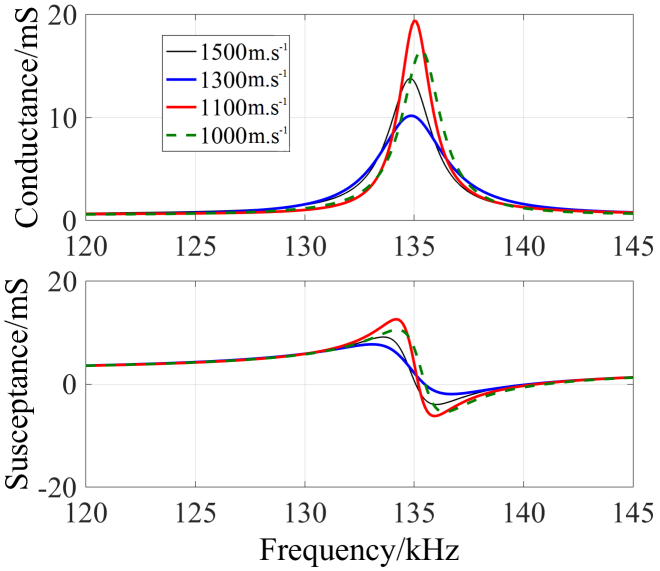

Figure 6.15: Simulated values of input electrical admittance of the transducer glued to the UAS device when using either bubble-free liquid (at c_m of 1500 m.s^{-1}, grey curve) or bubbly liquid (other curves), using the model shown in Figure 6.12.

The modelling thus requires investigations into the variation of F_b at different electrode currents and at different operating frequencies. The variables that can be employed to simulate the presence of bubbly liquid in the conical chamber are the liquid density (ρ_m) and speed of sound (c_m). The speed of sound c_m values can be taken from Figure 6.1 as a guideline, and the changes to ρ_m due to the addition of microbubbles can be neglected as long as void fractions are smaller than 10^{-2} (estimated using equation 2.18; also, see Figure 4.1).

To begin with, the importance of parameter F_b can be understood if we use the previous version of the model shown in Figure 6.12, whilst using different values of c_m. The results are shown in Figure 6.15, with different colours corresponding to different values for c_m in the water tank. A few important points can be gathered from Figure 6.15. Of those, the shift in the resonance frequency and corresponding variation in the amplitudes of G and B at these frequencies, as c_m reduces, are of particular importance.

As c_m reduces, the locii of G and B at resonance (in Figure 6.15), demonstrate trends similar to the experimental observations presented in Figure 6.6. However, the simulated amplitudes at the respective locations do not match with the experimental measurements. The differences can be remedied by taking the parameter F_b into the model, as shown in Figure 6.14. To start with, the locii demonstrated in Figure 6.15 can be understood by observing the variation in Bessel and Struve functions used for evaluating X_r and R_r respectively. The input to these functions is the wavenumber k_t

of the acoustic signal in the medium [113] which is dependent on the speed of sound c_m. As c_m drops from 1500 m.s^{-1} to 1100 m.s^{-1}, the parameter $2k_t a_t$, which is used as an input to Bessel and Struve functions, increases by 14 and 25 units respectively. The values of G and B being strongly linked to R_r and X_r follow their trend with frequency. In this high frequency limit, the value of R_r dominates the value of X_r and the wave propagation can be characterised by an equivalent plane wave carrying the same power [113, 197].

For a specific void fraction present within the conical chamber, the simplest way to estimate the contribution by F_b at different frequencies is to compare Figures 6.6 and 6.15 and to match the corresponding curves with an objective of achieving least mean square error.

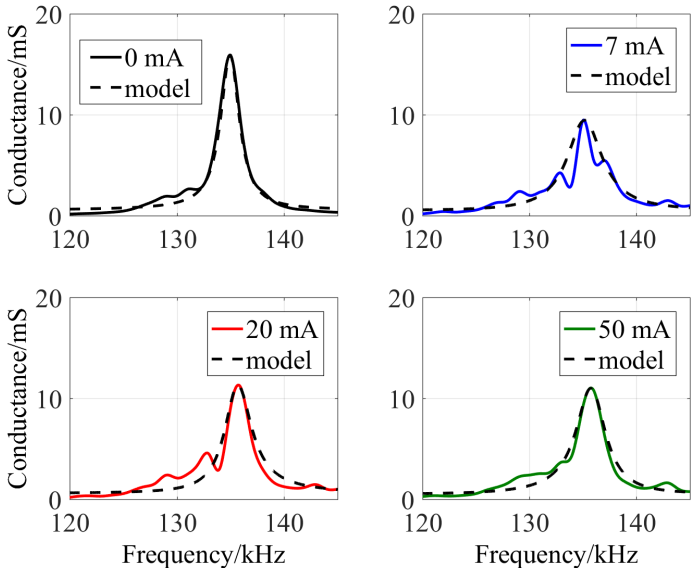

Figure 6.16: Comparison between experimentally measured and simulated input electrical conductance for UT_1 transducer connected to the UAS device using working liquid with different void fractions (0 mA implies bubble-free liquid), after taking F_b into account. Also, see Figures 6.18.

By adding F_b to the model, Figures 6.16 and 6.17 present the comparison of simulated and experimental values for real and imaginary parts of admittance for the transducer connected to the UAS device. The model accuracy is best at 0 mA and 50 mA. Since F_b eventually lends its influence to M_r and R_r, their individual contributions to different plots in Figure 6.16 and 6.17 are drawn in Figure 6.18 in their electrical equivalents.

In Figures 6.16 and 6.17 the estimated values of G and B when using bubbly liquid at I value of 7 mA and 20 mA have some discrepancies at frequencies outside the resonance frequency of the transducer. These discrepancies are prominent particularly

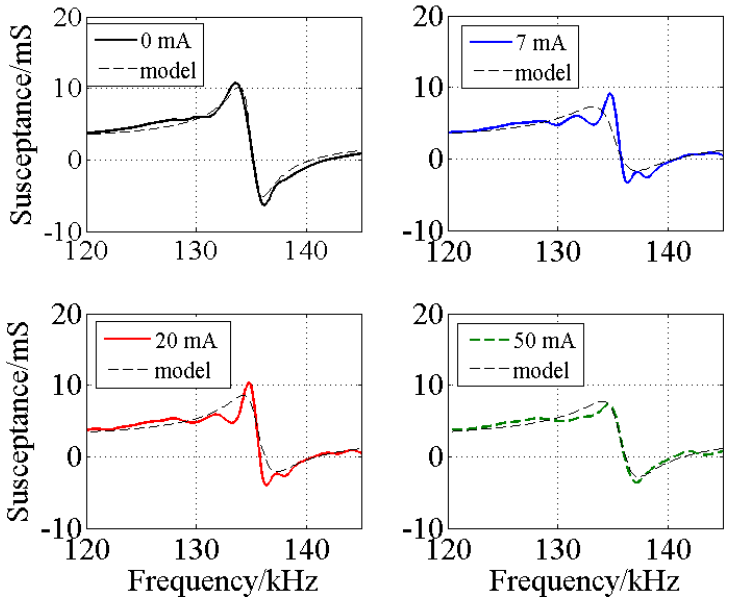

Figure 6.17: Comparison between experimentally measured and simulated input electrical susceptance for the UT_1 transducer, connected to the UAS device using working liquid with different void fractions (0 mA implies bubble-free liquid), after taking F_b into account.

around the minor resonances frequencies for Figure 6.16, which were earlier excluded from the modelling; and at maxima of Figure 6.17. The influence of these minor resonances (along with the discrepancies) reduces as the electrode current reaches 50 mA. At this juncture, the error bars observed during the experimental measurement of electrical input admittance as shown in Figures C.2 and C.3 should be revisited. The figures demonstrate that relatively larger errors (in the order of 1 mS) were recorded at different frequencies, at electrode currents of 7 mA and 20 mA. The standard error values reported for measurement of G and B reduce as electrode current reaches 50 mA, which reiterates our earlier observation on the experimental error recorded during the measurement of the speed of sound c_m.

The values of F_b for the four curves shown in Figure 6.18 consider:

- A: the difference between loading the UT_1 in a large water tank with bubble-free liquid vs loading the UAS device with bubble-free liquid,
- B: difference between loading the UAS device with bubble-free liquid vs loading the UAS device with bubbly liquid at I of 7 mA,
- C: difference between loading the UAS device with bubble-free liquid vs loading the UAS device with bubbly liquid at I of 20 mA,
- D: difference between loading the UAS device with bubble-free liquid vs loading the UAS device with bubbly liquid at I of 50 mA.

Curves of M_{er} and R_{er} marked by letter "A" in Figure 6.18 includes the influence of a larger value of r_t required at 18.4 mm, corresponding to the average radius of the glue bond used between the transducer and the PTFE sheet. The curve "A" also reflects the influence of reverberation in the conical chamber at different frequencies of interest, when using bubble free liquid. Curves of M_{er} and R_{er} marked by letters "B" to "D" in Figure 6.18 take into account the influence of microbubbles (at different c_m values) introduced into the liquid, compared to their bubble-free UAS counterparts.

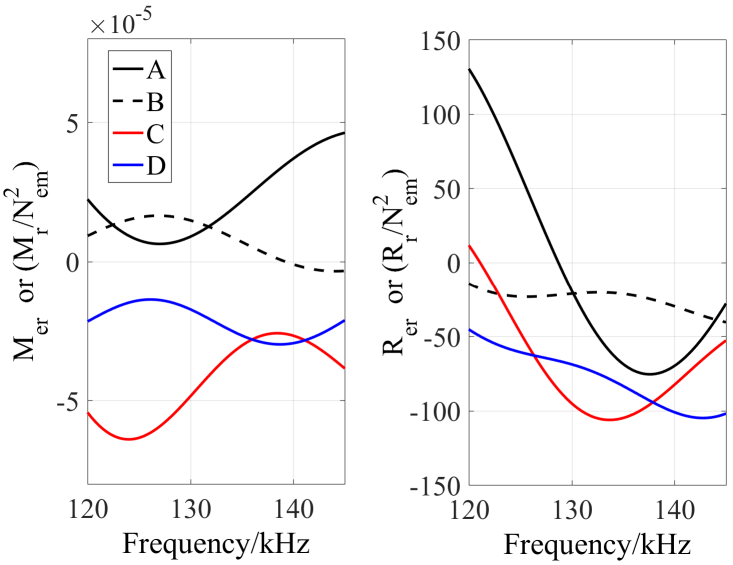

Figure 6.18: Variation in the values of R_{er} and M_{er} with frequency, employed to match the modelling with experimental results, as shown in Figure 6.16 and 6.17.

The results presented in Figure 6.18 are important because it quantifies the values of M_{er} and R_{er} to completely estimate the response of the transducer connected to the UAS device when using either bubble-free liquid or bubbly liquid generated from chamber G, in the linear regime. It also explains the trends in the locus of G and B at resonance frequency as c_m reduces. Figure 6.14 can now successfully represent the working of the UAS device in the linear regime.

Although best modelling practices based on recommendations from the literature were employed in developing the modelling routine discussed in this chapter, errors in the model could include the measurement of c_m, the estimation of N_{em}, and the estimation of R_1 and C_1 from impedance analyzer results. With the lumped parameter model at hand, the discussions will now proceed towards pressure measurement in the stream at off-resonance frequencies, when using both bubble-free and bubbly liquids.

6.4 Pressure output at off-resonance frequencies

From the observations presented in Section 6.3, it is obvious that the acoustic radiation impedance experienced by the transducer is different in different loading conditions. The value of G can now be taken either from the measurements of the impedance analyzer or from the modelling results presented in Section 6.3. Operating the transducer within the linear regime at different frequencies of interest implies considering the contribution primarily from the insonation frequency and not its harmonics. In order to investigate the response of the UAS device, the value of V_t must be kept constant at each insonation frequency. To achieve this, and to work as far away as possible from the non-linear regime, the value of V_t was monitored and a value of 3 V peak-to-peak was chosen.

When the acoustic output of the UAS device is investigated at off-resonance frequencies, importance must be given to the recorded pressure-time traces, to quantify the transient response of the transducer. An example of the transient response of the UT_1 transducer is indicated in Figure 6.19. The plot shows pressure-time data recorded in the stream, averaged over 128 pulses, when using a test signal at a frequency of 100 kHz with V_t of 31.5 V_{pp}. This value of V_t implies that there could be contributions from the multiples of driving frequency in the response. During this experiment, the pulse length t_2 was 50 ms and PRP was 100 ms. The sampling frequency (f_s) was lowered to 1 MHz (for this measurement) to enable the recording and averaging of the data.

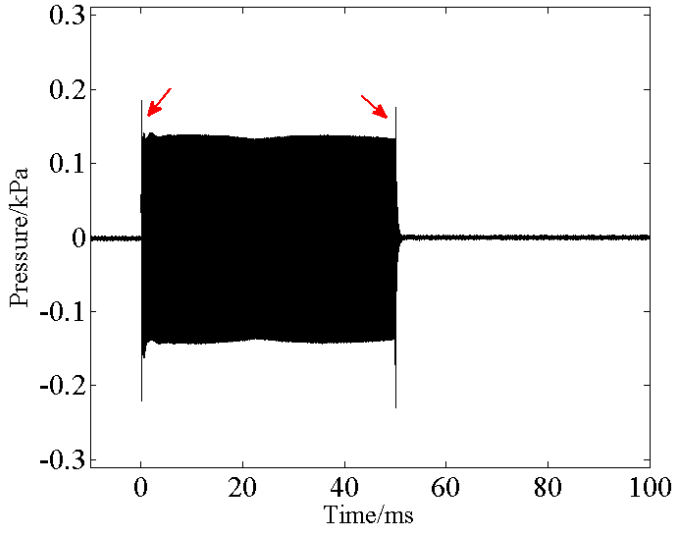

Figure 6.19: An averaged sample hydrophone signal from the UAS device, demonstrating the transient response of the transducer (highlighted by red arrows).

It can be observed from Figure 6.19 that for a pulse length of 50 ms, the pressure-time data recorded in the hydrophone extends from 0 ms to slightly beyond the 50 ms mark, due to the reverberation in the conical chamber. The pressure profile is uniform

in time (because of the outgasser) and the transient response of the transducer at the start and the end of the plot are marked by red arrows. The transient response seen in Figure 6.19 is characterized by a sudden spike and subsequent oscillatory pattern, before settling down. The time period of the transient region is a characteristic of the forced response of the transducer and corresponds to the overall damping at the frequency of insonation. The amplitude of the pressure in the transient region is a combination of transducer response, conical chamber dynamics, and the hydrophone transients if any.

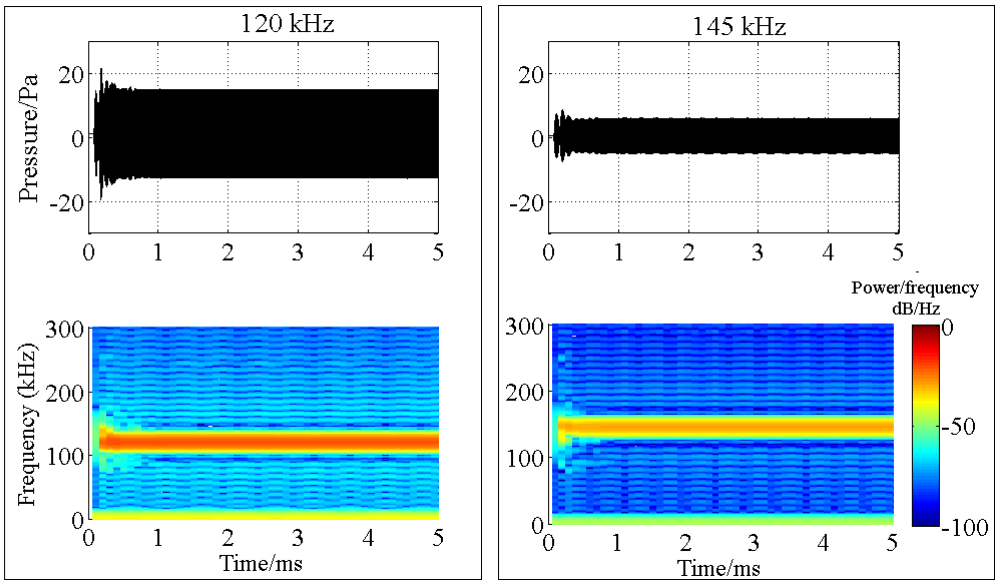

Figure 6.20: An observation of the transient response of the UT_1 transducer driven at off-resonance frequencies, quantified using the pressure-time plots recorded in the stream. The spectrograms of the pressure-time plots are also shown.

As the transient region is generally short lived (in this case, around 1 ms long), observing pressure-time traces (recorded at different input frequencies to UT_1) up to 5 ms after trigger will provide further information on it. By choosing the two ends of the frequencies of interest to this study (120 kHz and 145 kHz) and when V_t was held at 3 V peak-to-peak, the pressure-time traces were recorded and the transient response is represented in Figure 6.20. The pressure plots demonstrate differences in amplitudes and shape of the transient region at these two frequencies of insonation. The transient region can be further understood by employing the spectrogram[3] of the recorded data. When insonated with a 120 kHz signal, which is below the resonance frequency, the contributions to the transient pressure amplitude could be observed (from the spectrogram) at frequencies around 120 kHz and tending towards the resonance frequency. Similarly, in the transient region recorded at 145 kHz the contributions to the pressure amplitude are around 145 kHz and particularly tending towards resonance (as

[3]Spectrogram options: Hamming window of size 1024 samples, overlap of 16 samples, and 8192 points of Discrete Fourier Transform. Parameters are chosen based on best representation.

expected). The plots shown in Figure 6.20 can be compared with a similar spectrogram plot recorded at the resonance frequency of the transducer, shown in Figure 5.15.

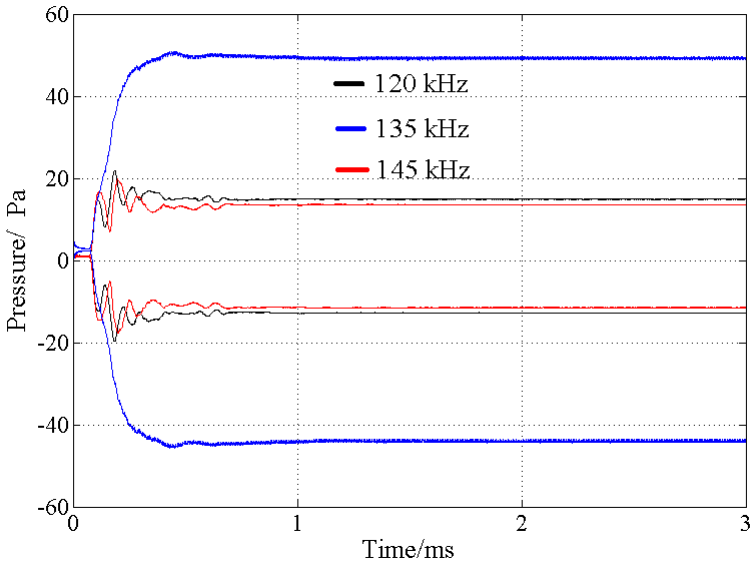

Figure 6.21: Comparing the envelopes of the pressure-time plots recorded at three different insonation frequencies. Note that the length of the transient region is independent of the insonation frequency.

The envelope of the pressure-time plots provides further information on the temporal length of the transient region. The pressure-time plots recorded when the transducer was driven at frequencies 120 kHz, 135 kHz, and 145 kHz are drawn in Figure 6.21. It is interesting to see that the time taken by the transient response to settle down is independent of the insonation frequency and is approximately equal. This is because, in the transient region, a time period equivalent to Q_e cycles of the resonant frequency is required by the transducer (or the projector) to achieve an amplitude that is 96% of its steady state [163]. The value of Q_e can be evaluated using admittance measurements or from the established lumped parameter model. This value was 0.135 units, which implies that the time taken to reach 96% of steady state amplitude at any frequency (within linear limits) is 1.01 ms. This value correlates with the observations presented in Figure 6.21.

With the transient response of the pressure measurements quantified, the influence of bubble-free and bubbly liquids on the pressure output of the UAS device can be reported.

Figure 6.22 presents the steady state peak-to-peak pressure amplitude measured in the stream, with the following input conditions to the transducer at all the frequencies of operation: V_t at 3 V peak-to-peak, pulse length t_2 at 20 ms, and PRP at 200 ms. The influence of the prismatic block holding the hydrophone (Figure 5.3) and the variation in

the hydrophone sensitivity with frequency (Figure 3.3) were taken into account during data processing. The error bars are presented only for the 0 mA and 50 mA curves for the sake of clarity. As the prismatic block has acoustic impedance value matched to that of bubble-free water, impedance mismatch between the prismatic block and the bubbly liquid will cause a reduction in the transmission of acoustic energy into the prismatic block. Hence, using plane-wave acoustic propagation assumption (which is valid for waveguides carrying high frequency acoustic signal [113, 197]), the transmission coefficient of acoustic energy based on the individual characteristic acoustic impedances of the bubbly liquid and the prismatic block were also taken into account during data processing.

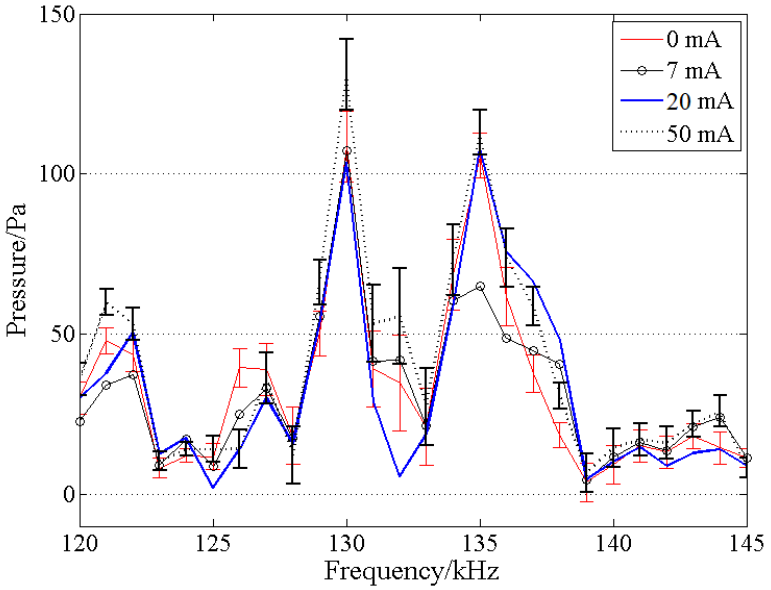

Figure 6.22: Acoustic pressure (peak-peak) measured in the stream at different frequencies to the UT_1 transducer, when using either the bubble-free liquid (0 mA) or bubbly liquids (other curves).

A few curious observations can be gathered from Figure 6.22, including dominant peaks at 130 kHz and 135 kHz frequencies and some outliers when using 7 mA electrode current. It is interesting to note that, within the experimental error limits, only a very slight reduction in acoustic pressure was recorded at few frequencies as microbubbles are introduced into the conical chamber. In contrast to the trends demonstrated in Figure 6.23 (electrical power dissipated in the transducer at off-resonance frequencies), the results shown in Figure 6.22 also demonstrate a few peaks in pressure amplitude at the following frequencies: 121, 122, 127, and 130 kHz. These trends thus could be considered as corresponding to the influence of the conical chamber on the acoustic propagation at different frequencies.

This minor influence of microbubbles on pressure output can be understood if we look at Figure 6.23. For the sake of clarity, only the experimental error contributions from the 0 mA and 50 mA curves were drawn in Figure 6.23. The plot follows the expected trend with a maximum at the resonance frequency, which is similar to the trends demonstrated in Figure 6.6. However, within the experimental error limits (considering both the electrical power and impedance measurements, see Figure C.2), there is a very little reduction in the power dissipated in the transducer as microbubbles are introduced. From Figure 6.6, when microbubbles are introduced into the liquid at I of 50 mA electrode current the mean value of G at 135 kHz drops by approximately 4.2 mS (from its bubble free value) and shifts by 0.8 kHz. A proportional reduction in the power dissipated in the transducer is 27% (calculated using equation 6.1, for example, from 25 mW to 18.5 mW). This reduction falls within the experimental error values recorded during the experiments as shown in Figure 6.23.

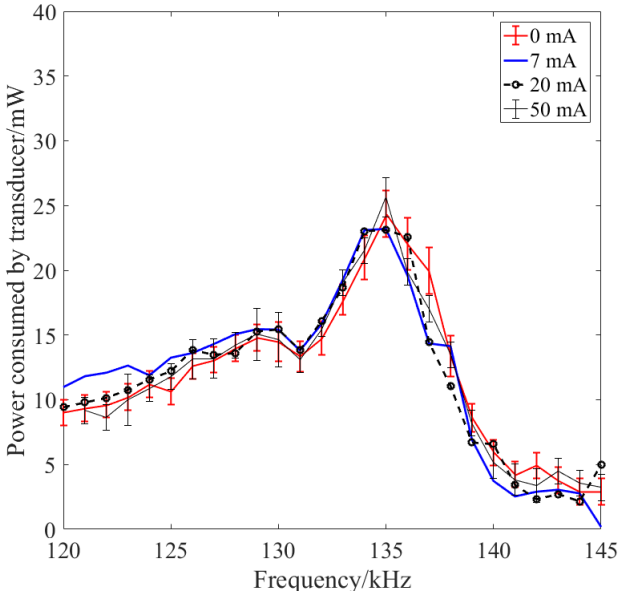

Figure 6.23: Electrical power dissipated in the transducer at different insonation frequencies, in the presence and absence of microbubbles in the conical chamber.

It is interesting to compare Figure 6.23 with Figure 6.24, where power measured in the UT_1 transducer at off-resonance frequencies under air and water loaded conditions is reported. In Figure 6.23 when the transducer UT_1 is connected to the UAS device, the power consumption at frequencies below 130 kHz is between 10 mW and 15 mW, which gradually increases with frequency. On the other hand, under air and water-tank loaded conditions, the electrical power dissipated in the transducer at frequencies below 130 kHz is between 16 mW and 18 mW. The presence of a minor resonance at 130 kHz in the air-loaded trace (black trace of Figure 6.24) can be noted. Since W_e is directly proportional to G, trends shown in the inset in Figure 6.7, provide more light

on the trends reported in Figures 6.23 and 6.24 around the resonance frequency. The results presented here should be considered in terms of the very little amount of power dissipated in the transducer ($\leq$ 40 mW), and within the experimental standard error limits.

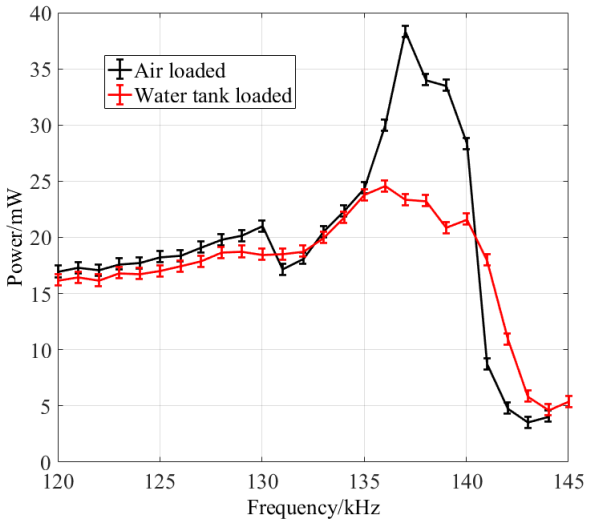

Figure 6.24: Electrical power dissipated in UT_1 transducer in free field and water tank loaded conditions.

A brief note must also be provided here on the discussion of forward and reflected electrical power parameters during the experiments carried out on UT_1 at off-resonance frequencies. The power amplifier has an electrical output impedance fixed at 50 Ω, which is best matched to the ultrasonic transducer around the resonance frequency (≈11 Ω), in air, when operating in the linear regime. An impedance mismatch can occur when the transducer is driven off-resonance. Then, either more voltage or more current is required to be supplied by the power amplifier to maintain the same radiated power output [198]. In the case of an impedance mismatch, a standing wave of electrical energy between the driver (power amplifier) and receiver (ultrasonic transducer) will be set up [198]. This standing electrical wave on the line can be split into a forward travelling wave and a reverse travelling wave [199], the measurement of power in each wave corresponding to forward and reflected power.

A measurement of forward and reflected power is possible with a bi-directional coupler, which splits the forward power and reverse power into separate output ports. However, bidirectional couplers are designed to work at a load resistance of 50 Ω and are generally tested on externally placed 50 Ω load impedances. The forward and reflected powers in the electrical circuit between the transducer and the power amplifier under different loading conditions (air, water tank, UAS device) can be calculated by using the knowledge of electrical impedance characteristics of the transducer (as reported in

Section 6.3). By using the established equations for reflection coefficient and transmission coefficient (from [113], section 6.2) at normal incidence, the equivalent reflected and transmitted electrical powers can be calculated (if needed) at different frequencies.

These results and discussions conclude the work on the response of the UAS device to bubbly liquid generated using electrolysis of working liquid in chamber G. The next section presents the conclusions of this chapter.

6.5 Conclusions

The acoustic response of the UAS device depends on a complex combination of transducer response, acoustic properties of the liquid, drive levels provided to the transducer, and the frequency of insonation. If the drive level (V_t) across the transducer terminals is kept constant and small enough, the linearised response of the device at different operating frequencies can be investigated and compared.

As the acoustic properties of the liquid inside the conical chamber are modified by introducing microbubbles (here, by electrolysis), the radiation impedance encountered by the transducer changes. This influences the input electrical impedance of the transducer at different frequencies and loading conditions. Although the electrical response of a piezo based transducer is well established under known loading conditions (air and water), the influence of a reverberant chamber (such as the conical chamber of the UAS device) on the UT_1 transducer needed to be quantified.

A validated lumped parameter model estimating the response of a piezo based transducer radiating into a water tank was upgraded to estimate the response of the UT_1 transducer connected to the UAS device using bubble-free liquid. This was done by the addition of element F_b to the model (Figure 6.14) which takes into account the reverberation of the conical chamber and the influence to the averaged acoustic pressure amplitude on the face of the transducer. By employing the characteristic acoustic impedance values of bubbly water $\rho_m c_m$, the parameter F_b can also be used to investigate the response of the UAS device to bubbly liquid. The upgraded model was successfully developed with least square error estimates between experimental and simulated results of electrical input admittance on UT_1 transducer (Figures 6.16 and 6.17).

Using experimental acoustical measurements in the stream, the transient response of the UT_1 transducer was measured and quantified. The response of the UAS device at the resonance frequency of the transducer in the presence of bubbly liquid was experimentally evaluated. It was shown that in the linear regime (and below the transition regime) microbubbles could be used to reduce the pressure amplitude in the stream.

However, in the non-linear regime, it was observed that microbubbles are influenced by large pressure amplitudes.

At off-resonance frequencies, due to the small value of V_t employed during experiments (3 V_{pp}), only minor influence to the power dissipated or the acoustic pressure measured in the stream (within the experimental error limits) was observed in the presence of the microbubbles. The result presented in Figure 6.22 can be considered as a representation of the influence of the UAS device as a whole at different insonation frequencies, at constant V_t values.

The next chapter presents the experimental investigations of capillary instability generated on the liquid stream when the device is working in its non-linear regime at the resonance frequency of the transducer. The temporal evolution of the instability was characterised using high-speed videography and will be correlated with the acoustical measurements taken in the stream at different distances from the nozzle tip, parts of which were previously presented in Chapter 5.

Chapter 7

Capillary instability of the stream

7.1 Introduction

This chapter deals with the capillary instabilities observed on the liquid stream when the UAS device is operating in its non-linear regime. In this regime, it was observed that the liquid in the conical chamber was known to demonstrate sonoluminescence [179] and the working of the device was associated with audible cavitation noise. The capillary instabilities formed on the liquid stream were observed during the experiments conducted in Chapter 5. When UT_1 was turned on and when V_{pa} was generally above 0.4 V_{rms}, the stream - instead of flowing as a tapered cylindrical column - was observed to exhibit capillary surface oscillations. These oscillations grew in size (radially) and after propagating some distance along the length of the stream, cause the stream to disintegrate into droplets. Formation of capillary waves limits the distance to which ultrasound could be propagated in the stream, due to the acoustic impedance mismatch at the air-liquid interface after the breakup.

The study of these capillary instabilities is important to understand the relationship between propagating ultrasonic energy (at 135 kHz) and the threshold for their initiation. This investigates the influence of region "C" of the UAS device on its performance (see Figure 1.3). Using equations 2.30 and 2.32, it was shown in Chapter 2 that the excitation frequencies that can trigger the fastest growing capillary wave on the stream are between 3 to 7 Hz (with the maximum instability at approximately 5 Hz)[1]. This chapter discusses the non-linear nature of these low frequency capillary wave generation, triggered by the large amplitude ultrasonic signals in the liquid.

[1]For a liquid stream whose capillary surface was excited by an external disturbance of frequency f_{cap} (i.e., $\omega_{cap}/2\pi$), the wavenumbers that propagate along the stream surface k_{cap} and frequency f_{cap} are related by the capillary instability dispersion relation. This dispersion relation is solved for different values of k_{cap}, with increasing f_{cap}. The solutions of k_{cap} (real and imaginary) give either the propagating or evanescent wave solutions. The dispersion relation is dependent on - stream radius a, flow velocity

Although stream breakup is unwanted in the case of the UAS device, the Rayleigh-Plateau type capillary phenomenon is widely exploited to trigger capillary instabilities by using small piezoceramic transducers working at 25 MHz (f_{cap}). Transducers are generally placed on the outside of a micrometer sized nozzle to match the forced wavelength with the unstable wavelength of the stream. In the literature, cavitating liquid streams were indeed reported to demonstrate shorter breakup lengths [126], when compared to liquid streams that were non-cavitating. However, the cavitation in liquid streams as reported by Lin (2003) was achieved by using high velocity liquid flow [126] (in the order of Reynolds number Re = 45,000 to 76,000) [200] in very thin nozzles (4 mm x 1 mm) to exploit the flow separation. Although ultrasonic propagation in liquid cylindrical waveguides [201] was used to initiate capillary breakup, the focus of those studies does not fall under the scope of this thesis. Hence a detailed temporal evolution of the breakup process and associated acoustical observations were deemed important to quantify these capillary instabilities.

This chapter begins with the results of optical observations of capillary wave formation on the stream with the aid of a high-speed camera (Section 7.1.1). An experimental setup designed to study the formation, growth and eventual breakup of the liquid stream will be presented in Section 7.2. Observations from the high-speed camera were then correlated with simultaneous observations of acoustic pressure recorded from a hydrophone placed in the stream path (Section 7.3). The input signal to the transducer was varied using amplitude modulation to gain further understanding of the instability phenomenon (Section 7.4). To observe the influence of system parameters on the formation of instabilities, as is generally reported for studies involving capillary breakup [125], the surface tension of the liquid (τ), and the liquid viscosity (μ) were modified using different additives[2] (Section 7.5). Finally, an external control measure that was designed to control the surface waves is reported.

The next section defines the assumptions that are valid for a liquid stream that is issued into air, is acting as a waveguide, and the corresponding coordinate system. It also introduces the capillary wave formation that will be studied in this chapter.

7.1.1 Capillary waves

For a stream emanating out of a nozzle, the following assumptions can be considered. The air around the cylindrical stream is inviscid and stationary - implying that the effect

u_0, surface tension τ and viscosity μ of the fluid. Study of capillary instability using dispersion relations was not undertaken in the present thesis, as the objective is to understand the instability phenomenon caused by high energy ultrasound and not the influence of different frequencies.

[2]It is interesting to note that G G Stokes suggested that the viscosity of a liquid could be calculated by carefully studying the capillary wave formation on water streams [202].

of air velocity on the growth of capillary disturbances is negligible. This assumption is generally valid for water streams flowing at low to moderate flow rates [201], issuing into air. It can also be assumed that the stream is subjected to axi-symmetric disturbances.

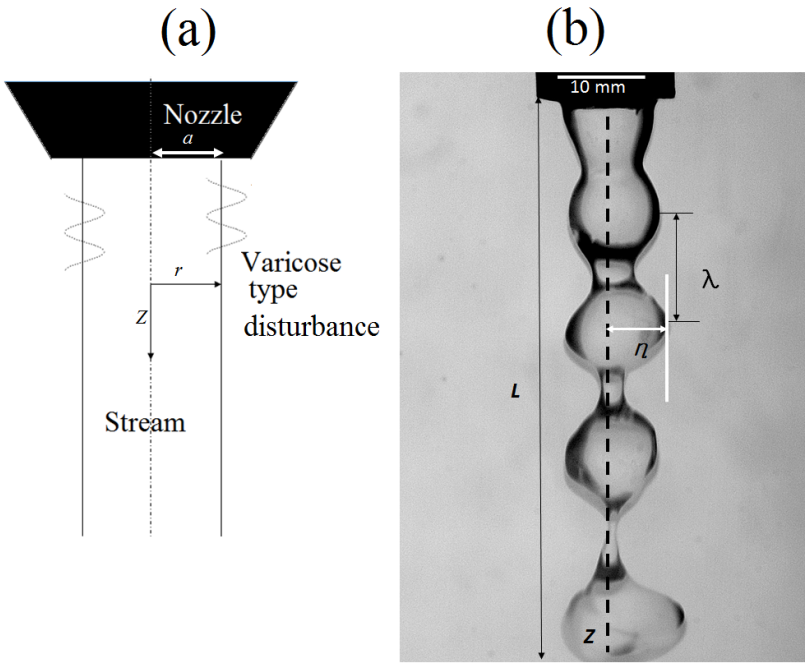

Figure 7.1: The coordinate system used for investigating capillary instabilities on the stream (the sketch on the left represents a stable stream) with the axis of symmetry marked by a dotted line (along the Z axis). A snapshot from a high-speed video, with measurement parameters, is shown on the left.

Figure 7.1a shows the coordinate system representing a stream and the parameters that define the capillary oscillations that might be generated on it, with liquid flow in Z direction. The radial parameter is r, the mean radius of the cylindrical stream at the nozzle tip is a, and the varicose type capillary oscillations are representatively drawn. Using a snapshot of the stream, the parameters that can be measured from a high-speed video are also marked, which are: L represents the breakup length (or intact length [125]) of the stream, η is the measured instantaneous radius - the distance between white outer line and the axis of symmetry of the stream, and λ is the capillary wavelength.

The radial thinning of the stream along its length, due to gravitational influence, is dependent on its flow velocity. When the flow rate within the device was at 3.2 litre.min^{-1} the stream diameter narrows down from[3] 10 mm (at nozzle tip) to 8 mm at a distance of 20 mm from the nozzle tip. However at flow rate of 1.2 litre.min^{-1} the stream diameter, at a distance of 20 mm from nozzle tip, was recorded at 4.03 mm. This reduction in the radial size of the stream would play an important role in acoustic propagation [115, 122] through it and in subsequent instability formation (will be discussed in Section 7.5). It is important to note that the pressure amplitude that

[3]These observations were extracted from the high-speed video recordings reported in Section 7.2.

causes the liquid inside the conical chamber and the stream to undergo cavitation is also the primary driving force (via the restoring surface tension force) to displace the stable surface of the stream.

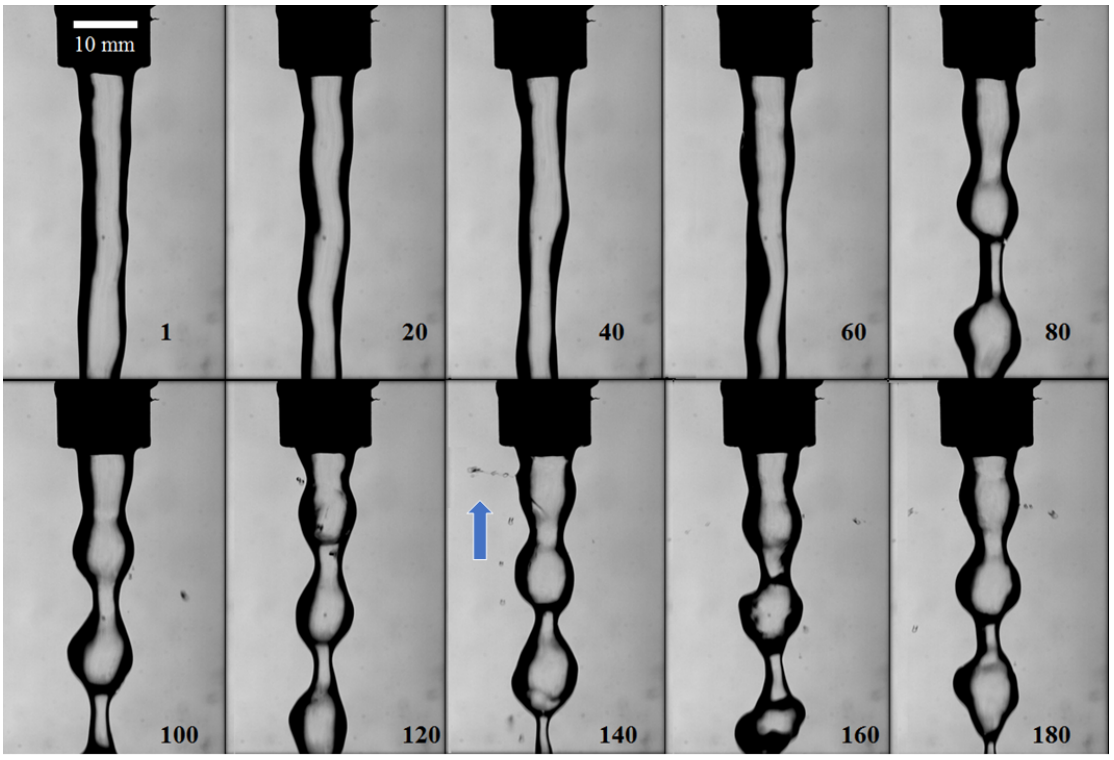

Figure 7.2: Ten snapshots spaced $1/30^{th}$ s apart, taken from a high-speed video, demonstrating the formation of capillary waves on the stream. The scale bar in 1^{st} frame is 10 mm long and the numbers at the bottom right represent the frame number.

With the aim of introducing the capillary wave formation observed on the stream, a collage of snapshots from a high-speed recording is presented in Figure 7.2. Figure 7.2 shows the unstable behaviour observed when transducer UT_1 was driven continuously at 135 kHz (implying that the pulse length was larger than the video recording length, 2 s). During the experiments carried out to investigate the capillary wave formation, the value of V_{pa} was generally held at 0.7 V_{rms}. This ensured that the device is operating in the non-linear regime and is well above the transition regime. The transition point marks the minimum value in V_{pa} required for initiating the capillary disturbances on the stream. The flow rate of the liquid during the experiments was 2.1 litre.min^{-1} and the liquid temperature was around 22^oC (the influence of liquid temperature will be discussed in Section 7.5.3.1). Unless otherwise stated, DI (deionized) water without any surfactant was used as the working liquid. The electrochemical microbubble generator, G, was disconnected from the liquid loop and the outgasser was turned off.

The frame rate used for the high-speed recording shown in Figure 7.2 was 600 fps with an exposure time of 990 μs per frame. Each individual image shown here was

spaced $1/30^{th}$ s apart, with the transducer and the camera triggered simultaneously in frame 1 (or at 0 ms). For high-speed photography, background lighting was provided by a small array of LED lights and a diffuser paper was used to create an even light distribution in the field of view. The light rays from the LED array that passed through the centre of the stream made it brightly illuminated and the light rays passing through the edges of the stream diffracted away from the line of sight of the camera, creating dark edges for the stream profile.

At the flow rate used for optical observation, shown in Figure 7.2, the liquid is in the transition region between laminar and turbulent flow (see Section 7.5.1, for influence of flow rate on the instability formation) as is obvious from the surface of the stream in frame 1. After triggering the transducer, radial surface waves start to appear in-between frames 60 and 80 (i.e., 100 ms to 133 ms after trigger). In addition to radial capillary instabilities, the formation and burst of air cavities at the edge of the liquid stream could also be observed, as marked by the blue arrow in frame 140 of Figure 7.2. These bursting air cavities are termed "microjetting" or "jetting" action and is further discussed in Section 7.2.1. Once surface waves were formed (either at the nozzle tip or further downstream) they grew in amplitude, convect along the length of the stream and eventually breakup the stream. This reduces the intact length of the stream (not marked in Figure 7.2) and restricts the propagation of the ultrasonic signal beyond the breakup point (although formation of necking zone also obstructs the propagation of acoustic energy).

Formation of surface waves and analysis of the temporal delay in their appearance (relative to the start of the ultrasonic signal) will be discussed in conjunction with Figures 7.4 and 7.5. The recordings shown in Figure 7.2 were made using the experimental setup discussed in Section 7.2.

7.2 Characterising instability using a high-speed camera

The experimental setup used to investigate the capillary wave formation on the stream surface (shown in Figure 7.3) is a modified version of the experimental schematic shown earlier in Figure 3.1. The UAS device was placed in an observation glass tank with the stream falling vertically. A Phantom v5.1c high-speed camera (placed rigidly on the floor) was used to record the dynamics of the stream, in conjunction with Phantom 663 software. Different frame rates were employed for the video recording, starting from 600 fps and increasing to 3100 fps (details mentioned in individual figures). The triggering signal to simultaneously start the function generator and the high-speed camera was provided by an external trigger box.

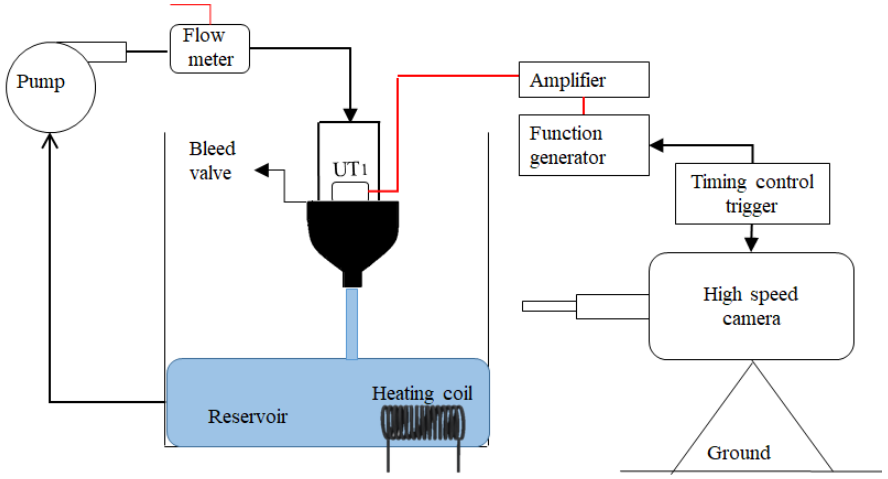

Figure 7.3: Experimental setup used for recording the capillary instabilities formed on the stream.

From optical observations and using the coordinate system shown in Figure 7.1, a shifted mean value of the stream surface displacement η_1 could be defined, as

$$\eta_1(t) = \eta(t) - a_1. \tag{7.1}$$

The value of η_1 can be used to track the variation of local stream radius as capillary waves appear, with a_1 as a measure of the local mean stream radius at a specific distance from the nozzle tip, and t is the time parameter. The value of a_1 is generally equal to a at the tip of the nozzle and is constant at a given flow rate.

Figure 7.4 presents the variation of η with time, measured on the stream surface at three different distances from the nozzle tip: 10 mm, 20 mm, and 30 mm. A snapshot of the stream is shown on the right-hand side of Figure 7.4, with a transparent ruler for scale. At 10 mm distance from the nozzle tip, η_1 was measured at 2.3 mm peak-to-peak; at 20 mm from the nozzle tip, η_1 was at 2.8 mm peak-to-peak; and at 30 mm from the nozzle tip, η_1 was 3.2 mm peak-to-peak. The magnitude of η_1 was observed to increase as the measurements proceeded downstream from the nozzle. The radial thinning of the stream (or the measurement of a_1) could be observed by comparing the starting points of the three traces shown. Figure 7.4 also presents another case for temporal delay in the formation of radial surface waves relative to the start of the ultrasonic signal. The time difference between the start of ultrasound (0 ms) and the formation/detection of the first radial instability on the stream surface, measured at a distance of 10 mm from the tip, was observed to be around 60 ms (in this case).

Upon careful investigation, it is evident that the spatial growth rate of capillary waves (i.e., growth rate along the Z direction) does not follow an exponential law (the

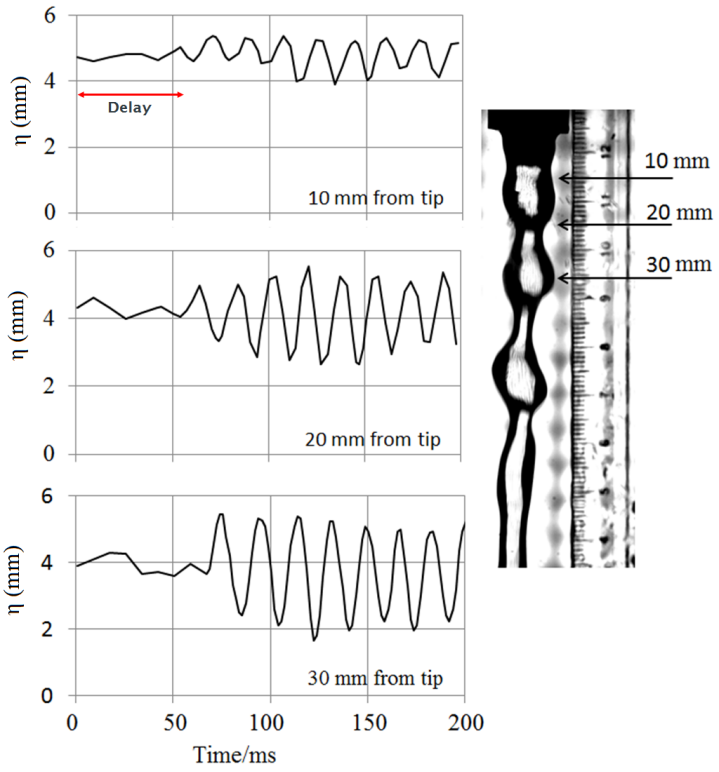

Figure 7.4: Variation of the stream radius η with time at measurement distances 10 mm, 20 mm, and 30 mm from the nozzle tip. The alternative black and white shapes in the snapshot (to the right) is the outline of LED lamp used for illumination.

equation 2.31). The exponential growth rate of capillary disturbances is a characteristic of the classical Rayleigh-Plateau instability (as presented in various references [124, 125, 128, 131]; also see Figure 2.4). In the present case, it was observed that once the radial surface waves were initiated they reached their maximum amplitude and stop growing in the radial direction. Once the growth stops, the swelled region was observed to convect with the flow. This temporal evolution in the instability wave formation and subsequent convection was not reported in literature.

In an attempt to understand this temporal growth pattern, the frame rate was increased to 3100 fps (maximum permissible for the aperture size used) and exposure time was dropped to 240 μs. A sequence of images (with a timestamp) from this recording is shown in Figure 7.5. For this experiment, a lower flow rate of 1.8 litre.min^{-1} was used to employ laminar flow conditions. Ultrasound was turned on at 0 ms and the stream, which initially flows as a tapered cylindrical column, starts demonstrating very small amplitude and small wavelength azimuthal capillary waves (wavelength compared to radial instability waves) after 26 ms. These are marked by a dotted rectangle in frame "b" of Figure 7.5. At 33 ms the first microjetting action was observed (an example event was marked with a white arrow in frame "d" at 78 ms). This microjetting action continues until 100 ms, when a low frequency radial surface undulation (frequency compared

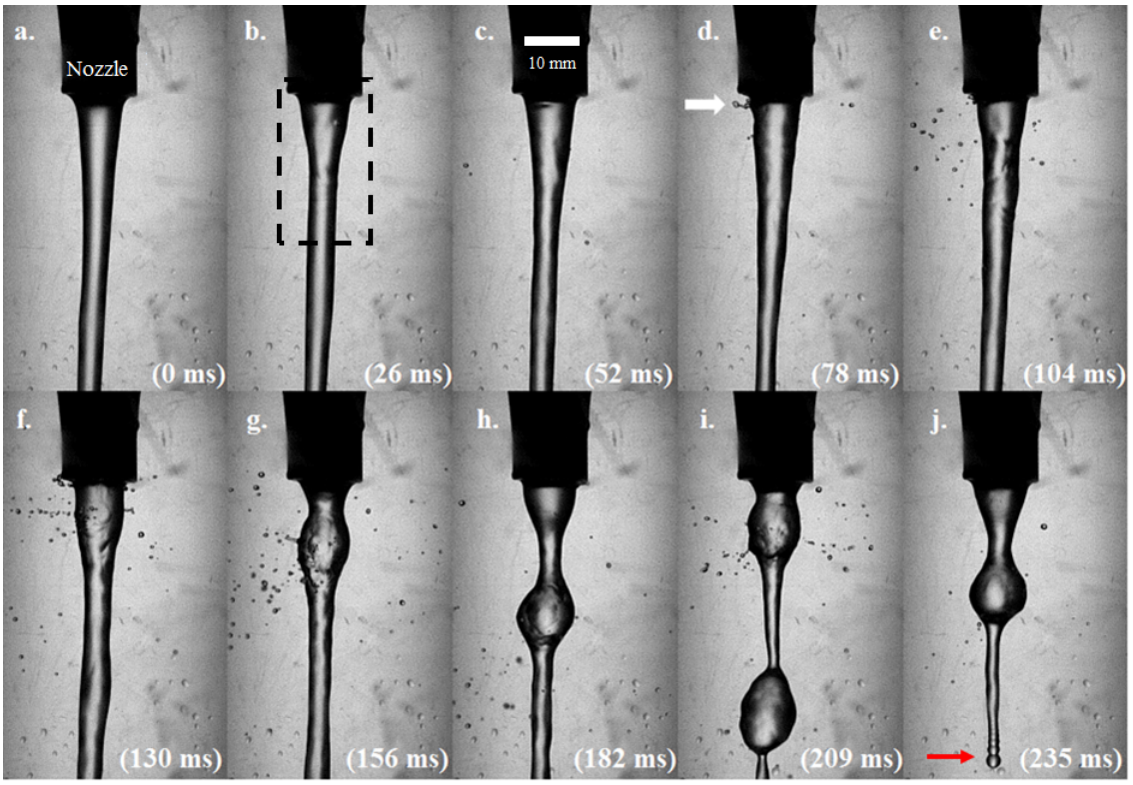

Figure 7.5: Frames extracted from a high-speed video (recorded at 3100 fps) showing the formation of surface waves on the stream. The white scale bar in frame "c" is 10 mm long. The red arrow in frame "j" represents the classical Rayleigh-Plateau instability formed at the broken stream tip.

with azimuthal waves) begin to build up at the tip of the nozzle. It was observed that, with the formation of large amplitude radial waves, more liquid becomes available at the nozzle tip, causing more microjets to burst out. The radial surface wave then forms completely, defined by a neck formation at both its ends, which constricts the flow of ultrasound (see Section 7.3). With no additional energy available from the transducer (due to constricted neck formation), the radial instability stops increasing (frame "g"), convects along with the flow and breaks the stream into a large droplet downstream. This cycle repeats again as fresh liquid is issued from the nozzle.

It is interesting to observe frame "j" of Figure 7.5 carefully (which shows a snapshot of the stream 235 ms after the start of ultrasound). The stream has just broken up and a large droplet has convected downstream (and out of the frame). The lower tip of the broken stream now displays the classical Rayleigh-Plateau instability (marked by the red arrow) with spatial exponential growth along the stream. This local instability is triggered by a droplet separating from the main stream, unlike the large amplitude radial instabilities which are driven by a large amplitude ultrasonic signal.

From these high-speed observations, the capillary wavelength λ and evaluated capillary frequency (f_{ins}) is presented in Table 7.1. The error values presented in the

table refer to one standard deviation of error (extracted from 25 measurements). At 2.0 litre.min^{-1} flow rate, the evaluated capillary frequency (f_{ins}) was approximately 4 Hz or approximately 3.2 Hz for the UAS device with nozzle opening at 15 mm diameter[4]. These values are similar to the theoretical values reported earlier in Figure 2.5. The most unstable capillary frequency for a 10 mm (mean) diameter liquid stream flowing at 2 litre.min^{-1} rate is approximately at 5 Hz. For the assumptions used in evaluating f_{ins} from λ (refer to [203]) the results presented in Table 7.1 are a good enough approximation. However, from the evidence presented in Figures 7.4 and 7.5, it can be argued that the instability pattern observed in this chapter (where the spatial growth rate does not follow an exponential pattern) is not a Rayleigh-Plateau instability and therefore equation 2.30 is not applicable to this study.

Table 7.1: Measurements of radial capillary wavelength (λ) and corresponding capillary frequency (f_{ins}) for surface oscillations on the liquid stream, using observations from high-speed videography. Capillary frequencies are evaluated using equation 2.30.

10 mm nozzle opening		15 mm nozzle opening	
λ(mm)	f_{ins}(Hz)	λ (mm)	f_{ins}(Hz)
14.2 ($\pm$0.1)	4	16.2 ($\pm$0.1)	3.2

The breakup length (L) of the stream exhibiting capillary instabilities was observed to vary between 50-75 mm. The variation in the measured value of L was observed to be related to the formation and growth of individual radial surface undulations closer to the nozzle tip. At large flow rates (above 2 litre.min^{-1}), uninterrupted availability of liquid at the nozzle tip implies a continuous formation of surface waves and very little necking formation at to the nozzle tip. At flow rates below 1.8 litre.min^{-1}, the lower flow velocity affects both λ and L. This is further discussed in Section 7.5.1.

The microjetting action, seen in Figure 7.5 as an ejection of liquid droplets out of the surface of the stream, is the characteristic of the capillary instability phenomenon reported here. Although ejection of droplets from liquid streams was reported in the literature in conjunction with the collapse of voids triggered by a high-intensity focused laser [141], the source and evolution of the liquid droplets ejected from the stream in the present case were thought to be driven by the influence of ultrasonic energy from UT$_1$. The mechanism thought to be behind the microjetting is presented in the next section.

[4]Preliminary experimental observations of instability formation on the stream, issuing from the UAS device with nozzle opening at 15 mm diameter and activated by 135 kHz continuous ultrasonic signal were carried out by colleague Douglas Offin, prior to the start of this project.

7.2.1 Microjetting

A microjetting event was marked in frame "d" of Figure 7.5. The number of microjetting events that could be observed (per second) and the distribution of microjetting events (with respect to their distance from the nozzle tip) was found to be dependent on the flow rate and the type of additives used. For example, very few ejections (or very little misting action[5]) were observed when the working liquid was laden with 2 mM SDS surfactant. The microjetting ejections were observed to be cylindrically symmetric to the stream axis, recorded with the help of simultaneous photographic observations using perpendicularly aligned vertical mirrors. The microjetting ejection velocity was recorded at 1.1 m.s^{-1} ($\pm$ 65 mm.s^{-1}) using the high-speed recordings made at 1200 fps. This jetting action causes a loss of fluid at the burst zone and the necking zone accelerates as a result.

Figure 7.6 shows a sketch demonstrating the principle (thought to be) [204] behind the formation of microjets on the cylindrical stream. The nozzle (in black) and the tapered cylindrical liquid stream (in blue) are drawn, along with the stream surface (not to scale). The numbers 1 to 8 in the cartoon represent different stages/events that correspond to the formation and eventual ejection of microjets from the stream. The steps [204] (in the absence of the ultrasonic outgasser in the liquid loop) are:

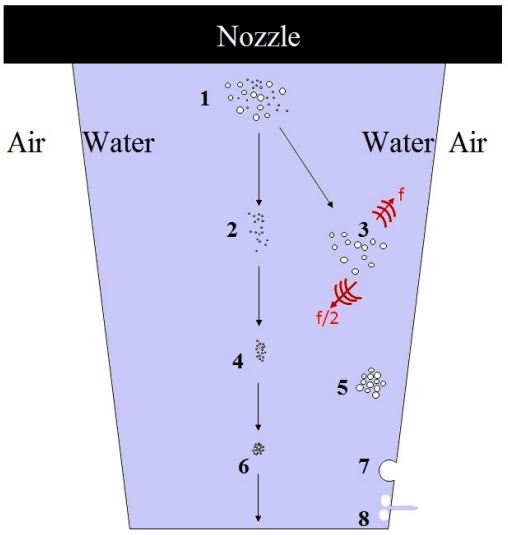

Figure 7.6: A sketch demonstrating the (hypothesized) mechanism for the formation of microjets on the liquid stream. Numbers denote specific events in the formation of microjets and are discussed in the text. Sketch not to scale.

[5]The word microjetting refers to observation of (relatively) large globules of water ejected from the stream. Misting refers to the relatively smaller droplets of water ejected when using tap water with the commercial version of Starstream device.

1. intermittent bubble clouds in a mixture of small and large radii are infrequently flushed out of the cone [205], which could be detected by the pressure-time history recording in the stream [205],
2. primary Bjerknes forces cause both the larger and the smaller microbubbles to clump into two separate groups. Since the pressure is zero at the interface, the smaller bubble groups stay at the centre and larger bubble groups move away from the axis of symmetry,
3. scattering of acoustic signal from bubble clouds creates pressure signals at f (from breathing mode oscillations) and $f/2$ (from surface oscillations of bubbles),
4. secondary Bjerknes forces cause the two bubble groups to clump individually,
5. the larger bubble group is driven to the wall creating a void at the stream edge,
6. this void is unstable and thus creates microjets, expelling the air into the atmosphere,
7. this ejection is detected as the microjetting or misting action (at velocity 1.1 m.s^{-1} out of the stream).
8. the smaller bubble group will travel down with the stream,

These steps will be revisited for discussion related to the experimental results reported in Section 7.5, which presents the influences of system parameters, namely, surface tension, flow rate, and viscosity on the capillary wave formation.

It is important to correlate the photographic observations (for example, Figure 7.5) with acoustic recordings made in the stream to completely quantify the capillary wave formation. The next section discusses the relationship between the acoustic pressure measured in the stream and the surface undulations observed using a high-speed camera.

7.3 Pressure measurement in the stream

The amplitude of pressure plays a prominent role in initiating the surface waves. When using DI water as the working liquid, and at a room temperature of 18.6^{o}C, it was observed that as V_{pa} increases from 0 V_{rms} to 0.8 V_{rms} the surface waves were triggered only when the V_{pa} value reaches or exceeds the threshold point. This is demonstrated using Figure 7.7, which presents the changes to the parameter η_1, with increasing V_{pa}. Above the threshold input voltage (0.4 V_{rms}) the value of η_1 (recorded at a distance of

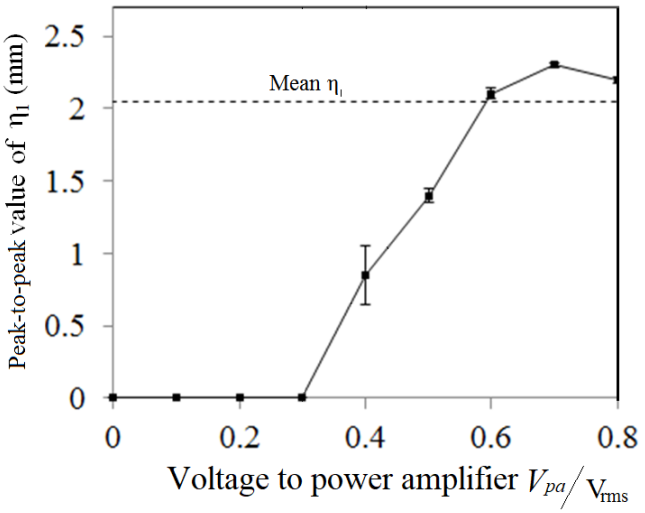

Figure 7.7: Variation of peak-to-peak value of η_1 with V_{pa}. Also, see Figure 5.5 for correlation of this result with pressure-output vs V_{pa} plot.

20 mm from the nozzle tip) was observed to increase with an increase in V_{pa}. The value of η_1 averages to 2.05 mm (peak-to-peak) as marked in Figure 7.7.

The similarities between trends demonstrated in Figure 5.5 and Figure 7.7 can be noted. Since the outgasser was absent, the demarcation between linear and non-linear regions is prominent in Figure 5.5 and influences observations reported in Figure 7.7. In the linear regime, no surface waves were formed and the stream was observed to flow along the Z direction as a tapered cylindrical waveguide (depending on the flow rate).

For the stream exhibiting surface oscillations, the necking region will restrict the propagation of ultrasound. This can be quantified by recording the pressure amplitude in the stream at different distances from the nozzle tip. Some of these results were reported earlier in Section 5.4. The results shown in Figure 5.12 will be used again in Section 7.3.1, along with the supporting optical observations to correlate and to aid discussion.

7.3.1 Influence of target distance on instability formation

A rectangular obstacle, in this case, a steel plate whose dimensions are larger than the stream diameter, was held rigidly in the stream. High-speed videography was used to observe the stream surface as the distance between the tip of the nozzle and the outer edge of the obstacle gradually increased. It was observed that, at distances closer than 15 mm (or at values less than λ), the free surface of the stream that exits the nozzle was found to remain cylindrical, exhibiting no radial surface oscillations (when the UAS was operating in the non-linear regime). However, the microjetting action and the azimuthal surface instabilities were present and were observed. As the distance increases beyond

15 mm, a complete radial capillary wave ($\lambda \approx 14.2$ mm) could be formed. Figure 7.8 presents two snapshots taken from two different high-speed videos recorded when: (a) the obstacle was placed at a distance of 10 mm from the nozzle tip, and (b) the same obstacle was at a distance of 27 mm from the nozzle tip.

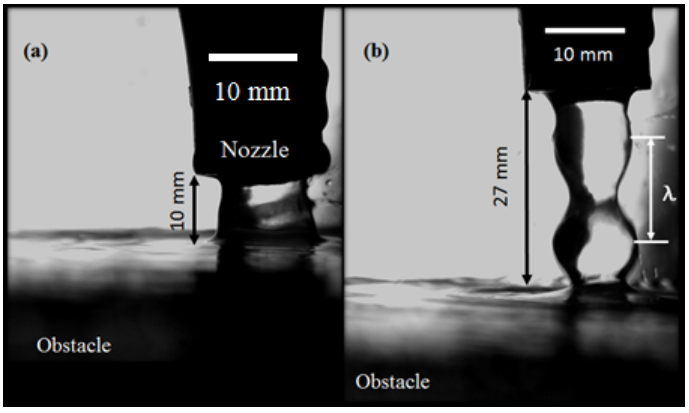

Figure 7.8: Two snapshots from two different high-speed videos demonstrating the influence of target distance on the formation of radial capillary waves. Part (a) when the distance between obstacle and nozzle is less than capillary wavelength λ, and part (b) when the distance is greater than the capillary wavelength.

This result implies that, unless radial capillary waves could be completely formed, the stream will not breakup and could conveniently carry the ultrasonic energy to the target surface (limited to an approximate distance of 14 mm). The microjetting action might cause a loss of liquid from the stream, but it will be shown that this microjetting does not impact the averaged value of the pressure amplitude recorded in the stream. As the distance between the nozzle tip and the obstacle increases, the radial surface waves are completely formed and the passage of ultrasound could be restricted beyond the necking region. This is demonstrated using results shown in Figure 7.9.

To track the temporal evolution of the stream surface and to correlate it with the pressure amplitude within the stream, simultaneous acoustic and optical observations were carried out. The outer surface of the prismatic block carrying the hydrophone was used as an obstacle (for high-speed measurements of the stream surface) and the hydrophone was used to record the pressure in the stream. The results are presented in parts (a) and (b) of Figure 7.9, when measurements were recorded at distances of 5 mm and 25 mm (distance measured from the nozzle tip to the outer surface of the prismatic block). The acoustic observations reported in Figure 7.9 were presented earlier in Figure 5.12.

When the outer surface of the prismatic block was held at a distance of 5 mm from the nozzle tip, no radial surface oscillations were observed (see η-time plot, Figure 7.9) in the stream and η has a mean value of 6.2 mm (red trace). An increase in the recorded stream radius (η) is due to the fact that, when a stream comes in contact with the

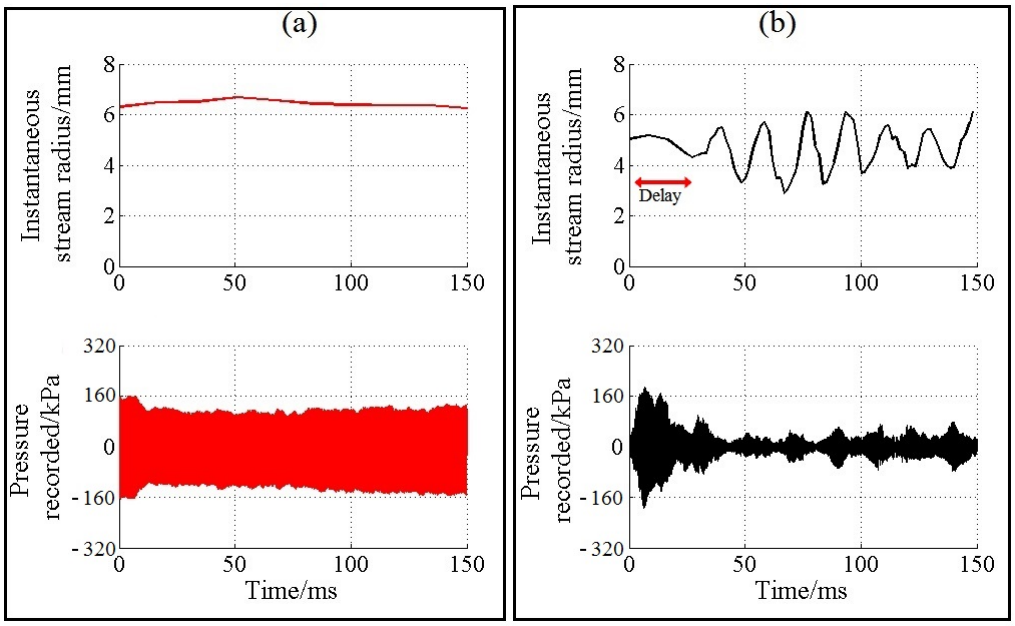

Figure 7.9: The result from simultaneous optical and acoustical recording of the stream. Part (a) presents the results when the distance between the nozzle tip and the prismatic block is 5 mm (red traces) and (b) when the distance is 25 mm (black traces).

target surface, it expands slightly in the radial direction like a liquid sheet. The acoustic pressure measured in the stream begins at a peak-to-peak value of 430 kPa (between 0 to 10 ms) but drops to 330 kPa over a span of the next 100 ms. The absence of the outgasser can be observed as the small undulations on the pressure-time trace.

When the distance was increased to 25 mm (which is larger than λ), the radial surface waves were completely formed (with measured local stream radius, a_1 at 5 mm) and the influence of instability waves on the stream can be observed in both η-time and pressure-time plots. A case for the temporal delay in the detection of radial surface waves was shown in Figure 7.9b, η-time plot. In the delay period marked, the pressure recorded in the stream was 400 kPa peak-to-peak, similar to the values in the pressure-time trace of Figure 7.9a, but as soon as the radial surface waves were initiated, the recorded pressure value reduces. The acoustic pressure rises and falls in unison with the radial surface undulations (with minor temporal delay). This is in regard to the occurrence of the radial maximum at the nozzle tip (for the surface waves) when a radial minimum occurs at the target location (near the prismatic block) implying that the temporal location of peaks for the η-time and pressure-time traces lag slightly.

The acoustic and photographic observations of stream instability reported in this section were activated by driving the UT_1 in the non-linear regime, with a pulse length generally in the order of a couple of seconds. The next section discusses the influence of using different pulse lengths (t_2) and different PRPs (t_1) on the capillary wave formation.

7.4 Influence of pulse length and PRP

This section reports the results on the pulsing the transducer, the patterns similar to those presented in Figure 3.4, and to determine the relationship between pulsing and the formation of instabilities. For this purpose, a signal from an external trigger box was used to simultaneously start both the high-speed camera and the function generator. The pulse repetition frequency (PRF or $t_1{}^{-1}$)was increased in steps from 1 Hz to 5 Hz and the rising edge of the pulse sent out was used to drive transducer UT_1 at 135 kHz for different pulse lengths at either 10 ms, 20 ms, or 30 ms. The value of η at a distance of 20 mm from the nozzle tip (i.e., away from the breakup zone) was recorded and measured. The value of V_{pa} was held at 0.7 V_{rms}, liquid flow rate at 1.9 litre.min^{-1}, and liquid temperature 22.1^{o}C. The frame rate for video recording was 1200 fps, with 1600 μs exposure per frame, to achieve good contrast.

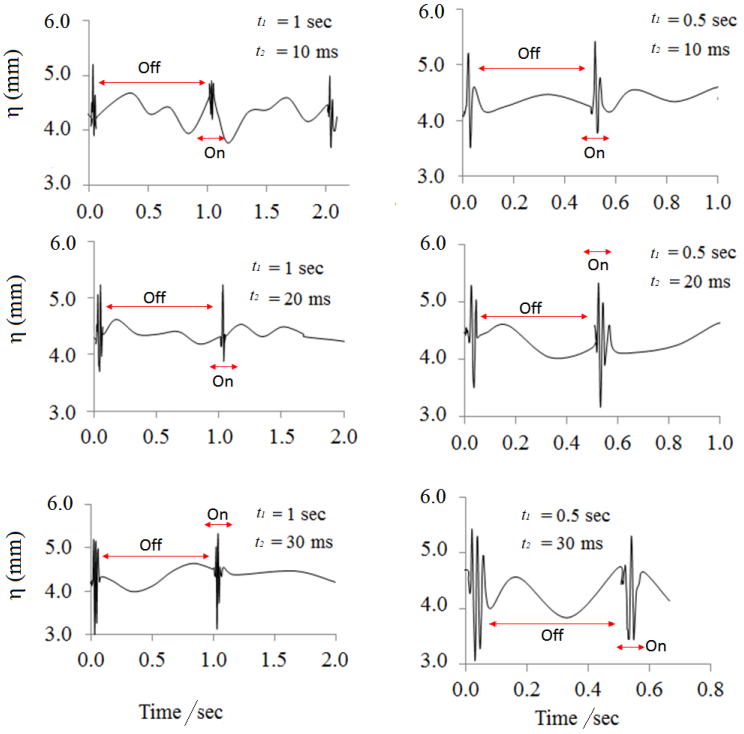

Figure 7.10: The variation of η with time, at different duty cycle on the transducer UT_1. The regions ON and OFF, as marked by the red lines, refer to the ON and OFF times of ultrasonic signal in the duty cycles.

The left-hand column of Figure 7.10 presents results (η-time plot) for t_1 of 1 s and the right-hand column presents results when using t_1 of 0.5 s. The mean radius of the undisturbed stream (a_1), measured at 20 mm from the nozzle tip, was around 4.4 mm. The value of η and the number of capillary waves formed on the stream per pulse was observed to be dependent on the pulse lengths used. Smaller values of t_2 were observed to initiate smaller amplitude radial disturbances (in η) and less number of capillary

waves per pulse. Whereas larger values of t_2 generated larger radial amplitudes and a greater number of radial waves per pulse. It should be noted that the reference time '0 s" in each of the subplots was chosen at one of the rising edges of the trigger signal. For pulse length values less than 10 ms no surface waves were observed to form on the stream.

The temporal delay in formation of the surface waves (from Figure 7.10) was observed to be smaller than the temporal delay values presented in Figures 7.4 and 7.5. It was observed that in a scenario where UT_1 was run continuously (pulse length t_2>2 s) and when the transducer UT_1 was triggered after a considerable resting time (in the order of 20-30 min), temporal delays between 75 to 150 ms were observed. However, if the transducer was working in pulsed mode and was in operation for few pulses, delay times of around 2 ms were observed. It was also found that there was a wide distribution in the delay times (for radial surface wave formation), starting from 2 ms and up to 150 ms depending on the working conditions.

Since pulsing the transducer did not hinder the formation of capillary waves (unless when the pulse length was below 10 ms), the eventual aim of controlling the formation of surface waves, so that ultrasonic energy could propagate up to or beyond 50 to 60 mm from the nozzle tip could not be achieved. Modulated input signal supplied to ultrasonic transducer was used in the literature to control capillary wave formation [201] on liquid streams. Using similar working principles to those presented in references [134, 201], the results of supplying a modulated input signal to UT_1 on the instability formation of the stream are reported below.

7.4.1 Influence of input signal modulation

The input signal to the transducer could be modulated to study the influence of ultrasound on capillary wave formation [134]. Although a choice of either frequency modulation or amplitude modulation was available, it was observed that the pressure generated in the stream was large enough to initiate capillary waves only when the excitation frequency f to UT_1 was closer to the fundamental frequency of the transducer. The influence of amplitude modulation on the signal supplied to the transducer (at 135 kHz) is interesting to observe, because of the presence of a transition regime in the pressure output. For this purpose, a low frequency signal at PRF value of either 1 Hz or 2 Hz was used. This low frequency (envelope) signal was used to drive UT_1 with V_{pa} varying from 0 V_{rms} to 0.8 V_{rms} within the cycle time t_1. Simultaneous photographic and acoustic observations of the stream (at 20 mm from the nozzle tip to the outer surface of the prismatic block) were recorded and are presented in Figure 7.11.

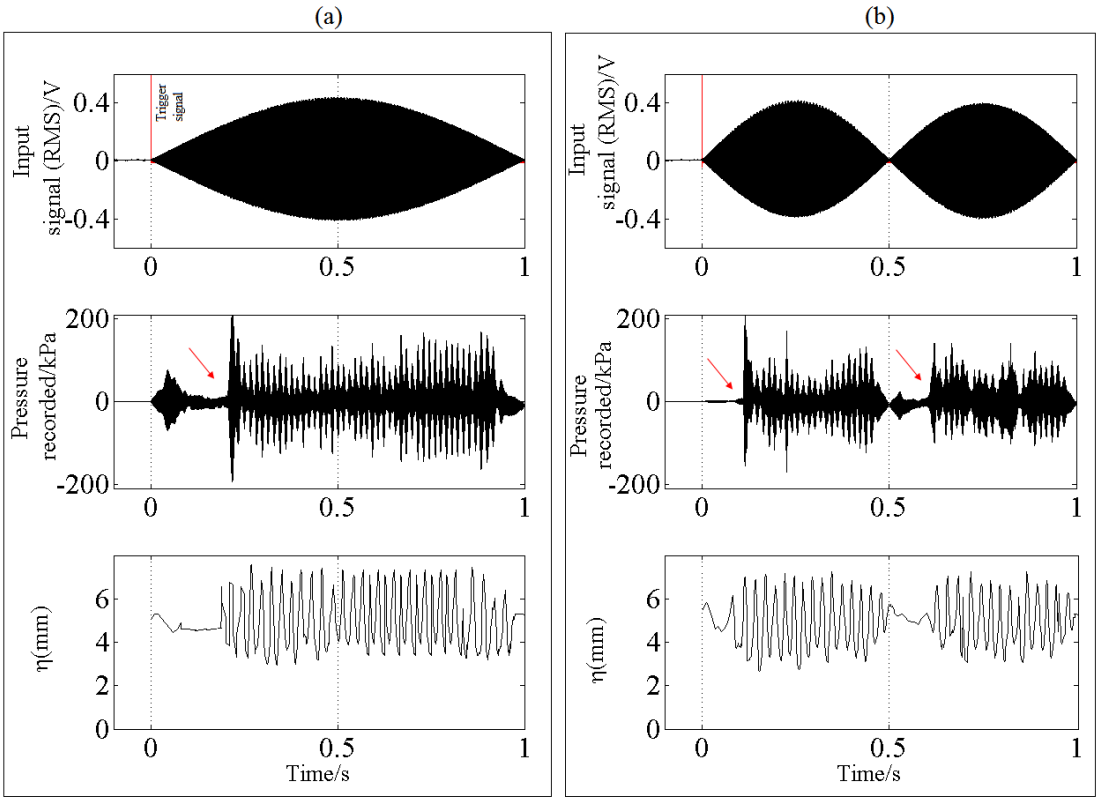

Figure 7.11: The effect of an amplitude modulated ultrasound signal supplied to UT_1 on the stream displacement and pressure output. Part (a) uses a modulation frequency of 1 Hz and part (b) at 2 Hz. Plots from top to bottom present: V_{pa} vs time plot, pressure recorded in the stream, and radial displacement of the stream. The red arrows point the transition between the linear to non-linear regimes.

The transition from linear to non-linear regime (in the absence of the outgasser) was earlier shown to be sudden (Figure 5.5) and in this chapter was shown to be related to the initiation of capillary disturbances on the stream (Figure 7.7). In Figure 7.11 the transition regime and its relationship with capillary wave initiation on the stream can be clearly observed (comparing η-time plot and the red arrows on pressure-time plots). No surface waves were observed when the measured pressure recorded in the stream was below 100 kPa (peak-to-peak), which occurs both in the ramp-up and ramp-down phases of the modulated signal. The trace of the pressure-time plot in the linear regime (prior to the red arrow mark) is similar to the trace of the pressure-time plot shown in Figure 7.9b. Once this regime is crossed, the series of spikes in the pressure-time plot can be associated with the formation of radial surface waves on the stream and the influence of necking zone on acoustic propagation (η-time plot).

No changes were observed in the peak-to-peak value of η at either of the modulation frequencies employed. It was observed that the instability formation on the stream for PRF values more than 10 Hz was no different to driving the transducer (UT_1) using a continuous ultrasound signal. This implied that there was no strong influence of PRF

on either the temporal delay in the formation of radial surface waves or on the measured radial amplitude η. Hence this study was not extended to modulation frequencies of 100-200 Hz (as used by Lonzaga (2007) [134] in his thesis).

The next important step is to evaluate the influence of different system variables on the formation of capillary instabilities. It is important to observe the influence of different flow rates, different surface tension value of the liquid (by the addition of SDS), different liquid temperatures, and liquid viscosities (by the addition of Glycerol) on the performance of the device. These can be evaluated by using acoustical and optical observations.

7.5 Influence of system variables

7.5.1 Variation of flow rate

In literature, the stability of liquid streams was also studied in relation to their flow velocities [125]. The liquid flow rate is generally related to the capillary instability (wavelength) by the Weber Number ($We = \rho u_0^2 a/\tau$), a non-dimensional number defined as the ratio of inertia forces of the liquid to the surface tension forces. For the UAS device, since the nozzle opening is fixed at 10 mm, changes in the flow rate would simulate different Weber numbers[6]. However, in the present study, it is convenient to quantify the variations in flow rate by evaluating the Reynolds number ($Re = \rho V(2a)/\mu$) of the stream. The hydrodynamic stability of liquid streams at different values of Re was studied extensively [22], with the conclusion that turbulent flows are known to be more unstable compared to laminar flows. The UAS device during normal operation operates at a flow rate of around 2.0 litre.min^{-1}, which corresponds to a Re of approximately 4150 for 10 mm (mean) diameter stream, implying the liquid is in the transition between laminar and turbulent flows.

In the present section, observations from the high-speed camera were used to track the evolution of capillary instabilities at different flow rates. Snapshots were taken at different flow rates varying from 0.5 to 3.2 litre.min^{-1} and are shown as collages in Figure 7.12. The flow rates shown in subplots “a”, “b”, “c” and “d” in Figure 7.12 correspond to Re values of 1061, 2500, 5305 and 6790 respectively. The white scale bar in each sub-figure is 10 mm long.

At Re number of approximately 1000, the equilibrium diameter (at 20 mm from the tip) of the steam was measured at 2.87 mm implying that the gravitational thinning

[6] At a fixed flow rate, changing the surface tension of the liquid also changes the Weber number.

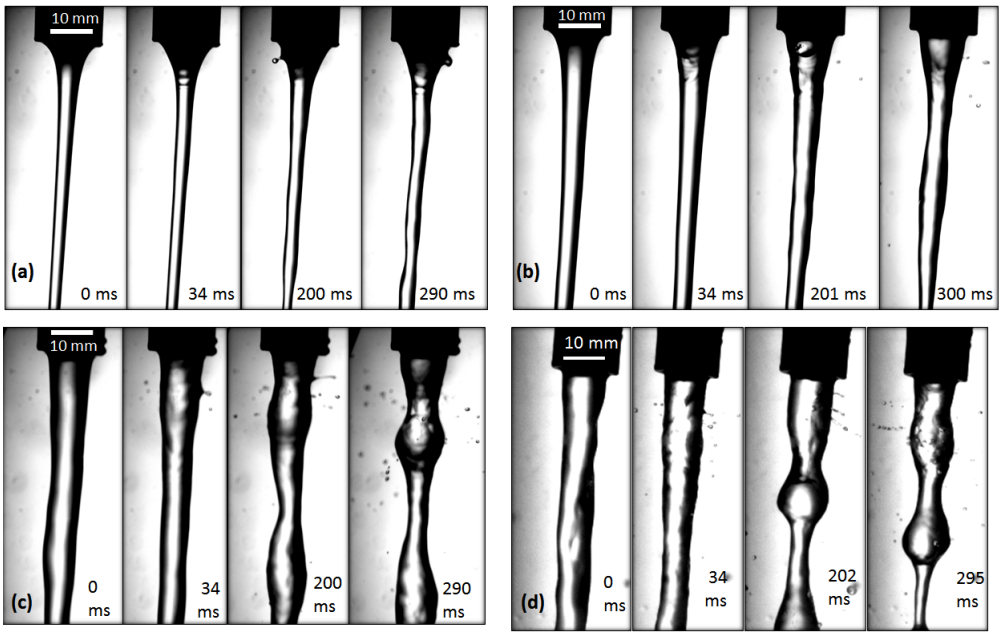

Figure 7.12: A sequence of photographs taken from high-speed videos recorded at 1200 fps using different flow rates - "a": 0.5 litre.min^{-1}, "b": 1.2 litre.min^{-1}, "c": 2.5 litre.min^{-1} and "d": 3.2 litre.min^{-1}. The timestamps are at the bottom right.

is dominant. Subsequently, the ultrasonic energy is restricted to the tip of the nozzle. This can be observed in Figure 7.12a, where the microjetting is concentrated at the tip (seen at 200 ms), and no radial surface waves could be formed along the length of the stream. The liquid stream, however, is influenced by the azimuthal instability waves that travel downstream (see snapshots at 34 ms and 290 ms). In general, radial surface waves were observed to form on the stream only at flow rates beyond 1.8 litre.min^{-1}.

The number of microjetting events recorded per second was observed to increase with the flow rate. The breakup length L and capillary wavelength were also observed to be influenced by changes in flow rate. The value of λ increases with flow rate and stabilises to approximately 14 mm at flow rates beyond 2.0 litre.min^{-1}. As the flow rate increases beyond 2.5 litre.min^{-1}, the increase in turbulence in the liquid stream can be observed in plots "c" and "d" at snapshots shown at 0 ms. At 3.2 litre.min^{-1} it was observed that swirling instabilities on stream along the length sometimes influenced the formation of radial capillary instabilities. Subsequently, the temporal evolution of instability recorded at flow rates beyond 3.2 litre.min^{-1} (maximum value of flow rate used was 3.5 litre.min^{-1}) was found to be less reproducible with time. The threshold voltage V_{pa} required to generate instabilities on the liquid stream was found to be independent of flow rate.

7.5.2 Influence of liquid surface tension

In studies associated with Rayleigh-Plateau instability formation on liquid streams, reducing the surface tension of liquid reduces the growth rate of instabilities [22]. Thus surface tension acts as both the restoring and driving force for the formation and growth of capillary waves [125]. The influence of surface tension on capillary growth rate was earlier demonstrated in Figure 2.5. In this thesis, reduction of surface tension was generally achieved by using SDS as an additive and its influence on the threshold point was presented in Figure 7.13.

In the absence of the outgasser, the pressure output from the UAS device was earlier shown to be influenced by the unwanted microbubble population. Surfactant reduces the surface tension value of the liquid (see Table 3.1) and subsequently increases the probability for entraining microbubbles at various locations in the liquid loop of the UAS device. This influences the location of the transition point as seen in Figure 7.13.

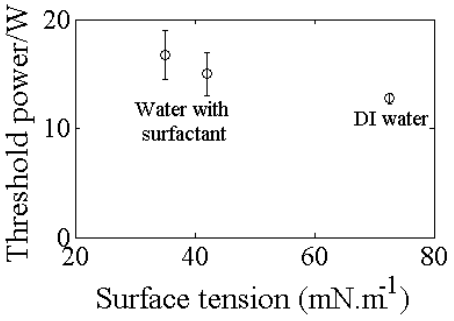

Figure 7.13: Change in the location of the transition point in the pressure output plot at different surface tension values for the working liquid.

Using the high-speed camera, it was observed that the capillary wavelength (λ), and the breakup length (L) of capillary waves triggered were unaffected by the presence of surfactant in the liquid. The number of microjetting events (recorded per second) however was reduced in the presence of the surfactant, when compared to those measured in its absence. This can be understood by revisiting Figure 7.6. If the radii of the microbubbles flushed out of the conical chamber are small (i.e., no large bubbles are formed in the liquid, due to the presence of surfactant), then the possibility for the formation of large clusters of big bubbles is also small. This implies that clusters with tiny microbubbles could be restricted to the centre of the stream and subsequently very few microjetting events could be observed per second.

As surfactant concentration increases, the maximum pressure recorded in the stream (in the absence of the outgasser) at V_{pa} of 0.8 V_{rms} was observed to drop by 10%. This drop in acoustic pressure in the non-linear regime could be attributed to the

additional absorption provided by microbubbles probably seeded either at the pump or in the reservoir (due to the absence of the outgasser).

The next section presents the influence of liquid viscosity on the performance of the UAS device and the threshold power for initiating capillary instabilities.

7.5.3 Influence of Viscosity

The viscosity of the liquid can be changed in two ways: (i) by changing the liquid temperature, and (ii) by using an additive to the working liquid such as Glycerol. In this section, results concerning the performance of the UAS device using these two techniques are presented.

7.5.3.1 Influence of fluid temperature

As the temperature of the water increases, the viscosity of the water predominantly reduces [206] (see Table 3.1). The threshold V_{pa} for the initiation of capillary instabilities on the stream, as temperature (of DI water) changes, was observed using the high-speed camera. It was observed that as the liquid temperature increases slowly from room temperature (18^{o}C during the experiment) to 60^{o}C, the threshold for generating capillary waves on the surface of the stream was observed to reduce (Figure 7.14a), also see Figure D.1. The measured value of viscosity of water reduces from 1.02 mm^2/s to approximately 0.45 mm^2/s, as liquid temperature increases from 18^{o}C to 60^{o}C (Table 3.1). Liquid temperature could not be increased further due to the working limit imposed on the tubing used for the experimental kit, along with the difficulty in measuring the viscosity at elevated temperatures.

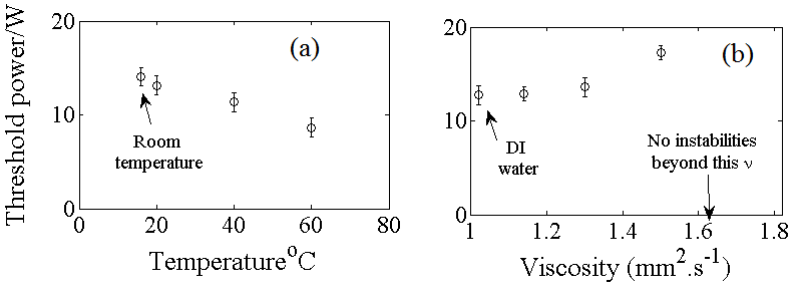

Figure 7.14: Change in the location of transition point at different working parameters. Influence of (a) increase in liquid temperature by using an immersion heating coil and (b) increase in viscosity by addition of Glycerol.

The pressure recorded in the non-linear regime at elevated liquid temperatures was observed to be 10% smaller than the pressure amplitude recorded when using the liquid

at room temperature (see Figure 7.15). The shift in the location of transition point as liquid temperature increases can also be noted in Figure 7.15. Thus the UAS device could be successfully used with liquid at elevated temperatures for cleaning operations without any appreciable drop in performance. However, using the existing experimental setup it was found that maintaining liquid temperature at values higher than 30^{o}C for longer periods of time was difficult

7.5.3.2 Addition of Glycerol

Increasing the viscosity of water by reducing its temperature has limitations. Glycerol was used by various authors [127, 130] experimentally to study the capillary stability of liquid streams. A higher value for the liquid viscosity implies a slower growth rate of capillary waves, with thin liquid streams made out of honey demonstrating very long narrow threads before breaking up [125]. The measured values of viscosity and surface tension of the working liquid when using different volumes of Glycerol (added to DI water) are presented in Table 7.2. The error values provided in parentheses refer to standard error for those measurements.

Table 7.2: Measurements of viscosity and surface tension of DI water containing different quantities of Glycerol by volume.

S.No	Volume of water (ml)	Volume of Glycerol (ml)	% Glycerol in water by volume	Viscosity mm^2/s (cSt)	Surface tension mN/m
1	1000	0	0.00	1.02 (±0.04)	76.2 (±0.3)
2	1000	50	4.76	1.14 (±0.08)	71.5 (±0.1)
3	1000	100	9.09	1.3 (±0.07)	69.1 (±0.2)
4	1000	150	13.04	1.47 (±0.05)	65.3 (±0.1)
5	1000	200	16.67	1.67 (±0.09)	61.3 (±0.3)

It was observed (as expected) that, as the viscosity of the working liquid increases, the threshold for initiating capillary instabilities (Figure 7.14b) increases gradually. However, at and beyond 16.67% Glycerol in liquid (by volume i.e., measured viscosity at or beyond 1.66 mm^2.s^{-1}) no surface waves were detected in the liquid stream. This was observed to be caused by the cessation of cavitation (and associated phenomena) in the liquid at ν larger than 1.66 mm^2.s^{-1}. This absence of cavitation in the liquid chamber was confirmed by the absence of audible cavitation noise emission from the UAS device. In the literature, under similar operating conditions, viscous liquids (for example, castor oil) were shown not to undergo inertial cavitation [34] when compared to less viscous liquids (water) which would undergo inertial cavitation.

From Figure 7.15b it can be observed that as liquid viscosity increases, the pressure output from the device slowly reduces. At measured viscosity beyond 1.66 mm^2.s^{-1} it is no longer possible to initiate surface instabilities on the stream as pressure recorded in the non-linear regime is smaller than the threshold pressure required (approximately

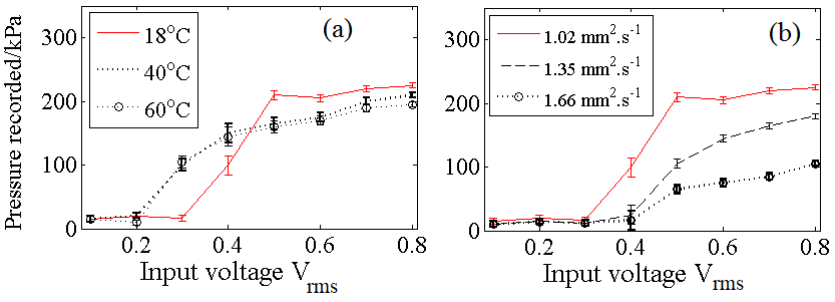

Figure 7.15: Variation of pressure amplitude measured in the stream at different working conditions. The solid red line (without marker) in each subplot presents the pressure recorded when using: 2.0 litre.min^{-1}, no surfactant, no glycerol and at a liquid temperature 18^{o}C. The individual subplots present (a) the influence of liquid temperature and (b) the influence of viscosity by addition of glycerol.

100 kPa). Thus an increase in viscosity is influencing the mechanism that drives the surface wave formation (cavitation of liquid inside UAS device). It is interesting to note the contrast with Rayleigh-Plateau type instability, where an increase in viscosity of the working liquid reduces the growth rate of capillary waves.

From the previous sections it could be concluded that, the capillary instabilities initiated on the stream activated by UT$_1$, could not be controlled either by varying either the input signal to the transducer (except when pulse length values $t_2 < 10$ *ms*), or by changing the system variables, or even by using different additives (except when increasing the viscosity of the liquid beyond 1.66 mm^2.s^{-1}). The next section presents an external method to control the radial surface waves formed on the stream in an attempt to increase its intact length.

7.6 External control measure

Since the objective of this chapter was to analyse the instability formation and then to develop techniques that either counteract or reduce the capillary waves, external control methods had to be employed. The external control method discussed here uses a bunch of hydrophobic spray coated paint brush bristles placed at the exit of the nozzle, with the aim of making the bristles work against the radial surface waves.

A small bunch of lightweight paint brush bristles[7] were moulded into a hollow cylindrical mould. The outer (OD) and inner diameters (ID) of the hollow cylinder were matched with the OD and ID of the nozzle and the length of the hollow cylinder (along the Z axis) was 5 mm. The bristles were slightly angled towards the axis of

[7]Mechanically stronger bristles cut from a PTFE wire with hydrophobic coating were also tested in place of paint brush bristles. However, the PTFE bristles were found to be too rigid and did not respond in unison with the radial instability waves.

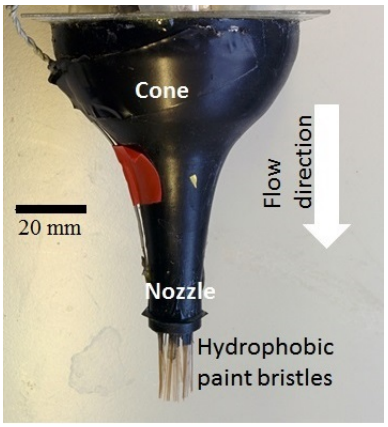

Figure 7.16: Hydrophobic spray paint coated bristles attached to the exit of the nozzle to counteract radial capillary wave formation on the stream.

symmetry of the stream and were coated with a commercially available hydrophobic spray (Nikwax TX-direct spray, with measured water contact angle at 125^o) to repel the working liquid. This assembly was glued onto the nozzle of the device carefully to match its axis with that of the UAS device. The use of hydrophobic coating on the bristles and their inclination meant that when the surface of liquid radially bulges out, the bristles work against the instability to counteract it. Figure 7.16 shows a snapshot of hydrophobic bristles, 20 mm in length, and the hollow cylindrical mould attached to the nozzle tip.

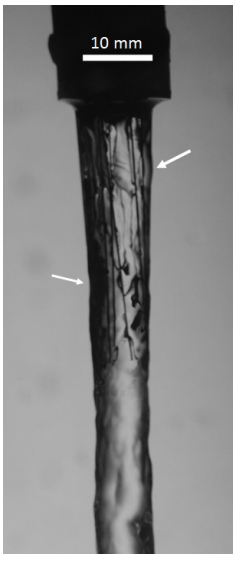

Figure 7.17: A snapshot taken from a high-speed video demonstrating the influence of hydrophobic spray coated bristles counteracting radial surface waves. Microjetting is not visible in this snapshot because of the presence of surfactant in the liquid.

Different lengths of these bristles varying from 20 mm (Figure 7.16) to 40 mm (see Figure 7.17) were used to study their influence on reducing the radial surface waves and for achieving sufficient acoustic pressure (measured by placing the prismatic block at

the end of the bristles). The optimal length of bristles satisfying these constraints was found to be between 25 to 30 mm. Although the 40 mm long bristles were as effective at reducing the surface waves as 25 mm long bristles, their longer length obstructed the flow of liquid (due to their inclination) and affected subsequent pressure measurement. Shorter bristle lengths (less than λ, 14.2 mm) were found to incapable of removing the radial surface oscillations. A bristle length of 25 mm was chosen as a compromise between achieving effective control over radial surface waves and to have recorded pressure in the non-linear regime at approximately 200 kPa (zero-to-peak).

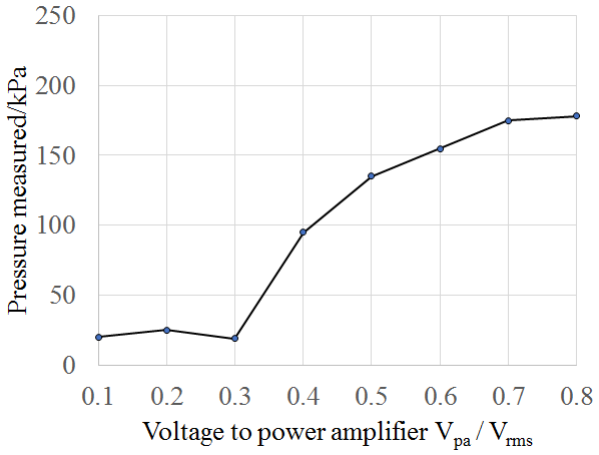

Figure 7.18: Variation in the zero-to-peak value of pressure in the stream with V_{pa}, measured at the end of the 30 mm long hydrophobic spray coated bristles.

Figure 7.18 presents the pressure measured in the stream when using 30 mm long hydrophobic coated bristles, with the prismatic block placed at the edge of the bristles. The radial surface waves were observed to be effectively counteracted thus increasing the intact length of the stream, although the azimuthal surface waves (see Figure 7.17) and microjetting action could not be controlled.

7.7 Conclusions

This chapter studied the influence of large ultrasonic pressure generated from the UAS device (in the order of 200 kPa zero-to-peak) on the equilibrium stream surface. The main focus was towards understanding stream stability and its influence on cleaning distance. The stream stability in the non-linear regime was affected by the formation of capillary instabilities. The temporal evolution of the instability formation was recorded and quantified using observations from the high-speed camera. Simultaneous acoustic recordings showed the transition point was linked to the initiation of capillary instabilities (see Figures 7.7, 7.11 and 5.5).

From photographic observations, it could be reported that the instabilities do not seem to confirm with the classical form of Rayleigh-Plateau instability (see Figure 7.5). The instabilities observed on the stream were characterised by small amplitude azimuthal waves, large amplitude radial capillary waves (of measured wavelength λ) and distinctive microjetting action (see Figure 7.2). The formation of radial capillary waves meant that the cylindrical stream broke up into droplets after flowing intact for some distance. This radial capillary wave formation was observed to restrict the propagation of ultrasound (see Figures 7.9) and subsequently the breakup length of the stream varied between 50 to 75 mm.

The azimuthal surface waves and the distinct microjetting action were studied using photographic observations and the possible series of events that are thought to be causing the microjetting events were detailed in Section 7.2.1. The influence of driving the ultrasonic transducer UT_1 in the pulsed mode and the influence of amplitude modulation was reported. It was observed that when the transducer was pulsing, the temporal delay between triggering the transducer and formation of radial surface waves on the stream is very small (in the order of 2 ms, see Figure 7.10). The influence of target distance from the nozzle tip on the radial surface wave formations (see Figure 7.8) was studied carefully.

The influence of flow rate, liquid viscosity, and surface tension on the non-linear regime and the capillary instabilities was reported. It was found that, at flow rates below 1.8 litre.min^{-1} the stream diameter is too narrow for the propagation of ultrasonic energy. However, the instabilities on the stream could be triggered if V_{pa} was high enough (Figure 7.12a). The use of surfactant does not influence/hinder the formation of surface waves on the stream surface, but it does influence the transition region and reduces microjetting action. With an increase in liquid viscosity it was observed that the acoustic pressure generated in the stream reduces and this, in turn, influences the formation of surface waves on the stream.

In order to control the radial oscillations in the stream, a series of externally mounted hydrophobic spray coated paint brush bristles were found to be effective. These bristles were glued onto the outside of the nozzle and were slightly angled towards the axis of the stream. Bristles of length between 25 to 30 mm were observed to provide a balance between radial surface wave reduction, in generating sufficient acoustic pressure, and are recommended.

Chapter 8

Conclusions and future work

The studies reported in this thesis employ the Starstream device or the UAS device as a primary focus for research and discussion. The broad and overarching purpose that has driven the work reported in this thesis was to understand and improve the performance of the device. When the device was inherited at the start of this project, it demonstrated effective cleaning [11, 12] of various contaminant mimics placed on different target substrates. Nevertheless, there was scope for carrying out detailed investigations based on the following observations:

- the pressure output was highly non-linear,
- the presence of a large quantity of unwanted microbubble population in the working liquid adversely affected the pressure output, and
- the effective cleaning distance (as measured from the nozzle tip) was influenced by capillary instabilities formed on the stream surface.

This thesis takes steps to understand the trends in the acoustic pressure generated by the UAS device as measured in the stream. The relationship between the pressure generated and the inherent characteristics of the piezoceramic based tonpilz type transducer are reported. The non-linear shape of the pressure-output vs voltage input to the power amplifier or V_{pa} (reported in Figure 5.5) with its characteristic regimes (marked in Figure 5.9) were revisited throughout the thesis.

8.1 Chapterwise summary

Based on the regimes marked in Figure 5.9, the chapters in this thesis were divided into two major strands of work. One strand focuses on the non-linear response of the ultrasonic transducer and its relationship with the pressure output under different

operating conditions. A strong focus on the influence of the working variables and power input to the transducer on the performance of the device in the non-linear regime was reported. The second strand of work reports the investigations on the linear regime and the response of the device to bubble-free and bubbly liquids. The experimental set up (shown in Figure 3.1) was employed, its individual components were tested, and were successfully utilized for carrying out different experimental measurements in this thesis.

The next few paragraphs detail the conclusions of the individual chapters.

Chapter 2 provided a literature review on various physical phenomena that are generally encountered when employing ultrasonic energy in liquids. The primary focus was on discussing acoustic cavitation, different cavitation regimes, and relevant phenomena such as cavitation harmonics, sonoluminescence, and radiation forces on microbubbles. This chapter also included a brief review on the propagation in acoustical waveguides. An introduction to capillary instabilities generated on liquid streams (also known as classical Rayleigh-Plateau instability) was presented, which served as a precursor to Chapter 7.

It was shown in Chapter 3, that the individual components of the new experimental setup developed, especially the ultrasonic outgasser, were very successful in achieving their objectives. Optical observations of liquid leaving the outgasser have shown that it is completely free of unwanted microbubbles (see Figure 3.16), with Figure 3.10 demonstrating that the outgasser is very quick (in the order of few seconds, when compared with the settlement tube) to contain the unwanted microbubble population in its column. Figure 3.9 demonstrated that, by employing the outgasser in the experimental setup, the acoustic pressure generated by the UAS device could be improved. Chapter 3 also provided introductions to a four-port inlet into the conical chamber, the bubble generation chamber, G, and an established technique to measure pressure in a stream of liquid using a hydrophone.

Once unwanted microbubbles (generally generated at the pump or in the reservoir) were restrained in the cylindrical column of the ultrasonic outgasser, the liquid entering the bubble generation chamber, G, is bubble-free. This liquid could be allowed to flow into the conical chamber of the UAS device. Alternatively, microbubbles of known distribution could be added to it, to modify its acoustical properties. The generation chamber in the liquid path was designed to quickly electrolyse microbubbles so that the performance of the UAS device can be investigated when using bubbly liquid.

The size and distribution of microbubbles generated by electrolysis in the chamber G were optically measured, quantified, and reported in Chapter 4. It was found that the BSD generated at operating conditions regularly used in the UAS device has a maximum

between 7 to 10 μm. The influence of different working variables on microbubbles generated was studied and reported. These variables are the surfactant concentration (Figure 4.10), electrode orientation, flow rate (Figure 4.12), electrode current (Figure 4.13), and trigger pulse length. Using these results, the right combination of system parameters that would aid in a continuous generation and supply of microbubbles (i.e., using a DC control pulse) into the conical chamber was chosen.

Chapter 5 presented the experimental investigations on the response of the UAS device to bubble-free liquid at the resonance frequency of the transducer (135 kHz). In the process, the influence of the prismatic block that was employed for pressure measurements was quantified (Figure 5.2) and the measured variation of V_t with increasing values of V_{pa} was reported in Figure 5.4. The non-linear response of the transducer (Figure 5.8) and its relationship to the linear, transition, and non-linear regimes of the pressure output plot was discussed (Section 5.2.4). The influence of different PRP values employed during experiments was reported and the influence of working distance between the nozzle tip and the hydrophone on the performance of the UAS device was quantified. The improvement in the pressure output when using the outgasser in the liquid loop was outlined (Section 5.5). The results reported in in this chapter helped in determining the input conditions required (for example, the amplitude of V_t) to run the transducer at the frequencies of interest (120 to 145 kHz) in the linear regime.

Chapter 6 presented the investigations on the response of the UAS device to bubbly liquid at resonance and off-resonance frequencies. The transducer was primarily driven in its linear regime to avoid non-linear effects. The influence of bubbly liquid was experimentally evaluated in a sequential manner using measurements of the electrical input impedance of the transducer under different conditions (air loaded, water loaded, UAS device with bubble-free liquid, and UAS device with bubbly liquid; see Figures 6.6 and 6.7). These experimental measurements helped in the development of a lumped parameter model to estimate the linear response of the transducer. The lumped parameter model was upgraded (see Figure 6.14) to reflect the influence of the UAS device and the working liquids used in it. Discussions based on the variation of radiation impedance and the influence of power dissipated in the transducer at off-resonance frequencies helped in understanding the pressure output of the UAS device to bubbly liquids in the linear regime.

Chapter 7 dealt with the capillary instabilities generated on the stream (Figure 7.5) in the non-linear regime. The measured pressure output in this regime was found to be influenced by changes to the working variables, such as flow rate (which influences acoustic propagation), surfactant concentration, and liquid viscosity (Figure 7.15b). Detailed high-speed photographic and acoustic observations of the instability phenomenon were

presented. The temporal evolution of the instability waves suggested that the transition point and the formation of capillary instabilities on the stream were strongly related (Figures 7.7 and 7.11). The capillary instabilities formed were observed to be characterised by large amplitude radial waves, small amplitude azimuthal waves, and distinctive microjetting action (Figure 7.5). Using simultaneous optical and acoustic observations (see Figure 7.9) it was summarised that the instability formation observed on the stream exiting the nozzle does not confer to Rayleigh-Plateau instability principles. The radial instability wave formation could be controlled by employing hydrophobic spray coated paint brush bristles, attached externally at the nozzle tip, with an optimum length of 25 to 30 mm (Figure 7.16).

8.2 Suggested modifications

From the results reported in this thesis, the following changes were suggested as an addition to the UAS device (and to the experimental kit employing the device) to improve its performance:

1. to achieve consistency in pressure output over a longer period of time, use the four-port liquid inlet shown in Figure 3.6 and maintain the working liquid temperature around 28.5^{o}C using an immersion heater,
2. employ the ultrasonic outgasser in the liquid loop to remove the unwanted microbubble population and to improve the performance of the device,
3. employ UT_1 transducer in pulsed mode with PRP of 100 ms or above (depending on the working requirements and cleaning time), with a minimum duty cycle of 10%,
4. employ hydrophobic spray coated paint brush bristles, on the nozzle tip to reduce radial capillary wave formation, with lengths between 25 and 30 mm.

8.3 Scope for future work

The Starstream device employs technologies that are currently undergoing research and development, and its effectiveness is being evaluated for commercial potential. Using this device, applications in medical ultrasonics are now being pursued towards bio-film removal from different biological targets such as teeth, bone structure, etc. Further development of the device both in applied medical ultrasonics and in industrial ultrasonic cleaning could concentrate upon:

- possible cleaning of target substrates in the linear regime, by employing microbubbles and the ultrasonic outgasser to enhance the influence of low amplitude pressure,
- alternate design shapes for the chamber or alternate materials for manufacturing the chamber (for example using an outer metal shell with an inner pressure release boundary),
- investigation into other bubble generation techniques which do not place the electrodes in the stream path - such as by using custom made ring type electrodes or small strip shaped electrodes,
- research towards salt-free electrolysis to reduce the additives required for microbubble generation, which has potential use in tap water,
- possible design changes aiding in multiplicity and portability of the device for large scale commercial applications.

Focusing research in the suggested directions could make the Starstream device commercially valuable, by improving its effectiveness over different target specimen and contaminant combinations. This could make the device better suited to medical, nuclear, and chemical industries.

Appendix A

. Additional figures - Outgasser effectiveness

Figure A.1 demonstrates the effectiveness of the outgasser working on bubbles generated by injecting 2.5 ml air into the pump. This figure shows similar trends to Figure 3.11 presented in Section 3.3.1. Working parameters were: PRP at 200ms, signal to UT_1 at 105 kHz, with 100 mV_{pp} of V_{pa}, pulse length at 20 ms, flow rate 1.9 litre.min^{-1}, and temperature 28.4^{o}C.

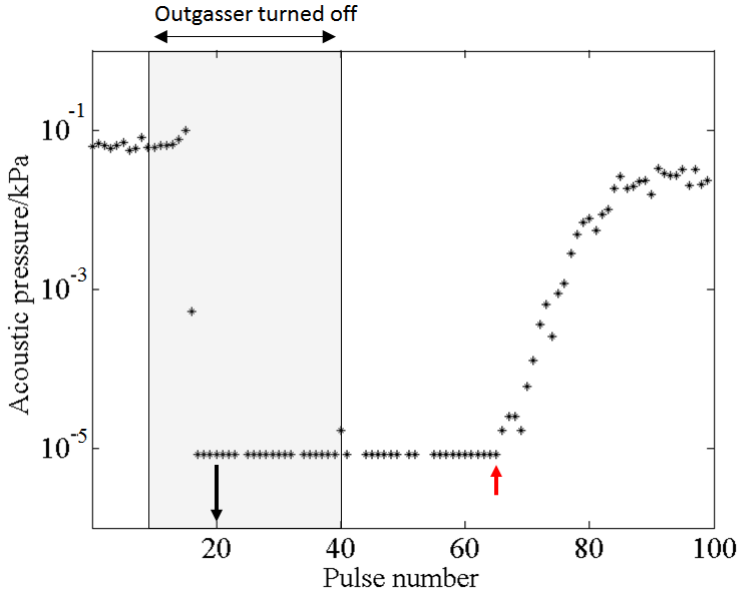

Figure A.1: Acoustic quantification for the effectiveness of the outgasser. The outgasser was turned on prior to the first pulse (1), turned off between pulses 10 and 40 and turned on again. Air injected at the start of 20^{th} pulse (indicated by black arrow) and pressure starts recovering from pulse number 64 (marked by red arrow).

Figure A.2 presents the observed BSD at different time bins corresponding to Figures 3.18 and A.4 respectively. The letters represent different timestamps as detailed in the captions. These figures are similar to Figure 3.17 (ii).

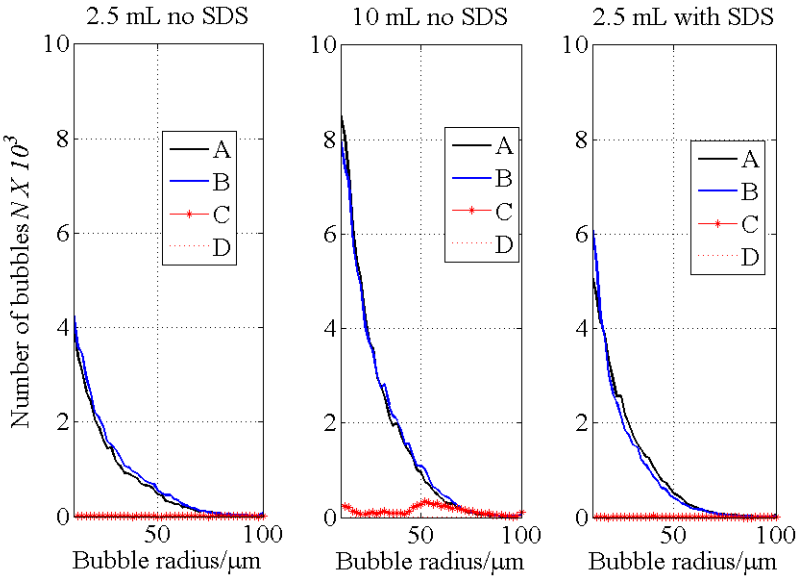

Figure A.2: BSD recorded in the observation chamber when using different working liquids with different volumes of air injected into the pump. The letters A to D represent the distribution observed at -0.43 to 0 s, 1 to 1.5 s, 3 to 3.5 s, and 5 to 5.5 s.

Figure A.3 presents the change in NV recorded in the observation chamber, used for removing microbubbles generated by injecting 2.5 ml (on left) and 10 ml (on right) air into the pump, when using surfactant-free liquid. These plots are similar to the plot shown in Figure 3.17(iii). The legend "1" represents time window of -0.43 s to 0 s, "2" represents time window of 1 s to 1.5 s, "3" represents time window of 3 s to 3.5 s and "4" represents time window of 5 s to 5.5 s

Figure A.4 presents the optical observation of N recorded in the observation chamber, working on 10 ml air injected into the pump, which is similar to the result presented in Figure 3.18. Each point on the curves represents N observed in a bin 500 ms wide, except for the first point which covers -430 ms to 0 ms. The start of the outgasser is marked by a black arrow.

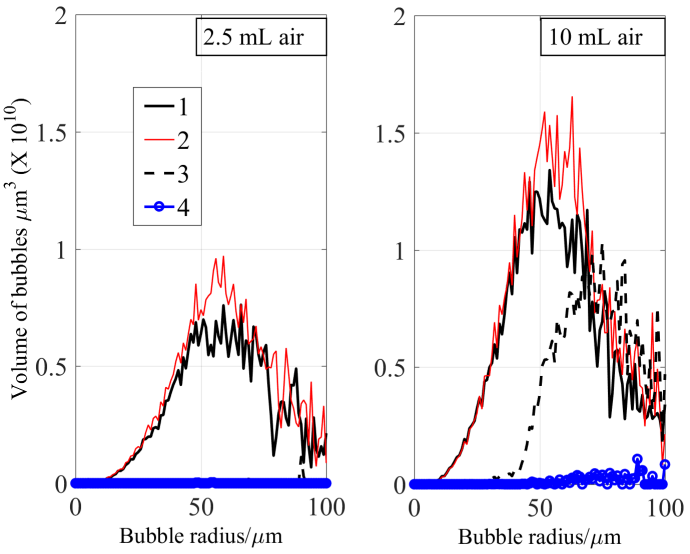

Figure A.3: Variation in NV with time, when using surfactant free liquid. Each of the legends "1" to "4" represents NV recorded at different times as detailed in the text.

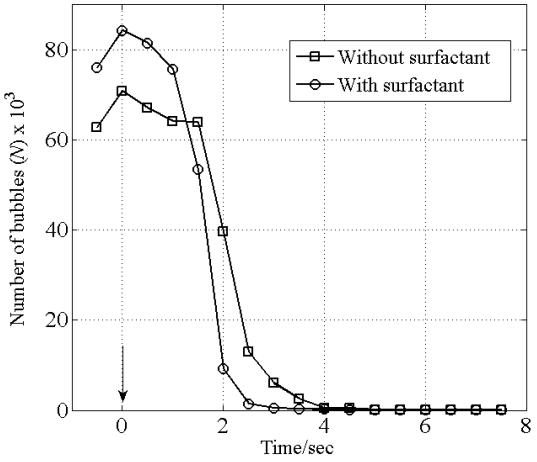

Figure A.4: The optical quantification for the effectiveness of the outgasser working on microbubbles generated by injecting 10 ml air into the pump. The curve with "o" presents N recorded in liquid laden with 2 mM SDS.

Appendix B

. Additional figures - Microbubble generation

Estimation of speed of sound in water at different void fractions β varying from 10^{-6} to 10^{0} evaluated using equations 2.20 and 4.3, is shown in Figure B.1. Compare this figure with Figure 4.1.

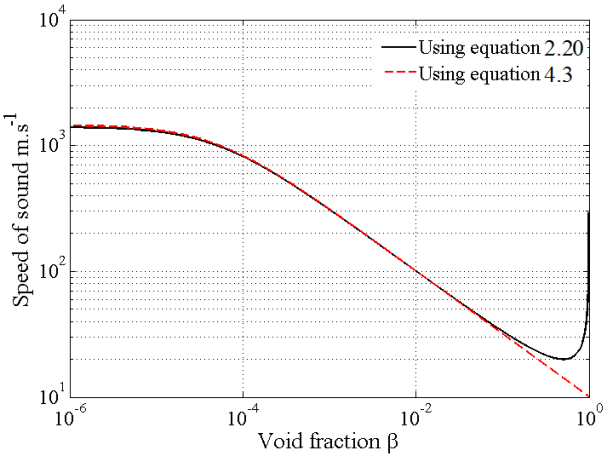

Figure B.1: Evaluation of c_m in a pipe of 10 mm mean diameter with flexible edges.

The reproducibility test on bubbles generated electrolytically in chamber G was shown earlier in Figure 4.9. A similar test result, but at different operating conditions (0.5 litre.min^{-1} flow rate, 176 mA with 10 ms square pulse as control, and 0.1 mM SDS as the surfactant) is presented in Figure B.2. This figure demonstrates a larger variation in the standard error, particularly around the 10 μm radius bin. However, it can be observed that within the experimental error limits, these results could be considered reproducible.

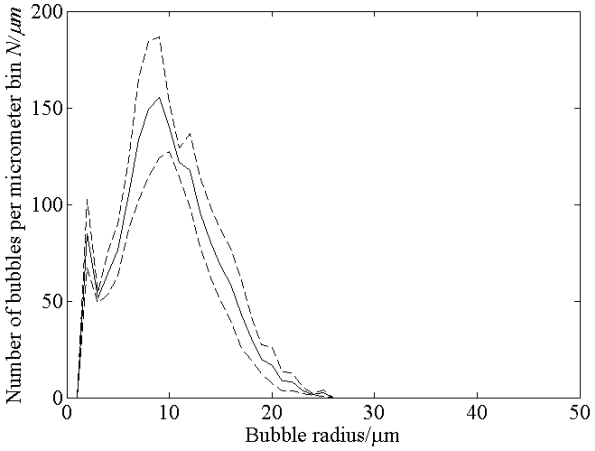

Figure B.2: Test to ensure reproducibility of the bubble generation and detection process. The solid line is the average BSD detected and the dotted outer lines are the standard error.

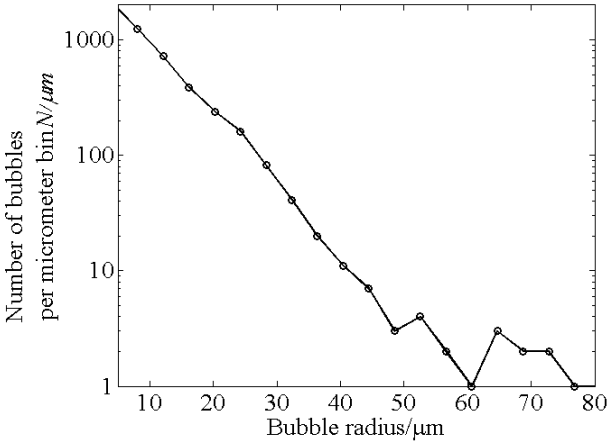

Figure B.3: Bubble size distribution generated using surfactant SDS at 1 mM. Operating conditions are 250 mA current at 1 ms square control pulse, 2.0 litre.min^{-1}. The Y-axis is in logarithmic scale.

Figures below demonstrate the BSDs recorded at different flow rates between 0.2 to 2.0 litre.min^{-1} with the absence of surfactant in Figure B.4 and with the use of 2 mM SDS as surfactant in Figure B.5.

In place of a square control signal where the "ON" and "OFF" time for bubble generation are equal, a signal with different "ON" and "OFF" times could be used. Results of BSD generated using one such signal (Figure B.6), is shown in Figure B.7.

Figure B.7 compares the normalized BSD (normalized to a maximum number of bubbles recorded in bins between 0 to 80 μm) generated while using a square type signal (Figure B.6a) and signal shown in Figure B.6. Three different flow rates i.e., 0.7, 0.5 and 0.2 litre.min^{-1} were used. The working conditions were: 176 mA current, electrolytic liquid with 0.1 mM SDS and liquid temperature around 29^{o}C. As obvious

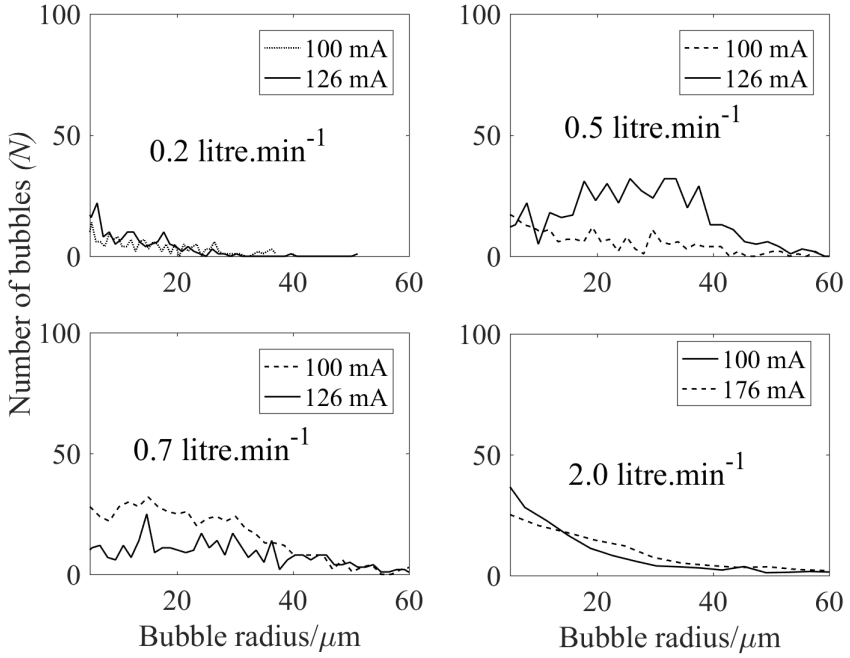

Figure B.4: BSD generated in chamber G at 0 mM SDS concentration, when using different flow rates.

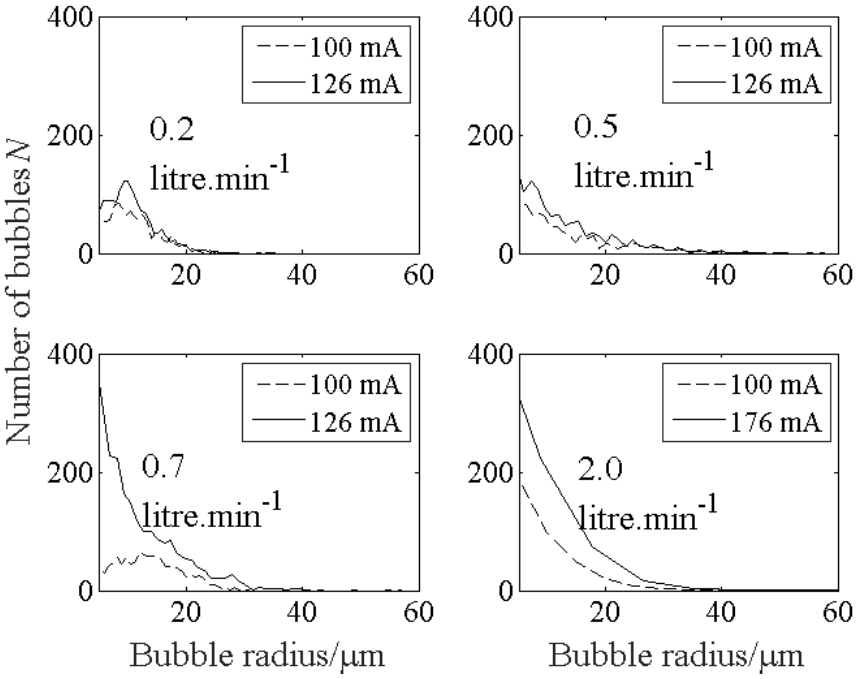

Figure B.5: BSD generated in chamber G at 2 mM SDS concentration, when using different flow rates.

from Figure B.7(a), (b) the normalized (normalization is done to the peak value of N of each distribution) BSD follows the influence of flow rate. The surfactant concentration is low (at 0.1 mM SDS) and hence BSDs have distinctive peaks for each of the flow

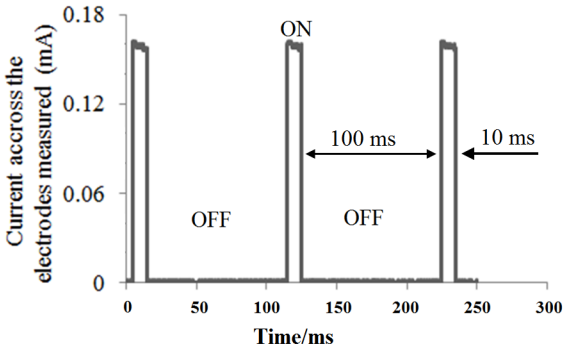

Figure B.6: Pulsed bubble generation control signal having an "ON" time of 10 ms and "OFF" time of 100 ms. The figure presents a single recording from an oscilloscope, using 176 mA pulsed signal recorded. Refer to Figure B.7b for the BSD generated at different flow rates using this pulse.

rates. These results show that, under the experimental limit, the BSDs generally do not depend on the pulse length or the ON-OFF time, also demonstrated in Figure 4.14.

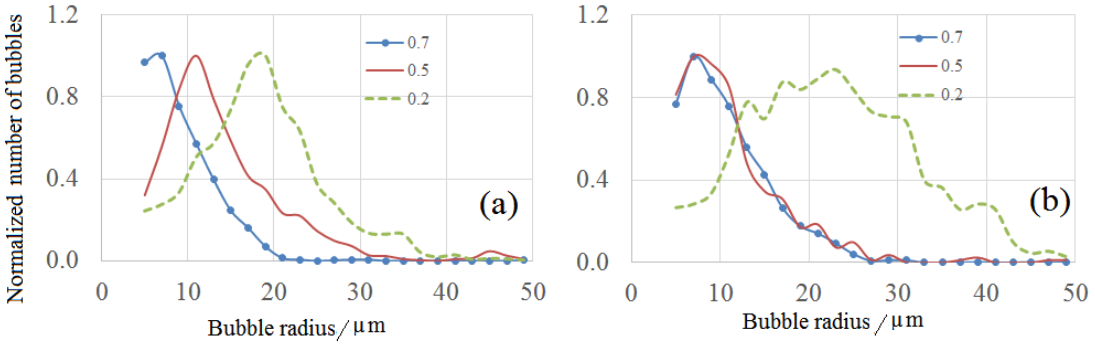

Figure B.7: Normalized bubble size distribution generated with a control signal (a) with equal ON-OFF times and (b) un-equal ON-OFF times. The pulse for part (b) is shown in Figure B.6.

An example of another method for comparing different BSD generated is shown in Figure B.8. This figure presents the BSD generated when using similar operating conditions to those shown in Figure 4.9, but for 250 mA current. Figure B.8a shows the normalized BSD (normalized to the maximum value of N, in this case approximately at 17 μm). The maximum of the distribution (number "1") was associated with the black colour and minimum value of the distribution (which is zero bubbles counted at 90 μm) was associated with the white colour. The distribution was then sorted into 23 bins each 2 μm wide (with starting bin from 4 μm and 6 μm). The grey scale distribution for BSD generated on three different days (as part of the reproducibility experiment) is presented in Figure B.8b.

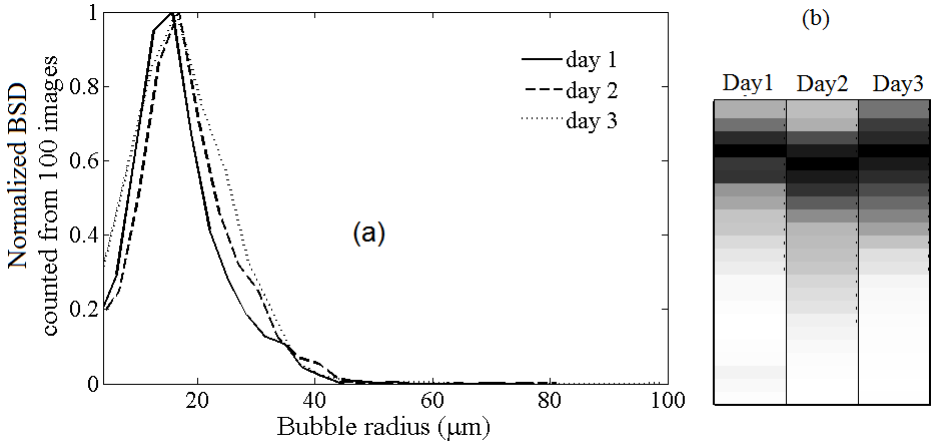

Figure B.8: A sample figure showing the representation of BSD using grey-scale colour pattern, (a) normalized BSD generated on three different days under same operating conditions; and (b) representation of normalized BSD as 1D grey-scale columns.

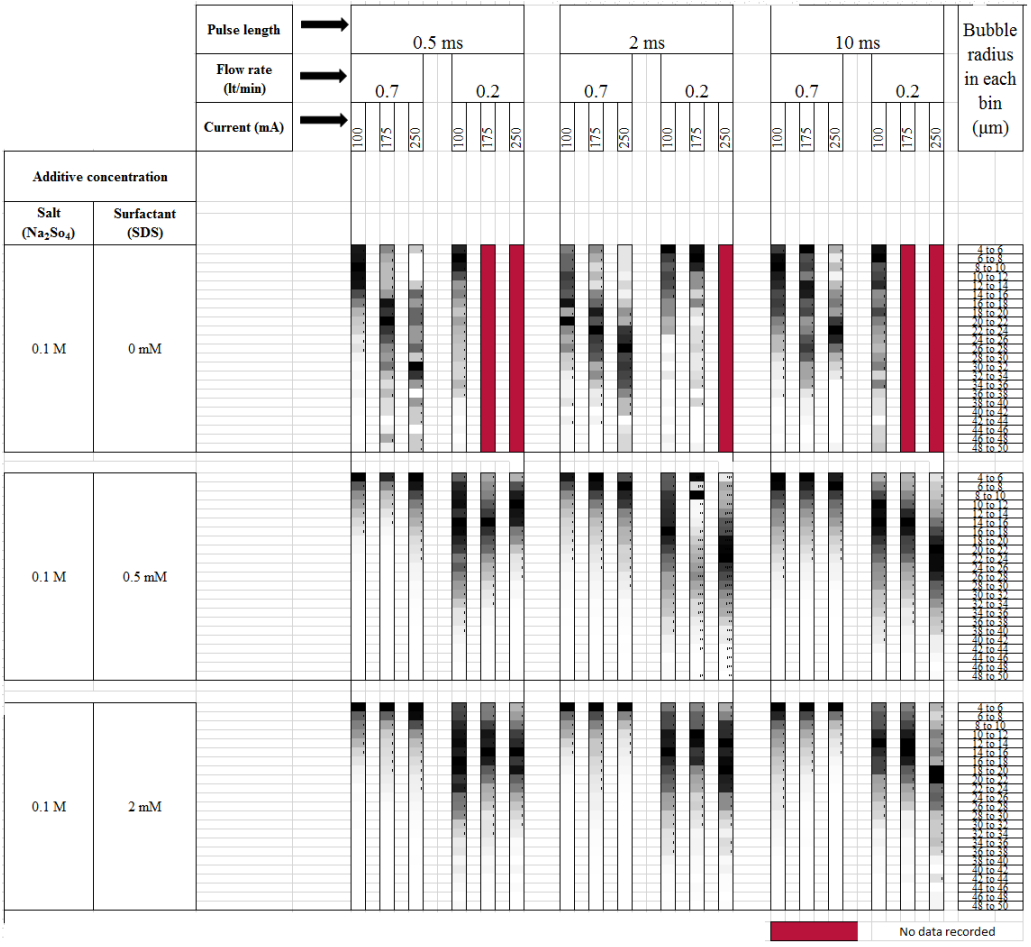

Figure B.9: Variation in BSD generated in the chamber G, across different flow rates, surfactant concentrations, and current across electrodes. Red represents that no data is recorded at working conditions.

Appendix C

. Additional figures - Influence of microbubbles

Working parameters for the results shown in Figure C.1 are pulse length at 20 ms, flow rate at 2.0 litre.min^{-1}, and liquid temperature at 28.3^{o}C.

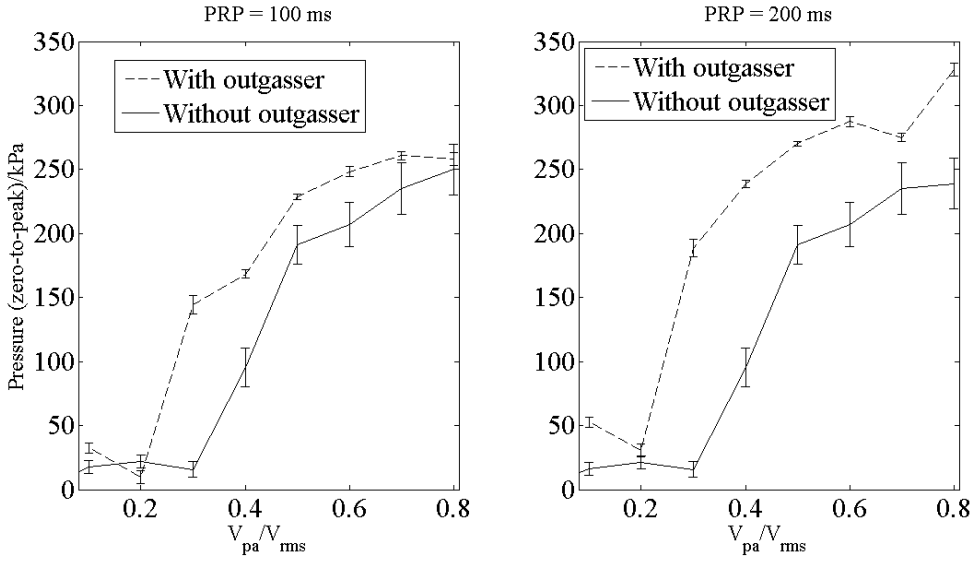

Figure C.1: Variation of pressure measured in the stream at 135 kHz with V_{pa}.

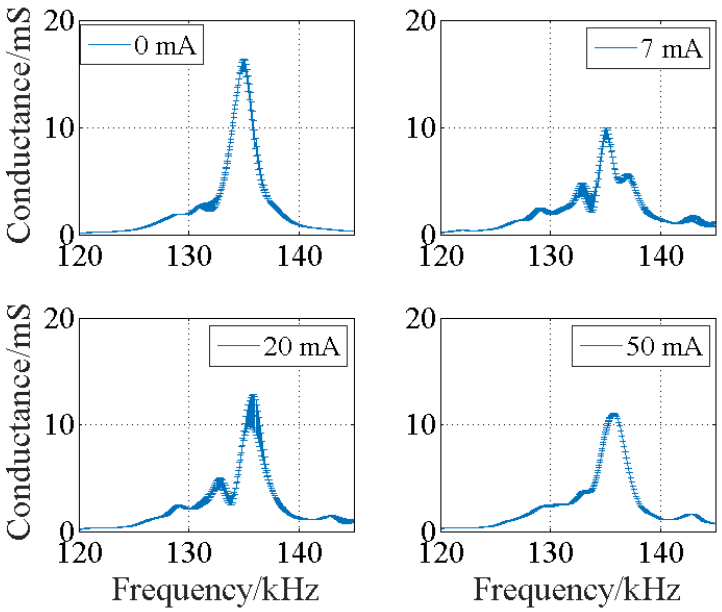

Figure C.2: Measurement of electrical conductance of UT_1 transducer connected to the UAS device, under different loading conditions, along with its statistical standard error.

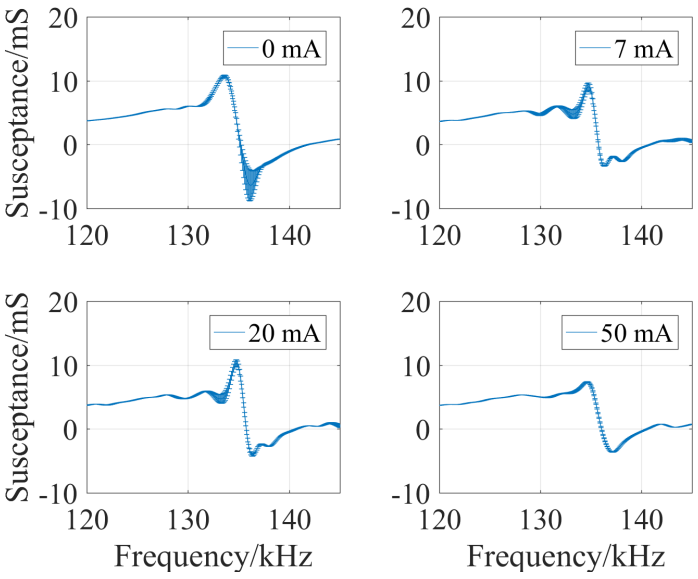

Figure C.3: Measurement of electrical susceptance of UT_1 transducer connected to the UAS device, under different loading conditions, along with its statistical standard error.

Appendix D

. Additional figures - Capillary instability

The threshold input voltage to the power amplifier to trigger capillary disturbances on the stream reported in Chapter 7 was recorded when the voltage was ramped up from 0.1 V_{rms} to 0.8 V_{rms}. The threshold point was also investigated as the V_{pa} was ramped down from 0.8 V_{rms} to 0.1 V_{rms}. Results are shown in Figure D.1 for different liquid temperatures and viscosity values.

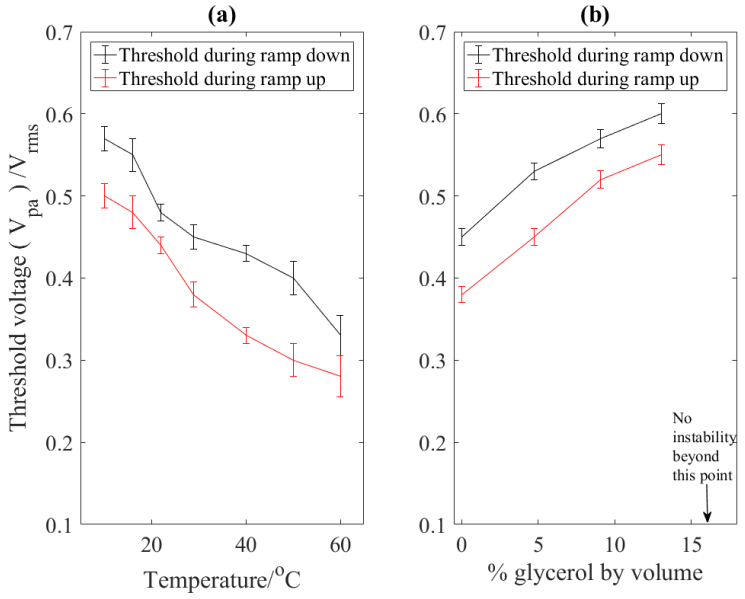

Figure D.1: Threshold values of V_{pa} recorded for initiating capillary instabilities on the stream when the voltage was either slowly ramped up or slowly ramped down. Part (a) presents the variation of this threshold V_{pa} at different liquid temperatures and part (b) presents the threshold at different glycerol concentrations.

Bibliography

[1] T.G. Leighton. What is ultrasound? *Progress in Biophysics and Molecular Biology*, 93(1-3):3–83, 2007.

[2] A. Shoh. Industrial applications of ultrasound - A review I. High-Power ultrasound. *IEEE Transactions On Sonics And Ultrasonics*, 22(2):60–71, 1975.

[3] W.L. Nyborg. Safety of medical diagnostic ultrasound. *Seminars in Ultrasound, CT and MRI*, 23(5):377–386, 2002.

[4] K.H. Ng. International guidelines and regulations for the safe use of diagnostic ultrasound in medicine. *Journal of Medical Ultrasound*, 10(1):5–9, 2002.

[5] T.G. Leighton, P.R. Birkin, and D.G. Offin. A new approach to ultrasonic cleaning. In *Proceedings of Meetings on Acoustics, International congress on Acoustics, Montreal, CA*, volume 19(1), page 075029, June 2013.

[6] P.R. Birkin, D.G. Offin, and T.G. Leighton. An activated fluid stream - new techniques for cold water cleaning. *Ultrasonics Sonochemistry*, 29:612–618, 2015.

[7] Precision Acoustics. Aptflex F21 Technical data sheet, 2017. URL http://www.acoustics.co.uk/product/aptflex-f21/.

[8] P.R. Birkin, D.G. Offin, C.J. Vian, and T.G. Leighton. Electrochemical "bubble swarm" enhancement of ultrasonic surface cleaning. *Physical Chemistry Chemical Physics*, 17(33):21709–21715, 2015.

[9] T.G. Leighton, A.J. Walton, and M.J.W. Pickworth. Primary Bjerknes forces. *European Journal of Physics*, 11(1):47–50, 1991.

[10] S. Brems, M. Hauptmann, E. Camerotto, P.W. Mertens, M. Heyns, H. Struyf, and S. De Gendt. Physical forces exerted by microbubbles on a surface in a travelling wave field. *Ultrasonics*, 54(2):706–709, 2014.

[11] T.G. Leighton, P.R. Birkin, M.N. Banda, J. Jiang, and D.G. Offin. Feasibility study to assess cleaning technology for nuclear applications. Technical Report 02, University of Southampton, 2012.

[12] R.P. Howlin, S. Fabbri, D.G. Offin, N. Symonds, K.S. Kiang, R.J. Knee, D.C. Yoganantham, J.S. Webb, P.R. Birkin, T.G. Leighton, and P. Stoodley. Removal of Dental Biofilms with an Ultrasonically-Activated Water Stream. *Journal of Dental Research*, 94(9):1303–1309, 2015.

[13] D.G. Offin, P.R. Birkin, and T.G. Leighton. Further development of a free flowing ultrasonic cleaning device. Technical report, ISVR reports, 2011.

[14] D.G. Offin, P.R. Birkin, T.G. Leighton, and V.F. Humphrey. Task6 - Ultrasonic cavitation and surface cleaning enhancement. Technical report, Southampton, ISVR reports, 2007.

[15] E.A. Neppiras. Acoustic cavitation series: Part One: Acoustic cavitation: An introduction. *Ultrasonics*, 22(1):25–28, 1984.

[16] K.S. Suslick, W.B. McNamara III, and Y. Didenko. Hot spot conditions during multi-bubble cavitation. In L.A. Crum, T.J. Mason, J. Reisse, and K.S Suslick, editors, *Sonochemistry and Sonoluminescence*, pages 191–204. NATO ASI Series (Series C: Mathematical and Physical Sciences), vol 524. Springer, Dordrecht, 1999.

[17] W.L. Nyborg. Acoustic Streaming near a boundary. *The Journal of the Acoustical Society of America*, 30(4):329–339, 1958.

[18] S.A. Elder. Cavitation microstreaming. *The Journal of the Acoustical Society of America*, 31(1):54–64, 1959.

[19] M.S. Plesset and R.B. Chapman. Collapse of an initially spherical vapour cavity in the neighbourhood of a solid boundary. *Journal of Fluid Mechanics*, 47(2): 283–290, 1971.

[20] T.G. Leighton. *The Acoustic Bubble*. Academic Press, Oval Road, London, UK, 1994.

[21] P.R. Birkin, Y.E. Watson, T.G. Leighton, and K.L. Smith. Electrochemical detection of Faraday waves on the surface of a gas bubble. *Langmuir*, 18(6):2135–2140, 2002.

[22] S.P. Lin. *Breakup of Liquid Sheets and Jets*. Cambridge University Press, Cambridge, UK, 2003.

[23] L.J. Briggs. Limiting negative pressure of water. *Journal of Applied Physics*, 21: 721, 1950.

[24] L.A. Crum. Nucleation and stabilization of microbubbles in liquids. *Applied Scientific Research*, 38(1):101–115, 1982.

[25] R.H.S. Winterton. Nucleation of boiling and cavitation. *Journal of Physics D: Applied Physics*, 10(15):2041–2056, 1977.

[26] T.G. Leighton. From seas to surgeries, from babbling brooks to baby scans: The acoustics of gas bubbles in liquids. *International Journal of Modern Physics B*, 18(25):3267–3314, 2004.

[27] C.E. Brennen. *Cavitation and Bubble Dynamics*. Oxford University Press, Oxford, NY, 1995.

[28] O. Reynolds. Experiments showing the boiling of water in an open tube at ordinary temperatures. *Scientific Papers on Mechanical and Physical subjects*, 2(1):579–587, 1897.

[29] J.W.S. Rayleigh. VIII. on pressure developed in a liquid during the collapse of a spherical cavity. *Philosophical Magazine Series6*, 34:94–98, 1917.

[30] M.S. Plesset and A. Prosperetti. Bubble dynamics and cavitation. *Annual review Fluid Mechanics*, 9:145–85, 1977.

[31] P.R. Birkin, D.G. Offin, P.F. Joseph, and T.G. Leighton. Cavitation, shock waves and the invasive nature of sonoelectrochemistry. *The Journal of Physical Chemistry B.*, 109(35):16997–17005, 2005.

[32] A. Prosperetti. Acoustic cavitation series part two: Bubble phenomena in sound fields: Part Two. *Ultrasonics*, 22(3):115–124, 1984.

[33] M. Longuet-Higgins. Resonance in nonlinear bubble oscillations. *Journal of Fluid Mechanics*, 224(1):531–594, 1991.

[34] P.R. Birkin, D.G. Offin, C.J.B. Vian, and T.G. Leighton. Multiple observations of cavitation cluster dynamics close to an ultrasonic horn tip. *The Journal of the Acoustical Society of America*, 130(5):3379–3388, 2011.

[35] R.E. Apfel. Acoustic cavitation prediction. *The Journal of the Acoustical Society of America*, 69(6):1624–1633, 1981.

[36] A. Prosperetti. A new mechanism for sonoluminescence. *The Journal of the Acoustical Society of America*, 101(4):2003–2007, 1997.

[37] C.L. Christman, A.J. Carmichael, M.M. Mossoba, and P. Riesz. Evidence for free radicals produced in aqueous solutions by diagnostic ultrasound. *Ultrasonics*, 25(1):31–34, 1987.

[38] L.A. Crum and A.I. Eller. Motion of Bubbles in a Stationary Sound Field. *The Journal of the Acoustical Society of America*, 48:181–189, 1970.

[39] L.A. Crum. Bjerknes forces on bubbles in a stationary sound field. *The Journal of the Acoustical Society of America*, 57(6):1363–1370, 1975.

[40] B.P. Barber, R.A. Hiller, R. Lofstedt, S.J. Putterman, and K.R. Weninger. Defining the unknowns of sonoluminescence. *Physics Reports*, 281(2):65–143, 1997.

[41] E.A. Neppiras. Subharmonic and other low-frequency signals from sound-irradiated liquids. *Journal of Sound and Vibration*, 10(2):176–186, 1969.

[42] E. Cramer and W. Lauterborn. Acoustic cavitation noise spectra. *Applied Scientific Research*, 38(1):209–214, 1982.

[43] W. Lauterborn and H. Bolle. Experimental investigations of cavitation-bubble collapse in the neighbourhood of a solid boundary. *Journal of Fluid Mechanics*, 72(02):391–399, 1975.

[44] J.R. Blake and D.C. Gibson. Cavitation bubbles near boundaries. *Annual Review of Fluid Mechanics*, 19(1):99–123, 1987.

[45] R.E. Apfel. Acoustic cavitation series: Part Four - Acoustic cavitation inception. *Ultrasonics*, 22(4):167–173, 1984.

[46] L. Crum. The polytropic exponent of gas contained within air bubbles pulsating in a liquid. *The Journal of the Acoustical Society of America*, 73:116–120, 1983.

[47] T.G. Leighton. Bubble population phenomena in acoustic cavitation. *Ultrasonics Sonochemistry*, 2(2):S123–S136, 1995.

[48] A. Prosperetti. Thermal effects and damping mechanisms in the forced radial oscillations of gas bubbles in liquids. *The Journal of Acoustical Society of America*, 61:17–27, 1977.

[49] A. Prosperetti. Acoustic cavitation series: Part Two: Bubble phenomena in sound fields: Part One. *Ultrasonics*, 22:69–77, 1984.

[50] S. Kumar and C.E. Brennen. Nonlinear Effects in the dynamics of clouds of bubbles. *The Journal of the Acoustical Society of America*, 89(2):707–714, 1991.

[51] C. Feuillade. The attenuation and dispersion of sound in water containing multiply interacting air bubbles. *The Journal of Acoustical Society of America*, 99(6):3412–3430, 1996.

[52] B.E. Noltingk and E.A. Neppiras. Cavitation produced by Ultrasonics. *Proceedings of the Physical Society. Section B*, 63(9):674–685, 1950.

[53] T.G. Leighton, P.R. Birkin, M. Hodnett, B. Zeqiri, J.F. Power, G.J. Price, T. Mason, M. Plattes, N. Dezhkunov, and A.J. Coleman. Characterisation of measures of reference acoustic cavitation (COMORAC): An experimental feasibility trial. *Bubble and Particle Dynamics in Acoustic Fields, Modern Trends and Applications,Trivandrum, India, Research Signpost*, 37:37–94, 2005.

[54] B. Zeqiri, N. D. Lee, M. Hodnett, and P. N. Gelat. A novel sensor for monitoring acoustic cavitation. Part II: Prototype performance evaluation. *IEEE Transactions on Ultrasonics, Ferroelectrics, and Frequency Control*, 50(10):1351–1362, 2003.

[55] E.B. Flint and K.S Suslick. The temperature of cavitation. *Science (New York)*, 253(5026):1397–1399, 1991.

[56] K.S. Suslick, Y. Didenko, M.M. Fang, T. Hyeon, K.J. Kolbeck, W.B. McNamara, M.M. Mdleleni, and M. Wong. Acoustic cavitation and its chemical consequences. *Philosophical Transactions of the Royal Society A: Mathematical, Physical and Engineering Sciences*, 357:335–353, 1999.

[57] P.R. Birkin, J.F. Power, and T.G. Leighton. Electrochemical evidence of h[radical dot] produced by ultrasound. *Chemical Communications*, 21:2230–2231, 2001.

[58] P. Tho, R. Manasseh, and A. Ooi. Cavitation microstreaming patterns in single and multiple bubble systems. *Journal of Fluid Mechanics*, 576:191–233, 2007.

[59] H.G. Flynn and C.C. Church. Transient pulsations of small gas bubbles in water. *The Journal of the Acoustical Society of America*, 84(3):985–998, 1988.

[60] Y.E. Watson, P.R. Birkin, and T.G. Leighton. Electrochemical detection of bubble oscillation. *Ultrasonics Sonochemistry*, 10(2):65–69, 2003.

[61] Y. Tomita and A. Shima. Mechanisms of impulsive pressure generation and damage pit formation by bubble collapse. *Journal of Fluid Mechanics*, 169(1):535–564, 2006.

[62] A.A. Atchley, L.A. Frizzell, R.E. Apfel, C.K. Holland, S. Madanshetty, and R.A. Roy. Thresholds for cavitation produced in water by pulsed ultrasound. *Ultrasonics*, 26(5):280–287, 1988.

[63] M. Longuet-Higgins. Nonlinear damping of bubble oscillations by resonant interaction. *The Journal of the Acoustical Society of America*, 91:1414–1422, 1992.

[64] D.F. Gaitan, L.A. Crum, C.C. Church, and R.A. Roy. Sonoluminescence and bubble dynamics for a single, stable, cavitation bubble. *The Journal of Acoustical society of America*, 91(6):3166–3183, 1992.

[65] P. R. Birkin, D. G. Offin, C. J. B. Vian, T. G. Leighton, and A. O. Maksimov. Investigation of noninertial cavitation produced by an ultrasonic horn. *The Journal of the Acoustical Society of America*, 130(5):3297–3308, 2011.

[66] C.K. Holland and R.E. Apfel. An improved theory for the prediction of microcavitation thresholds. *IEEE transactions on Ultrasonics, Ferroelectrics and Frequency Control*, 36(2):204–208, 1989.

[67] L.A. Crum. Measurements of the growth of air bubbles by rectified diffusion. *The Journal of the Acoustical Society of America*, 68(1):203–211, 1980.

[68] L.A. Crum. Acoustic cavitation series: Part Five: Rectified Diffusion. *Ultrasonics*, 22(5):215–223, 1984.

[69] P.R. Birkin, T.G. Leighton, and Y.E. Watson. The use of acoustoelectrochemistry to investigate rectified diffusion. *Ultrasonics Sonochemistry*, 11(3-4):217–221, 2004.

[70] K.S. Suslick, D.A. Hammerton, and R.E. Cline Jr. Sonochemical hot spot. *The Journal of American Chemical Society*, 108(6):5641–5642, 1986.

[71] F. Ahmadi, I.V. McLoughlin, S. Chauhan, and G. Ter-Haar. Bio-effects and safety of low-intensity, low-frequency ultrasonic exposure. *Progress in Biophysics and Molecular Biology*, 108(3):119–38, 2012.

[72] J. Sponer. Dependance of ultrasonic cavitation threshold on the ultrasonic frequency. *Czechoslovak journal of physics*, 40(10):1123–1132, 1990.

[73] R.E. Apfel and C.K. Holland. Gauging the likelihood of cavitation from short-pulse low-duty cycle diagnostic ultrasound. *Ultrasound in Medicine and Biology*, 17(2):179–185, 1991.

[74] International Electrotechnical Commission. Ultrasonics. Field characterization. Test methods for the determination of thermal and mechanical indices related to medical diagnostic ultrasonic fields. Technical Report IEC 62359:2010, 2010.

[75] T.G. Leighton, R.J. Lingard, A.J. Walton, and J.E. Field. Acoustic bubble sizing by combination of subharmonic emissions with imaging frequency. *Ultrasonics*, 29(4):319–323, 1991.

[76] W. Lauterborn and E. Cramer. On the dynamics of acoustic cavitation noise spectra. *Acta Acustica United with Acustica,*, 49(4):280–287, 1981.

[77] T.G. Leighton. Acoustic bubble detection - II. The detection of transient cavitation. *Environmental Engineering*, 8:16–25, 1995.

[78] J. Frohly, S. Labouret, C. Bruneel, I. Looten-Baquet, and R. Torguet. Ultrasonic cavitation monitoring by acoustic noise power measurement. *The Journal of the Acoustical Society of America*, 108(5):2012–2020, 2000.

[79] L.A. Crum and G.T. Reynolds. Sonoluminescence produced by "stable" cavitation. *The Journal of Acoustical Society of America*, 78:137–139, 1985.

[80] M.A. Beckett and I. Hua. Impact of ultrasonic frequency on aqueous sonoluminescence and sonochemistry. *The Journal of Physical Chemistry A*, 105:3796–3802, 2001.

[81] P.R. Birkin, J.F. Power, A.M.L. Vincotte, and T.G. Leighton. A 1 kHz resolution frequency study of a variety of sonochemical processes. *Physical Chemistry Chemical Physics*, 5:4170–4174, 2003.

[82] P.R. Birkin, T.G. Leighton, J.F. Power, M.D. Simpson, A.M.L. Vincotte, and P.F. Joseph. Experimental and theoretical characterization of sonochemical cells. Part 1. Cylindrical reactors and their use to calculate the speed of sound in aqueous solutions. *The Journal of Physical Chemistry A*, 107(2):306–320, 2003.

[83] Y. Yamakoshi, Y. Ozawa, M. Ida, and N. Masuda. Effects of bjerknes forces on gas-filled microbubble trapping by ultrasonic waves. *Japanese Journal of Applied Physics*, 40(Part 1, No. 5B):3852–3855, 2001.

[84] K. Yosioka and Y. Kawasima. Acoustic radiation pressure on a compressible sphere. *Acta Acustica united with Acustica*, 5(3):167–173, 1955.

[85] L.A. Crum. Bjerknes forces on bubbles in a stationary sound field. *The Journal of Acoustical society of America*, 57:1363–1370, 1975.

[86] R. Mettin, I. Akhatov, U. Parlitz, C. Ohl, and W. Lauterborn. Bjerknes forces between small cavitation bubbles in a strong acoustic field. *Physical Review E*, 56(3):2924–2931, 1997.

[87] N.A. Pelekasis, A. Gaki, A. Doinikov, and J.A. Tsamopolous. Secondary bjerknes forces between two bubbles and the phenomenon of acoustic streamers. *Journal of Fluid Mechanics*, 500:313–347, 2004.

[88] S. W. Yoon, L.A. Crum, A. Prosperetti, and N.Q. Lu. An investigation of the collective oscillations of a bubble cloud. *The Journal of the Acoustical Society of America*, 89:700–706, 1991.

[89] E. Stride and M. Edirisinghe. Novel microbubble preparation technologies. *Soft Matter*, 4:2350–2359, 2008.

[90] G. Corchero, J.L. Montanes, and J.C. Tellez. Effect of flow rate conditions on bubble formation. *International Journal of Heat and Mass Transfer*, 55(19-20): 5044–5052, 2012.

[91] L. d'Agostino and C.E. Brennen. Linearized dynamics of spherical bubble clouds. *Journal of Fluid Mechanics*, 199:155–176, 1989.

[92] H. Medwin. In situ acoustic measurements of bubble populations in coastal ocean waters. *Journal of Geophysical Research*, 75:599–611, 1970.

[93] L. d'Agostino and C.E. Brennen. Acoustical absorption and scattering cross sections of spherical bubble clouds. *Journal of the Acoustical Society of America*, 84(6):2126–2134, 1988.

[94] K.W. Commander and A. Prosperetti. Linear pressure waves in bubbly liquids: Comparison between theory and experiments. *The Journal of the Acoustical Society of America*, 85(2):732–746, 1989.

[95] C. C. Coussios, C. H. Farny, and G. Ter Haar. Role of acoustic cavitation in the delivery and monitoring of cancer treatment by high-intensity focused ultrasound (HIFU). *International Journal of Hyperthermia*, 23(2):105–120, 2007.

[96] E. E. Lamarre and W.K. Meleville. Void-fraction measurements and sound-speed fields in bubble plumes generated by breaking waves. *The Journal of the Acoustical Society of America*, 95:1317–1328, 1993.

[97] T.G. Leighton, S.D. Meers, and P.R. White. Propagation through nonlinear time-dependent bubble clouds and the estimation of bubble populations from measured acoustic characteristics. *Proceedings of the Royal Society A: Mathematical, Physical and Engineering Sciences*, 460(2049):2521–2550, 2004.

[98] T.R. Hahn, T.K. Berger, and M.J. Buckingham. Acoustic resonances in the bubble plume formed by a plunging water jet. *Proceedings of the Royal Society A: Mathematical, Physical and Engineering Sciences*, 459(2035):1751–1782, 2003.

[99] P.S Wilson, C.N. Dolder, R.A. Roy, and A.D. Pierce. From Wood to Carey to Mallock: A review of Bill Carey's work associated with the Mallock-Wood equation and the acoustics of bubbly liquids and gas-bearing sediments. *The Journal of the Acoustical Society of America*, 135:2232, 2014.

[100] E. Lamarre and W.K. Meleville. Sound-speed measurements near the ocean surface. *The Journal of Acoustical Society of America*, 96(6):3605–3616, 1994.

[101] L. van Wijngaarden. One-dimensional flow of liquids containing small gas bubbles. *Annual Review of Fluid Mechanics*, 4:369–395, 1972.

[102] T.G. Leighton, K. Baik, and J. Jiang. The use of acoustic inversion to estimate the bubble size distribution in pipelines. *Proceedings of the Royal Society A: Mathematical, Physics and Engineering Sciences*, 468(2145):2461–2484, 2012.

[103] T.G. Leighton, P.R. White, C.L. Morfey, J.W.L Clarke, G.J. Heald, H.A. Dumbrell, and K.R. Holland. The effect of reverberation on the damping of bubbles. *The Journal of the Acoustical Society of America*, 112(4):1366–1376, 2002.

[104] D.M. Farmer, S. Vagle, and D. Booth. Reverberation effects in acoustical resonators used for bubble measurements. *The Journal of Acoustical Society of America*, 118:2954–2960, 2005.

[105] P.R. Birkin, D.G. Offin, and T.G. Leighton. Experimental and theoretical characterisation of sonochemical cells. part 2: Cell disruptors (ultrasonic horns) and cavity cluster collapse. *Physical Chemistry Chemical Physics*, 7(3):530–537, 2005.

[106] P.R. Birkin, T.G. Leighton, Y.E. Watson, and J.F. Power. Acoustoelectrochemistry. *Acoustics Bulletin*, 26 (5):24–37, 2001.

[107] K.S. Suslick. Sonochemistry. *Science (New York)*, 247(4949):1439–1445, 1990.

[108] K.S. Suslick. The chemical effects of ultrasound. *Scientific American*, 260:80–86, 1989.

[109] T.J. Mason. *Sonochemistry: The uses of Ultrasound in Chemistry*. The Royal Society of chemistry, Cambridge, UK., 1989.

[110] T.J. Mason, J.P. Lorimer, and D.M. Bates. Quantifying sonochemistry: Casting some light on a "black art". *Ultrasonics*, 30(1):40–42, 1992.

[111] P. Riesz, D. Berdahl, and C.L. Christman. Free radical generation by ultrasound in aqueous and nonaqueous solutions. *Environmental Health Perspective*, 64:233–252, 1985.

[112] D.G. Offin. *Acoustoelectrochemical characterisation of cavitation and its use in the study of surface processes*. PhD thesis, School of Chemistry, University of Southampton, Jan 2006.

[113] L.E. Kinsler, A.R. Frey, A.B. Coppens, and J.V. Sanders. *Fundamentals of Acoustics*. John Wiley & Sons, Inc, New York, 2000. ISBN 0-471-84789-5.

[114] S.W. Rienstra and A. Hirschberg. *An Introduction to Acoustics*. online at - http://www.win.tue.nl/ sjoerdr/papers/boek.pdf, 2004.

[115] W.J. Jacobi. Propagation of sound waves along liquid cylinders. *The Journal of the Acoustical Society of America*, 21(2):120–127, 1949.

[116] L.M.B.C. Campos. On longitudinal acoustic propagation in convergent and divergent nozzle flows. *Journal of Sound and Vibration*, 117(22):131–151, 1987.

[117] A.H. Nayfeh and D.P. Telionis. Acoustic propagation in ducts with varying cross sections. *The Journal of the Acoustical Society of America*, 54(6):1654, 1973.

[118] C.J. Gurney. *The stability and control of curved liquid jet break-up*. PhD thesis, Mathematics, University of Birmingham, 2009.

[119] B. Kolbrek. Horn Theory: An introduction, Part 1. Technical report, AudioXpress, 2008. URL https://www.grc.com/acoustics/an-introduction-to-horn-theory.pdf.

[120] B. Kolbrek. Horn Theory: An introduction, Part 2. Technical report, AudioXpress, 2008. URL http://www.audioxpress.com/assets/upload/files/kolbrek2885.pdf.

[121] D. Mapes-Riordan. Horn modeling with conical and cylindrical transmission-line elements. *Journal of the Audio Engineering Society*, 41(6):471–484, 1993.

[122] J.B. Lonzaga, D.B. Thiessen, and P.L. Marston. Uniformly valid solution for acoustic propagation in weakly tapered circular waveguides: Liquid jet example. *The Journal of Acoustical society of America*, 124(1):151–160, 2008.

[123] S.W. Rienstra. Cut-on, cut-off transition of sound in slowly varying flow ducts. Department of Mathematics and Computing Science, Eindhoven University of Technology, The Netherlands, Reports, 19-03-2001. URL http://www.win.tue.nl/analysis/reports/rana01-14.pdf.

[124] J.W.S. Rayleigh. On the instability of liquid jets. *Proceedings of London Mathematical Society*, s1-10:4–13, 1878.

[125] J. Eggers and E. Villermaux. Physics of liquid jets. *Reports on Progress in Physics*, 71(3):036601(79pp), 2008.

[126] S.P. Lin and R.D. Reitz. Drop and spray formation from a liquid jet. *Annual Review of Fluid Mechanics*, 30(1):85–105, 1998.

[127] R.J. Donnelly and W. Glaberson. Experiments on the capillary instability of a liquid jet. *Proceedings of the Royal Society of London. Series A, Mathematical and Physical Sciences*, 290(1423):547–556, 1966.

[128] H.E. Cline and T.R. Anthony. The effect of harmonics on the capillary instability of liquid jets. *Journal of Applied Physics*, 49(6):3203–3208, 1978.

[129] J.B. Keller, S.I. Rubinow, and Y.O. Tu. Spatial instability of jets. *Physics of Fluids*, 16(12):2052–2055, 1973.

[130] E.F. Goedde and M.C. Yuen. Experiments on liquid jet instability. *Journal of Fluid Mechanics*, 40(3):495–511, 1970.

[131] S.J. Leib and M.E. Goldstein. The generation of capillary instabilities on a liquid jet. *Journal of Fluid Mechanics*, 168:479–500, 1986.

[132] M.C. Yuen. Non-linear capillary instability of a liquid jet. *Journal of Fluid Mechanics*, 33(1):151–163, 1968.

[133] K.C. Chaudhary and L.G. Redekopp. The nonlinear capillary instability of a liquid jet. Part 1. Theory. *Journal of Fluid Mechanics*, 96(2):257–274, 1980.

[134] J.B. Lonzaga, C.F. Osterhoudt, D.B. Thiessen, and P.L Marston. Liquid jet response to internal modulated ultrasonic radiation pressure and stimulated drop production. *The Journal of Acoustical Society of America*, 121(6):3323–3330, 2007.

[135] R.J. Lang. Ultrasonic atomization of liquids. *The Journal of the Acoustical Society of America*, 34(1):6–8, 1962.

[136] S. Chandrasekhar. *Hydrodynamic and Hydromagnetic Stability. Vol 1, Equation - 158.* Dover Publications Inc, 1998.

[137] J.W.S. Rayleigh. XVI. On the instability of a cylinder of viscous liquid under capillary force. *Philosophical Magazine Series 5*, 34:145–154, 1892.

[138] J.M. Mir. Cavitation-induced capillary waves in ultrasonic atomization. *The Journal of the Acoustical Society of America*, 67(1):201–205, 1980.

[139] W. Eisenmenger. Dynamic properties of the surface tension of water and aqueous solutions of surface active agents with standing capillary waves in the frequency range from 10 kc/s to 1.5 Mc/s. *Acta Acustica United with Acustica*, 9(4):327–340, 1959.

[140] K.M. Awati and T. Howes. Stationary waves on cylindrical fluid jets. *American Journal of Physics*, 64(6):808–811, 1996.

[141] E. Robert, J. Lettry, M. Farhat, P.A. Monkewitz, and F. Avellan. Cavitation bubble behaviour inside a liquid jet. *Physics of Fluids*, 19(6):67–106, 2007.

[142] K. Baik, J. Jiang, and T.G. Leighton. Acoustic attenuation, phase and group velocities in liquid-filled pipes: Theory, experiment, and examples of water and mercury. *The Journal of the Acoustical Society of America*, 128(5):2610–2624, 2010.

[143] K. Ferrara, R. Pollard, and M. Borden. Ultrasound microbubble contrast agents: fundamentals and application to gene and drug delivery. *Annual Review of Biomedical Engineering*, 9:415–447, 2007.

[144] D.G. Offin, P.R. Birkin, T.G. Leighton, and P.F. Joseph. Acoustoelectrochemistry: The application of sound to electrochemical processes. In *Proceedings of the Institute of Acoustics*, volume 28(1), pages 821–829, 2006.

[145] P.R. Birkin, T.G. Leighton, D.G. Offin, and C.J.B. Vian. Observations of bubble clusters within different cavitation environments - electrochemistry, acoustics and imaging studies. In *20th International Congress on Acoustics, ICA 2010*, pages 23–27, Sydney, AU, Aug, 2010.

[146] K. Baik, J. Jiang, and T.G. Leighton. Investigation of a method for real time quantification of gas bubbles in pipelines. *The Journal of the Acoustical Society of America*, 136(2):502–513, 2014.

[147] E. Stride and M. Edirisinghe. Novel preparation techniques for controlling microbubble uniformity: a comparison. *Medical and Biological Engineering*, 47(8): 883–892, 2009.

[148] F.L. Smith and A.H. Harvey. Avoid common pitfalls when using Henry's law. *AICHE group - Environmental Management*, 126:33–39, 2007.

[149] P.R. Birkin, D.G. Offin, C.J.B. Vian, R.P. Howlin, J.I. Dawson, T.J. Secker, R.C. Herve, P. Stoodley, R.O.C. Oreffo, C.W. Keevil, and T.G. Leighton. Cold water cleaning of brain proteins, biofilm and bone - harnessing an ultrasonically activated stream. *Physical Chemistry Chemical Physics*, 17(32):20574–20579, 2015.

[150] T. Foley. *A Study of Acoustic Cavitation and Hydrogen Production*. PhD thesis, School of Chemistry, University of Southampton, Dec 2014.

[151] H. Rhody. Lecture 10: Hough circle transform. Chester F. Carlson Center for Imaging Science, Rochester Institute of Technology, https://www.cis.rit.edu/class/simg782/lectures/lecture_10/lec782_05_10.pdf, October 2013.

[152] RSB web ImageJ. Analyze button - used for measuring particles. http://rsbweb.nih.gov/ij/docs/guide/146-30.html, October 2014.

[153] H. Matsushima, T. Nishida, Y. Konishi, Y. Fukunaka, Y. Ito, and K. Kuribayashi. Water electrolysis under microgravity: Part 1. Experimental technique. *Electrochimica Acta*, 48(28):4119–4125, 2003.

[154] B.C. Donose, F. Harnisch, and E. Taran. Electrochemically produced hydrogen bubble probes for gas evolution kinetics and force spectroscopy. *Electrochemistry Communications*, 24:21–24, 2012.

[155] T.G. Leighton, A.D. Phelps, D.G. Ramble, and D.A. Sharpe. Comparison of the abilities of eight acoustic techniques to detect and size a single bubble. *Ultrasonics*, 34(6):661–667, 1996.

[156] H.J. Rath. Unsteady pressure wave and shock waves in elastic tubes containing bubbly air-water mixtures. *Acta Mechanica*, 38:1–17, 1981.

[157] C. Gabrielli, F. Huet, and M. Keddam. Characterization of electrolytic bubble evolution by spectral analysis. Application to a corroding electrode. *Journal of Applied Electrochemistry*, 15(4):503–508, 1985.

[158] National Measurement Office, Marine Scotland, The Crown Estate, S.P. Robinson, P.A. Lepper, and R.A. Hazelwood. Good practice guide for underwater noise measurements. Technical report, NPL Good Practice Guide No. 133, ISSN: 1368-6550, 2014.

[159] Sigma-Aldrich. Material properties of Sodium Do-Decyl Sulphate (SDS), 2014. URL http://www.sigmaaldrich.com/catalog/product/sigma/71725?lang=en&region=GB. Accessed: 2014-12-01.

[160] Sigma-Aldrich. Material properties of Triton-X100 (TX100), 2014. URL http://www.sigmaaldrich.com/catalog/product/sial/x100?lang=en&region=GB. Accessed: 2014-12-01.

[161] M. Johnson. Detergents: Triton X-100, Tween-20, and More. Technical report, Labome, MATER METHODS 2013;3:163, Synatom Research, Princeton, New Jersey, United States, 18-01-2013. URL https://www.labome.com/method/Detergents-Triton-X-100-Tween-20-and-More.html. Date accessed: 26/03/2017.

[162] D. Stansfield. *Underwater Electroacoustic Transducers*. Bath University press and Institute of Acoustics, Bath, 1991.

[163] BRITISH STANDARD. Underwater acoustics - Hydrophones - Calibration in the frequency range 0.01 Hz to 1 MHz. Technical Report BS EN 60565:2007, 2007.

[164] H. Kuttruff. Sound fields in small rooms. In *15th International Conference: Audio, Acoustics and Small Spaces*, Oct 1998.

[165] H. Kuttruff. *Room Acoustics*. Spon Press, Oxon, 5th edition, 2009.

[166] B. Zeqiri and A.D. Bond. The influence of waveform distortion on hydrophone spatial-averaging corrections - Theory and measurement. *The Journal of the Acoustical Society of America*, 92:1809–1821, 1992.

[167] N. Aurelle, D. Guyomar, C. Richard, P. Gonnard, and L. Eyraud. Nonlinear behavior of an ultrasonic transducer. *Ultrasonics*, 34(2-5):187–191, 1996.

[168] C.H. Sherman and J.L. Butler. *Transducers and Arrays for Underwater Sound*. Springer, New York, 2007. ISBN 0-387-32940-4.

[169] Y.-S Tung, J.J. Choi, B. Baseri, and E.E. Konofagou. Identifying the inertial cavitation threshold and skull effects in a vessel phantom using focused ultrasound and microbubbles. *Ultrasound in medicine & biology*, 36(5):840–852, 2010.

[170] J.F. Tressler. *Piezoelectric transducer designs for sonar applications. In: Piezoelectric and Acoustic Materials for Transducer Applications (Chapter 11), Ed. A. Safari and E.K. Akdoggan.* Springer US, Boston, 2008.

[171] T. Jordan, Z. Ounaies, J. Tripp, and P. Tcheng. Electrical properties and power considerations of a piezoelectric actuator. Technical Report NASA/CR-2000-209861:2000-8, NASA ICASE Report, 2000.

[172] S. Li, W. Cao, and L.E. Cross. The extrinsic nature of nonlinear behavior observed in lead zirconate titanate ferroelectric ceramic. *Journal of Applied Physics*, 69(10): 7219–7224, 1991.

[173] D.A. Hall. Review Nonlinearity in piezoelectric ceramics. *Journal of Material Science*, 36(19):4575–4601, 2001.

[174] Y. Kikuchi and H. Shimizu. On the variation of acoustic radiation resistance in water under ultrasonic cavitation. *The Journal of the Acoustical Society of America*, 31(10):1385–1386, 1959.

[175] C.H. Sherman. Effect of the nearfield on the cavitation limit of transducers. *The Journal of the Acoustical Society of America*, 35(9):1409–1412, 1963.

[176] K. Hashiba, K-I. Kawabata, and S-I. Umemura. Specific impedance of liquids during ultrasonic cavitation. *Japanese Journal of Applied Physics*, 40(7R):4726–4729, 2001.

[177] C.P. Chong, W.P. Chen, H.L.W. Chan, and P.C.K. Liu. Nonlinear behaviour of piezoceramics and piezocomposites under various ac fields. *Sensors and Actuators A: Physical*, 116(2):320–328, 2004.

[178] D. Guyomar, B. Ducharne, and G. Sebald. High nonlinearities in langevin transducer: A comprehensive model. *Ultrasonics*, 51(8):1006–1013, 2011.

[179] C.J.B. Vian, P.R. Birkin, T.G. Leighton, and V.F. Humphrey. Task6 - Ultrasonic cavitation and surface cleaning enhancement. Technical report, Southampton, ISVR reports, 2009.

[180] F.J. Arnold, M.S. Goncalves, L.L. Bravo-Roger, S.S. Muhlen, and Non-members. Electric impedance of piezoelectric ceramics under acoustic loads. *ECTI Transactions on Electrical Engineering, Electronics, and Communications*, 12(2):48–54, 2014.

[181] H.A.C. Tilmans. Equivalent circuit representation of electromechanical transducers: I. Lumped-parameter systems. *Journal of Micromechanics and Microengineering*, 6(1):157, 1996.

[182] S.C. Butler, J.B. Blottman III, and R.E. Montgomery. A thermal analysis of high-drive ring transducer elements. Technical report, DTIC Document, ADA439915 (11,467), Naval Undersea Warfare Centre DIV, Newport, RI, 2005.

[183] B. Verhaagen and D.F. Rivas. Measuring cavitation and its cleaning effect. *Ultrasonics Sonochemistry*, 29:619–628, 2016.

[184] F.E. Fox, S.R. Curley, and G.S. Larson. Phase velocity and absorption measurements in water containing air bubbles. *The Journal of the Acoustical Society of America*, 27(3):534–539, 1955.

[185] R.A. Roy, C.E. Ormonde, P.V. Chitnis, R.O. Cleveland, and R.G. Holt. An acoustic resonator for determining the void fraction of bubbly mercury flows. *The Journal of Acoustical Society of America*, 123(5):3559, 2008.

[186] J. Jiang, K. Baik, and T.G. Leighton. Acoustic attenuation, phase and group velocities in liquid-filled pipes II: simulation for Spallation Neutron Sources and planetary exploration. *The Journal of the Acoustical Society of America*, 130(2): 695–706, 2011.

[187] A. Bozkurt. A lumped-circuit model for the radiation impedance of a circular piston in a rigid baffle. *IEEE Transactions on Ultrasonics Ferroelectrics and Frequency Control*, 55(9):2046–2052, 2008.

[188] Q. Yao and L. Bjorno. Broadband tonpilz underwater acoustic transducers based on multimode optimization. *IEEE Transactions on Ultrasonics Ferroelectrics and Frequency Control*, 44(5):1060–1066, 1997.

[189] J.H. Jeng, X.Q. Bao, V.V Varadan, and V.K. Varadan. A complete finite element-eigenmode analysis for a 1-3 type of piezoelectric composite transducer including the effect of fluid loading and internal losses. In *IEEE 1988 Ultrasonics Symposium Proceedings*, pages 685–688, October, 1988.

[190] M.B. Moffett, J.M. Powers, and M.D. Jevnager. A tonpilz projector for use in an underwater horn. *The Journal of the Acoustical Society of America*, 103(6): 3353–3361, 1998.

[191] Y-C Chen, S. Wu, and C-C. Tsai. Lump circuit modeling and matching consideration on acoustical transmitters for underwater application. *Journal of Marine Science and Technology*, 12(3):152–158, 2004.

[192] S.C. Butler. Triply resonant broadband transducers. *Oceans'02 MTS/IEEE*, 4: 2334–2341, October, 2002.

[193] P.H.G. Crane. Method for the calculation of the acoustic radiation impedance of unbaffled and partially baffled piston sources. *Journal of Sound and Vibration*, 5(2):257–277, 1967.

[194] R. Causse, J. Kergomard, and X. Lurton. Input impedance of brass musical instruments-Comparison between experiment and numerical models. *The Journal of the Acoustical Society of America*, 75(1):241, 1983.

[195] J. Arenas and M. Crocker. Characterization of a cosine-shaped horn. *The Journal of the Acoustical Society of America*, 107(5):2839–2842, 2000.

[196] TPI Electronics. BNC to BNC coax cable assemblies, 2008. URL https://media.digikey.com/pdf/DataSheets/TPIPDFs/BNC_Cable_Assemblies.pdf.

[197] K.S. Won, M.J Kim, and S.J. Im. Study on acoustic radiation impedance at aperture of a waveguide with circular cross section taking account of interaction between different guided modes. *arXiv preprint arXiv:1411.4367, Cornell University library*, 2014.

[198] S. Delgado, L. Leija, and A. Vera. Power meter for hifu transducers using logarithmic amplifiers. In *Health Care Exchanges (PAHCE), 2015 Pan American*, pages 1–5. IEEE, 2015.

[199] R.A. Scholl. Forward and reflected powers. What do they mean? Technical report, Advanced Energy Industries, Inc., 1998. URL http://www.advanced-energy.com/upload/file/white_papers/sl-white7-270-01.pdf.

[200] A. Sou, S. Hosokawa, and A. Tomiyama. Effects of cavitation in a nozzle on liquid jet atomization. *International Journal of Heat and Mass Transfer*, 50(17-18): 3575–3582, 2007.

[201] J.B. Lonzaga. *Capillary jets in normal gravity: Asymptotic stability analysis and excitation using Maxwell and ultrasonic radiation stresses*. PhD thesis, Department of Physics and Astronomy, Washington State University, Dec 2007.

[202] F. Behroozi, J. Smith, and W. Even. Stokes' dream: Measurement of fluid viscosity from the attenuation of capillary waves. *American Journal of Physics*, 78(11): 1165–1169, 2010.

[203] J.W.S. Rayleigh. *The Theory of Sound: Volume II*. Dover Publications, London, Second edition, 1929.

[204] T.G. Leighton. Lateral cartoon explaining the proposed mechanism behind microjetting or misting action of the startream device - email communication. Personal communication, 2014.

[205] D.G. Offin and P.R. Birkin. Observations of intermittent flushing of gas microbubbles, trapped inside the conical chamber, using high speed camera recordings. Personal communication, 2014.

[206] J. Kestin, M. Sokolov, and W.A. Wakeham. Viscosity of liquid water in the range -8^{o}c to 150^{o}c. *Journal of Physical and Chemical Reference Data*, 7(3):941–48, 1978.